UNIVERSITY OF OKLAHOMA

GRADUATE COLLEGE

NEW AND IMPROVED TECHNIQUES FOR CHARACTERIZING BRITTLE ROCK

RESPONSE

A DISSERTATION

SUBMITTED TO THE GRADUATE FACULTY

in partial fulfillment of the requirements for the

Degree of

DOCTOR OF PHILOSOPHY

By

YAWEI LI
Norman, Oklahoma
2017

NEW AND IMPROVED TECHNIQUES FOR CHARACTERIZING BRITTLE ROCK
RESPONSE

A DISSERTATION APPROVED FOR THE
MEWBOURNE SCHOOL OF PETROLEUM AND GEOLOGICAL ENGINEERING

BY

_____
Dr. Ahmad Ghassemi, Chair

_____
Dr. Jean-Claude Roegiers

_____
Dr. Matthew Pranter

_____
Dr. Xingru Wu

_____
Dr. Ahmad Jamili

To my family

Acknowledgements

I would like to express my gratitude to Dr. Ghassemi for his advice and support, I am thankful to companionship and help from every officemate and lab mates, I am also grateful to my family for their patience and support.

Table of Contents

List of Tables

List of Figures

Abstract

To improve the production from shale, stimulation technique such as hydraulic fracturing with proppants is essential. To maximize the effectiveness of hydraulic fracturing, brittle intervals with the minimum creep deformation are preferable as the target zone. A literature review on rock brittleness evaluation is first conducted to analyze the pros and cons of each assessment method. To capture the Class II behavior of brittle shale, damage-controlled compression test is improved using inelastic strain as the control parameter. Indentation test as a simple and fast brittleness evaluation method is used to indent on four lithologies, the indentation displacement (depth) is considered as the brittleness index; Hydraulic fractures are thought to initiate from tensile fractures, however, currently no brittleness indices are derived from tensile failure. This mismatch of failure mechanism renders existing brittleness indices not representative for application in hydraulic fracturing. To mitigate the mismatch, a new brittleness evaluation method is proposed, that is damage-controlled Brazilian test, brittleness of different lithologies have been measured and compared, Brittle-Ductile Transition and strength envelope are obtained, and fracture angle inclination is observed in different confining pressure.

To assess the contribution of creep to closure rate and conductivity loss of hydraulic fractures in gas shale, the viscoelastic characteristics of shale have been investigated. A series of creep tests were conducted on reservoir shale core samples. First, a few uniaxial creep tests were performed on several selected samples, and then multistage triaxial creep tests were carried out at room temperature. Samples used in the

tests come from three different gas shale reservoirs. Creep strain can be described by a power-law function of time. The clay and carbonate contents of these shale samples vary noticeably. Results indicate that rocks with more quartz and less clay have higher elastic moduli. Pseudo-steady creep rate increases linearly with deviatoric stress and higher confining pressures increase the amount of creep strain under the same deviatoric stress. Creep tests at elevated temperatures have also been carried out to show that temperature increase creep rate.

The key findings and contribution of this dissertation include:

1. Indentation test and damage controlled Brazilian test are effective and fast methods to evaluate the brittleness of rocks, the Crack Opening Displacement (COD) can be used as a brittleness index (reverse relation). The indentation depth (displacement) is the brittleness index of indentation test.

2. An alternative damage (inelastic strain) controlled compression test is developed based on the original method (linear combination of load and displacement). A brittleness formulation $\frac{\varepsilon_p}{\varepsilon_r l}$ is derived based on material characteristic length.

3. The Brittle-Ductile Transition of tensile failure is first obtained from confined Brazilian test.

4. Fracture angles in confined Brazilian test progressively increase with confining pressure.

5. Brazilian discs no longer fail in tensile fracturing under high confining pressure when the minimum principal stress in the middle of the disc is compressive; this provides convincing laboratory evidence for the existence of hybrid fractures that constitute transition from extension to shear fractures.

6. Clay content and TOC in shale determine their brittleness and creep properties.

7. For the joint test, multistage compression tests, multistage shear tests and joint stiffness test have been combined to maximize the dataset from one single core plug.

Chapter 1: Introduction and Motivation

The successful exploitation of unconventional shale gas reservoir requires hydraulic fracturing in the brittle interval with low proppant embedment to maximize stimulated rock volume, effective stimulation of the reservoir requires a good knowledge of mechanical properties the reservoir rock. In the past, the geomechanical characterization of various shales was conducted showing that the strength, static elastic moduli and acoustic velocities of these shales depend on the applied pressure, temperature, strain rate, and bedding plain. Also, brittleness indices were formulated to evaluate the propensity of gas shale plays. Traditionally in the laboratory, the most commonly used indices are derived from compression tests.

STATEMENT OF THE PROBLEM

For hard shale, the post-peak failure behavior of compression test is often abrupt and self-sustaining, steady and controlled failure cannot be achieved using conventional axial strain control.

Hydraulic fractures are thought to initiate from tensile fractures, however, currently, no brittleness indices are derived from tensile failure. This mismatch of failure mechanism renders existing brittleness indices not representative for application in hydraulic fracturing.

The fracture closure due to proppant embedment and proppant crushing has been studied, the issue of viscous deformation and creep has been considered, but data and creep models need to be developed for better understanding its contribution to permeability loss.

The mechanical and hydraulic properties of intact rock and jointed rock are needed for numerical simulation of water injection in enhanced geothermal system.

STATEMENT OF THE PURPOSE

To obtain a gradual or controlled failure process of compression test on hard shale, an improved damage (inelastic strain) controlled compression test is attempted.

To mitigate the mismatch of failure mechanism when assessing brittleness, it is reasonable to investigate brittle failure and evaluate brittleness in tensile mode.

Creep data of shale needs to be acquired and creep models need to be developed for better understanding its contribution to permeability loss.

To obtain the required mechanical properties of intact and jointed Welded Tuff, it is necessary to measure the properties in laboratory tests. Triaxial compression and shear tests are commonly used for determining the failure properties of intact rock and the friction properties of a jointed rock specimen, respectively.

DISSERTATION OUTLINE

This dissertation consists of five chapters; this chapter presents the general introduction and motivation of this dissertation.

Chapter 2 includes a detailed and critical literature review on brittleness evaluation. Damage (inelastic strain) controlled compression test is utilized to capture the Class II post-peak failure behavior, the Axial gauge displacement when fracturing process ends (residual strength begins) is proposed as a new brittleness index, different shale samples were tested using inelastic strain control. Sharp cone indentation test is proposed an alternative method to test brittleness quickly, indentation displacement (depth) is considered as the brittleness index, the smaller the displacement is, the more brittle the rock is.

Chapter 3 focuses on the fracturing of confined Brazilian discs. To evaluate brittleness in tensile mode, damage controlled Brazilian tests were performed in

different confining pressures, Crack Opening Displacement (lateral displacement at the end of fracturing process) is considered as the brittleness index, the smaller the displacement is, the more brittle the rock is. Several shale lithologies were tested to compare their brittleness in tensile failure. Controlled triaxial Brazilian test proves to be a versatile experiment that produces multiple sets of results.

Chapter 4 concentrates on the viscoelastic characteristics of gas shale reservoir rocks. A series of creep tests were conducted on gas shale core samples. First, a few uniaxial creep tests were performed on several selected samples, and then multi-stage triaxial creep tests were carried out at room temperature. Samples used in the tests come from three different gas shale reservoirs. A power law function of time can describe the creep strain. Results indicate that rocks with more quartz and less clay have higher elastic moduli. Pseudo-steady creep rate increases linearly with deviatoric stress and higher confining pressures increase the amount of creep strain under the same deviatoric stress.

Chapter 5 presents the results of a testing program to characterize the rock mechanical properties of welded tuff from Newberry Volcano. Multistage triaxial compression tests were performed to determine Young's modulus, Poisson's ratio, and failure envelope. Subsequently, multistage triaxial shear tests were conducted to determine the mechanical properties and shear strength of the fractures developed in triaxial compression tests. Joint roughness coefficient (JRC) and Joint Wall Compressive Strength (JCS) were obtained through back-analysis of the shear tests. It was found that the JCS of tested joints are larger than the intact rock Uniaxial Compressive Strength. The joint surfaces were characterized by a laser profilometer to correlate the surface roughness profile to the JRC from back-analysis of experimental

data. Joint normal stiffness and shear stiffness were estimated, and results demonstrate that a higher confining pressure results in higher joint shear stiffness. The stiffness gradually reduces as the contact surfaces become smoother with additional shear displacement.

Chapter 2: Rock Brittleness and Its Evaluation

INTRODUCTION

Rocks are considered as brittle materials, compared to soil or other ductile geomaterials, because most rocks fail by localized fracturing. The brittle failure of rock is of major interest in reservoir stimulation to enhance unconventional reservoir permeability. A major issue in petroleum reservoir development is the ability to identify the brittle zones that could be targeted for fracturing. Additionally, its understanding is also a prerequisite for engineering practice in other areas such as, mining, tunneling, drilling, designing rock excavation and civil engineering structures. Therefore, the study of brittle fracturing of rocks forms a fundamental research area in rock mechanics and rock engineering.

Brittleness is a comparative rock characteristic. However, the definition and measurement of brittleness are still fuzzy, there are many brittleness definitions and their corresponding measurement methodologies in the literature, and there is no consensus among investigators on the definition and measurement of brittleness in engineering rock mechanics community. This study aims to improve the current understanding of the brittle response of rocks and find robust alternative techniques for its quantitative evaluation.

REVIEW OF BRITTLENESS INDICES

There is no standard definition and measurement of brittleness; these definitions are usually phenomenological observation which only describes the behavior of rock deformation and failure subjected to loading. Morley (1994) and Hetenyi (1966) define brittleness as the lack of ductility. Obert and Duvall (1967) consider solid materials that fail by fracturing at or only slightly beyond the yield stress as brittle. Ramsay (1967)

states that as the internal cohesion is broken, the rock can be considered as brittle. In Glossary of Geology and Related Sciences, brittleness is defined as a property of materials that fracture with little or no plastic flow. Hucka and Das (1974) summarize the brittle characteristics of rock; they state that with greater brittleness, no appreciable deformation before fracturing, higher ratio of compressive to tensile strength, higher internal friction angle, and formation of cracks in indentation are the commonly observed characteristics.

The brittleness indices reported in the literature often are empirical, defined based on rock properties obtained from laboratory and field data (Table 2.1), which do not necessarily represent a whole coherent picture. Hucka and Das (1974) enumerated some measurement principles that could serve as brittleness indicator. Andreev (1995) reviewed around 20 different formulations of brittleness index available in the literature. Singh (1986) investigated the correlation between coal brittleness (B_2 and B_{30}) and the cuttability, penetrability, disintegratability of coal; he concluded that brittle coal is more resistant to cutting, generates less dust and yields larger chunk of coal. Kahraman (2002) examined the relationships between three brittleness indices (B_1, B_2, and B_{22}) and the drillability and borability of rock. He reported that the penetration rates of a tunnel boring machine and rotary drilling machine correlate to B_1 and B_2 well, and the penetration rate of percussion drilling machine correlates to B_{22}. Altindag (2002, 2003) put forward a new brittleness index (B_4) and demonstrated that the drillability of rocks correlates with B_4 very well. Altindag (2010) examined the relations of penetration rate and the modified brittleness index (B_5) and found that the normalized penetration rate by UCS (uniaxial compressive strength) decreased exponentially with increasing brittleness. Goktan (1991) found no correlation between brittleness B_2 and the cutting

efficiency (specific energy) of chisel picks. Goktan and Yilmaz (2005) discovered a negative linear correlation between the normalized specific energy and UCS and B_1. Hajiabdolmajid and Kaiser (2003) proposed a strain-based brittleness index (B_9) that can be used to estimate the shape and extent of the excavation damage zones. Yagiz (2009) introduced a direct measurement method for brittleness (B_{23}) utilizing a punch penetration test. Tarasov and Potvin (2012, 2013) proposed two new brittleness indices (B_{11} and B_{12}) based on the balance between accumulated elastic strain energy and rupture energy; these two indices can quantify the brittleness of Class I and Class II (positive post-peak slope) rock behavior in a monotonic and continuous manner. Meng et al. (2015) critically assessed commonly used brittleness indices and proposed two new indices (degree of brittleness B_{13} and brittle failure intensity) based on post-peak stress-strain curves. Jin et al. (2015) proposed an improved mineralogical brittleness index by including brittle carbonate content; Zhang et al. (2016) conducted a comprehensive review of existing brittleness indices.

In the field of material science and solid mechanics, investigators of glass and ceramic developed various engineering definition of brittleness in connection with hardness (indentation) testing. Bernhardt (1941) considered brittleness as the reciprocal of the Vickers indent diagonal size that just caused one crack to form and showed data for seven glasses. Lysaght (1946) stated that brittleness could be appraised by measuring the first load to induce fracture in Knoop indentations. Mott (1956) stated that the occurrence and extent of cracking around indentation was an inverse measure of brittleness. After the advent of fracture toughness K_{Ic} and critical strain energy release rate G_{Ic}, many material parameters characterizing brittleness incorporated K_{Ic} and G_{Ic}, K_{Ic} or G_{Ic} alone are also used as brittleness indicator (inverse relationship). Puttick

(1980) credits Irwin (1958) for having first recognized the significance of the material parameter $E\gamma_f/\sigma_y^2$ (inverse of brittleness) particularly as it is a measure of crack tip plasticity, the experimental results of Puttick (1980) confirmed that the transitional ring crack radius of Hertzian indentation tests on PMMA is proportional to the material parameter $E\gamma_f/\sigma_y^2$ or K_{Ic}^2/σ_y^2. The general importance of this material parameter in ductile-brittle transitions has been pointed out by Gurney et al (1974). Mouginot (1988) formulated a transitional radius of a blunt punch as a function of $E\gamma_f/H^2$ (H as hardness). Lawn et al (1976) proposed similar parameter $H^2/G_{Ic}E$ or H^2/K_{Ic}^2 as brittleness indicator, Lawn and Marshall (1979, 1986) further compared the different load dependencies of crack size and indentation impression size that led them to propose H/K_{Ic} as a brittleness index. Quinn and Quinn (1997) derived brittleness H_cE/K_{Ic}^2 from an energy ratio or balance at the transitional Vickers hardness plateau of ceramic. Evans and Wilshaw (1976) suggested that comparison of measured crack length c and the indentation size d, (i.e. c/d ratio) could be developed into method of measuring fracture toughness and brittleness. Evans and Charles (1976) and Seghal et al (1996) pursued this, and using a dimensional analysis, they derived that the c/d ratio related well to $K_{Ic}/(Hd^{-\frac{1}{2}})$, but only if a correction factor of $(H/E)^{0.4}$ was applied, thus $(c/d) \propto (K_{Ic}/Hd^{-\frac{1}{2}})(H/E)^{0.4}$. Lawn et al (1980) showed that the ratio of the radius of the plastic zone to the radius of the indentation contact area was not constant but varied with $(E/H)^{0.5}$. Therefore, the relationship of the ratio c/d and brittleness becomes $(c/d)^{-\frac{3}{2}} \propto (K_{Ic}/Hd^{-\frac{1}{2}})(H/E)^{1/2}$, which can be rearranged to $(HE/K_{Ic}^2) \propto c^3/d^4$.

In the civil engineering field, investigators of brittleness also used different formulations of brittleness. In soil mechanics, the brittleness of soil is often described by over-consolidation ratio; in construction engineering, concrete and cement brittleness is usually evaluated by the material parameter (characteristic length) $l_{ch} = EG_f/\sigma_t^2$ and fracture energy G_f. Bazant (1990, 1997) and Hillerborg et al (1985) did intensive research work on measuring the fracture energy and characteristic length of concrete and cement. Hillerborg (1985) and coworkers proposed that $l_{ch} = EG_f/\sigma_t^2$ is a measurement of the intrinsic brittleness of concrete, bigger l_{ch} corresponds to a more ductile concrete. A tendency for more heterogeneous concretes to have larger characteristic lengths has been observed. Incorporating structural size, Elfgren (1989, p.399) introduced a brittleness number as the quotient of the elastic energy stored in the structure and the fracture energy. The elastic energy U_E is controlled by the volume of the structure L^3, whereas fracture energy U_s depends on L^2 only, Elfgren brittleness number is expressed as $U_E/U_s = (L^3\sigma_t^2/E)/(L^2 G_f) = L/l_{ch}$.

In Bazant's (1997) size effect law, the brittle-ductile transition is controlled by a critical structure size $d_0 = G_f E/(\sigma_t^2 B^2 g(\alpha_0))$, Where B and g(α_0) are dimensionless parameters controlled by geometry and loading condition. For geometrically similar structures, when the structure size is significantly smaller that the critical size d_0, the fracture process zone occupies a large portion of the structural volume, and the strength theory governs the failure, size effect diminishes. The failure will shift to LEFM (linear elastic fracture mechanics) as the structure size is significantly larger than d_0. By incorporating the structure size d, Bazant's brittleness number can be expressed as

$$\beta = d/d_0 = d\sigma_t^2 B^2 g(\alpha_0)/(G_f E)$$

Carpinteri (1980) proposed a parameter $s = K_{Ic}/\sigma_y\sqrt{b}$ as a measure of concrete structural brittleness, later (1986) he introduced the energy brittleness number (or Carpinteri number) $s_e = G_f/\sigma_y b$, where b is structural dimension.

Jenq-Shah (1985) proposed a material parameter Q in their two parameter fracture model $Q = E \cdot CTOD_c/K_{IC}^S$, in which Q has the dimension of length, it correlates to brittleness, and the material is more brittle if Q value is higher.

Utilizing a scratch test machine, Richard (1999) found the parameter K_{Ic}^2/σ_c^2 (Irwin, 1958) controls the transition from ductile to brittle failure mode in rock cutting. When the cutting depth is smaller than a critical transition depth d_c, the energy dissipates into the volume of crushed rock. Therefore, the cutting force is proportional to the UCS σ_c and cutting depth. In other case, the energy is consumed by the area of cracks, thus the cutting force is proportional to the fracture toughness K_{Ic} and the square root of cutting depth.

Huang and Detournay (2008) used dimensional analysis and recast the similar intrinsic length scale as $l_i = K_{Ic}^2/\pi\sigma_c^2$, using discrete element simulation, they confirmed that the governing failure mode is controlled by this intrinsic length scale.

Table 2.1 Compilation of brittleness indices

Formula:	Parameter Description:	Test Methods	Reference
$B_1 = \sigma_c / \sigma_t$	σ_c is UCS, σ_t is tensile strength σ_{ci} is crack initiation stress	UCS and Brazilian test	Hucka & Das, 1974
$B_2 = (\sigma_c - \sigma_t)/(\sigma_t + \sigma_c)$			
$B_3 = \sigma_{ci} / \sigma_c$			Altindag, 2003 Andreev, 1995
$B_4 = (\sigma_c \sigma_t)/2$			
$B_5 = \sqrt{\dfrac{\sigma_c \sigma_t}{2}}$			
$B_6 = (\tau_p - \tau_r)/\tau_p$	τ_p and τ_r are peak and residual strength	Compression test	Bishop, 1967
$B_7 = \varepsilon_{li} \times 100\%$	ε_{li} is irreversible longitudinal strain at failure, $\varepsilon_{li} < 3\%$ brittle		Andreev, 1995
$B_8 = \varepsilon_r / \varepsilon_t$	ε_r and ε_t are recoverable and total strain		Hucka & Das, 1974
$B_9 = (\varepsilon_f^p - \varepsilon_c^p)/\varepsilon_c^p$	ε_c^p and ε_f^p are the plastic stain at cohesion loss and frictional strengthening	Compression test (damage controlled)	Vahid & P Kaiser, 2003
$B_{10} = W_r / W_t$	W_r and W_t are reversible and total strain energies	Loading-unloading test	Hucka & Das, 1974
$B_{11} = (M-E)/M$	E and M are pre-peak and post-peak modulus	Compression test (damage controlled)	Tarasov & Potvin, 2013
$B_{12} = E/M$			
$B_{13} = \dfrac{(\tau_p - \tau_r)}{\tau_p} \dfrac{\lg|k_{ac(AC)}|}{10}$	$k_{ac(AC)}$ is the post-peak slope of stress-strain curve	Compression test	Meng et al., 2015
$B_{14} = \dfrac{\sigma_p - \sigma_r}{\varepsilon_r - \varepsilon_p} + \dfrac{(\sigma_p - \sigma_r)(\varepsilon_r - \varepsilon_p)}{\sigma_p \varepsilon_p}$	p signifies peak stress or strain, r indicates residual stress or strain		Xia et al., 2017
$B_{15} = H \times E/K_{IC}^2$	K_{IC} is fracture toughness, H is hardness	Hardness and toughness test	Quinn & Quinn, 1997
$B_{16} = H^2/K_{IC}^2$			Lawn1979 & Marshall, 1986
$B_{17} = H/K_{IC}$			
$B_{18} = (H_m - H)/K$	H and H_m are macro and micro-hardness, K is bulk modulus, γ_f is fracture surface energy	Hardness or Indentation test	Honda & Sanada, 1956
$B_{19} = E\gamma_f/H^2$			Mouginot, 1988
$B_{20} = \gamma P^{-1/4}\left[\dfrac{C}{a}\right]^{3/2}$	P is indentation load, C is crack size, a is contact size		Sehgal, 1999
$B_{21} = S_{20}$	S_{20} is the percentage of fines less than 11.2 mm	Impact test for NTNU model	Blindheim, & Bruland, 1998
$B_{22} = q\sigma_c$	q is the percent of debris (<0.6 mm diameter)	Protodyakonov impact test	Protodyakonov, 1962

$B_{23}=F_{max}/P$	F_{max} is maximum force, P is penetration depth	Indentation test	*Yagiz, 2009*
$B_{24}=P_{inc}/P_{dec}$	P_{inc} and P_{dec} are average increment and decrement of forces		*Copur et al., 2003*
$B_{25}=K_b$ $K_S P/h^2=S_t-K_b P$	K_S is shape factor, P is applied load, h is distance between loading points, S_t is tensile strength	Point load test	*Reichmuth, 1967*
$B_{26}=(W_{qtz}+W_{carb})/W_T$	W_{qtz}, W_{dol} and W_{carb} are weight of quartz, carbonate and dolomite, W_T is total mineral weight	Mineral composition	*Jin,2015*
$B_{27}=W_{qtz}/W_T$			*Jarvi, 2007*
$B_{28}=(W_{qtz}+W_{dol})/W_T$			*Wang et al.,2009*
$B_{29}=S_F G_F F_F$	$S_F G_F F_F$ are stiffness, texture, and foliation factors		*Suorineni, 2009*
$B_{30}=sin\varphi$	Φ is internal friction angle	Well log or compression test	*Hucka & Das, 1974*
$B_{31}=45°+\varphi/2$			
$B_{32}=(E_n+v_n)/2$	E_n and v_n are normalized dynamic Young's modulus and dynamic Poisson's ratio	Density and sonic logging data	*Rickman, 2008*
$B_{33}=E/v$	E is Young's modulus, v is Poisson's ratio, ρ is density		*Luan et al., 2014*
$B_{34}=E\rho/v$			*Sun et al., 2013*
$B_{35}=OCR^b$	OCR is over-consolidation ratio, b is a constant	In-situ stress ratio	*Ingram,1999*
$B_{36}=\dfrac{EG_f}{\sigma_t^2}=\dfrac{K_{Ic}^2}{\sigma_t^2}$	G_f is fracture energy	Size effect test	*Irwin, 1958* *Hillerborg, 1976 & Puttick, 1980*
$B_{37}=\dfrac{G_f E}{\sigma_t^2 B^2 g(\alpha_0)}$	$g(\alpha_0)$ is geometry-dependent function of cracked specimen, B is calculated from curve fitting		*Bazant, 1987*
$B_{38}=\dfrac{d\sigma_t^2 B^2 g(\alpha_0)}{G_f E}$			
$B_{39}=L\sigma_t^2/(EG_f)=L/l_{ch}$	l_{ch} is the characteristic length		*Elfgren, 1989*
$B_{40}=K_{Ic}^2/\sigma_c^2$	σ_c is UCS		*Richard, 1999*
$B_{41}=K_{Ic}/\sigma_y\sqrt{b}$	σ_y is yield strength, b is size of structure		*Carpinteri, 1991*
$B_{42}=G_f/\sigma_y b$			
$B_{43}=\dfrac{E\cdot CTOD_c}{K_{IC}^S}$	$CTOD_c$ is critical tip opening displacement		*Jenq&Shah,1985*

CRITICAL APPRAISAL OF EXISTING BRITTLENESS INDICES

The existing brittleness indices and their formulations are summarized in Table 2.1. They are categorized into four broad groups by the measurement method. Group A (B_1 to B_{14}) is the indices extracted from compression test; stress-strain curves, and the rock strengths, deformations, and strain energy are the input parameters. The brittleness indices of Group B (B_{15} to B_{25}) are measured by small scale tests such as indentation, hardness, punch penetration, and impact test. Group C (B_{26} to B_{35}) is calculated from well logging data. Group D (B_{36} to B_{43}) is size effect (nonlinear fracture mechanics) based brittleness indices. Most indices in group B and D are variants of intrinsic material constants such characteristic length EG_f/σ_t^2 (or K_{Ic}^2/σ_t^2) and fracture energy (Irwin, 1958).

Indices Derived From Stress-Strain Curve

Because of the simplicity and availability of rock compression tests, rock strengths and deformation characteristics can easily be extracted from stress-strain curves. Therefore, indices derived from stress-strain curve are common.

Compressive strength to tensile strength ratio ($B_1=\sigma_c/\sigma_t$) is the most widely used index to evaluate rock brittleness due to its simplicity; it is widely believed that a higher B_1 corresponds to a more brittle rock (Hucka and Das 1974, Kahraman 2002, Suorineni et al. 2009, Heidari et al. 2014). However, Nejati and Ghazvinian (2014) reported some test results which contradict this notion of B_1. In their work, they have found that hard Onyx marble with almost no plastic deformation under uniaxial compression has a smaller B_1 value than that of sandstone and a soft limestone with more plastic deformation. Another example which renders the B_1 questionable has been reported by

Goktan (1991); it is found that the strength ratio for sandstone immersed in water for up to 3 months was larger than that of dry sandstone, which contradicts to the fact that water weakens sandstone (Hadizadeh, 1991; Baud, 2000). Altindag (2002, 2010) found no meaningful relationship between B_1 and other rock properties. The UCS and tensile strength data from Altindag (2009, 2010), Yarali (2011) and Wang Yu (2014) were used to show the variation of B_1 with UCS; as illustrated in Fig. 2.1, rocks samples from different lithologies and different UCS could have the same B_1, their brittleness would be different if other indices were used. Fig. 2.1 also illustrates that B_1 mostly falls between 8 and 20. In addition to the above issues, B_1 is strongly influenced by the stress state; high confining pressures make rock more ductile, however the B_1 value will be higher due to use of a uniaxial tensile strength, T. thus as defined, the B_1 index is not self-consistent with confining pressure. It is evident that B_1 contains no information on elastic strain, inelastic strain, and the post-peak energy dissipation and it is purely phenomenological. However, the macro failure modes of the rock under uniaxial compression are linked to B_1, a high B_1 value corresponds to axial splitting, and low B_1 value links to shear fracturing (Nemat-Nasser and Hori, 1993), and thus B_1 can be a quantifier of failure mode. Index B_2 has the same limitations as B_1 because it is a function of B_1 when the denominator and numerator are divided by tensile strength. Cai (2010) pointed out that Griffith's failure criterion fails to predict the tensile strength of rock from UCS because it only applies to crack initiation instead of final failure, thus $\sigma_{ci}/\sigma_t = 8$ holds true instead of $\sigma_c/\sigma_t = 8$. Therefore, the index B_3 is equivalent to $8/B_1$.
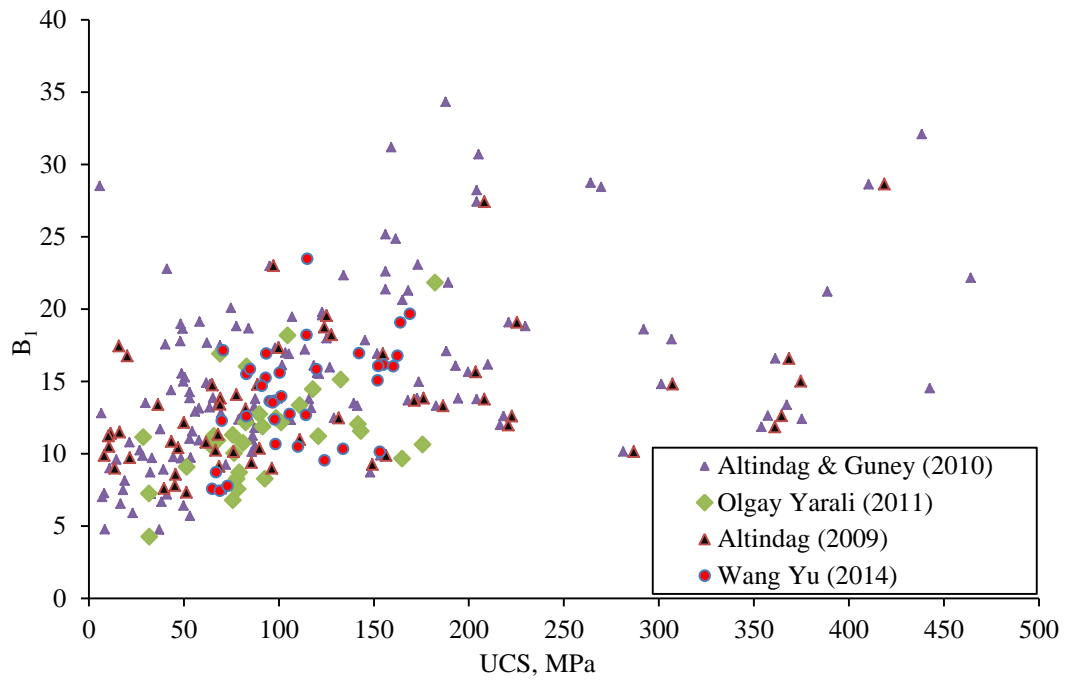
Figure 2.1 Relation between B_1 and UCS of different rocks, digitized from the

dataset of Altindag et al.

Altindag (2002, 2003a, 2010) introduced two indices $B_4 = (\sigma_c \sigma_t)/2$ and $B_5 = \sqrt{(\sigma_c \sigma_t)/2}$ to relate brittleness to drillability. A good correlation between the penetration rate, specific energy, and B_4 has been established. However, similar to B_1, B_4 and B_5 indices contain no information on elastic, plastic strain and post-peak energy dissipation, the physical meaning of the strength products is not clear. The same datasets from Altindag (2009), Yarali (2011) and Wang Yu (2014) are used to illustrate the correlation of B_4 to UCS. As shown in Fig. 2.2, B_4 is a quadratic function of UCS. This analysis demonstrates that B_4 and B_5 are good indicators of rock strength; the research work conducted by Altindag could also prove that rock drillability is strongly influenced by its strength (UCS), which is the most common input parameter in various rock-drilling models. Therefore, using B_4 or B_5 to describe brittleness is implausible,

and there is a good correlation between B_4 or B_5 and drillability, they are unnecessary considering that UCS is already a good indicator of drillability of rocks.
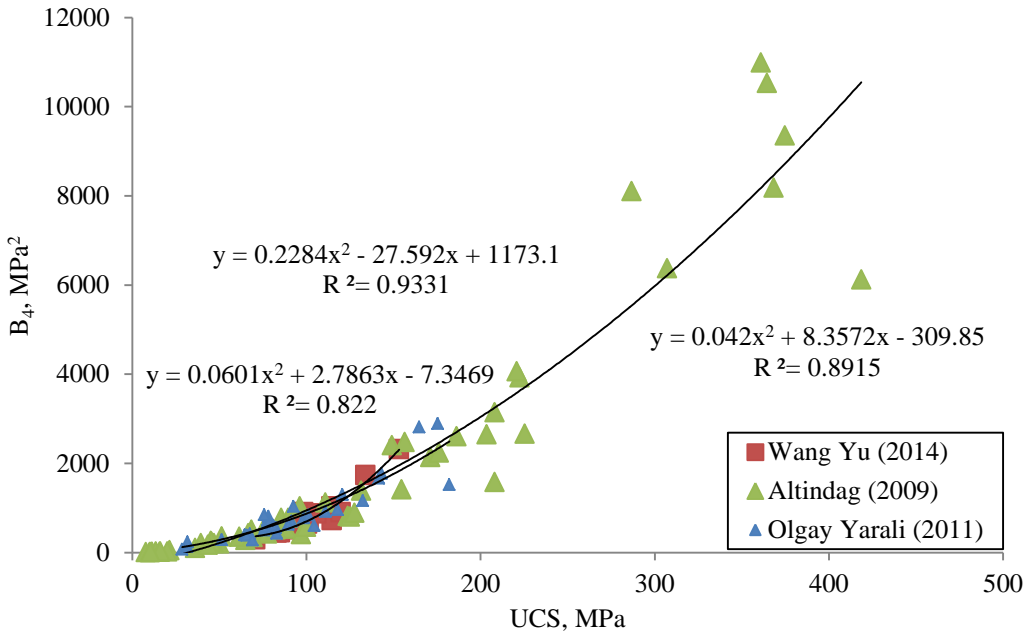
Figure 2.2 Relation between B_4 and UCS of different rocks

Bishop (1967) proposed to use index $B_6=(\tau_p-\tau_r)/\tau_p$ as a function of peak strength and residual strength. As pointed out by Hajiabdolmajid and Kaiser (2003), this index neglects the strength loss rate (post-peak descending slope) and the stress path followed between peak and residual strength levels. Therefore, the brittleness of rocks with the same peak and residual strengths but with different post-peak slope is difficult to distinguish, a good example is in Fig.2.32, the B_6 brittleness of Indiana Limestone and Berea Sandstone would be identical, this contradicts to the brittleness comparison in Fig.2.29. In rock mechanics literature, the brittle-ductile transition of the same rock lithology under different confining stress level shows that residual strength of different sample increases with confining pressure, the ductility also increases, B_6 applies to this

16

case. However, using B_6 to compare brittleness of different rock lithologies may lead to a contradiction.

$B_7 = \varepsilon_{li} \times 100\%$ is an index based on the irreversible longitudinal strain at or before failure; the inelastic strain (contains plastic and damage) can be obtained from loading-unloading tests. The disadvantage of this index is that the unloading point on the stress-strain curve is difficult to determine if the peak strength is unknown. $B_8 = \varepsilon_r/\varepsilon_t$ has a similar physical meaning as B_7 and emphasizes the fraction of reversible strain in the total strain; B_8 has the same drawbacks in measurements with B_7. Moreover, the post-peak strain energy dissipation is very important in brittleness measurement; neither B_7 nor B_8 can provide any information on post-peak strain energy consumption. These two brittle indices can be used if destructive testing (fracturing the rock samples) are not allowed.

$B_9 = (\varepsilon_f^p - \varepsilon_c^p)/\varepsilon_c^p$ assumes that the cohesive strength and frictional strength of rock are not mobilized simultaneously (Hajiabdolmajid, V., and P. Kaiser, 2003). The main shortcoming of B_9 is that the measurement of ε_f^p and ε_c^p requires a specialized damage controlled compression test which takes around 8 hours to complete.

$B_{10} = W_r/W_t$ is the ratio of reversible strain energy to the total strain energy at the peak stress, resembling the form of B_8. The total energy and elastic energy are represented graphically by the areas constrained by the loading and unloading stress-strain curve with the x-axis (Hucka and Das 1974). B_{10} suffers the same drawbacks with B_7 and B_8.

Tarasov and Potvin (2012, 2013) stated that post-peak slope M of stress-strain curve should be considered as characteristic of brittleness. They proposed $B_{11} = (M-E)/M$

and $B_{12}=E/M$ as the ratio of the post-peak rupture energy to the elastic energy withdrawn from the specimen during the failure process; they suggest B_{11} and B_{12} can be used to assess rock brittleness from absolute brittleness to ductility monotonically under triaxial compression. To derive the final formulation, an assumption was made for simplification, the unloading modulus at different stress levels in the post-peak period was the same and equal to the elastic modulus E. Therefore, the brittleness is only controlled by E and the post-peak modulus M. This assumption indicates that if different rocks have the same E and M, their brittleness are the same. These two indices suffer a drawback for not considering the peak strength and residual strength. With the same E and M, fracturing of higher strength rock certainly consumes more strain energy. It should be noted that these two brittleness indices change with specimen size (brittleness increases with size) as mentioned by Tarasov and Potvin (2012, 2013).

Hucka and Das (1974) proposed that rock brittleness could be assessed by the inner friction angle obtained from Mohr-coulomb's strength envelope. Indices from friction angle have rarely been used, except by Singh (1986) who investigated the cutting resistance of three types of coal with different brittleness and friction angle. Friction angle-based indices can be criticized for relating to B_1; a higher friction angle would correspond to a high strength ratio, Fig. 2.1 illustrates that rocks of different strength or stiffness and lithology could have the same strength ratio. Naturally they could have the same friction angle too, although the relationship between strength ratio B_1 and friction angle has never been systematically investigated.

A common drawback for indices derived from stress-strain curves is that the post-peak behavior depends on the stiffness of loading frame, a soft frame can cause

explosive failure; a stiff frame coupled with damage control produces real stress-strain curves.

Indices Derived From Small Scale Test

In ceramic engineering, various combinations of hardness, stiffness, fracture toughness and other parameters have been used to describe brittleness. Lawn and Marshal (1979, 1986) introduced $B_{16}=H^2/ K_{IC}^2$ and $B_{17}=H/K_{IC}$ as brittleness indices. Quinn and Quinn (1997) proposed $B_{15} =H{\times}E/K_{IC}^2$ as an alternative brittleness index of ceramic by incorporating modulus E. These three indices are very similar to the material characteristic length K_{Ic}^2/σ_t^2 and its variants used in concrete or cement brittleness, because their roots can be traced back to an energy balance theory whereby the energy for crack formation and propagation is converted from accumulated strain energy $\sigma^2/(2E)$. Analogous to Puttick (1980)'s finding for Hertzian ring crack size, Quinn and Quinn (1997) observed the proportionality of the inverse of transitional indentation size (or indentation depth) at cracking to B_{15}. B_{15} has practical potential for quick rock brittleness evaluation if the indentation depth at fracturing can be accurately measured. It should be noted that conical or Vickers indentation is more advantageous than Hertzian or Brinell ball indentation because indentation (impression) size on the indented material by conical or Vickers indenter can change continuously and proportionally to indentation depth. For Hertzian indentation, stiff balls of various sizes are required.

Yagiz (2009) proposed to use punch penetration tests to measure brittleness, described by B_{23}. The force is applied and until the indenter penetrates 6.5 mm into the rock surface. The brittleness of the rock is the slope of the force-penetration graph. This brittleness index appears to be an indirect measurement of rock stiffness or rock

strength, rather than brittleness, without any information of post-peak strain energy consumption.

B_{26}, B_{27}, and B_{28} are mainly used in the selection of fracturing intervals in shale gas reservoir. These mineralogy based indices are used along with other brittleness indices derived from well log. The drawback of these indices is that they do not consider the influence of the stress state and diagenesis on rock brittleness. Rocks with the same mineral compositions in both type and quantity can have different brittleness under different confining pressure and different diagenesis process.

Suorineni et al. (2009) introduced the rock tenacity rating index (RTRI) B_{29} to describe the ability of rocks to resist stress-induced damage and established a correlation between the brittle parameters of Hoek-Brown damage initiation criterion and the RTRI. Mineral stiffness variation, grain size, and foliation are incorporated into the index. Thus, the determination of the RTRI is rather complex, the stiffness of an individual mineral must be known and a petrographic analysis must be conducted to determine the mean grain size of the minerals. Besides, a foliation factor need to be calculated based on the percentage of platy/prismatic minerals.

Indices Derived From Size Effect of Quasi-Brittle Materials

Size effect of quasi-brittle materials has been well documented and well established through many studies. In civil engineering, investigators of concrete failure behavior had been using Weibull's statistical theory to explain the size dependence of structural strength, until Hillerborg (1985), Bazant (1990) and coworkers developed deterministic size effect theory. The mismatch of strain energy ($\propto (\sigma^2/2E) \times$ volume D^3) in a solid and the energy needed by fracture ($\propto G_f \times$ area D^2) would cause a

deterministic (cubic-square) size effect if the structure scales up or down, for the same material, small structure fails with a ductile response, whereas large structure fails in a brittle manner. Brittle response of a quasi-brittle solid depends on its size, whereas the fracture energy G_f and the internal characteristic length are intrinsic material constants that can quantify the brittleness of the solid. Bazant and coworkers have developed a size effect method to measure the two parameters by loading several geometrically similar notched specimens of different sizes to fracturing without resorting to measuring post-peak slope or area. The drawback of the size effect method is that sample preparation is time consuming, the requirement for sample homogeneity is high, and the size range of geometrically similar samples should at least be 1:4.

Among all the brittleness indices derived from characteristic length, indentation based indices have the potential of practical application for evaluating rock brittleness due to the simplicity of the test and the fact that the indentation depth at crack transition is proportional to material characteristic length.

BRITTLENESS EVALUATION USING INDENTATION TEST

Indentation is one powerful test technique for the investigation of deformation and fracture responses in brittle solids. It is widely used in material science to evaluate material parameters such as hardness and toughness with great simplicity. The indentation technique for metals, ceramic and glasses is well established and standardized, for brittle solids like ceramic and glasses, the transitional indentation depth (impression size) at cracking is found to be proportional to a material characteristic length $E G_f / \sigma_t^2$ (or K_{Ic}^2 / σ_t^2). However, the experimental results of the intrinsic characteristic length (brittleness) affecting indentation fracturing is lacking for

rocks in the literature, All previous rock indentation testing focus on the correlation between hardness and UCS. This section focuses on the relationship between the critical or transitional indentation depth at cracking and the intrinsic characteristic length.

Experimental Program

The testing procedure in this study is in line with the proposed/recommended standard indentation method by Szwedzicki (1998). The standardized indenter has a conical tip of the same shape as a conical platen used to determine the point load strength index (Brown, E.T. 1981 and Farmer, 1992). The conical indenter has a 60° cone and 1 mm tip radius. The indentation testing is illustrated in Fig. 2.4. Because radial strain of the cylindrical samples is very sensitive to micro-cracking, a radial strain extensometer is installed on samples to measure the radial strain.

Figure 2.3 Indenter used in this investigation
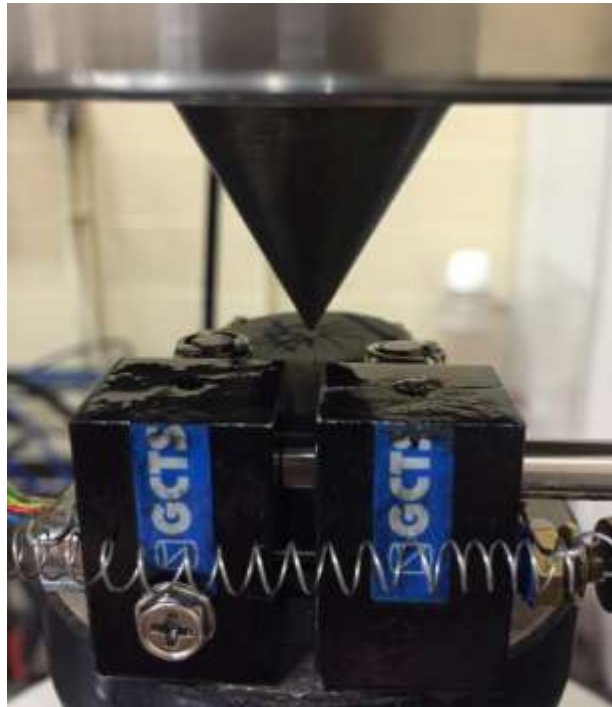
Figure 2.4 Indentation testing configuration

The majority of tested samples in this work have a dimension of 1-inch diameter and 1-inch length; a few rock pieces of irregular shape were also tested. The lithologies of the tested samples are Grey Berea Sandstone and Indiana Limestone. All cylindrical samples are cut into shape using a rock lathe technique where a rock piece of irregular shape is clamped in the axial direction and rotated against a high-speed saw blade. Over 20 samples are turned into cylindrical shape in rock lathe and tested. The indentation loading rate is set to 0.2 mm/min. After a rock cylinder is split into two halves by indenting at the center, further indentation on the two halves (two semi-circular cylinders or half cylinders) were conducted with the same procedure of cylinder indentation.

Experimental Result Interpretation

Figure 2.5 Amplified view of indented Grey Berea Sandstone surface
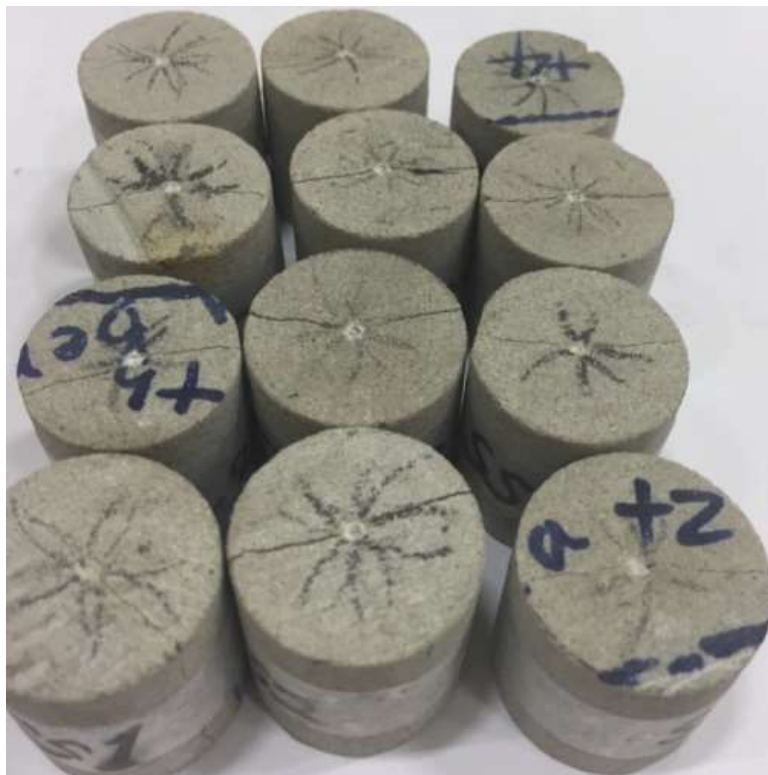
Figure 2.6 All indented Sandstone cylinder
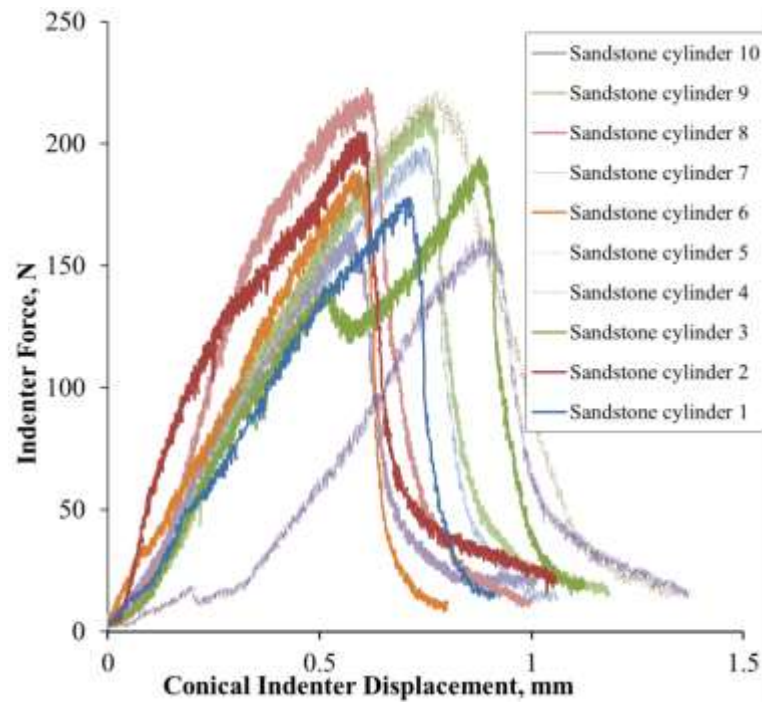
Figure 2.7 Load-Displacement curves of indentation on Sandstone cylinder center

13 Grey Sandstone cylinders were indented; load-displacement curves and load-radial strain curves were recorded. It appears that the load-displacement curves of Grey Sandstone indentation are more uniform than those of Limestone cylinder indentation, the indentation crack initiation depth is taken as the displacement at peak load; when the peak load is reached, Sandstone cylinder is split into two halves after a very small displacement. The averaged crack initiation depth is 0.68 mm, and the average final indentation depth is 1.04mm.

Table 2.2 Indentation crack initiation depth, final indentation depth and peak load of Sandstone cylinder indentation

Sample #	1	2	3	4	5	6	7	8	9	10	11	12	13	Aver
Initiation depth, mm	0.69	0.58	0.51	0.78	0.75	0.57	0.73	0.60	0.74	0.57	0.66	0.88	0.74	0.68
Final depth, mm	0.91	1.22	1.10	1.40	1.22	0.75	0.97	0.91	1.06	0.83	0.93	1.31	0.97	1.04
Peak load, Newton	177	204	191	160	218	184	196	220.	213	163	194	193	167	191

Figure 2.8 Indented Indiana Limestone cylinders, note the chipped area around the crater
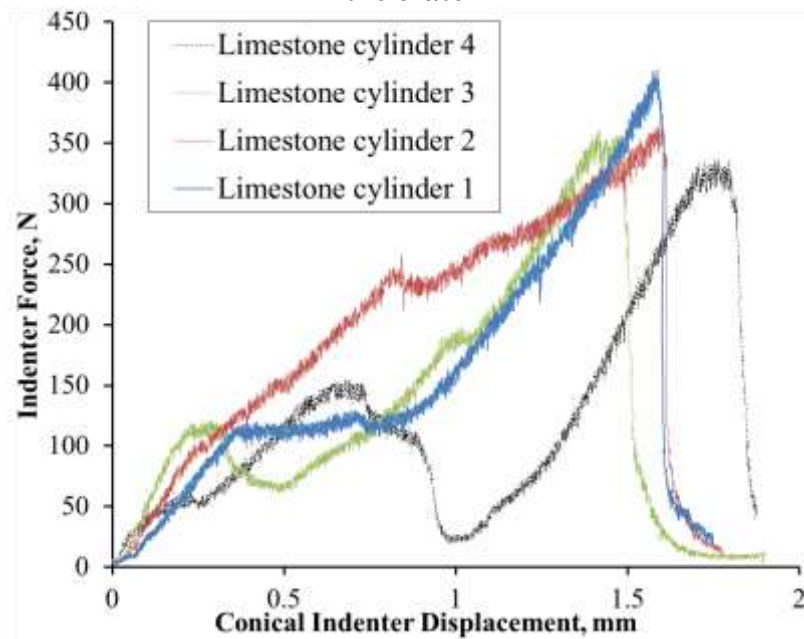
Figure 2.9 Load-Displacement curves of indentation on Limestone cylinder center

For Indiana Limestone cylinder indentation, the surface cracking (chipping around the crater) consistently appears before the indentation depth reaches 0.5mm; the crack initiation depth is taken as the point of first slope change on load-displacement curves (where first chipping occurs). The load-displacement curves appear considerably

different from those of Grey Berea Sandstone. It appears that Indiana Limestone cylinder fractures more than one times on the same load-displacement curve. The averaged initiation depth at failure (splitting) is 0.41 mm.

Table 2.3 Crack initiation depth and peak load of Limestone cylinder indentation

Sample #	1	2	3	4	average
Initiation depth, mm	0.33	0.8	0.25	0.24	0.41
Peak load, Newton	409.12	370.81	357.16	331.24	367.08
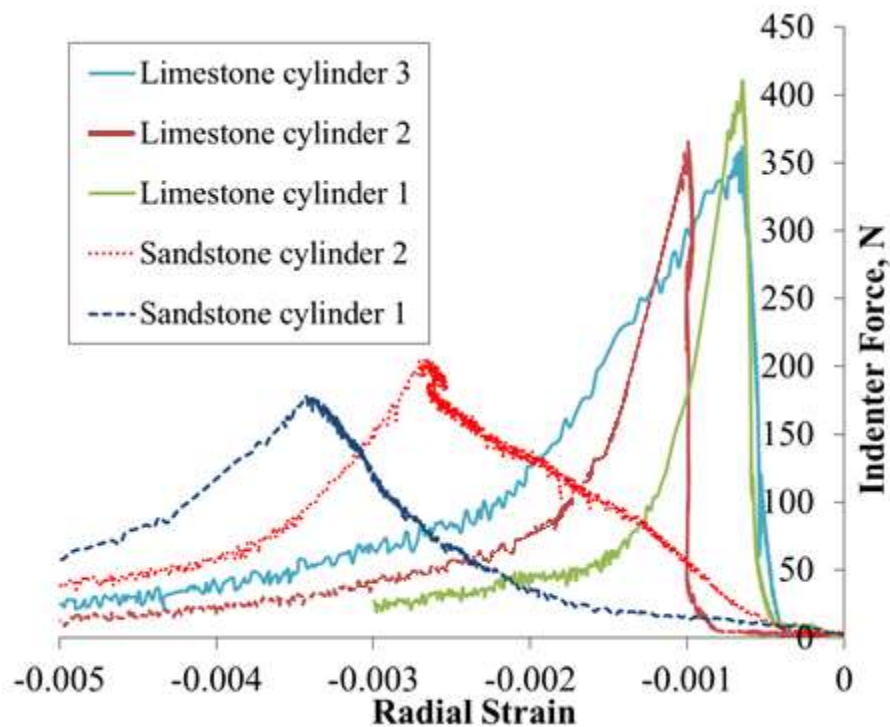
Figure 2.10 Comparison of radial strain response of the two rock types

From Fig. 2.10, one can see that the radial expansion of Grey Berea Sandstone at fracture initiation (peak load) is much larger than that of Indiana Limestone.

Figure 2.11 Indented semi-circular cylinder of Grey Berea Sandstone, note the fractures are more planner than that of Limestone
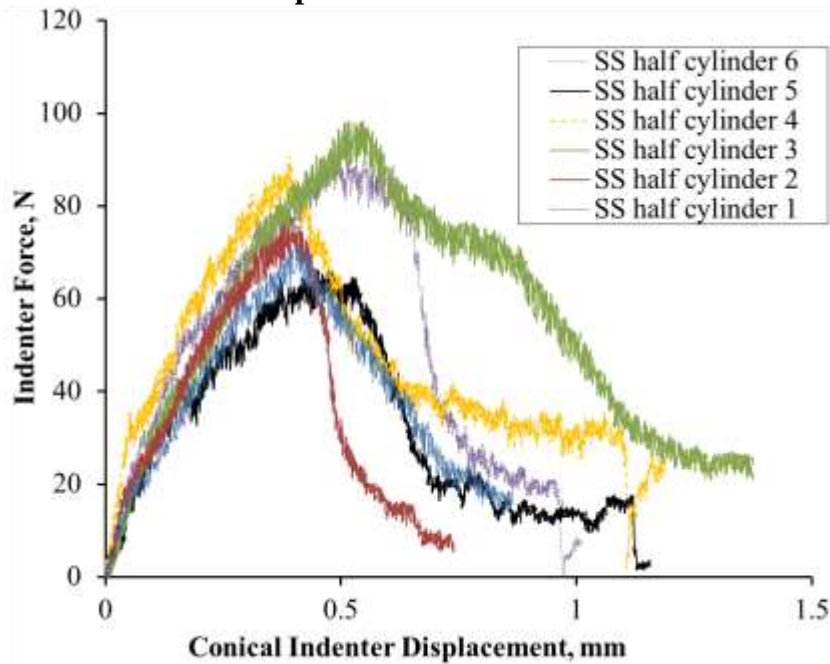
Figure 2.12 Load-Displacement curves of indentation on semi-circular Sandstone cylinders

In Fig. 2.12, one can observe that semi-circular cylinder behave more ductile than a full cylinder, as the post-peak curves of full cylinders drop more steeply than those of semi-circular cylinder. This indicates that the sample size affects the post-peak behavior. This is in line with cubic-square energy scaling of solid fracturing, as the rock volume reduces to one half, but the fracture surface area is approximately the same, the strain energy accumulated in a half cylinder is not enough to split the semi-circular cylinder,

28

more displacement after peak load is needed to complete the fracturing process. One important observation is that the averaged final displacements or depths are approximately the same for full cylinder and semi-circular cylinder.

Table 2.4 Indentation crack initiation depth, final indentation depth and peak load of Sandstone semi-circular cylinder indentation

Sample #	1	2	3	average
Crack initiation depth, mm	0.39	0.42	0.52	0.44
Final depth, mm	0.93	0.73	1.35	1.00
Peak load, Newton	70.20	73.45	97.52	80.39
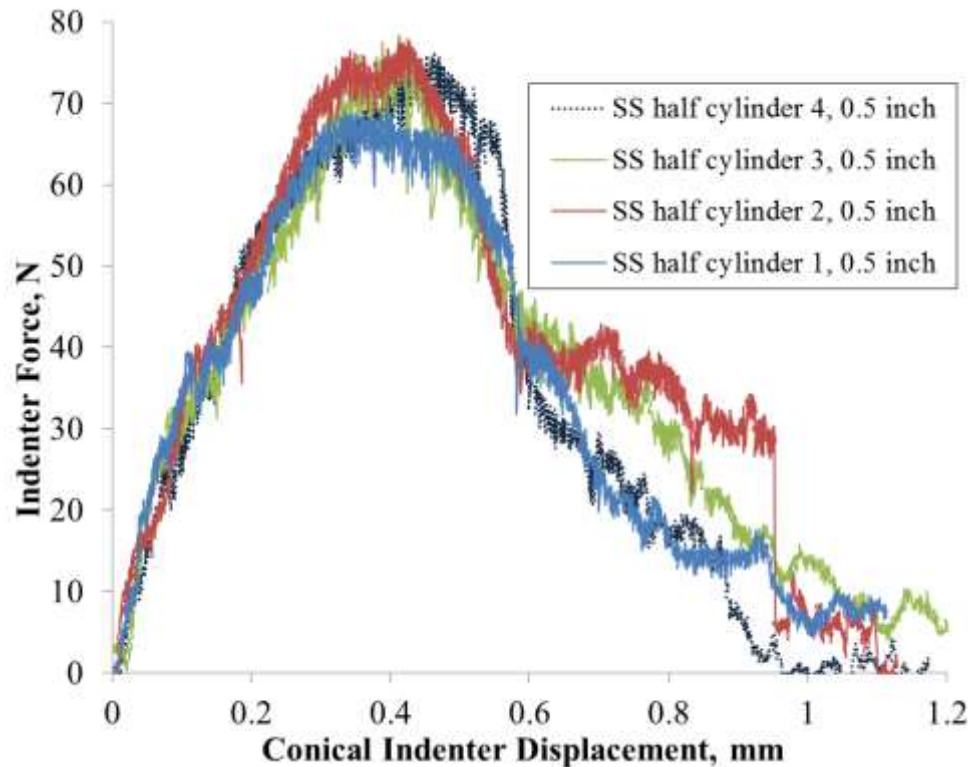
Figure 2.13 Load-Displacement curves of indentation on half Sandstone cylinder, 0.5-inch thickness

Some semi-circular cylinders (1-inch tall) were cut into 0.5-inch tall semi-circular discs to test the influence of sample thickness on indentation depth (displacement) at final fracture separation. The results as shown in Fig. 2.13 indicate that the final displacement is around 1 mm; this provides evidence that the final indentation depth at fracture separation is geometry and thickness independent.

29

Figure 2.14 Indented semi-circular cylinders of Limestone, note the fractures are more tortuous than Grey Berea Sandstone, and the near crater chipping is significant
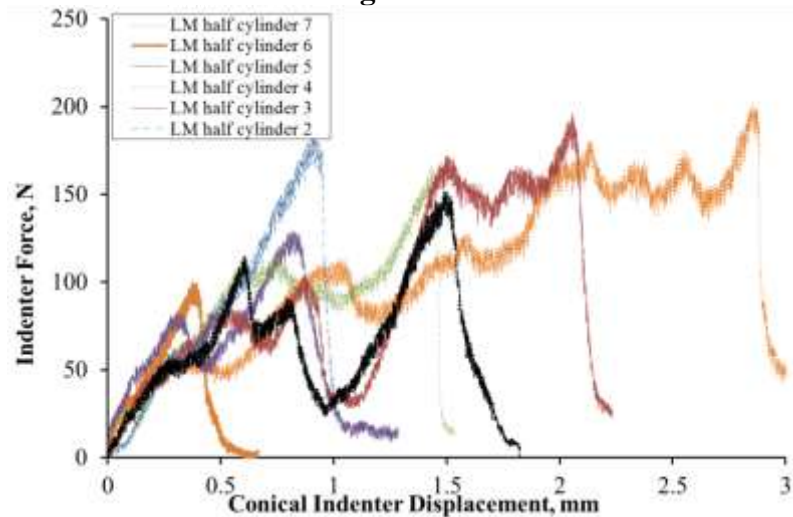
Figure 2.15 Load-Displacement curves of indentation on half Limestone cylinder

The load-displacement curves of Limestone semi-circular cylinder indentation are even more serrated and tortuous than that of a full cylinder indentation. From Fig. 2.7 and Fig. 2.12, for Grey Berea Sandstone, the semi-circular cylinder indentation behavior is more ductile than a full cylinder indentation, as can be observed from the post-peak slopes. However, for Indiana Limestone indentation, the post-peak slopes of semi-circular cylinder is as steep as that of a full cylinder in Fig. 2.9, that indicates

30

Indiana Limestone still behaves in a brittle manner when the volume is reduced to halves. From this perspective, Indiana Limestone is more brittle than Grey Berea Sandstone.

Table 2.5 Indentation crack initiation depth and peak load of Limestone semi-circular **cylinder indentation**

Sample #	1	2	3	4	5	6	7	Average
Initiation depth, mm	0.39	0.32	0.24	0.11	0.40	0.11	0.48	0.29
Peak load, Newton	151.69	182.49	189.97	162.54	182.488	99.84	199.47	166.92

Figure 2.16 Indented Marcellus shale disc, note the fractures are very planner and parallel with the bedding plane
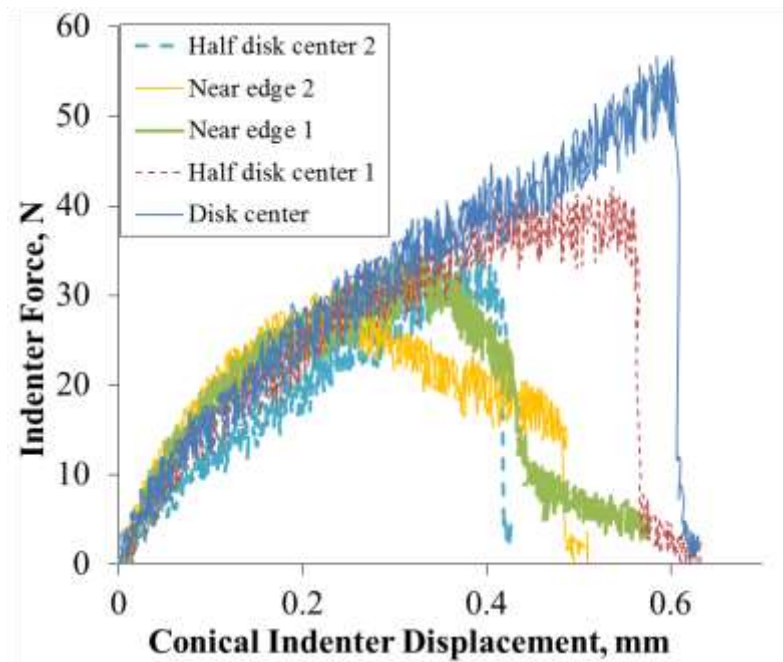
Figure 2.17 Load-Displacement curves of indentation on Marcellus shale disc

The same phenomenon is observed for the indented shale disc, i.e., the sample size affects the post-peak slopes, but the final indentation depths at the five indented locations on the disc are approximately the same (0.6mm). The depth for 'half disc center 2' location can be considered as an anomaly data point, as data point scattering cannot be avoided.
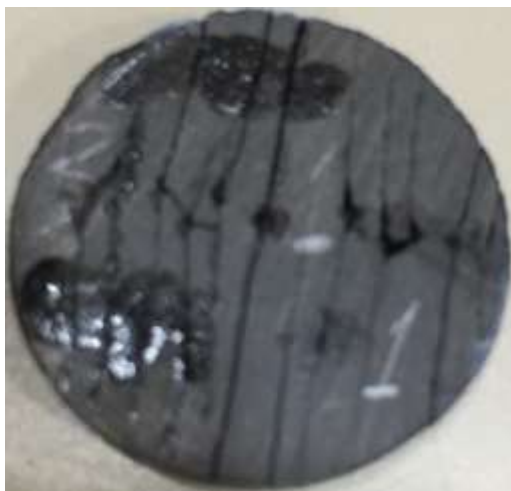
Figure 2.18 Indented Barnett shale disc, note the fractures are very planner and parallel with the bedding plane
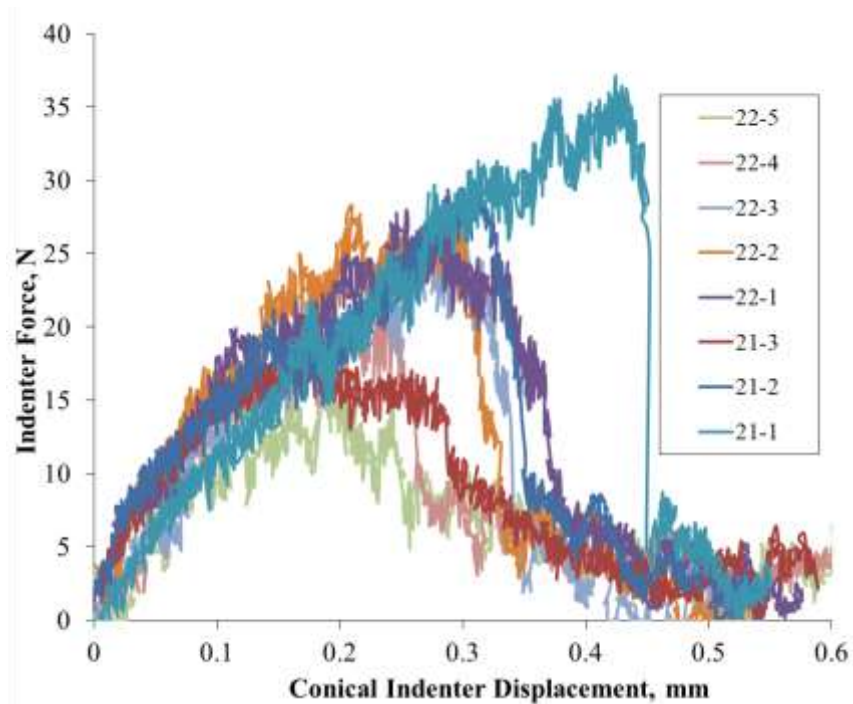
Figure 2.19 Load-Displacement curves of indentation on Barnett shale disc

Summary

Indentation test is capable of capturing the brittle and ductile behaviors of rocks, the crack initiation depth and post-peak slopes are strongly affected by the indented rock volume; this is caused by the energy balance controlled size effect. After a rock cylinder is indented into two halves at the center, further indentation on the semi-circular cylinder will behave in a more ductile manner. But the final indentation depth at the completion of the fracturing process (when the indenter force reaches zero) can be considered as constant for a certain rock type. It is reasonable to hypothesize that the final indentation depth is a form of or a reflection of the material characteristic length. The effect of cylinder height and irregular sample shapes on final indentation depth needs to be further investigated. It should be noted that the indentation size effect reported above is different from the Indentation Size Effect (ISE) in previous literature, ISE refers to the hardness (or Load displacement or area ratio) depends on indentation

load (Quinn and Quinn, 1997), whereas the indentation size effect observed in this study appears to be controlled by energy balance.

Indiana Limestone is more brittle than Grey Berea Sandstone, as can be observed on the comparison of the full cylinder and half cylinder post-peak curves, half Indiana Limestone cylinder still behaves in a brittle manner, because the post-peak slopes are as steep as those of full cylinder. More serrated and tortuous load-displacement curves of indentation correspond to a more brittle rock type; this is also confirmed by the finding and observation of Copur and Bilgin (2003).

More precise load and displacement measurement are needed, as the peak load for indentation fracturing is much lower than that of a regular compression test. A load cell of smaller load capacity and a small range displacement sensor would be preferable.

PROXY PARAMETERS FOR MATERIAL CHARACTERISTIC LENGTH

Many materials exhibit a wide range of fracture mode, depending on the test conditions, ranging from ductile/plastic failure to fracturing. This change in fracture mode is usually termed fracture transition. Fracture transition has been investigated extensively for brittle and quasi-brittle material in solid mechanics. Irwin (1958) proposed the material parameter $E\gamma_f/\sigma_y^2$ (or $(\frac{K_C}{\sigma_y})^2$) particularly to characterize the size of crack tip plastic zone. It is generally termed material characteristic length or intrinsic length scale. It is actually a critical structure length or size at which the strain energy stored in the solid at peak stress equals to energy required to fracture the solid. The expression $E\gamma_f/\sigma_y^2$ is the ratio of fracture energy density to strain energy density. This parameter controls fracture transition, when structure size is bigger than this critical

34

length, the solid will behave in very brittle manner (exhibit Class II stress-strain or load-displacement curve if stable fracturing or monotonic damage control is performed), in the other case, the solid will behave in a ductile manner under load. It should be noted that the critical structure length or size depends on the loading configuration and solid geometry, the value of the parameter is not the same for tensile, compression and indentation loading. The crack tip nonlinear zone or crack localization (damage and plasticity) band is proportional to this critical length scale by a dimensionless geometrical function.

In this section, a new parameter representing the characteristic length for compression test are derived from size effect. This new expression enables us to obtain the characteristic length from one single post-peak stress-strain curves.

Analogy of Indentation Size Effect to Uniaxial 1D Scaling Size Effect

Many researchers have investigated compression size effect (Hudson and Fairhurst, 1972; Jansen, 1997; Fakhimi & Hemami, 2015). As size effect plays a big role in controlling the post-peak strain response, measuring brittleness from post-peak stress-strain curves without awareness of size effect can lead to serious errors (except when all samples have the same size).
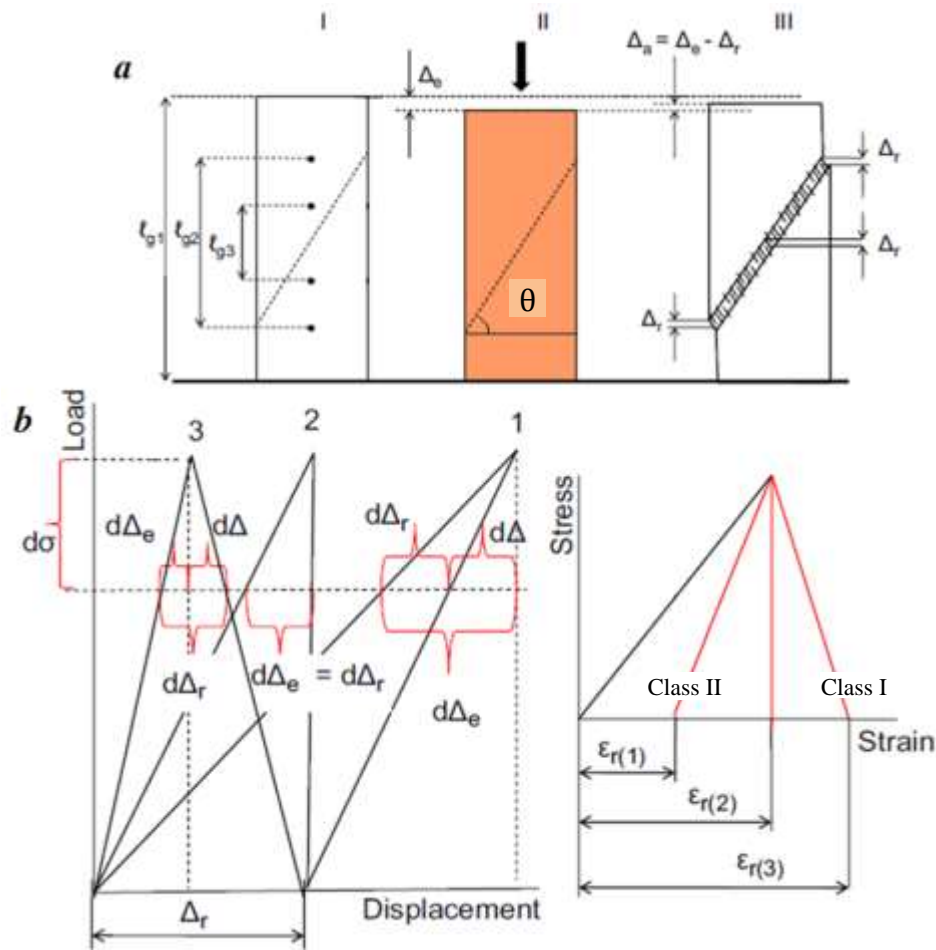
Figure 2.20 Load-displacement and stress-strain curves plotted for measurements involving three different rock volumes on the same sample. This is equivalent to testing three samples of different sizes.

Fig. 2.20 (Tarasov & Potvin, 2013) illustrates a specimen at three stages of deformation: I—before loading; II–at the peak stress with elastic energy (red) stored uniformly in the rock body; and III—after failure (completely unloaded). The amount of elastic energy stored in the specimen at peak stress is proportional to the specimen length, whereas, the fracture energy is the same for specimens of different length. Depending on the specimen length, we can have very different post-peak curves. Fig. 2.20a shows a situation when the elastic energy (associated with elastic deformation Δ_e) is greater than the fracture energy (associated with irreversible displacement Δ_r). To prevent instability during the failure development, the excess elastic energy must be

36

withdrawn from the specimen by the reverse deformation of the total value $\Delta_a = \Delta_e - \Delta_r$. In this case, we have Class II behavior. However, for a shorter specimen of the same rock, the amount of elastic energy stored at the peak stress is smaller and if $\Delta_r > \Delta_e$, the failure process corresponds to Class I behavior.

The position of axial (strain) gauges on the specimen is also very important. Fig. 2.20a-I shows symbolically three gauges fixed to different points on the specimen surface. The future shear fracture shown by the dotted line is located between the pin-points of gauges 1 (length l_{g1}), 2 (length l_{g2}) and 3 (length l_{g3}). Depending on the gauge length, load-displacement and stress-strain curves measured from gauges 1, 2 and 3 are very different. As can be seen, length l_{g2} corresponds to a transition from Class I to Class II behavior (Fig 2.20b and Fig 2.21), thus the length l_{g2} is the characteristic length because the elastic energy stored in volume covered by l_{g2} is equal to the fracture energy required by the shear fracture.
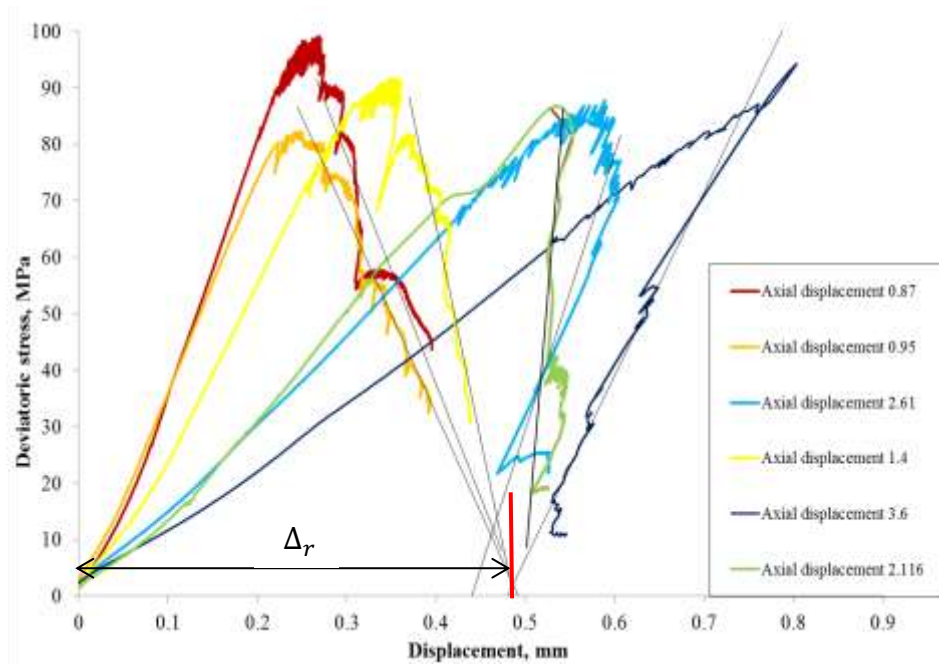
Figure 2.21 Stress-displacement curves of six Scioto sandstones of different length (from 0.87 inch to 3.6 inch)

37

From the energy balance view where the equation $(\sigma_c^2/(2E)) \times$ volume$= G_f \times$area

holds true, and assuming the cross-sectional area of the rock sample is S, the inclination

angle of shear fracture is θ, the energy balance equation becomes $\left(\frac{\sigma_c \varepsilon_r}{2}\right) \times S \times l =$

$G_f \times \frac{S}{\cos(\theta)} = \left(\frac{\sigma_c \varepsilon_p}{2}\right) \times S \times l_{ch}$. Rearranging yields: $\varepsilon_r \times l = \varepsilon_p \times l_{ch}$ where ε_p is the

strain at peak stress. In the case of Fig 2.20 $\varepsilon_p = \varepsilon_{r(2)}$, $l_{ch} = l_{g2}$. Thus, the

characteristic length, l_{ch}, can be expressed as $\frac{\varepsilon_r \times l}{\varepsilon_p}$. Because ε_p can be expressed

as $\varepsilon_p = \frac{\sigma_c}{E}$, and $\varepsilon_r \times l = \Delta_r$,

$$l_{ch} = \frac{\varepsilon_r \times l}{\varepsilon_p} = \frac{\Delta_r}{\varepsilon_p} = \Delta_r \frac{E}{\sigma_c} \tag{1}$$

in which ε_p is the strain at peak stress, ε_r is residual strain, and l is sample length. From

Fig. 2.20, Δ_r is a constant value for the same rock, it does not change with size, it can

be measured from load-displacement curves, on a stress-strain curve, ε_r and ε_p can be

located, if the sample size is known, then $\frac{\varepsilon_r \times l}{\varepsilon_p}$ can be used as a characteristic length.

Δ_r is the size of the fracture localization band as shown in Fig. 2.20a-III and

Fig.2.21, on load-displacement curves; it is the axial displacement at which all post-

peak slopes intersect with horizontal axis(Fig 2.21), thus the displacement where

fracturing process is completed (load reaches zero) can be considered as a material

constant. In the case of Fig. 2.19, shale disc of 8 different sizes were indented, but the

final indentation depth are approximately the same, it is analogous to the case in Fig.

2.21.

Summary

Displacement or length-based parameters such as characteristic length (critical structure size) $\varepsilon_r l/\varepsilon_p$ and the final displacement $\varepsilon_r l$ when fracturing process ends can be considered brittleness indices (reverse relation), the final displacement is a measure of crack tip nonlinear zone size or the size of crack band. On stress-strain curve, the final displacement is calculated from ε_r, the residual strain. A very thin (localized) crack band requires a small final axial displacement; a wider or more distributed crack band entails a larger final displacement.

BRITTLENESS EVALUATION USING INELASTIC STRAIN CONTROL METHOD

To measure residual strain (strain at fracturing process ends) accurately, stable post-peak stress-strain curve is required. In this section, a stable control method for post-peak failure behavior is developed.
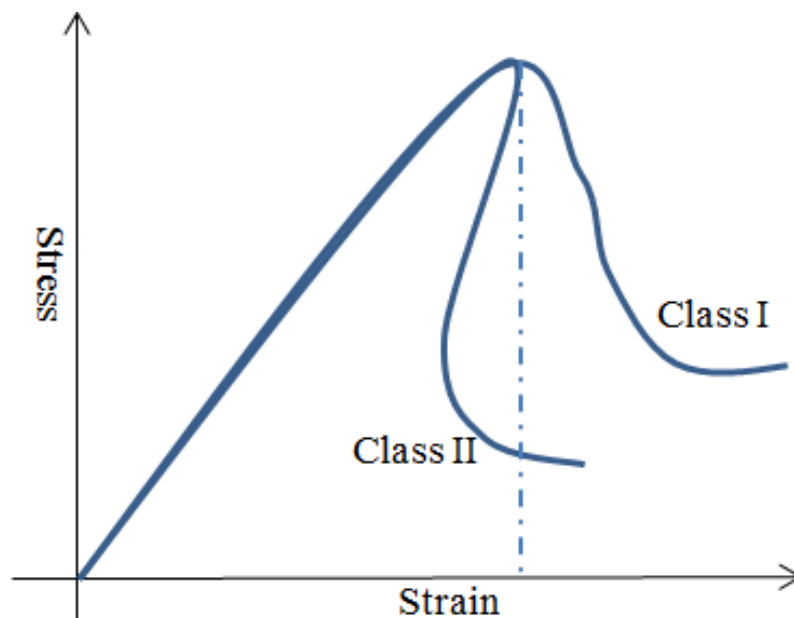
Figure 2.22 Typical stress-strain curves of Class I and Class II behavior of rock failure under compression

In rock mechanics research, much attention is focused on the post-peak behavior of rock failure. One difficulty with studying the post-failure behavior is that specimens often fail in an unstable or violent manner. Wawersik and Fairhurst (1970) classified rock behavior into Class I and Class II according to their post-peak failure behavior in uniaxial compression. They found that failure of some rocks under compression cannot be controlled even by a perfectly stiff testing machine and classified such self-sustaining failure behavior as Class II. They used a thermal contraction machine and obtained complete stress-strain curve from the envelope of unloading-reloading locus. Such stress-strain curves are characterized by a positive slope in the post-peak region, in contrast to the Class I behavior with negative post-peak slope. Later, many attempts have been made to achieve controlled failure of Class II rocks. Hudson et al.(1971) used lateral strain (or any independent variable that increases monotonically with time during failure process) as the feedback signal and many other authors modified and extended this idea (C.D. Martin., 1994). However, smooth complete stress-strain curves cannot be easily obtained because the local lateral failure or spalling makes it difficult to measure the lateral strain in the post failure accurately (Okubo and Nishimatsu, 1985). More sophisticated control methods were also proposed and attempted. Terada et al. (1984) conducted compression tests using the AE rate as the feedback signal, Sano et al. (1982) attempted triaxial tests using a constant inelastic volumetric strain rate, but few complete stress-strain curves were reported. Another method, using a linear combination of load and displacement as the feedback signal, was developed by Okubo and Nishimatsu (1985), and this proved to be a successful method to capture the Class II failure behavior. The original feedback variable has the form $\varepsilon - \frac{\sigma}{E'} = Ct$, where ε is the axial strain, C is the inelastic strain rate, and E' is a fixed chosen modulus value. The

condition for stable control is $E_{pre} < E' < E_{post}$, in which E_{pre} is the modulus before peak stress and E_{post} is the post-peak modulus. As a rule of thumb, the ratio E_{pre}/E' is recommended to be 0.8, but in Okubo's literatures, the ratio ranges from 0.4 to 0.8 for rocks of different lithologies. Jansen et al (1997) set the ratio to be 0.85 for concrete in compression. Thus for a new lithology, the ratio E_{pre}/E' has to be selected appropriately by trial and error.

Since then, many Class II stress-strain curves have been reported using this method (Okubo et al., 1987, Okubo et al., 1990, Okubo et al., 1996, Jansen et al., 1997). However, the linear combination method suffers from having to choose an empirical parameter for a specific lithology, which results in a lot of trial and error tests before a successful test. In this work, an improved damage (inelastic strain) controlled test based on the original linear combination method has been developed, and results have proved that inelastic strain controlled method is robust.

To improve the linear combination method, and eliminate the need for trial and error tests, we consider the unloading modulus E_u from a loading-unloading cycle (loading to the point of diltancy as determined by the volumetric strain deflection point and then unloading) to be E'. This improved method measures the total axial deformation and substracts true elastic deformation, leaving only inelastic(irreversible) deformation as a stable feedback signal. The feedback signal can be expressed as $\varepsilon - \frac{\sigma}{E_u} = Ct$, where σ is the axial deiviatoric stress; E_u is the unloading elastic modulus larger than the Young's modulus of the loading portion of the stress-strain curve, in this case, E_u can also be taken as the dynamic Young's modulus measured from ultra-sonic wave tests; C is the inelastic strain rate.

Compression test was conducted on Thistle 4H, 5H, 10H and 5V core plugs to obtain their mechanical properties. To achieve stable post-peak failure of these samples, the inelastic strain control method is used. Ultra-sonic wave velocity test on these plugs has indicated that these samples have high stiffness, brittle fracturing was anticipated before testing.
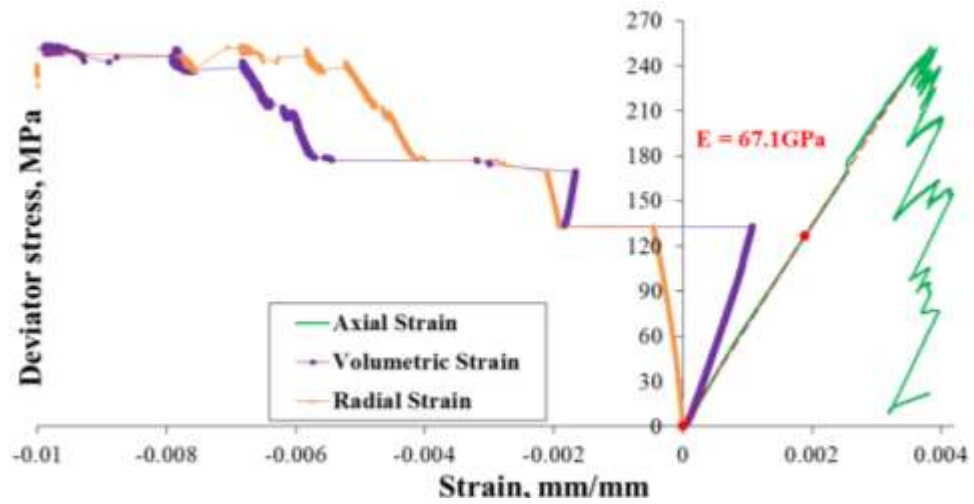
Figure 2.22 Stress-strain curves of Thistle-5V specimen, 1" ×1.47" dimension
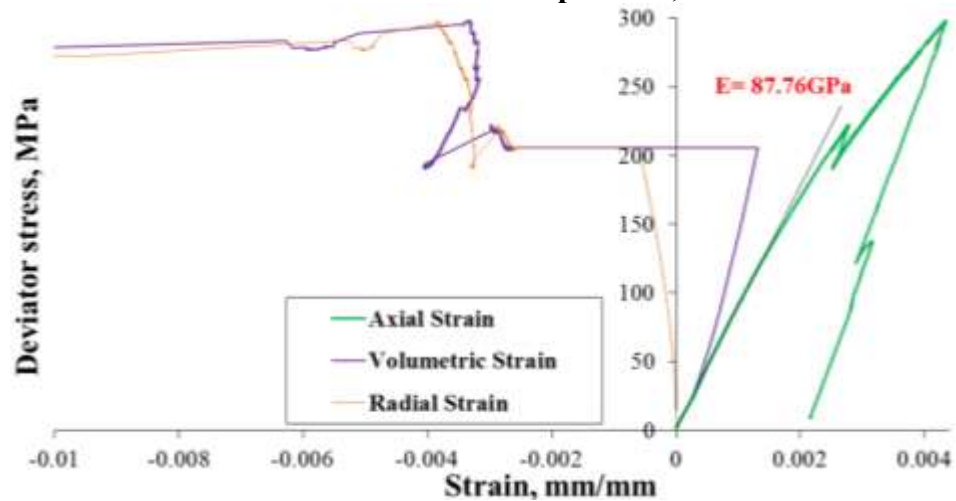
Figure 2.23 Stress-strain curves of Thistle-5H specimen, 1'' × 2'' dimension

As can be seen from the stress-strain curves of 5H and 5V, they fractured in a very brittle manner, 5H has a typical Class II post-peak response, 5V appears to be the transition between Class I and Class II stress-strain curves.
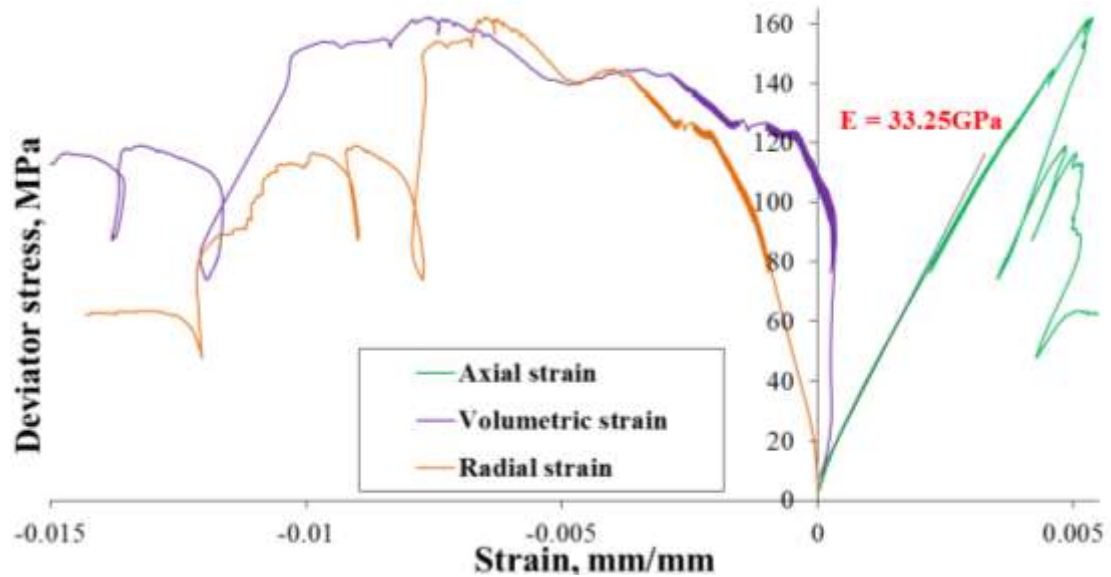
Figure 2.24 Stress-strain curves of Thistle-4H specimen under 150 psi confining pressure, 1''×2'' dimension
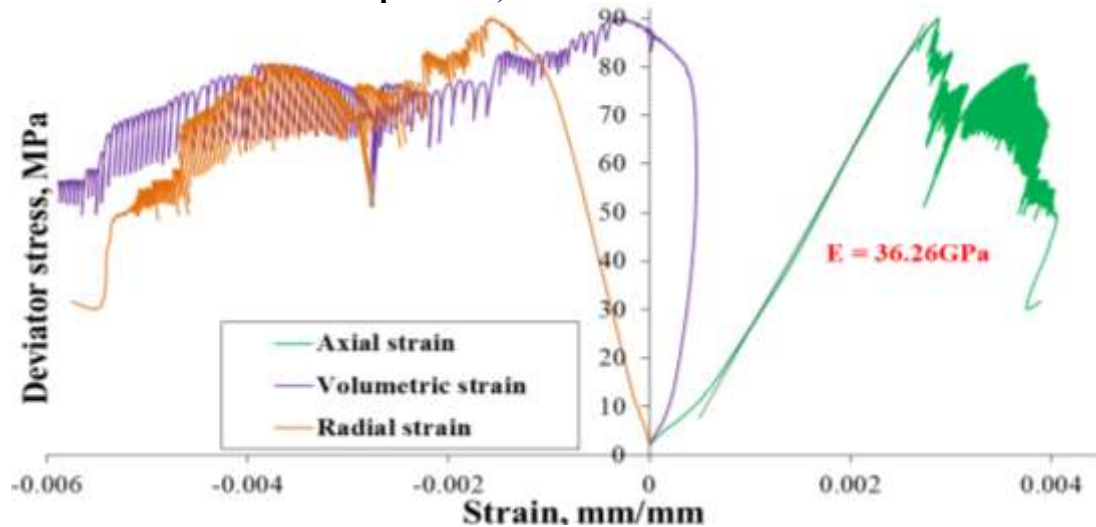
Figure 2.25 Stress-strain curves of Thistle-10H specimen under 150 psi confining pressure, 1'' ×1.42'' dimension
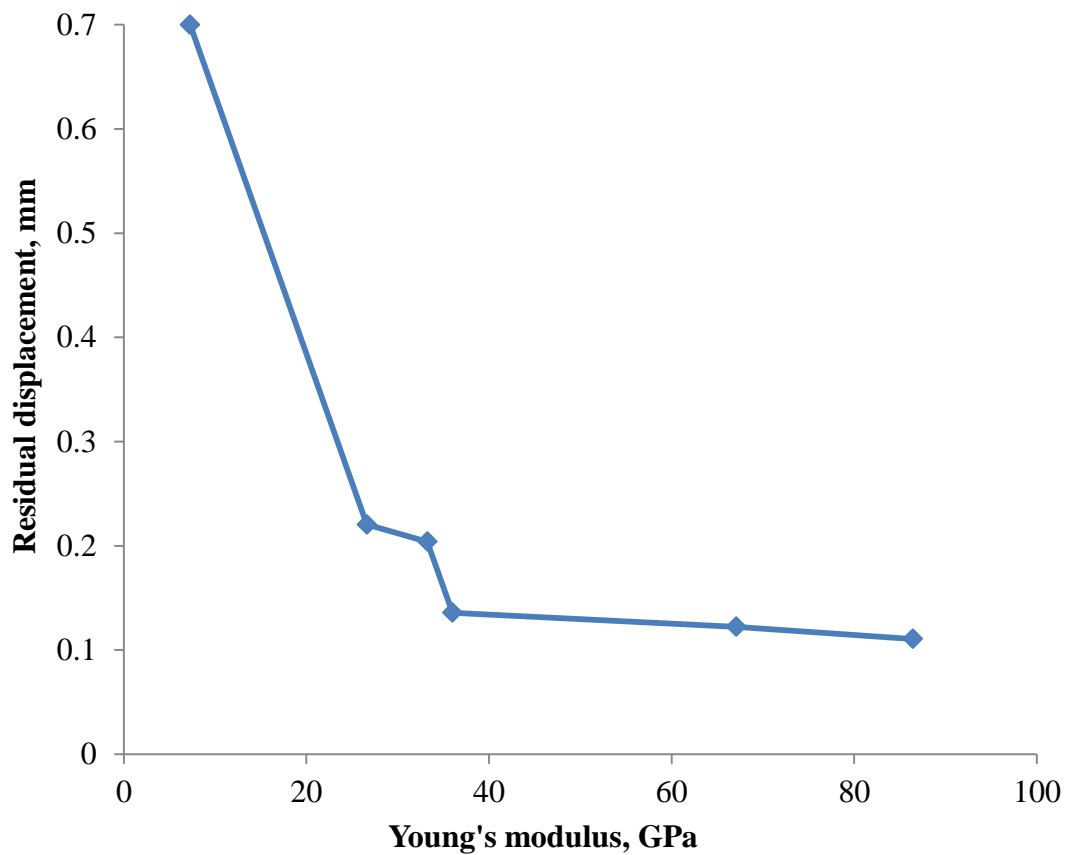
Figure 2.26 Young's modulus vs. final displacement

The displacement at residual strain is calculated by multiplying the residual strain ε_r by sample length (or gauge length), the displacement is plotted against its corresponding Young's modulus, as Fig. 2.27 shows, for uniaxial compression test, the higher the Young's modulus, the smaller the residual displacement, thus the more brittle the rock.

BRITTLENESS EVALUATION USING BRAZILIAN AND UCS TEST

Commonly used Brittleness indices are derived from laboratory compression test; so far, no brittleness index is based on the tension stress-strain curves, considering that tensile failure is a very important failure mechanism, hydraulic fractures are thought to initiate from tensile fractures. In this section, brittleness is assessed using Brazilian test.
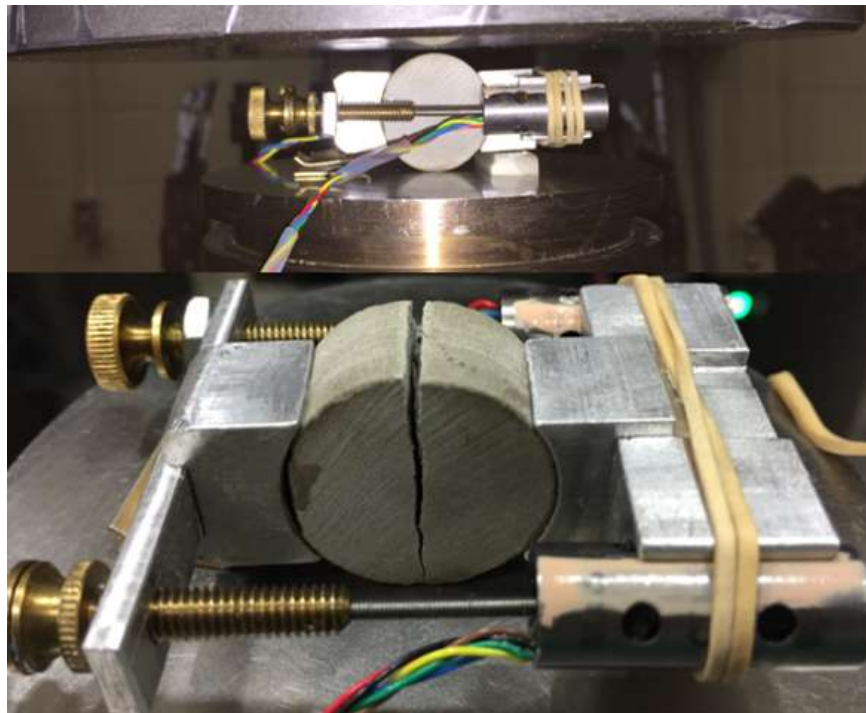
Figure 2.28 Experimental setup for laterally controlled Brazilian test

Lateral displacement (Crack Opening Displacement) of Brazilian disc is sensitive to crack opening, thus lateral displacement is used as the feedback signal of the electro-hydraulic servo systems. One pair of LVDT measure the lateral displacement, and one pair of LVDT holder is glued to the disc, as shown in Fig 2.28.
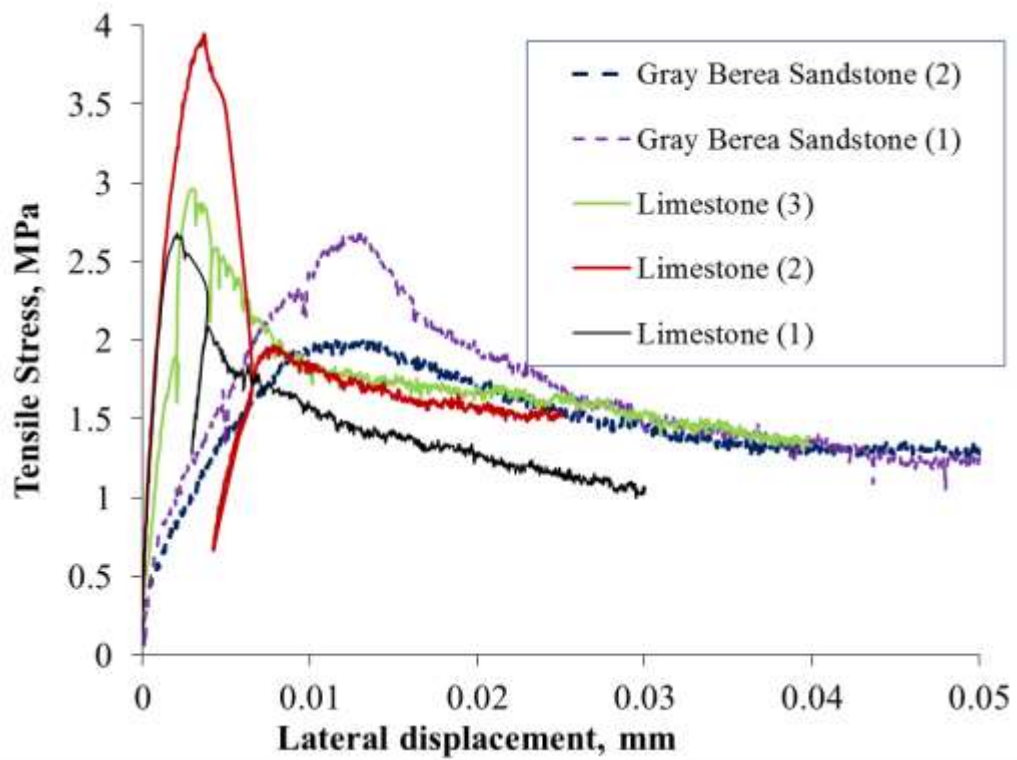
Figure 2.29 Laterally controlled Brazilian test (Damage control)
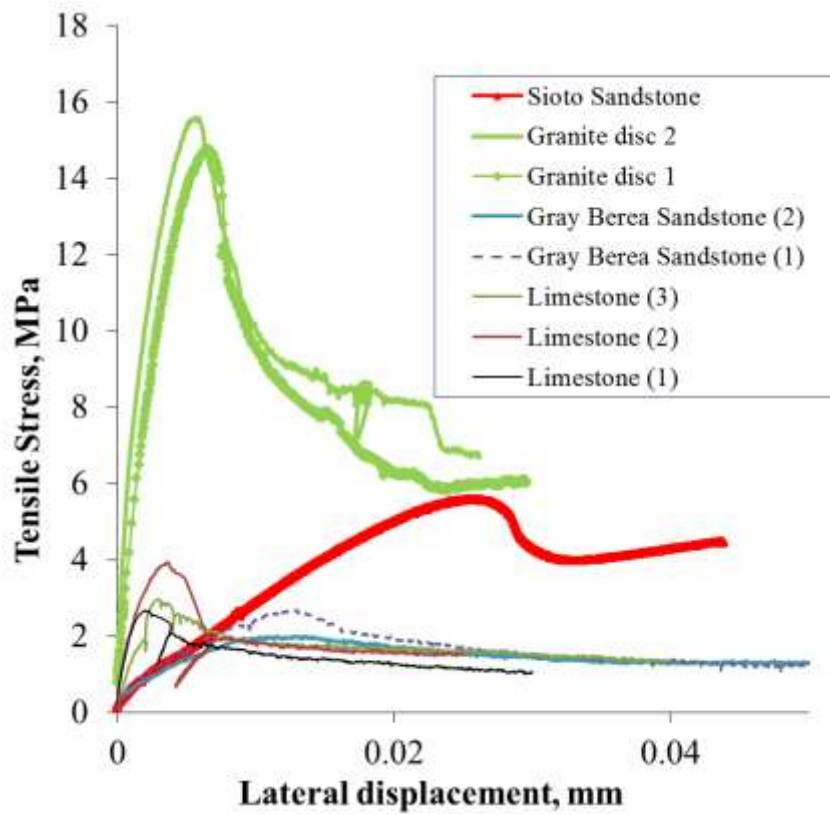
Figure 2.30 Laterally controlled Brazilian test, four lithologies

46
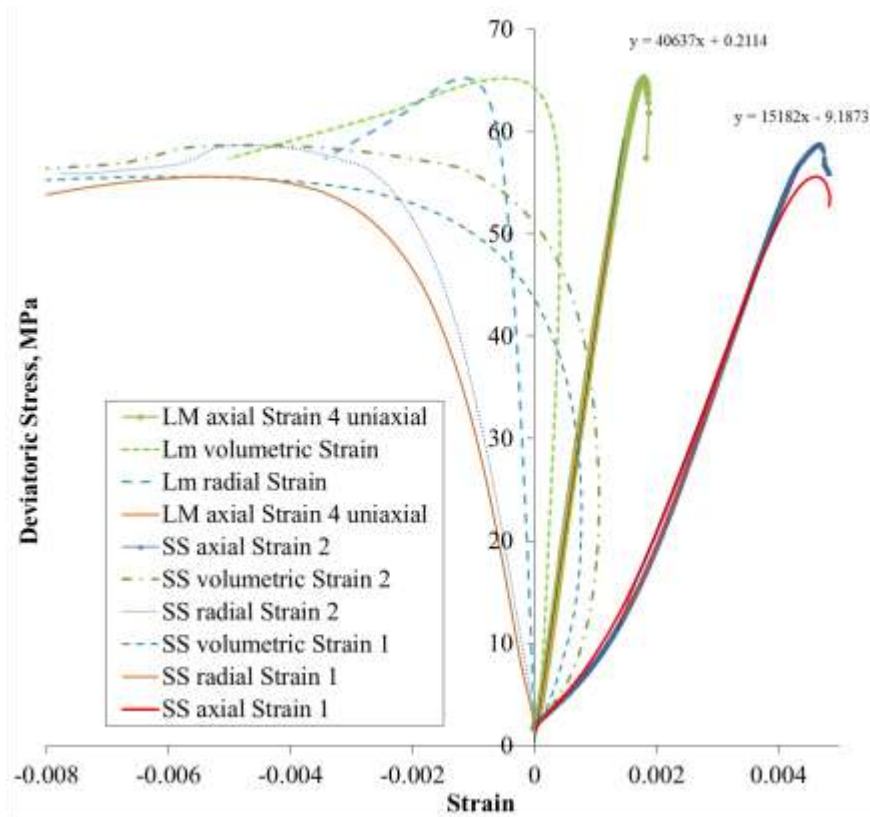
Figure 2.27 Stress-strain curves of two Grey Sandstone and one Indiana Limestone, 1-inch diameter
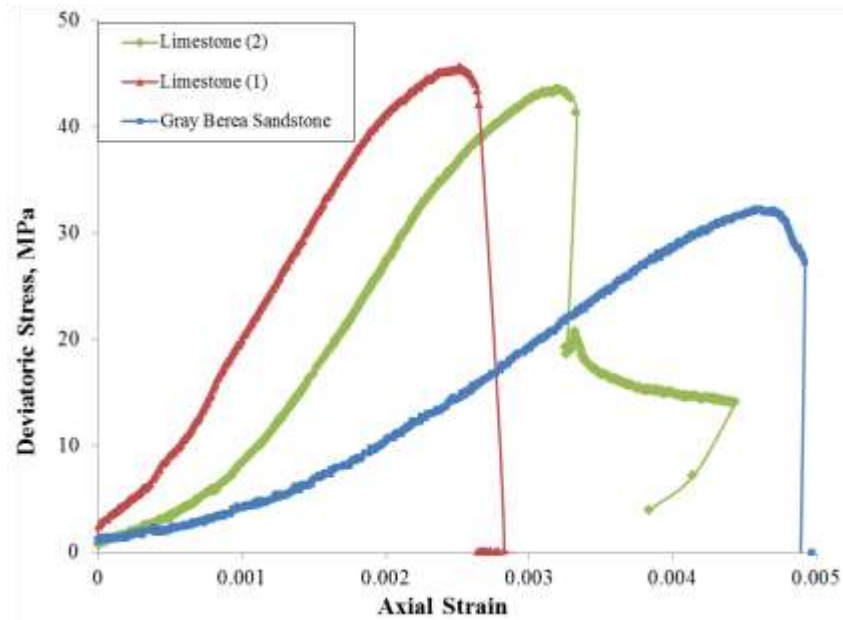
Figure 2.32 UCS tests on 0.5'' diameter Indiana Limestone and Gray Berea Sandstone samples

From Fig. 2.29, one can observe that the COD (lateral displacement) for Indiana Limestone are smaller than that of Gray Berea Sandstone. This demonstrates that tested Indiana Limestone samples are more brittle than Gray Berea samples, the post-peak slopes in Figs. 2.31-32 also attest to the more brittle nature of Indiana Limestone samples. On the other hand, the averaged UCS for Indiana Limestone is 44.35 MPa; the averaged Tensile strength is 3.15 MPa. Thus, the UCS to Tensile strength ratio is 14.08. UCS of Gray Berea Sandstone is 32.3 MPa; the averaged Tensile strength is 2.31. Therefore, the UCS to Tensile strength ratio is 14.01, judging by strength ratio index B_1, Indiana Limestone and Gray Berea Sandstone have the same brittleness.

CONCLUSION

Indentation test and Damage controlled Brazilian test are effective and fast methods to evaluate the brittleness of rocks, the Crack Opening Displacement (COD) can be used as a brittleness index (reverse relation). The crack separation displacement (indentation depth) is the brittleness index of indentation test. Other than the indentation test, three Brizilian tests were done on Indiana Limestone and two on Berea sandstone. Also, three compression tests were done on each of the two lithologies. Results indicate Indiana limestone is more brittle than Berea sandstone, as the indentation depth and Crack Opening Displacement indicates. An inelastic strain control method for stable post-peak failure process is developed. With this control method, stable Class II rock failure can be obtained. Brittleness index such as the final displacement calculated from residual strain is derived and plotted against Young's modulus, the plot proves that without confining pressure, the harder the shale is, the more brittle it is.

REFERENCES

Altindag, R. (2002). The evaluation of rock brittleness concept on rotary blast hole drills. Journal-South African Institute of Mining and Metallurgy, 102(1), 61-66.

Altindag, R. (2003), Correlation of specific energy with rock brittleness concepts on rock cutting, *Journal of the South African Institute of Mining and Metallurgy*, *103*(3), 163-171

Altindag, R., & DENKHAUS, H. (2003). Brittleness and drillability: Comment on'The evaluation of rock brittleness concept on rotary blast hole drills' and'Correlation of specific energy with rock brittleness concepts on rock cutting'. Journal of The South African Institute of Mining and Metallurgy, 103(8), 523-524.

Altindag, R. (2010). Assessment of some brittleness indexes in rock-drilling efficiency. Rock mechanics and rock engineering, 43(3), 361-370.

Altindag, R., & Guney, A. (2010). Predicting the relationships between brittleness and mechanical properties (UCS, TS and SH) of rocks. Sci Res Essays, 5(16), 2107-2118.

Andreev, G. E. (1995), *Brittle failure of rock materials: test results and constitutive models*, Taylor & Francis.

Aubertin, M., Gill, D. E., & Simon, R. (1994, June). On the use of the brittleness index modified (BIM) to estimate the post-peak behavior of rocks. In The First North American Rock Mech. Symposium (pp. 945-952). Rotterdam: AA Balkema.

Bazant, Z. P. (1984). Size effect in blunt fracture: concrete, rock, metal. Journal of Engineering Mechanics, 110(4), 518-535.

Bazant, Z. P., & Pfeiffer, P. A. (1987). Determination of fracture energy from size effect and brittleness number. ACI Materials Journal, 84(6).

Bazant, Z. P., & Pijaudier-Cabot, G. (1989). Measurement of characteristic length of nonlocal continuum. Journal of Engineering Mechanics, 115(4), 755-767.

Bazant, Z. P., & Kazemi, M. T. (1990). Determination of fracture energy, process zone length and brittleness number from size effect, with application to rock and concrete. International Journal of Fracture, 44(2), 111-131.

Bazant, Z. P., & Planas, J. (1997). Fracture and size effect in concrete and other quasibrittle materials (Vol. 16). CRC Press.

Bazant, Z. P. (2005). Scaling of structural strength. Butterworth-Heinemann.

Bishop, A. W. (1967), Progressive Failure-with special reference to the mechanism causing it., paper presented at Geotechnical Conference, Oslo, Norway.

Blindheim, O. T., & Bruland, A. (1998). Boreability testing, Norwegian TBM tunneling 30 years of experience with TBMs in Norwegian Tunneling, Norwegian Soil and Rock Engineering Association.

Baud, P., Zhu, W., & Wong, T. F. (2000). Failure mode and weakening effect of water on sandstone. *Journal of Geophysical Research: Solid Earth*, *105*(B7), 16371-16389.

Cai, M. (2010). Practical estimates of tensile strength and Hoek–Brown strength parameter m i of brittle rocks. Rock mechanics and rock engineering, 43(2), 167-184.

Carpinteri, A. (1991). Size-scale transition from ductile to brittle failure: structural response vs. crack growth resistance curve. International journal of fracture, 51(2), 175-186.

Copur, H., N. Bilgin, H. Tuncdemir, and C. Balci (2003), A set of indices based on indentation tests for assessment of rock cutting performance and rock properties, *Journal-South African Institute of Mining and Metallurgy*, *103*(9), 589-599.

Denkhaus, H. G. (2003). Brittleness and drillability. International Journal of SAIMM, 102(1), 61-66.

Elfgren, L. (Ed.) (1989). Fracture Mechanics of Concrete Structures: From Theory to Applications. London: Chapman & Hall.

Fakhimi, A., & Hemami, B. (2015). Axial splitting of rocks under uniaxial compression. *International Journal of Rock Mechanics and Mining Sciences*, *79*, 124-134.
Göktan, R. M. (1991). Brittleness and micro-scale rock cutting efficiency. Mining Science and Technology, 13(3), 237-241.

Goktan, R. M., & Yilmaz, N. G. (2005). A new methodology for the analysis of the relationship between rock brittleness index and drag pick cutting efficiency. Journal of the Southern African Institute of Mining and Metallurgy, 105(10), 727-733

Gong, Q. M., & Zhao, J. (2007). Influence of rock brittleness on TBM penetration rate in Singapore granite. Tunneling and underground space technology, 22(3), 317-324.

Hadizadeh, J., & Law, R. D. (1991, September). Water-weakening of sandstone and quartzite deformed at various stress and strain rates. In *International journal of rock mechanics and mining sciences & geomechanics abstracts* (Vol. 28, No. 5, pp. 431-439). Pergamon.

Hajiabdolmajid, V., and P. Kaiser (2003), Brittleness of rock and stability assessment in hard rock tunneling, *Tunnelling and Underground Space Technology*, *18*(1), 35-48.

Hetenyi M (1966) Handbook of experimental stress analysis. Wiley, New York, p 15

Hillerborg, A., Modéer, M., & Petersson, P. E. (1976). Analysis of crack formation and crack growth in concrete by means of fracture mechanics and finite elements. Cement and concrete research, 6(6), 773-781.

Hillerborg, A. (1985). The theoretical basis of a method to determine the fracture energy G_F of concrete. Materials and Structures, 18(4), 291-296.

Hillerborg, A. (1985). Results of three comparative test series for determining the fracture energy G_F of concrete. Materials and Structures, 18(5), 407-413.

Honda, H., and Y. Sanada (1956), Hardness of coal, *Fuel*, *35*, 451-461.

Huang, H., & Detournay, E. (2008). Intrinsic Length Scales in Tool-Rock Interaction 1. International Journal of Geomechanics, 8(1), 39-44.

Hucka, V., and B. Das (1974), Brittleness determination of rocks by different methods, *International Journal of Rock Mechanics and Mining Sciences & Geomechanics Abstracts*, *11*(10), 389-392.

Hudson, John A., Steven L. Crouch, and Charles Fairhurst. "Soft, stiff and servo-controlled testing machines: a review with reference to rock failure." Engineering Geology 6.3 (1972): 155-189.

Ingram, G. M., & Urai, J. L. (1999). Top-seal leakage through faults and fractures: the role of mudrock properties. Geological Society, London, Special Publications, 158(1), 125-135.

Irwin, G. R. (1958). Fracture. Encyclopedia of Physics, Vol. VI. Springer-Verlag, 1, 168.

Jansen, D. C., & Shah, S. P. (1997). Effect of length on compressive strain softening of concrete. *Journal of Engineering Mechanics*, *123*(1), 25-35.

Jarvie, D. M., R. J. Hill, T. E. Ruble, and R. M. Pollastro (2007), Unconventional shale-gas systems: The Mississippian Barnett Shale of north-central Texas as one model for thermogenic shale-gas assessment, *AAPG bulletin*, *91*(4), 475-499.

Jenq, Y., & Shah, S. P. (1985). Two parameter fracture model for concrete. Journal of engineering mechanics, 111(10), 1227-1241.

Jin, X., Shah, S., Roegiers, J. C., & Zhang, B. (2015). An Integrated Petrophysics and Geomechanics Approach for Fracability Evaluation in Shale Reservoirs. SPE Journal, (Preprint).

Kahraman, S. (2002). Correlation of TBM and drilling machine performances with rock brittleness. Engineering Geology, 65(4), 269-283.

Lawn, B., and D. Marshall (1979), Hardness, toughness, and brittleness: an indentation analysis, *Journal of the American ceramic society*, *62*(7-8), 347-350.

Luan, X., Di, B., Wei, J., Li, X., Qian, K., Xie, J., & Ding, P. (2014). Laboratory measurements of brittleness anisotropy in synthetic shale with different cementation. In *SEG Technical Program Expanded Abstracts 2014* (pp. 3005-3009). Society of Exploration Geophysicists.

Meng, F., Zhou, H., Zhang, C., Xu, R., & Lu, J. (2015). Evaluation methodology of brittleness of rock based on post-peak stress–strain curves. Rock Mechanics and Rock Engineering, 48(5), 1787-1805.

Morley A (1954) Strength of materials, 11th edn. Longmans, Green, London, p 532

Nejati, H. R., & Ghazvinian, A. (2014). Brittleness effect on rock fatigue damage evolution. Rock Mechanics and Rock Engineering, 47(5), 1839-1848.

Nemat-Nasser, S., & Hori, M. (2013). Micromechanics: overall properties of heterogeneous materials. Elsevier.

Obert L, Duvall WI (1967) Rock mechanics and the design of structures in rock. Wiley, New York, p 278

Puttick, K. E. (1980). The correlation of fracture transitions. Journal of Physics D: Applied Physics, 13(12), 2249.

Protodyakonov, M. M. (1962, May). Mechanical properties and drillability of rocks. In Proceedings of the 5th Symposium on Rock Mechanics, University of Minnesota, Minneapolis, Minnesota, USA (pp. 103-118).

Quinn, J. B., and G. D. Quinn (1997), Indentation brittleness of ceramics: a fresh approach, *Journal of Materials Science*, *32*(16), 4331-4346.

Ramsey JG (1967) Folding and fracturing of rocks. McGraw-Hill, London, p 289

Richard, T. (1999). Determination of rock strength from cutting tests (Doctoral dissertation, University of Minnesota).

Rickman, R., M. Mullen, J. Petre, W. Grieser, and D. Kundert (2008), A practical use of shale petrophysics for stimulation design optimization: All shale plays are not clones of the Barnett shale, paper presented at SPE Annual Technical Conference and Exhibition, Denver, Colorado, USA, September 21-24, 2008.

Reichmuth, D. R. (1967, January). Point Load Testing of Brittle Materials to Determine Tensile Strength And Relative Brittleness. In The 9th US Symposium on Rock Mechanics (USRMS). American Rock Mechanics Association.

Sehgal, J., & Ito, S. (1999). Brittleness of glass. Journal of non-crystalline solids, 253(1), 126-132.

Singh, S. P. (1986). Brittleness and the mechanical winning of coal. Mining Science and Technology, 3(3), 173-180

Suorineni, F. T., Chinnasane, D. R., & Kaiser, P. K. (2009). A procedure for determining rock-type specific Hoek-Brown brittle parameters. Rock mechanics and rock engineering, 42(6), 849-881.

Tao, Feng., Xuebin, Xie., & Wenxing, Wang. (2000). Brittleness of rocks and brittleness indexes for describing rockburst proneness. Mining and Metallurgical Engineering, 20(4), 18-19.

Tarasov, B. G., & Randolph, M. F. (2011). Superbrittleness of rocks and earthquake activity. International Journal of Rock Mechanics and Mining Sciences, 48(6), 888-898.

Tarasov, B. G., & Potvin, Y. (2012). Absolute, relative and intrinsic rock brittleness at compression. Mining Technology, 121(4), 218-225.

Tarasov, B., & Potvin, Y. (2013). Universal criteria for rock brittleness estimation under triaxial compression. *International Journal of Rock Mechanics and Mining Sciences,* 59, 57-69.

Wang, F. P., and J. F. Gale (2009), Screening criteria for shale-gas systems, *Gulf Coast Association of Geological Societies Transactions*, *59*, 779-793.

Wang, Yu.,Li Xiao., & Wu Yanfang (2014), Research on relationship between crack initiation stress level and brittleness indices for brittle rocks, *Chinese Journal of Rock Mechanics and Engineering*, 33 (2)

Xia, Y. J., Li, L. C., Tang, C. A., Li, X. Y., Ma, S., & Li, M. (2017). A new method to evaluate rock mass brittleness based on stress–strain curves of class I. *Rock Mechanics and Rock Engineering*, *50*(5), 1123-1139.

Yagiz, S. (2009), Assessment of brittleness using rock strength and density with punch penetration test, *Tunnelling and Underground Space Technology*, *24*(1), 66-74.

Yarali, O., & Soyer, E. (2011). The effect of mechanical rock properties and brittleness on drillability. Sci Res Essays, 6(5), 1077-1088.

Yilmaz, N. G., Karaca, Z., Goktan, R. M., & Akal, C. (2009). Relative brittleness characterization of some selected granitic building stones: Influence of mineral grain size. Construction and Building Materials, 23(1), 370-37

Zhang, D., Ranjith, P. G., & Perera, M. S. A. (2016). The brittleness indices used in rock mechanics and their application in shale hydraulic fracturing: A review. *Journal of Petroleum Science and Engineering*, *143*, 158-170.

Chapter 3 Rock Behavior and Brittleness under the Confined Brazilian Test

ABSTRACT

The Brazilian test, an indirect tensile test involving diametrical compression of a disc sample is normally conducted at zero confining pressure. In this study Brazilian test is extended by jacketing the specimen and applying additional confining pressure. The impact of confining pressure on the strength in the tension cut-off region, failure mechanism and brittle-ductile transition of a suite of rocks is investigated. The samples are wrapped with copper jacket such that the confining fluid does not communicate with the rock matrix. Then by applying a constant confining pressure, a state of triaxial stress is created in the disc. The disc center is under three nonzero and unequal principal stresses. By increasing the confining pressure, the least principal stress, σ_3, changes from tensile to compressive so that rock failure can be invesitigated over a wide range of stress conditions. Six lithologies are tested, these include Indiana limestone, Scioto sandstone, Tennesse sandstone, Barnett shale, Eagleford shale and Marcellus shale. Experimental results suggest that the discs fail under complex stress conditions, yielding the failure envelope in the tensile and compressive domain. For all lithologies, tensile fracturing disappears as confining pressure increases, exhibiting a typical brittle-ductile transition. The brittle-ductile transition plots of six lithologies are obtained, the inclination angles of the fracture plane with respect to σ_1 are observed to increase with confining pressure. the brittleness of three shales are compared, the brittleness correlates well to the minerological contents.

INTRODUCTION

Brazilian test consisting of a rock disc subjected to an increasing compressive line load is used as a convenient indirect tensile strength testing method for rocks and other solids. Jaeger (1966) suggested that if an additional confining pressure is applied to the specimen, the transition from tensile to compressive values of the least principal stress could be studied. Jaeger further presented experimental results for Bowral trachyte, Gosford sandstone, and Carrara marble which supported previous findings that the magnitude of the intermediate principal stress influences the conditions for failure in all three rocks.
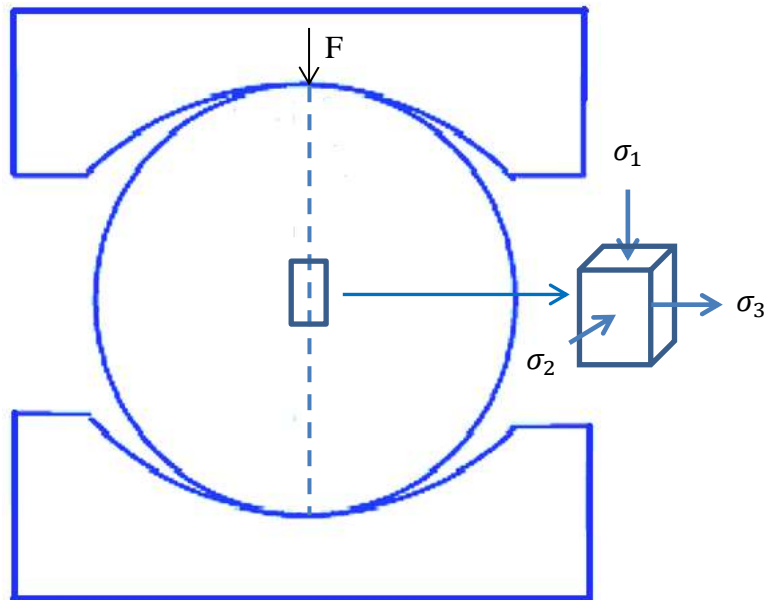

Figure 3.1 Principal stresses direction of Brazilian disc

In the original form of the Brazilian test, a line load F is applied to a rock cylinder of diameter D and thickness t and the principal stresses at the center of the cylinder, calculated from elastic theory (Jaeger, 1966) are:

$$\sigma_1 = \frac{6F}{\pi Dt}, \sigma_2 = 0, \sigma_3 = -\frac{2F}{\pi Dt} \tag{1}$$

If an additional hydrostatic pressure P is applied to the whole surface of the cylinder, the stresses at the center of the cylinder become

$$\sigma_1 = P + \frac{6F}{\pi D t}, \sigma_2 = P, \sigma_3 = P - \frac{2F}{\pi D t} \qquad (2)$$

Apparently, these three principal stresses are not independent of each other (Jaeger, 1966), they are connected by a relation:

$$\sigma_1 - 4\sigma_2 + 3\sigma_3 = 0 \qquad (3)$$

TEST SPECIMENS AND APPARATUS

Brazilian discs are one and two inches in diameter, cut from a six-inch diameter core samples; the core plugs were subsequently sliced into discs of more than half (0.5 inch and 1 inch) diameter thick. After slicing the specimens, the end faces were flattened with a grinding machine to ensure the parallelism is within ± 0.02 mm. The exact thickness of the discs then were measured, the thickness is usually around half of the diameter. The prepared discs were subsequently jacketed using 0.1 mm thick copper foil. The seams of the copper jacket were soldered, then a layer of super glue was applied to the seam to ensure no leakage of confining fluid into the sample.

Tested lithologies include Indiana limestone, Scioto sandstone, Tennesse sandstone, Marcellus shale, Eagle Ford shale and Barnett shale, in which Indiana limestone, Scioto sandstone and Tennesse sandstone are homogeneous and isotropic, the three shales were cored perpendicular to their bedding plane. It is better if rocks for confined Brazilian test are fine-grained, homogeneous and isotropic to reduce data point

scattering. Any test with leaked copper jacket due to bad soldering is considered invalid and rejected.

Brazilian discs were tested in a GCTS triaxial cell with an internal load cell to measure the load at failure accurately; one layer of masking tape (0.16mm thickness) is used to wrap around the periphery of the rock discs to distribute the line load. The ISRM (1978) standard suggests a curved set of loading jaws with a radius of 1.5 times the specimen radius. For the confined Brazilian test on Indiana limestone, two pairs of curved loading jaws are used, as shown in Fig. 3.2, one pair is for standard load-controlled Brazilian test, another pair for damage-controlled (or lateral displacement-controlled) Brazilian test with lateral displacement measured by LVDT. The specimen assembly and the GCTS triaxial cell are mounted inside MTS 810 load frame equipped with a hydraulic actuator for applying axial force.
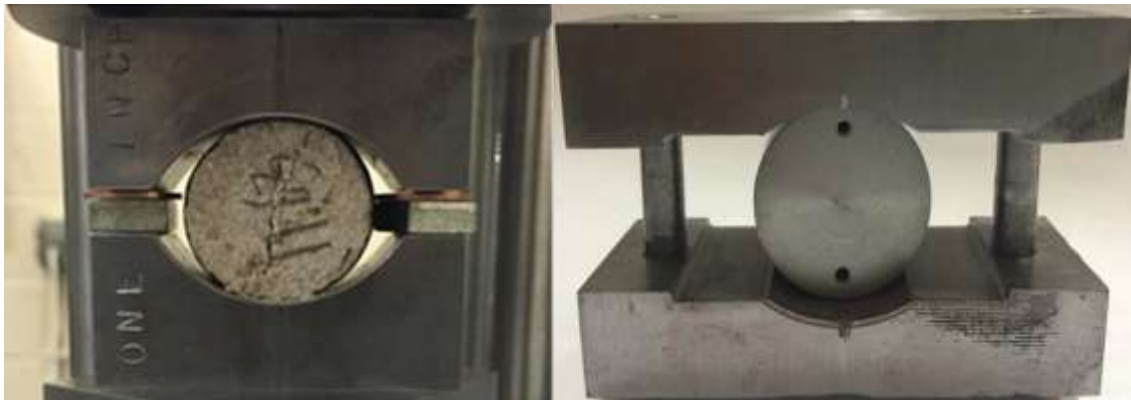
Figure 3.2 Two sets of loading jaws, one set for conventional load control Brazilian test (left), another set for damage controlled Brazilian test (right)
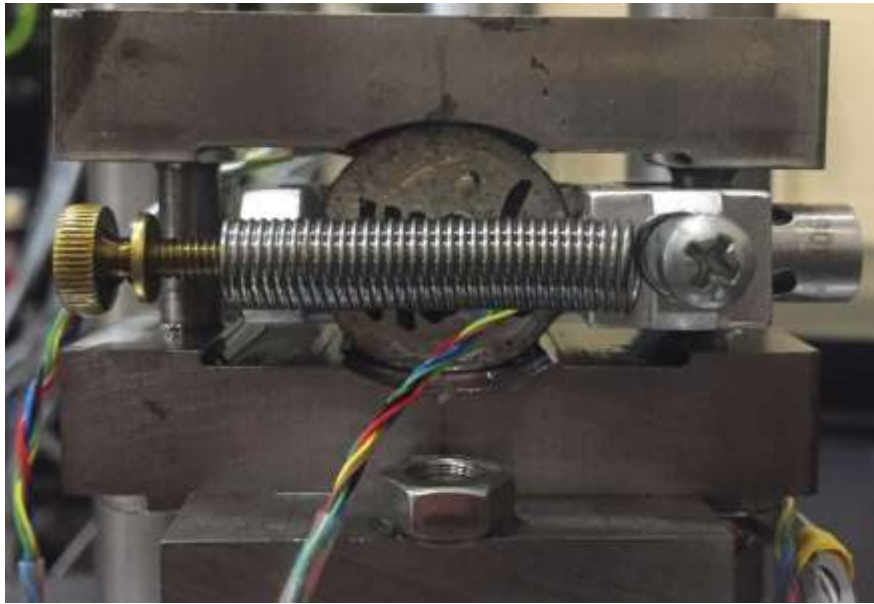
Figure 3.3 Specimen assembly of damage (lateral displacement) controlled Brazilian test

Conventional load controlled Brazilian test follows the ISRM suggested procedures. Controlled failure of Brazilian discs is achieved by maintaining a monotonically increasing lateral displacement (rate is 0.00002 mm/s) using a closed-loop servo control triaxial system. A pair of LVDT holder is glued on the two sides of a Brazilian disc in a diametrically opposed manner; two LVDT sensors are mounted in the holders to measure the average lateral displacement of Brazilian discs.
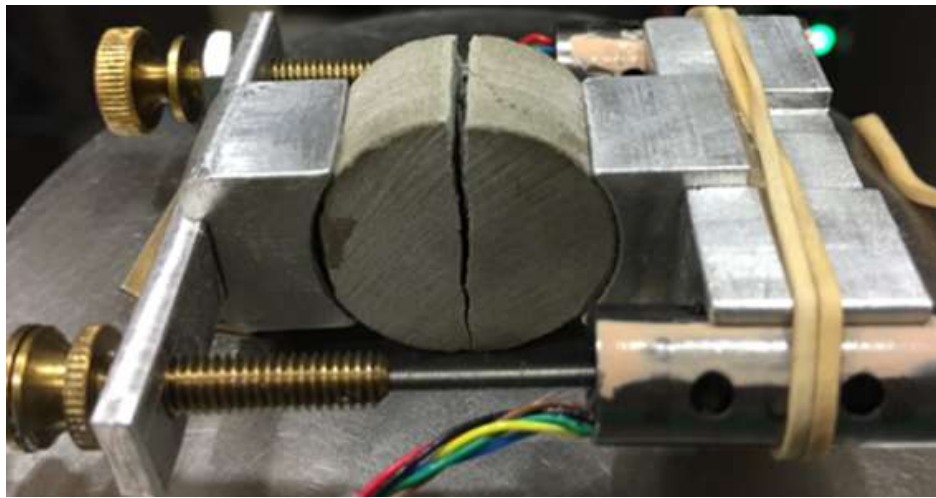
Figure 3.4 LVDT holder and sample assembly

Figure 3.5 MTS 810 frame and GCTS triaxial cell with internal S-shaped load cell and Brazilian specimen assembly

EXPERIMENTAL PROCEDURES

For Indiana limestone, the load controlled Brazilian test (loading rate 200 N/s) is first conducted in different confining pressure; because of the minimum requirement of instrumentation (only load and actuator displacement are measured and recorded), a confined load controlled Brazilian tests can be performed within 10 minutes. Then, several damage controlled Brazilian tests are carried out in selected confining pressures;

for all other lithologies, only damage controlled Brazilian tests are conducted. Two LVDT sensors, with a range of 2mm, measure the diametrical displacement which is normal to the load axis along the two opposite sides of the disc, their average is called lateral displacement or Crack Opening Displacement (COD). The loading rate of controlled Brazilian test is maintained at 0.00002 mm/s. The discs are unloaded when a post-peak plateau on the load-lateral displacement curve is observed. The time, force, actuator displacement, and lateral displacement from each LVDT as well as their average were recorded during tests. The test results were presented by plotting the average displacement of the two LVDTs with the indirect tensile stress. The indirect tensile stress is calculated as $\sigma = 2F/\pi Dt$, where F is the force applied to the specimen, t is the specimen length or thickness, D is the diameter.

EXPERIMENTAL RESULTS

For Indiana limestone, values of σ_1 and σ_3 at failure calculated from Eq.(2) under various confining pressures are shown in Fig. 3.6. Most values are the mean of two samples to reduce the data scatter. The strength values at higher confining pressures are chosen to correspond to the deviation point from linearity on stress-displacement curves because the primary fracture stress is hard to pinpoint at higher confining pressures. The compressive strength data points obtained from the confined Brazilian test are higher than those from triaxial compression test, this is attributed to the effect of the intermediate principal stress.
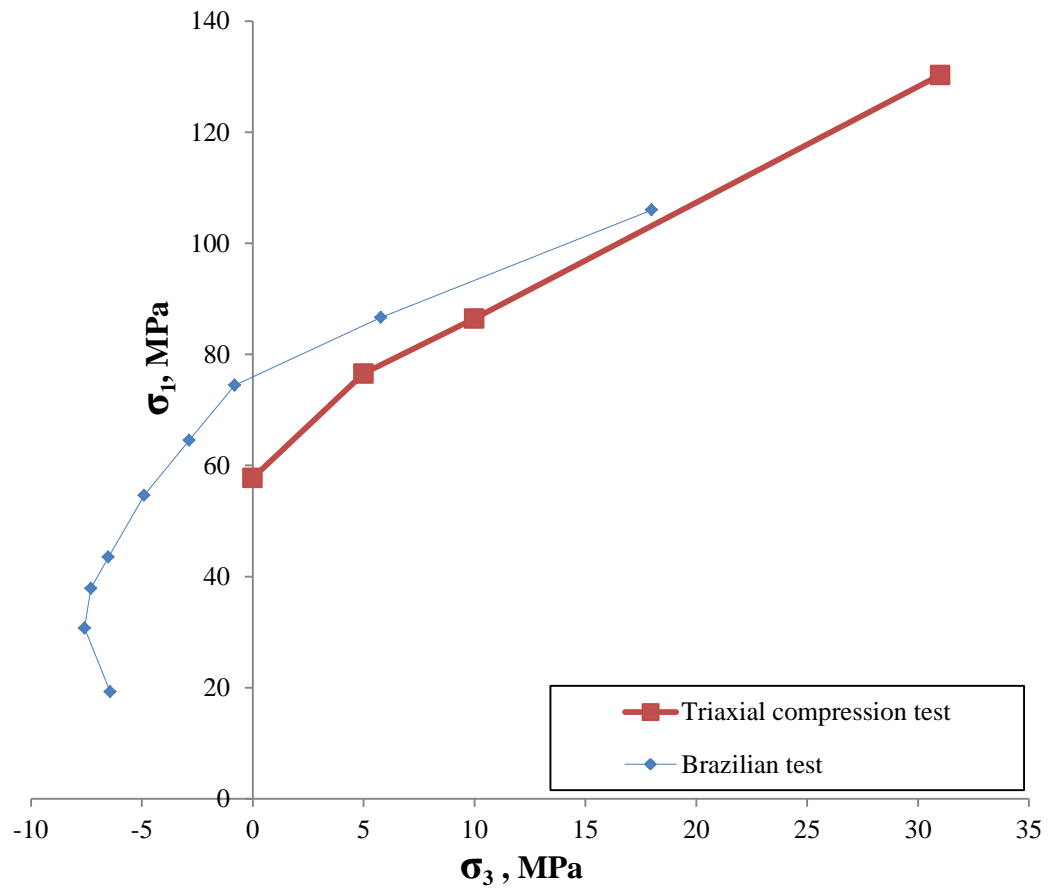
Figure 3.6 Variation of σ_1 with σ_3 for Indiana limestone at the center of the disc in the confined Brazilian test, σ_1 and σ_3 are calculated from Eq.(2) (Load control)
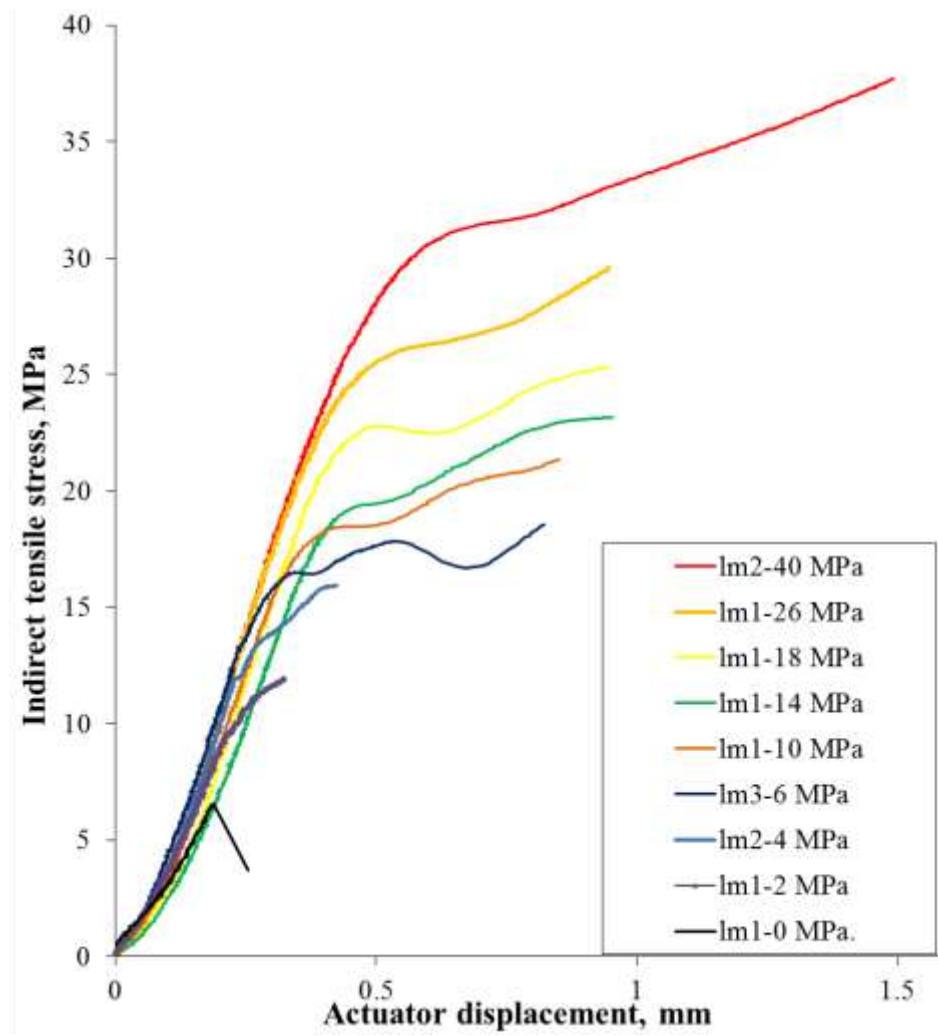
Figure 3.7 Stress-displacement curves for Indiana limestone in the confined Brazilian test (load controlled without lateral displacement measurement)
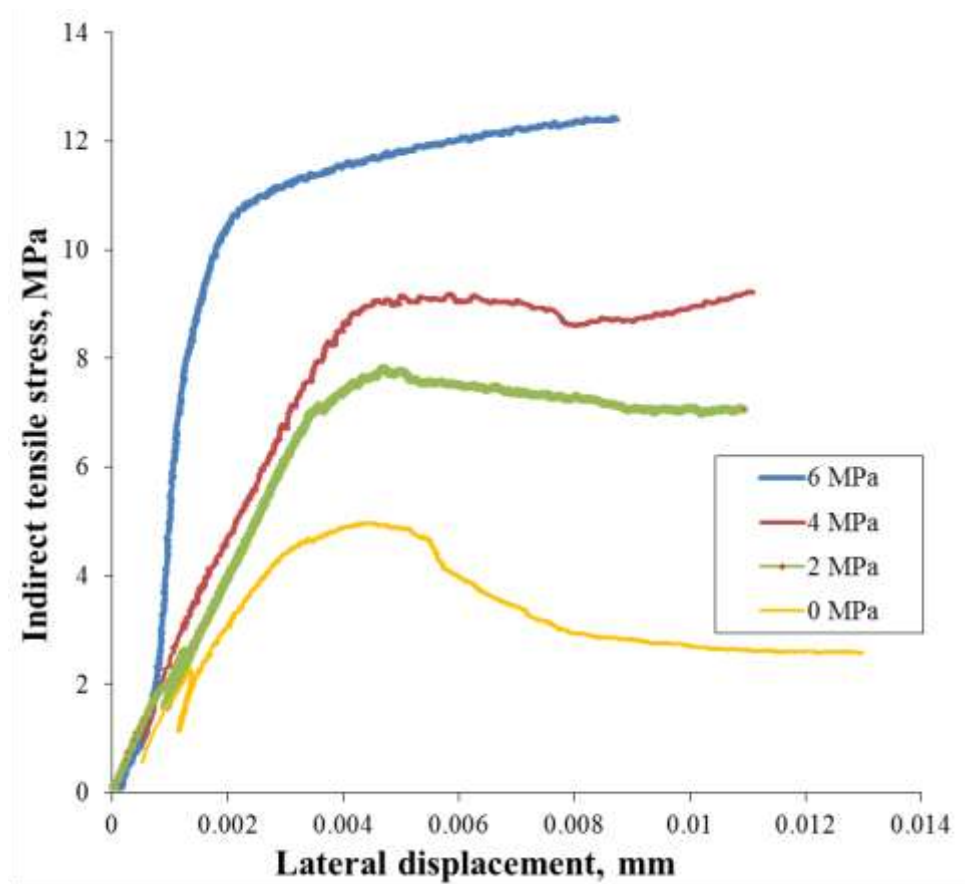
Figure 3.8 Stress-lateral displacement curves for Indiana limestone in the confined Brazilian test, similar to stress-strain curves of brittle-ductile transition of compression test

From Fig. 3.7 and Fig. 3.8, we can tell Indiana limestone becomes ductile at small confining pressures as manifested by the post-peak slope change; at 6 MPa confining pressure, it shows strain hardening, this is due to its small internal friction angle.

63
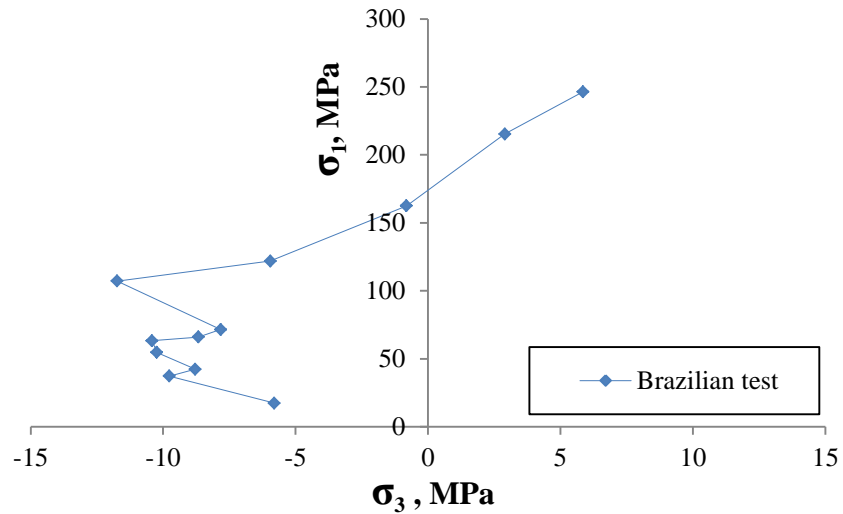
Figure 3.9 Variation of σ₁ with σ₃ for Scioto sandstone at the center of the disc in the confined Brazilian test, σ₁ and σ₃ are calculated from Eq.(2)

All Brazilian tests of Scioto sandstone are lateral displacement controlled. The data scattering (zig zag in Fig.3.9) in the tensile domain is most likely caused by sample heterogeneity. From Fig. 3.10, we can clearly see the Brittle-Ductile Transition of Scioto sandstone. At intermediate confining pressures such as 8 MPa, 10 MPa and 12 MPa, the samples behave in a very ductile fashion with less post-peak stress drop. However, at higher confining pressures, the rock exhibits embrittlement phenomenon characterized by abrupt post-peak stress drop, this can be attributed to the change of failure mechanism, at higher confining pressure, we speculate that the failure mechanism is shear failure, whereas, at the lower confining pressure, the mechanism is tensile failure.

Figure 3.10 Stress-lateral displacement curves for Scioto sandstone in the confined Brazilian test
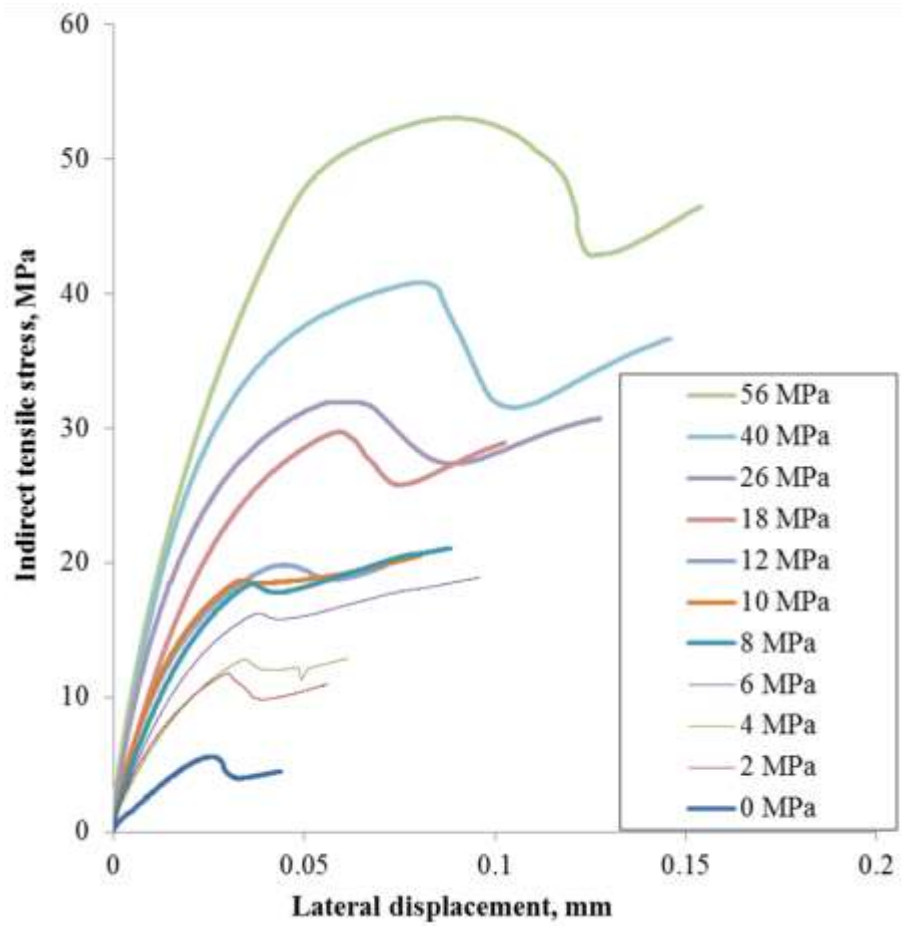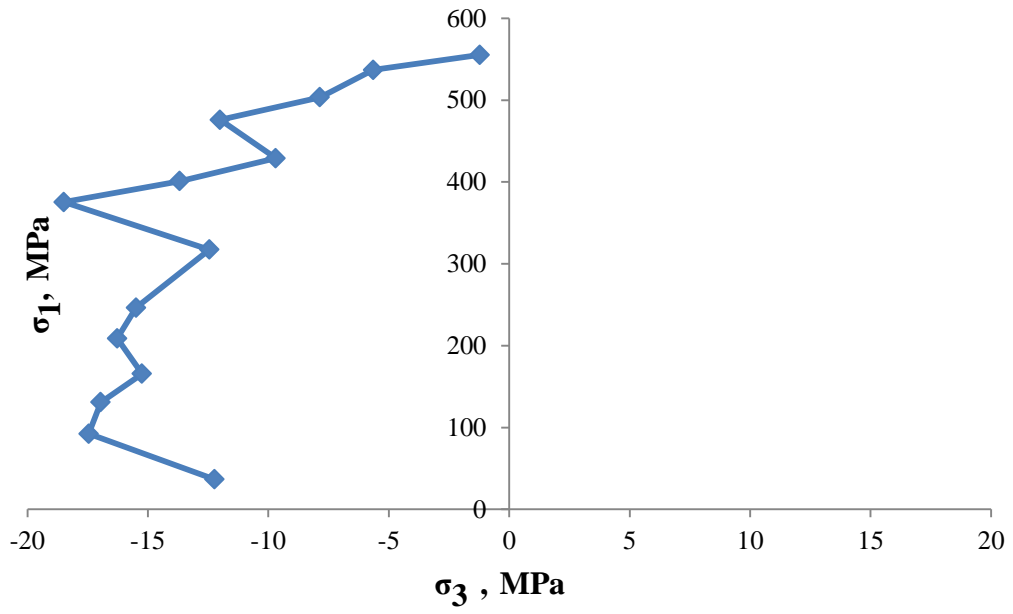
Figure 3.11 Variation of σ_1 with σ_3 for Tennessee sandstone at the center of the disc in the confined Brazilian test, σ_1 and σ_3 are calculated from Eq.(2)
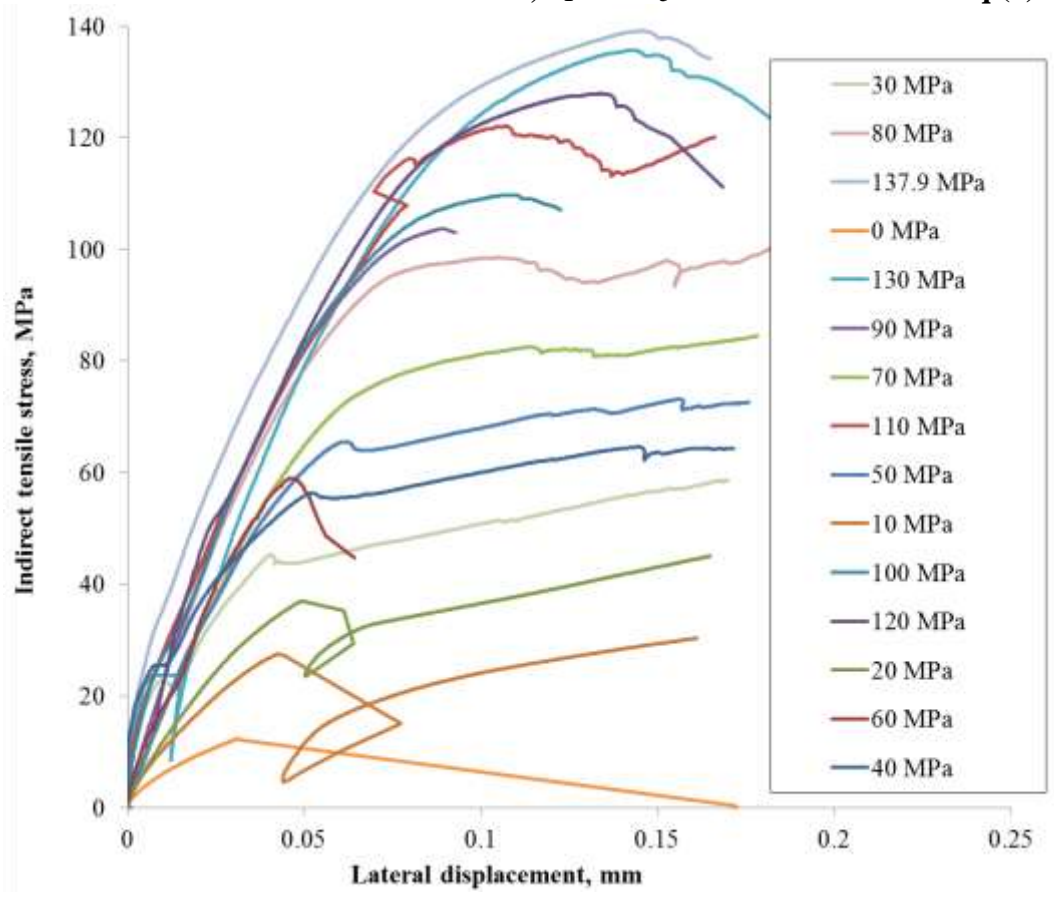
Figure 3.12 Stress-lateral displacement curves for Tennessee sandstone in the confined Brazilian test

The results of 15 tests on Tennessee sandstone are summarized in Table 3.1 to define failure strength and fracture angle as a function of confining pressure. Fracture angle is defined as the angle between fracture surface and σ_1 direction. Overall, there is an increase in fracture angle with confining pressure, as shown in Figs. 3.13-3.18.

Based on fracture angle and stress state at the center of the discs, three major classes of fractures are identified for Tennessee sandstone. Fractures formed at the lowest confining pressures (0-30 MPa) are oriented approximately parallel to σ_1 and perpendicular to σ_3, they are classified as extension fractures. Fractures formed at confining pressures between 40 MPa to 130 MPa are inclined 6.4^o to 16.9^o from σ_1 direction are classified as hybrid fractures (formed under a mixed tensile and compressive stress state). Fracture formed at confining pressures of 137.89 MPa is inclined 19.6^o from σ_1 direction, under a compressive stress state; it may be classified as shear fractures. Observation of the progressive increase in fracture angle with confining pressure, from extension fracture at low pressure to shear fracture at high pressure, provides laboratory evidence for the existence of hybrid fractures that constitute a continuous transition from extension to shear fractures. This is in agreement with the findings of Ramsay and Chester (2004).

Table 3.1 Results of triaxial Brazilian test of Scioto sandstone

Pc = σ_2 (MPa)	Failure strength (MPa)	σ_3 (MPa)	σ_1 (MPa)	Fracture angle (degree)	Fracture morphology
0	12.2	-12.2	36.7	0	Extension
10	27.5	-17.5	92.4	0	Extension
20	37.0	-17.0	130.9	0	Extension
30	45.2	15.2	165.7	0	Extension
40	56.3	-16.3	208.8	6.4	Hybrid
50	65.5	-15.5	246.5	8.9	Hybrid
60	59.0	1.0	237.0	7.2	Hybrid
70	82.4	-12.4	317.3	12.2	Hybrid
80	98.5	-18.5	375.5	13.5	Hybrid
90	103.7	-13.7	401.0	6.2	Hybrid
100	109.7	-9.7	429.1	14.9	Hybrid
110	122.0	-12.0	476.0	15.4	Hybrid
120	127.9	-7.9	503.6	16.8	Hybrid
130	135.6	-5.6	536.9	16.9	Hybrid
137.89	136.69	1.2	555.2	19.6	Shear

Figure 3.13 Fracture angle variations with confining pressure, 0-20 MPa, Tennessee sandstone

Figure 3.14 Fracture angle variations with confining pressure, 30-50 MPa, Tennessee sandstone

Figure 3.15 Fracture angle variations with confining pressure, 60-80 MPa, Tennessee sandstone

Figure 3.16 Fracture angle variations with confining pressure, 90-110 MPa, Tennessee sandstone

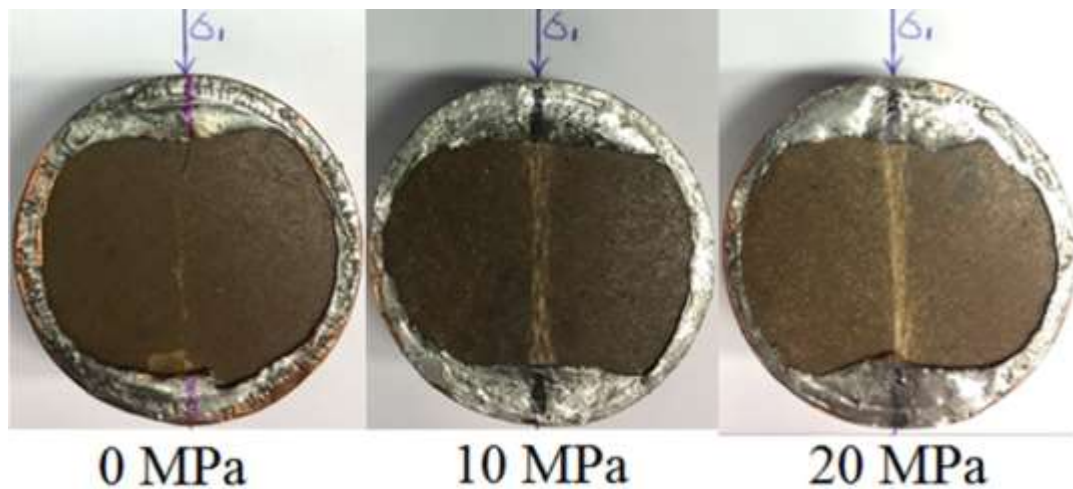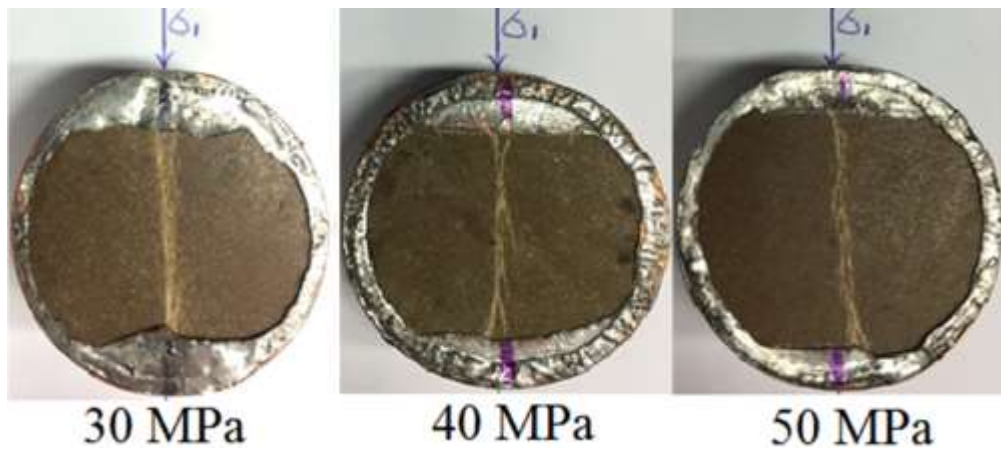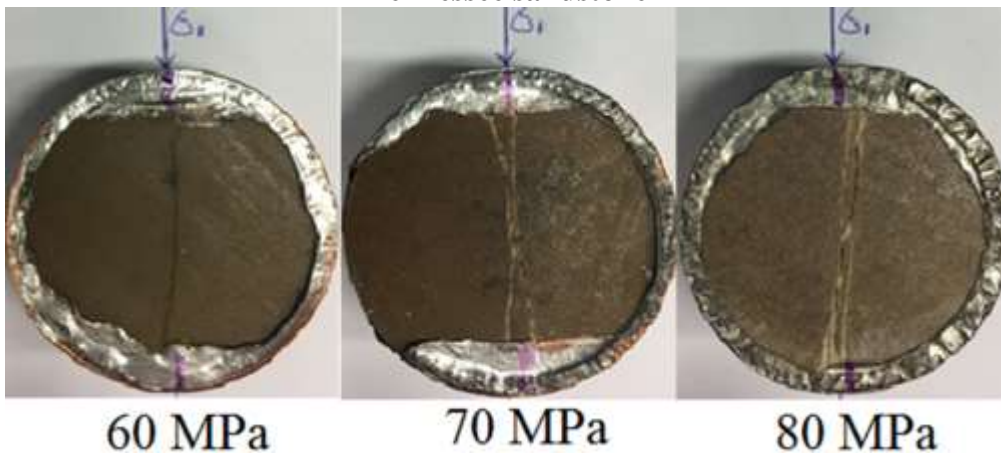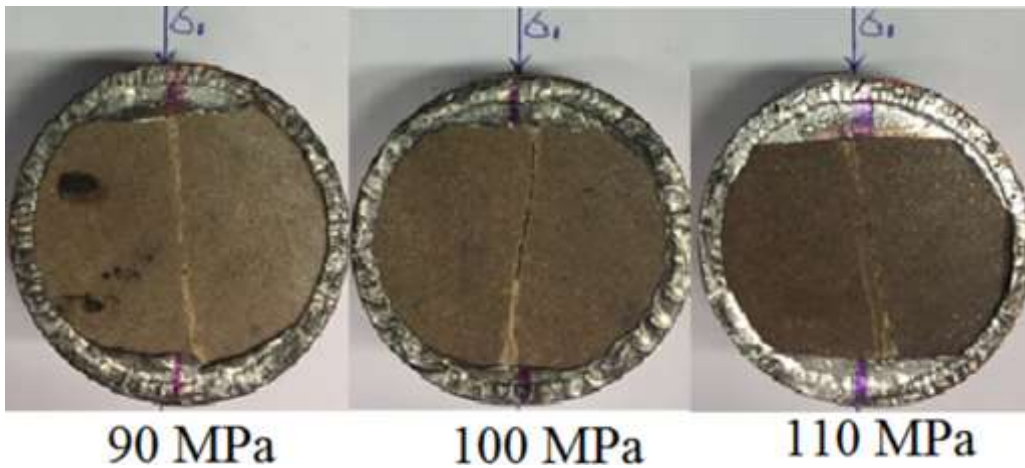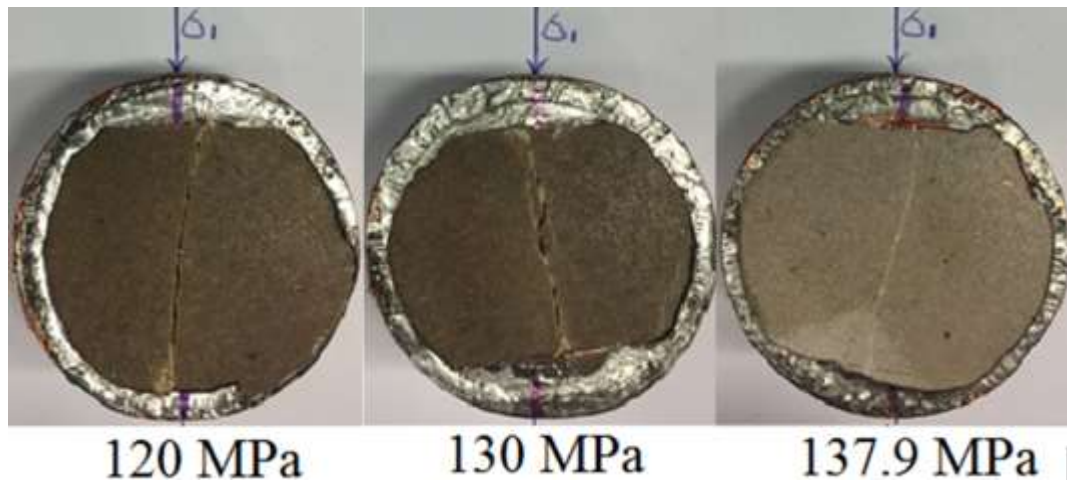**Figure 3.17 Fracture angle variations with confining pressure, 120-137.9 MPa, Tennessee sandstone**
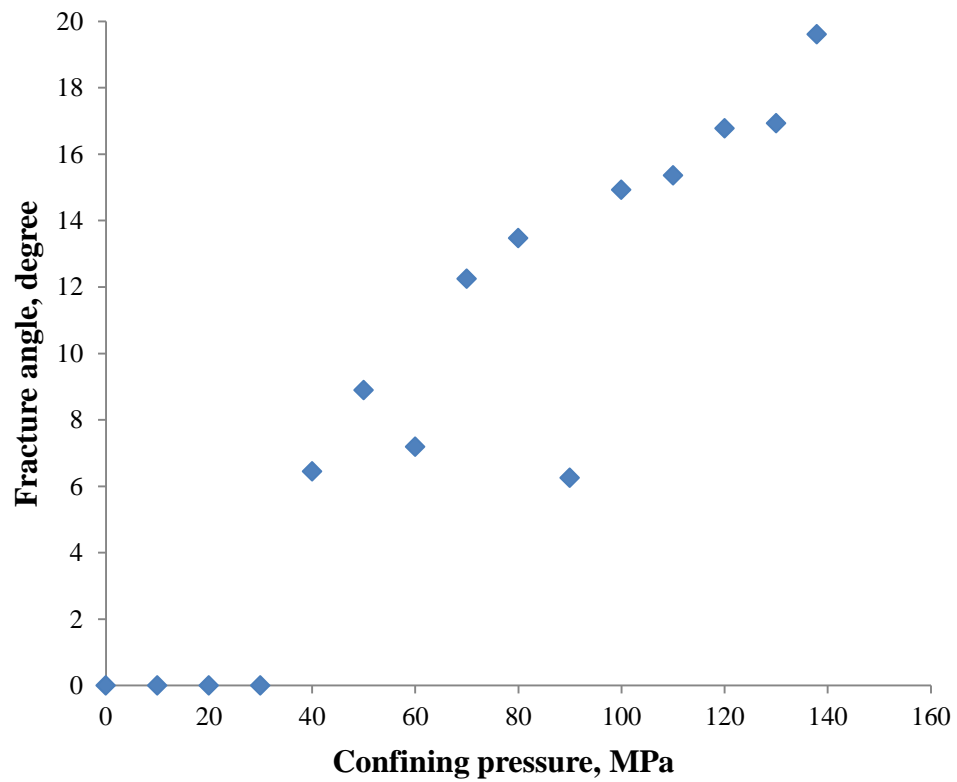
Figure 3.18 Fracture angle increases with confining pressure, Tennessee sandstone
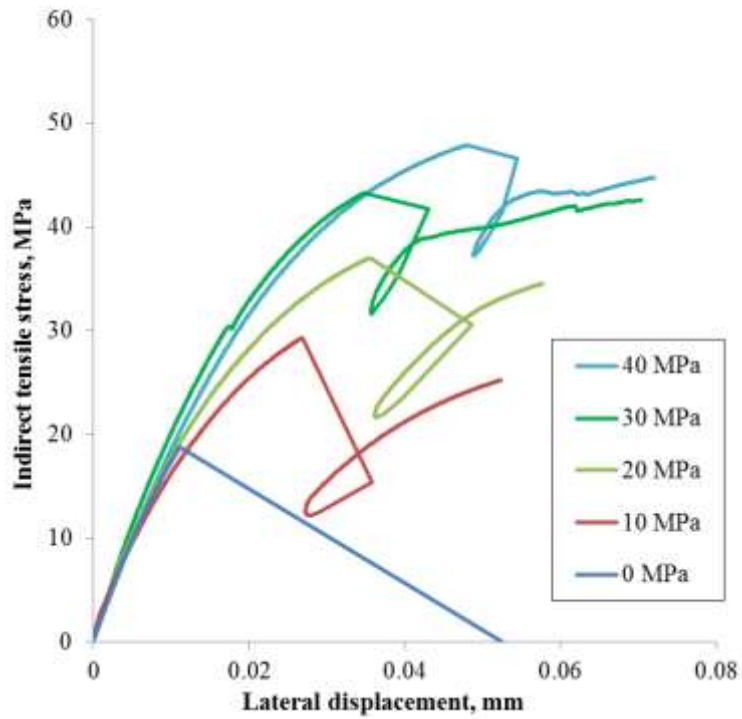
Figure 3.19 Stress-lateral displacement curves for Eagle Ford shale in the confined Brazilian test
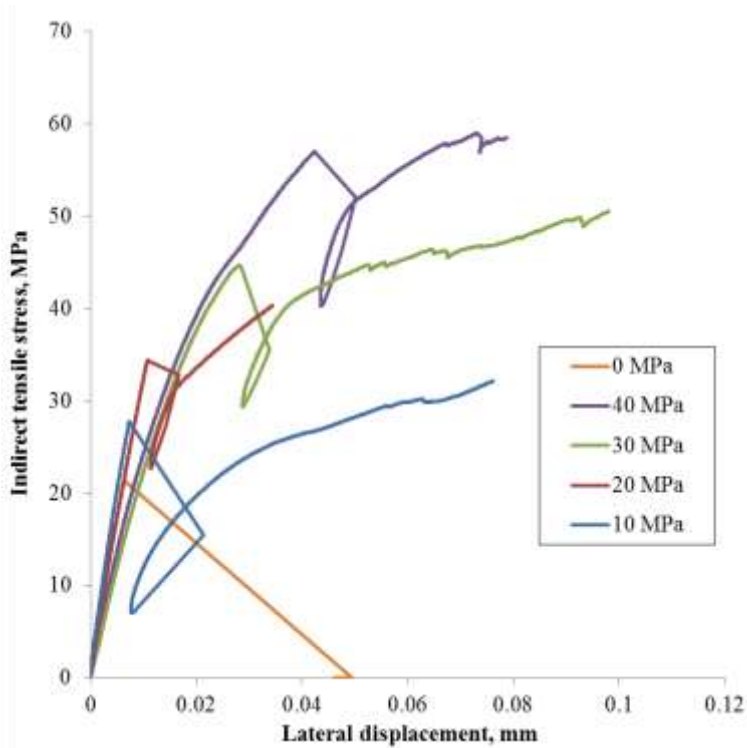
Figure 3.20 Stress-lateral displacement curves for Marcellus shale in the confined Brazilian test

71

The failure of Eagle Ford and Marcellus shale discs are characterized by a sudden increase of lateral displacement at failure, this is manifested by the post-peak straight line and sudden unloading and reloading cycle (Figs 3.19-20), and this is a character of brittle response. This sudden failure even occurred in 40 MPa confining pressure.
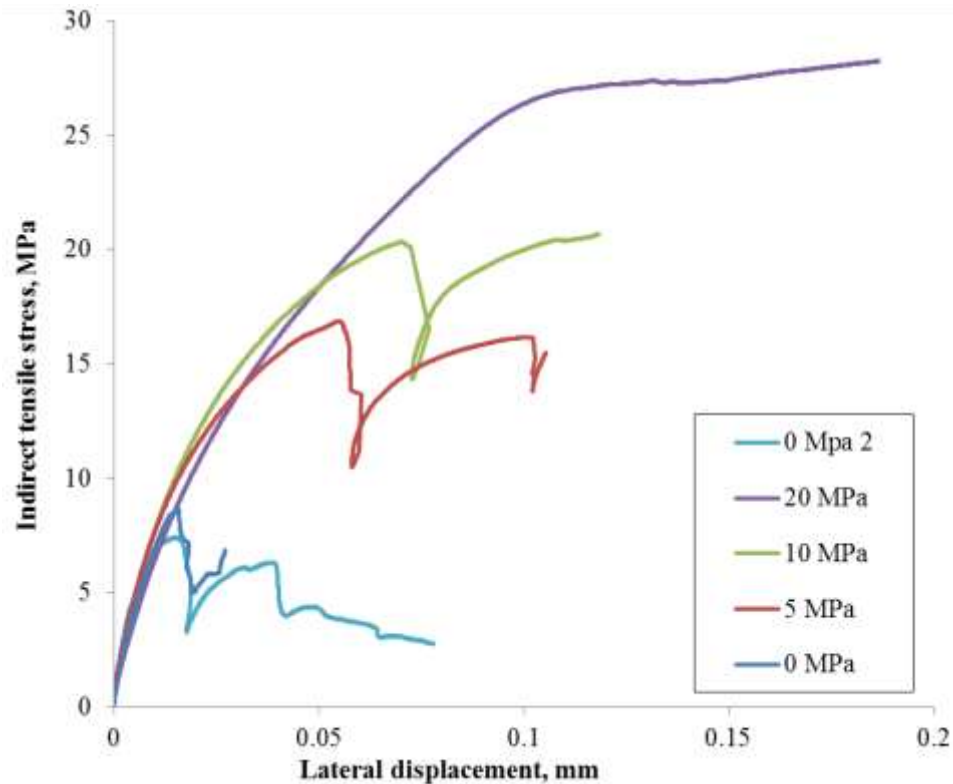
Figure 3.21 Stress-lateral displacement curves for Barnett shale in the confined Brazilian test

The failure behavior of Barnet disc is ductile; there is no sudden increase of lateral displacement at failure. Peeling off the copper jackets of Barnett discs reveals that the failure of discs are due to splitting along bedding plane and plastic deformation at the contact point, there is no extension cracks along σ_1 direction at the center of the discs, this is due to the strong ductile and anisotropic nature of tested Barnett discs.

Spectrum title	Quartz	Calcite	Dolomite	Illite	Smectite	Kaolinite	Chlorite	Pyrite	Oglioclase	Apatite	Aragonite
Eagleford	14	58	0	5	0	3	6	3	3	1	2
Barnett	14	0	1	51	6	1	1	6	2	14	0
Marcellus	0	81	0	3	0	0	3	3	0	1	3

Figure 3.22 Mineralogical compositions of three shale samples
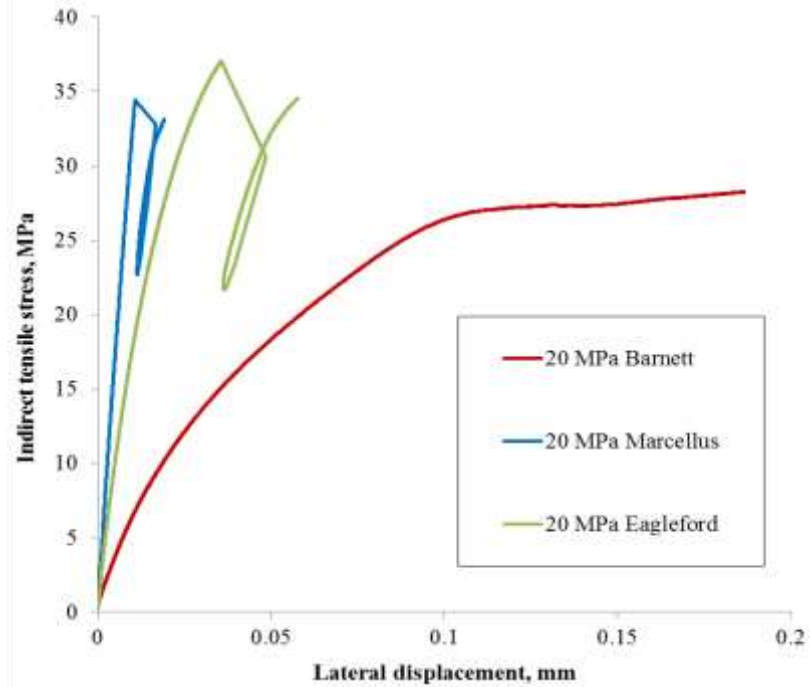
Figure 3.23 Brittleness comparisons of the three shales at 20 MPa
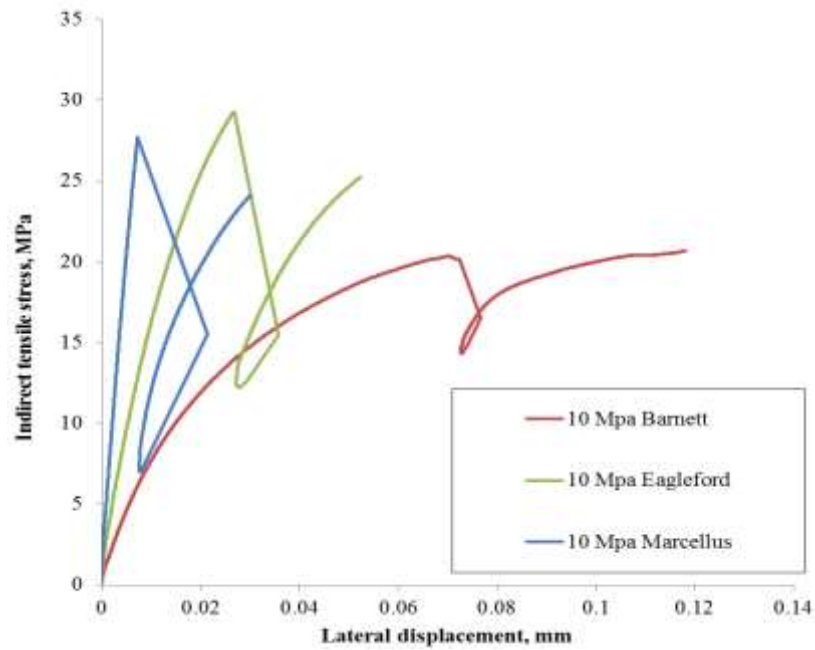
Figure 3.24 Brittleness comparisons of the three shales at 10 MPa

From the above two figures, one can tell that Marcellus shale is the most brittle one, Barnett shale is the most ductile one. The mineralogical content of the three shale samples correlate to their stress-displacement curves very well. The more quartz and calcite it has, the more brittle it is.

CONCLUSION

18 load controlled and 4 damage controlled confined Brazilian tests were conducted on Indiana Limestone; 12 damage controlled confined Brazilian tests were conducted on Scioto sandstone; 14 damage controlled confined Brazilian tests were conducted on Tennessee sandstone. Experimental results suggest that strength under complex stress condition can be measured to generate the failure envelope in the tensile and compressive domain. The failure envelope obtained from a confined Brazilian test is higher than the failure envelope obtained from triaxial compression test due to the contribution of σ_2. For all tested lithologies, tensile fracturing disappears as confining pressure increases, exhibiting a typical brittle-ductile transition, this is manifested by the load-lateral displacement curves in different confining pressures.

Scioto and Tennessee sandstones exhibit embrittlement at higher confining pressure due to a change in failure mechanism. Fracture angles in confined Brazilian test progressively increase with confining pressure; from extension fracture at low pressure to shear fracture at high pressure. This provides convincing laboratory evidence for the existence of hybrid fractures that constitute transition from extension to shear fractures.

For Eagle Ford shale and Marcellus shale (Figs.3.19 and 3.20), the failure of Brazilian disc is sudden and brittle even at high confining pressure; the response of

74

Barnett is much more ductile. The comparison reveals that Marcellus is the most brittle shale tested, Barnett is the most ductile shale tested. The mineralogical content of the three shale samples correlate to their stress-displacement curves very well.

REFERENCES

Jaeger, J. C., and E. R. Hoskins. "Rock failure under the confined Brazilian test." Journal of Geophysical research 71.10 (1966): 2651-2659.

Ramsey, J. M., & Chester, F. M. (2004). Hybrid fracture and the transition from extension fracture to shear fracture. *Nature*, *428*(6978), 63-66.

Chapter 4 Gas Shale Multistage Creep Test

ABSTRACT

The viscoelastic properties of six shale samples from the Barnett, Marcellus and Haynesville reservoirs were investigated using a triaxial creep apparatus. A series multistage triaxial creep tests were performed on these shale samples at various deviatoric stresses and confining pressures. Some samples were loaded hydrostatically to measure the volumetric creep properties. The tested samples vary in mineralogical composition, the total organic content, the maturity of the organic material, the degree of diagenesis. Test results show that rocks with more quartz and less clay have higher stiffness and higher strength. The creep strain of a certain time correlates strongly with Young's modulus and clay content of the samples. Higher confining pressure can increase the amount of creep strain at a given time under the same deviatoric stress. Experimental data indicate that the creep constitutive law governing the hydrostatic creep can be described using a power-law function of time. Under deviatoric loading, the samples exhibit linear viscoelastic creep which can be described by Burgers model. A four-element Burgers model and power law strain-time model are used to fit the strain-time curves obtained from the deviatoric creep tests. At higher deviatoric stresses, the deformation responses deviate from a linear viscoelastic trend and eventually fail at tertiary creep stage. It is proven that compaction is one of the mechanisms that contribute to creep deformation at lower deviatoric stress; we also postulate that microcracking plays a part in creep deformation at higher stresses.

INTRODUCTION

In shale reservoir development, hydraulic fracturing is used to induce a highly conductive fracture in shale formation to improve well productivity. It is widely accepted that the transient rock deformation under subsurface condition is a major factor in loss of permeability through fracture connectivity loss and proppant embedment (Huang and Ghassemi 2013). The fracture closure due to proppant embedment, proppant crushing, asperities embedment and crushing has been studied extensively. The issue of viscous deformation and creep has been considered but data and creep models need to be developed for better understanding its contribution to permeability loss. Fracture closure is controlled by the elastic, plastic and viscous property of the shale formation.

The elastic closure response occurs instantaneously when the net effective minimum horizontal stress increases as a result of reservoir depletion. The elastic response to close the fracture follows Hooke's law of elasticity and is controlled by Young's modulus of the formation. The early stage of fracture closure is governed more by the elastic property of the shale formation, but the creep property becomes significant to fracture closure with time.

The creep (viscous) effect is a slow, time-dependent deformation. The total deformation obtained from applying a constant stress is the sum of two components, deformation resulting from the elastic response and the creep function. The creep function characterizes the rheological properties of the shale formation and is best described experimentally for a given stress range, temperature, water content, and lithology.

To evaluate the influence of the elastic, viscous, and plastic property of shale formation on the fracture conductivity reduction, experimental work has been performed on shale to obtain its viscoelastic properties. Viscoelastic property of the shale samples from the Barnett, Marcellus and Haynesville shale formations were investigated using a series of multistage triaxial creep experiments at various differential stresses and confining pressures. A multistage creep test enables us to obtain creep parameters at different stress state and different temperatures from a single core sample by applying a step-wise loading path.

EXPERIMENT DESCRIPTION

Sample Description

The tested Barnett sample (#3-20) comes from a depth of 5552.35ft, Marcellus sample (#09-30) is from a depth of 5899.48ft, Haynesville samples (#05-21 and #05-22) are from depths of 12424.75ft and 12454.55ft. Also, Haynesville core plugs (#07-11 and #07-12) are from a depth of 12079.14 and 12080.14 ft., respectively. The samples were prepared by TerraTek-Schlumberger core preparation laboratory and were tested as received. The mineral content of the six samples and their elastic modulus are listed in Table 4.1.

All samples were wrapped in Teflon heat-shrink tube and kept at room condition prior to the test and experiments were conducted under dry and drained condition, in this way we were able to eliminate poroelastic effects, so the data represents the behavior of the dry rock frame. All samples except Marcellus 09-20 (length of 2.09") have standard 1×2" cylindrical shape, and the axes of the samples are perpendicular to the bedding plane.
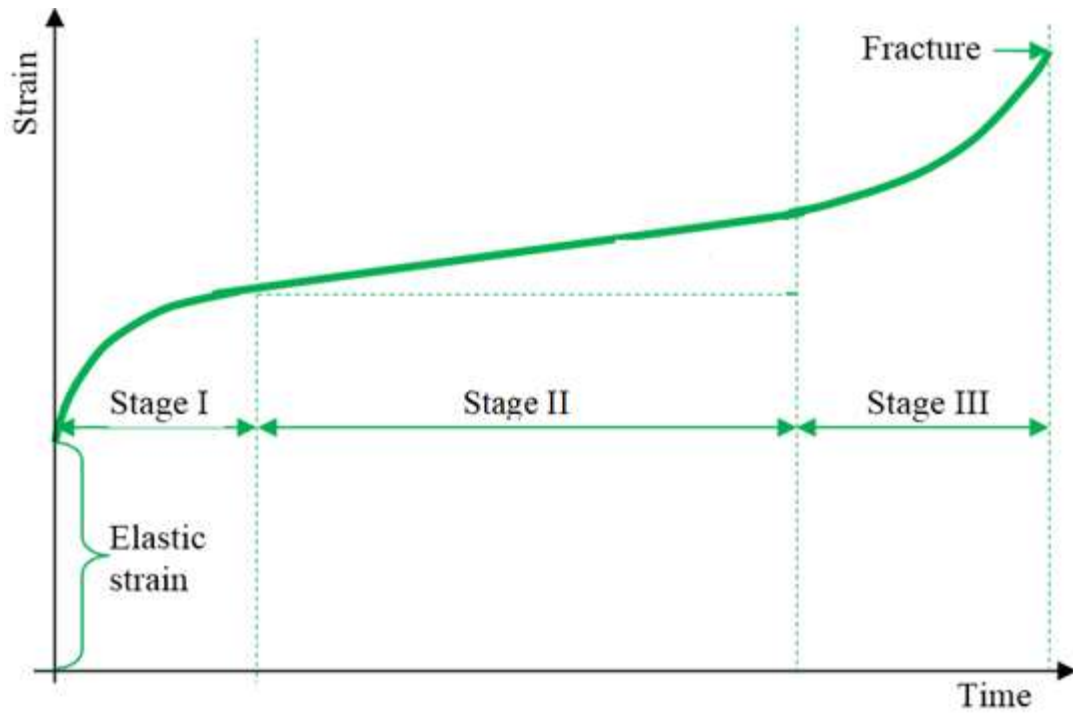
Figure 4.1 Strain variation with time of a typical creep test, stage I as primary, stage II as secondary, and stage III as tertiary stage

Table 4.1 Mineral contents of four shale samples

Sample name	Qtz/Feldspar %	Carbonate %	Clay %	Others %	Confining Pressure, psi	Young's modulus, psi
Marcellus 09-30	28	9	40	24	2755	2501320
					2320	2245619
					725	1840964
Barnett 3-20	60	10	25	5	2320	4661077
					0	4036689
Haynesville 05-21	25	23	33	18	0	2100146
Haynesville 05-22	25	23	33	18	2320	2554549

Figure 4.2 Four shale samples used for the creep test

Experimental Procedures

All the creep tests were performed on GCTS triaxial rock test system; two additional Teledyne syringe pumps were used to provide constant confining pressure and axial load, the axial load is applied to the samples with a hydraulic cylinder.

Typical loading path of a multistage triaxial creep test is illustrated in Fig. 4.4, and the loading paths of the six samples are listed in Table 4.2. After installing the sample and displacement sensor assembly in the confining cell, a constant confining pressure is applied first, and then the sample is loaded with a prescribed deviatoric stress (constant) for a prescribed period of time, increase the deviatoric stress to a higher value if required, and hold it constant. In this process, the deformation of the samples is monitored and recorded.

Figure 4.3 Hydraulic cylinder and Teledyne ISCO pump for applying axial load and GCTS pressure booster (HPC-070) for applying confining pressure
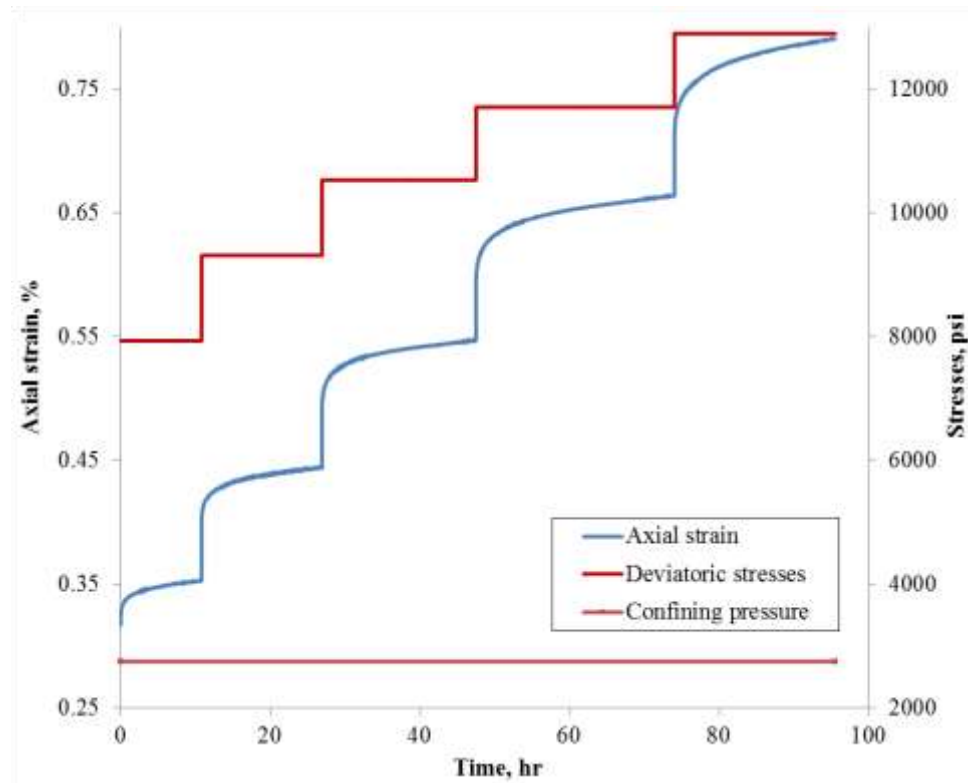

Figure 4.4 The multistage loading path and the axial strain response of Marcellus 09-30, the confining pressure is 19MPa (2750 psi)
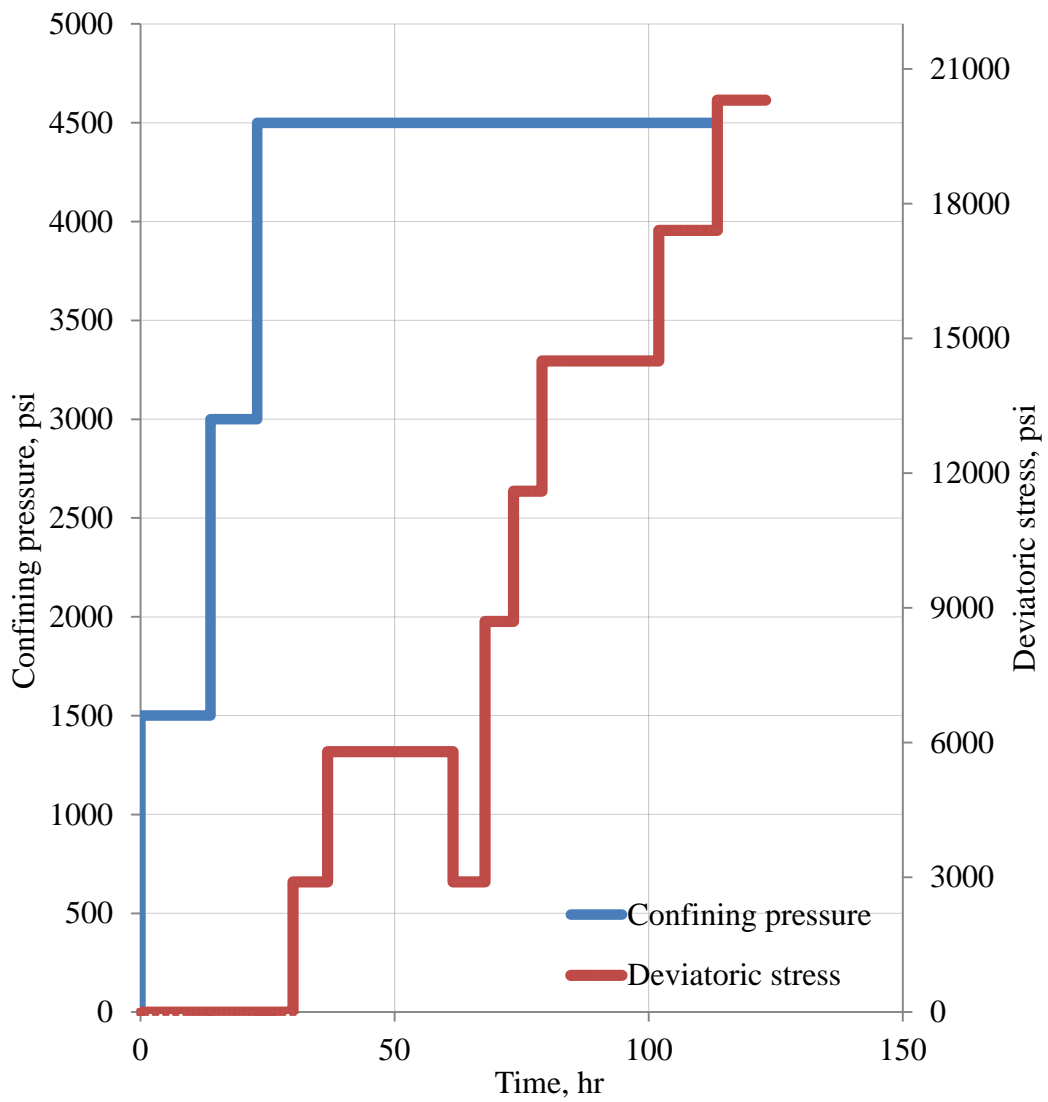
Figure 4.5 The confining pressure and deviatoric stress loading path of Haynesville 07-11, stress drop stage is for strain rebound.
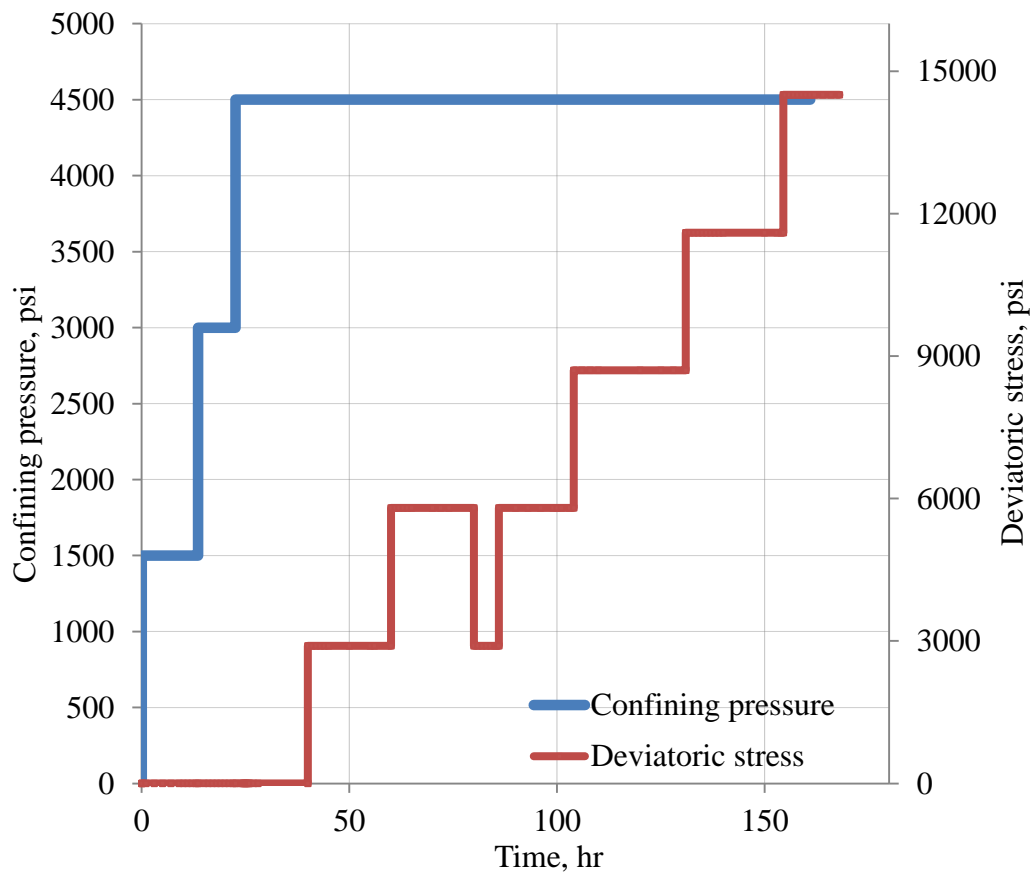
Figure 4.6 The confining pressure and deviatoric stress loading path of Haynesville 07-12, stress drop is for strain rebound.

Table 4.2 Loading path of the six samples

Sample name	Confining pressure, psi	Deviatoric stresses, psi
Marcellus 09-30	2320.6032	3900-5220
	2755.7163	8000-9300-10450-11750-12900
	725.1885	9300
Barnett 3-20	2320.6032	6740-7760-9140-10590-12040
	0	6525-8000-9300-10450-11750
Haynesville 05-21	0	4930-6525-9210-10440
Haynesville 05-22	1000-2000-3000	0-0-0
	2320.6032	5280-7980-9280
Haynesville 07-11	1500-3000-4500	0-0-0
	4500	2900-5800-2900-8700-11600-14500-17405-20305
Haynesville 07-12	1500-3000-4500	0-0-0
	4500	2900-5800-2900-5800-8700-11600-14500
Haynesville 07-12 (high temperature)	1500-3000-4500	0-0-0
	4500	2900-5800-8700-11600-14500

TEST RESULT AND INTERPRETATION
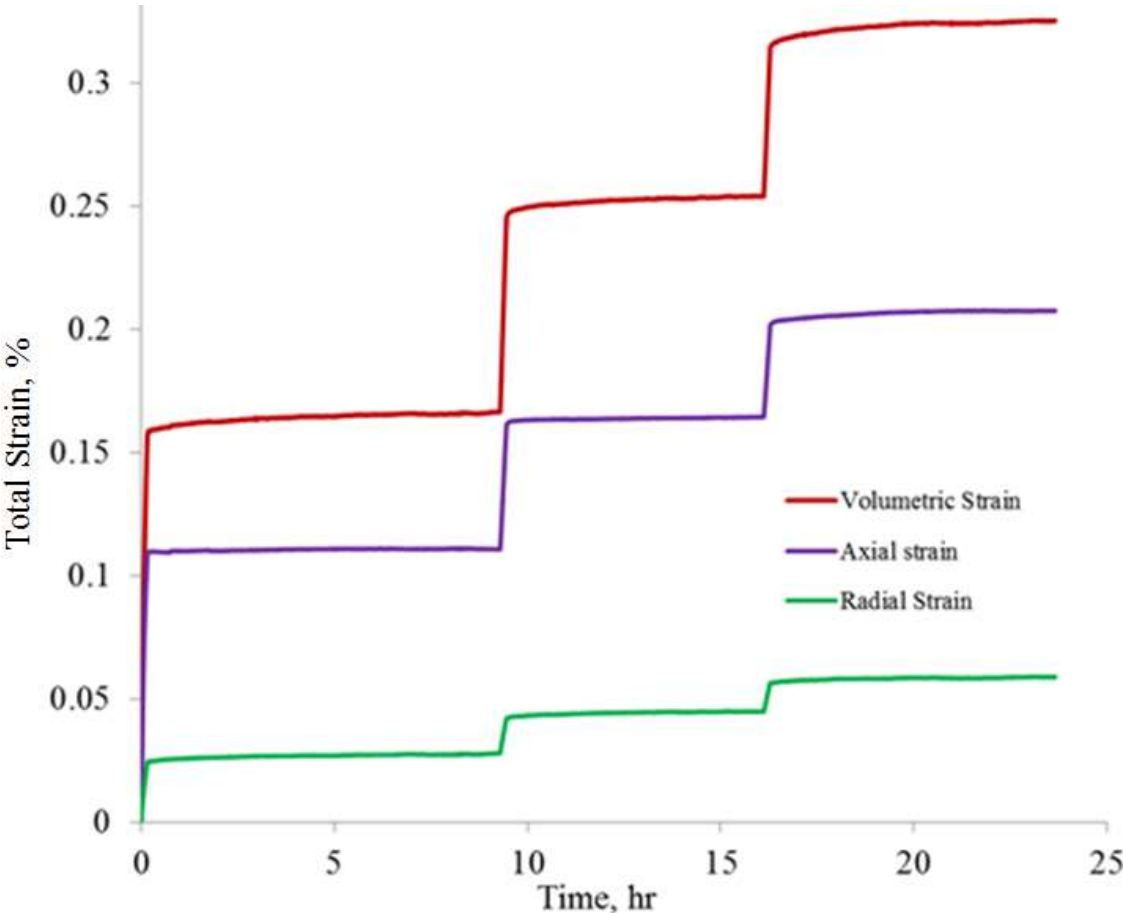
Hydrostatic Creep

Figure 4.7 Axial strain, radial strain and volumetric strain response of hydrostatic creep, three pressure stages, Haynesville 05-22
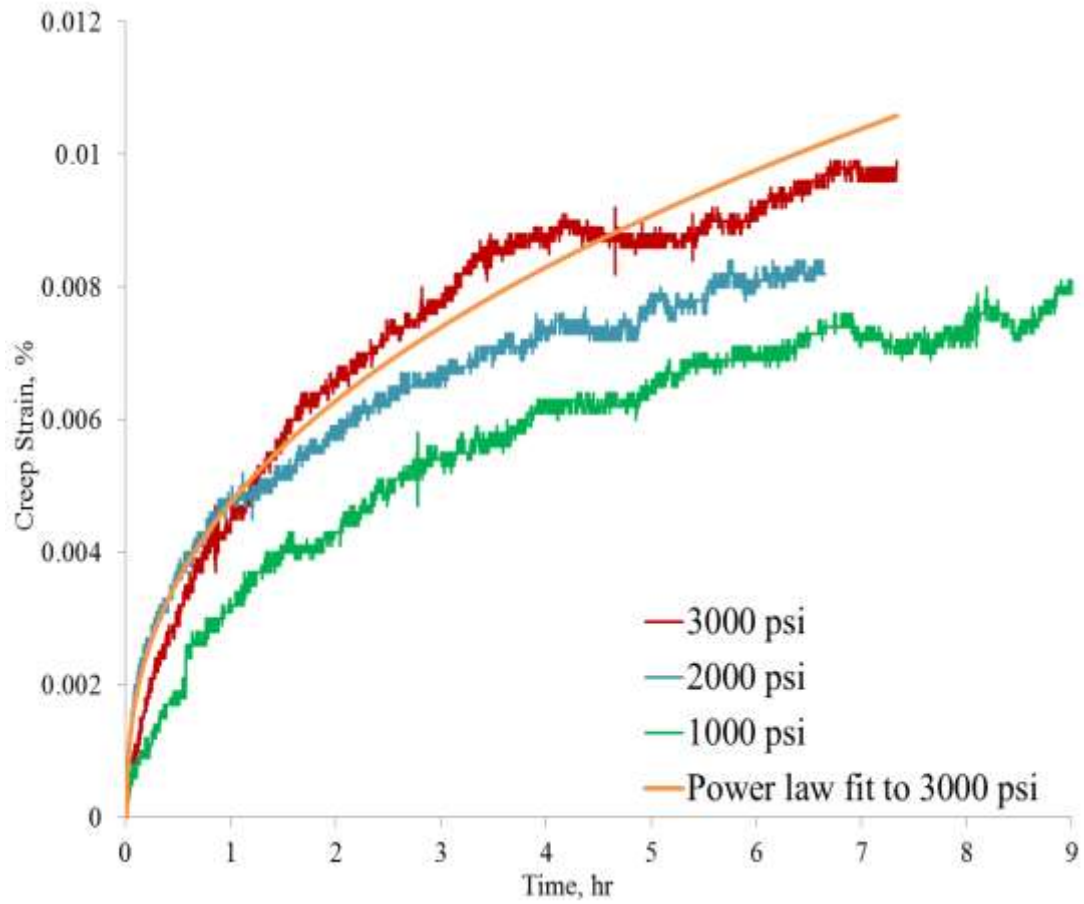
Figure 4.8 Volumetric creep strains (strain minus instantaneous elastic part) of three hydrostatic pressures, Haynesville 05-22
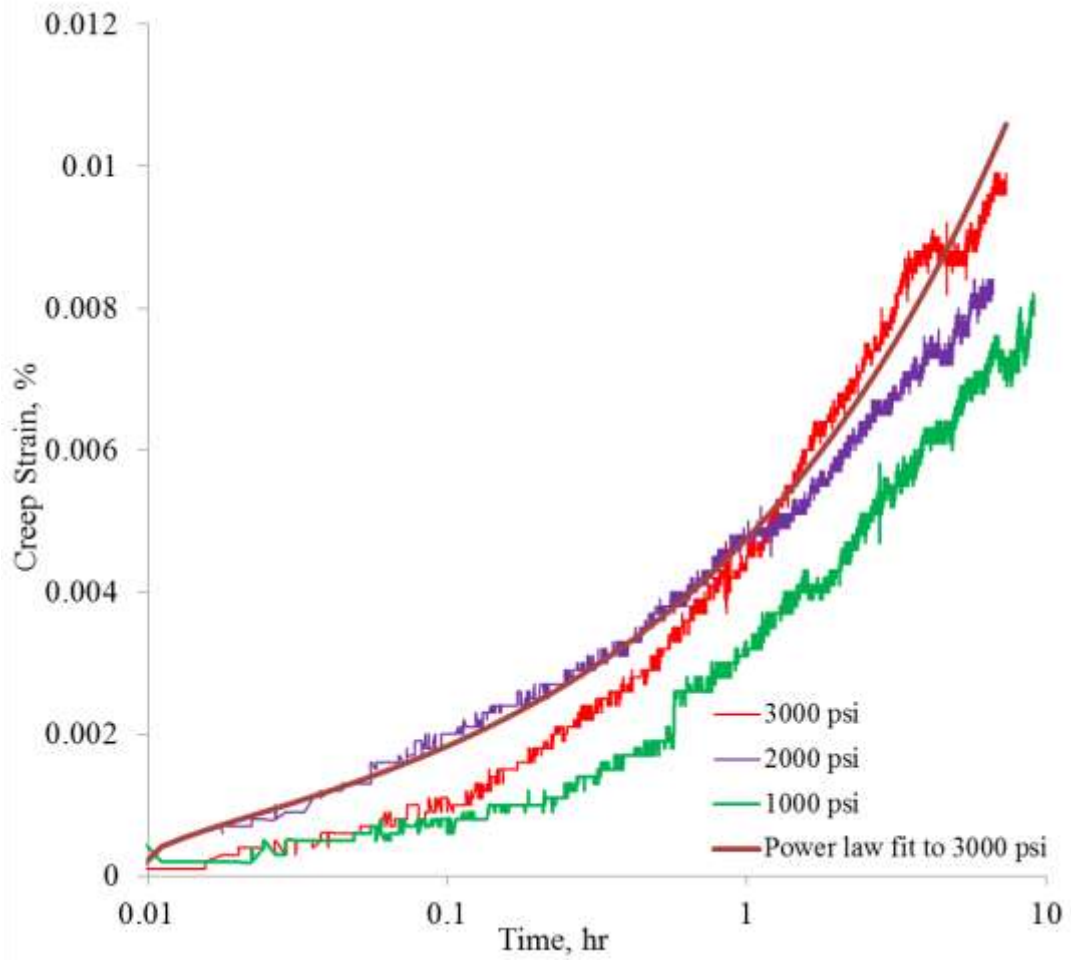
Figure 4.9 Volumetric creep strains of three hydrostatic stages, in logarithmic time scale, Haynesville 05-22
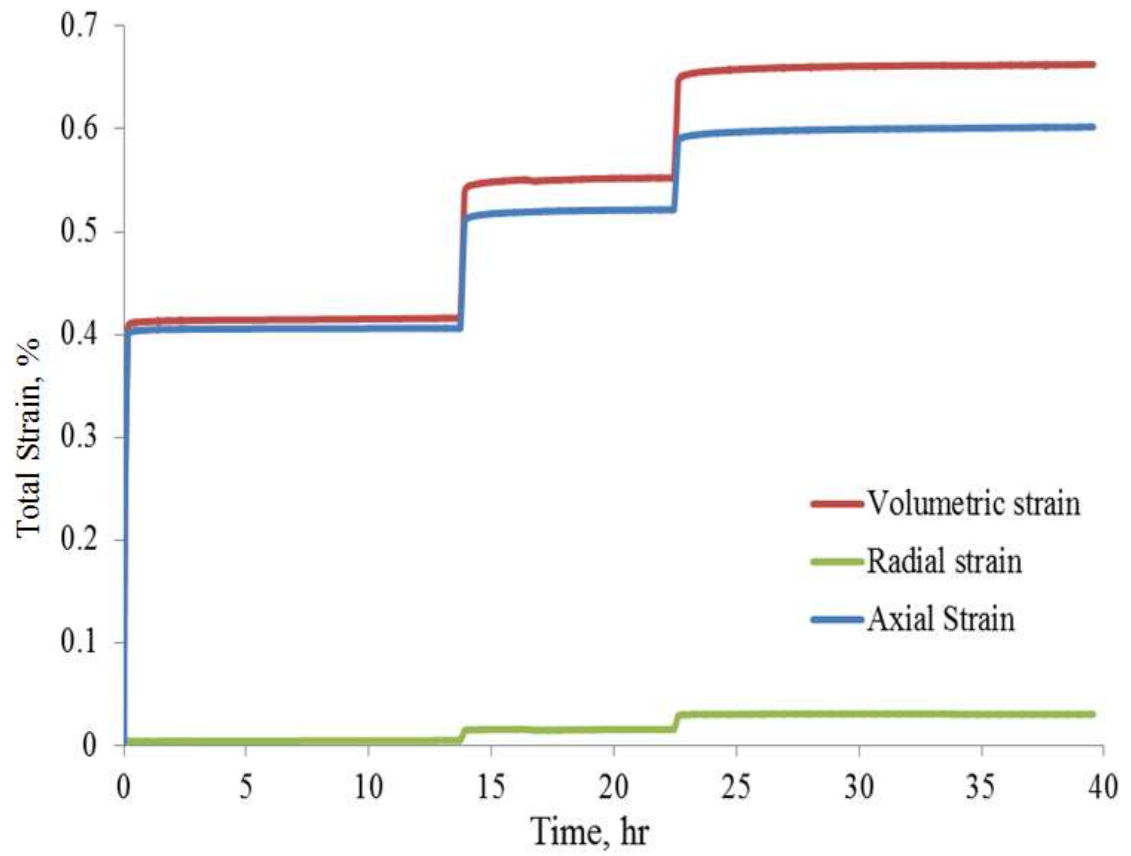
Figure 4.10 Axial strain, radial strain and volumetric strain response of hydrostatic creep, three pressure stages, Haynesville 07-12
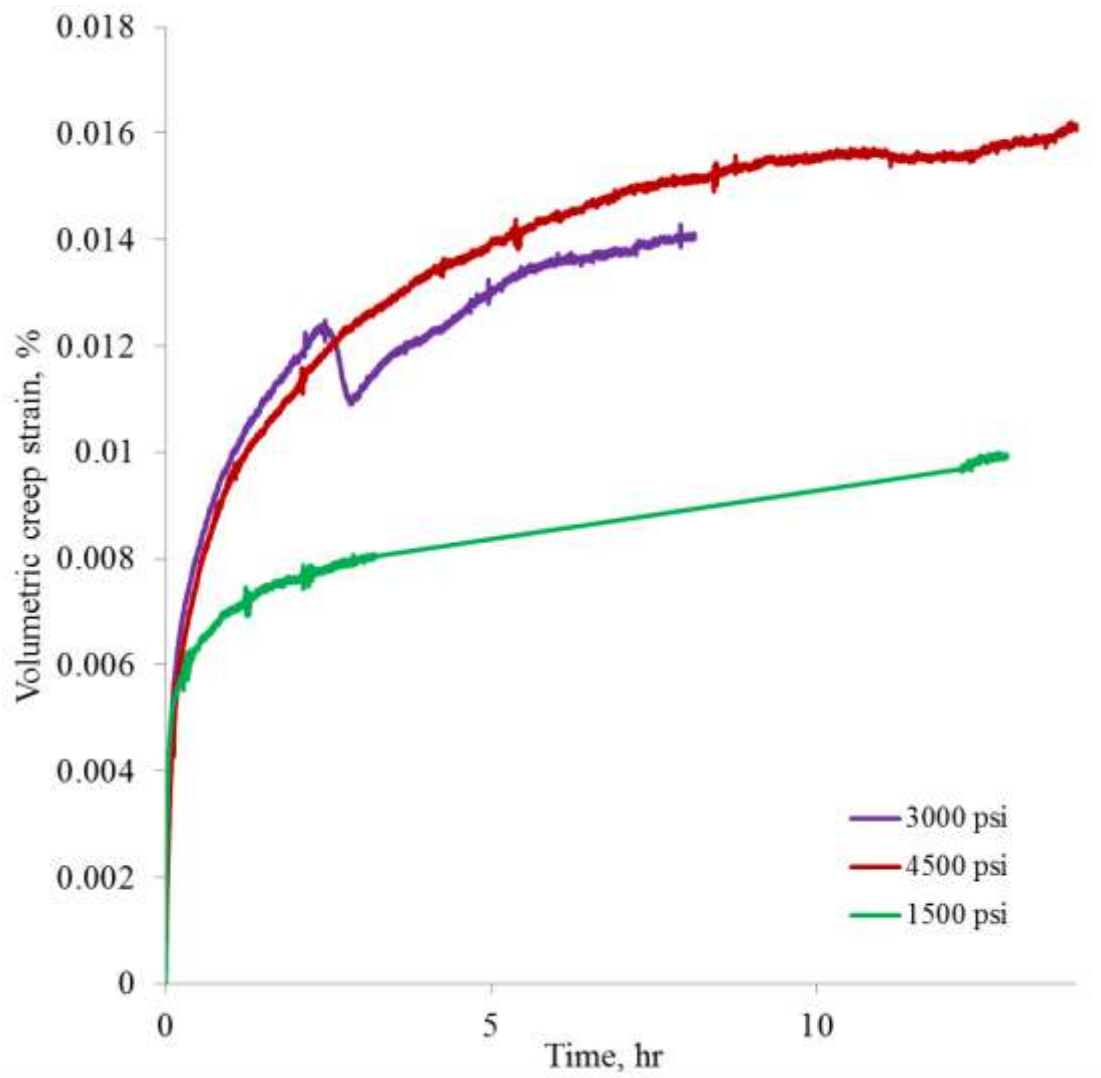
Figure 4.11 Volumetric creep strains of three hydrostatic pressures, Haynesville 07-12.
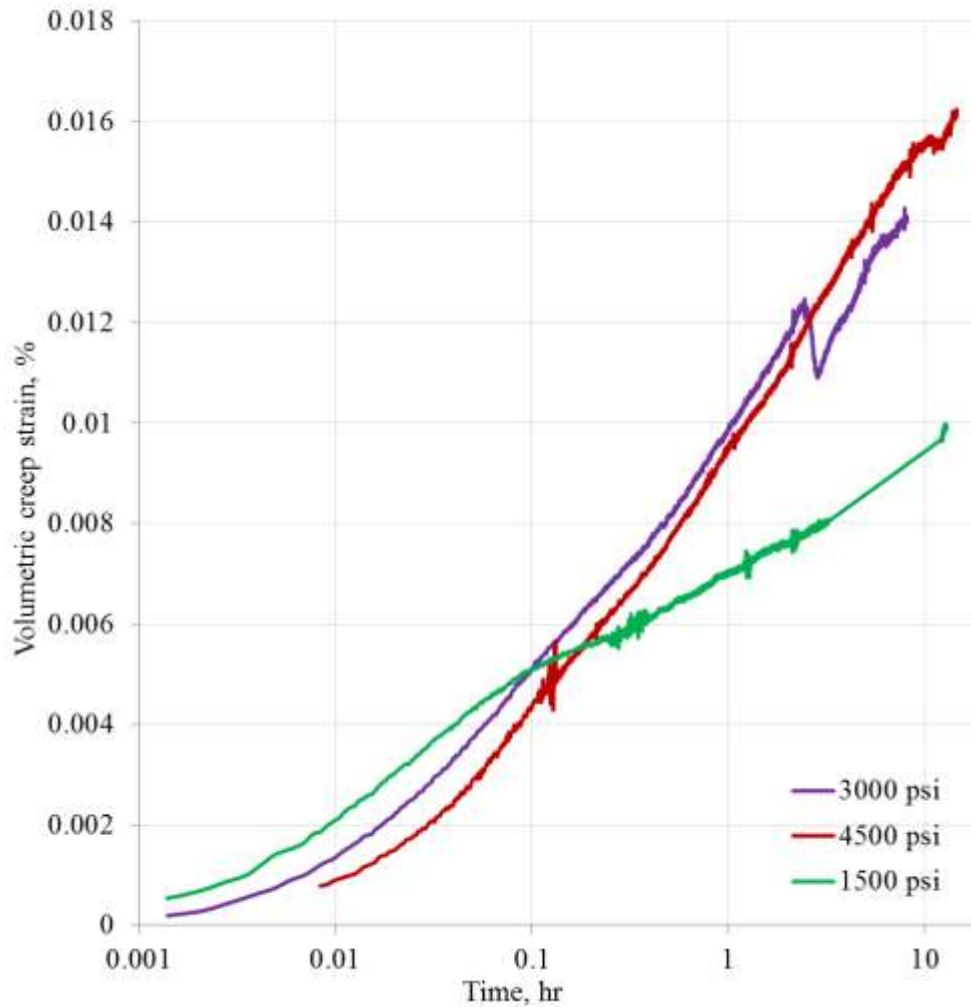
Figure 4.12 Volumetric creep strains of three hydrostatic stages, in logarithmic time scale, Haynesville 07-12

From Figs.4.8-4.12, one can tell the form of creep constitutive law governing the hydrostatic creep can be described as a power-law function of time and logarithm function of time.

Deviatoric Creep

For Marcellus 09-30 sample, the first intended confining pressure is 2320 psi (16 MPa), the confining pressure was applied using GCTS pressure booster, at the earlier stage of the two stage creep test, the confining pressure was around 2320 psi, but in the middle of the two stages test, the confining pressure jumps to 2755 psi (19 MPa)

gradually. To keep the consistency, the confining pressure of all the later stages was kept 2755 psi (19 MPa) using a more stable Teledyne ISCO pump.
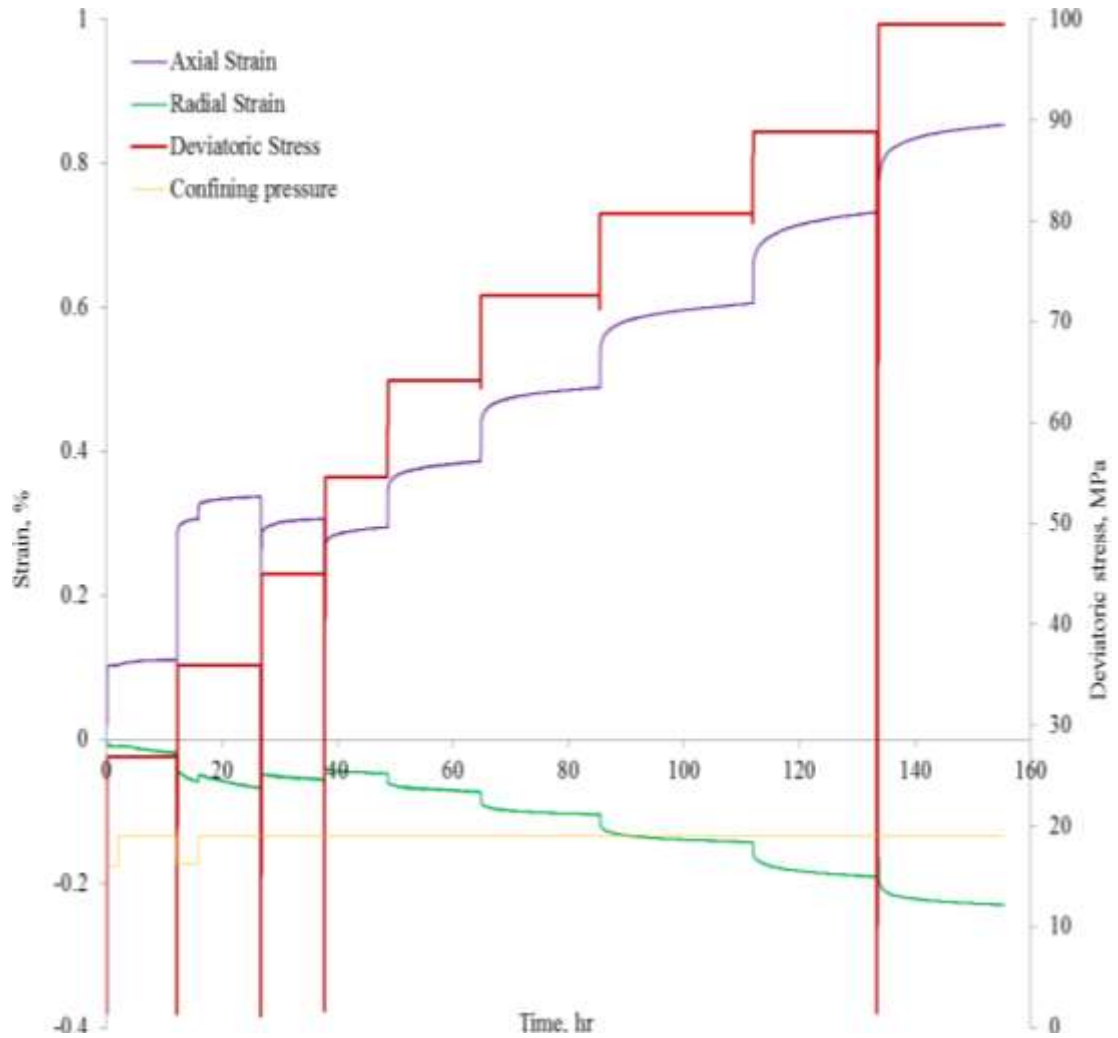
Figure 4.13 The deviatoric loading path, confining pressure, the axial strain response, and radial strain response of Marcellus 09-30
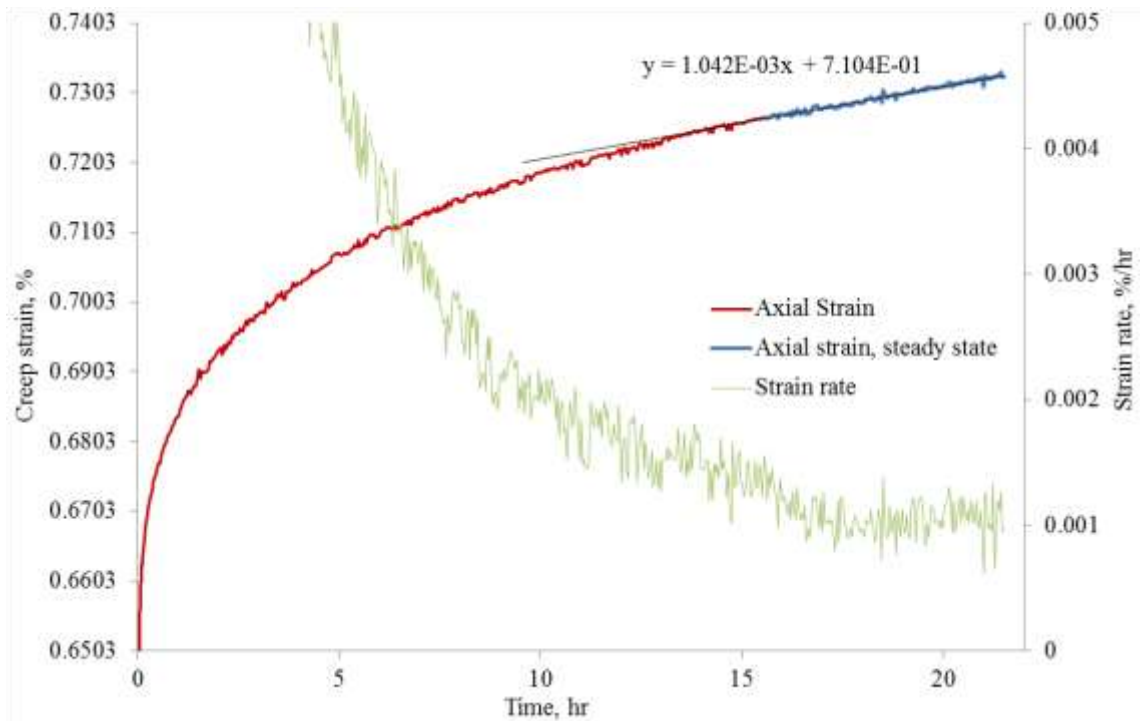
Figure 4.14 The axial creep strain and strain rate of Marcellus 09-30, the 7th stage

The strain rate $\frac{d\varepsilon_1}{dt}$ decrease with time until a constant value is reached, but similarly to other tests on other shales (Zoback et al., 2011) the strain-time plots do not level off even after 6 days. Thus, we choose the last portion of the strain-time curves as the "pseudo-steady" strain rate. The strain rates of the 3rd to 7th stage of creep test were obtained by fitting a straight line to the last portion of the strain-time curves, as shown in Fig. 4.14. The strain rate vs. stress relation is plotted in Fig 4.15.
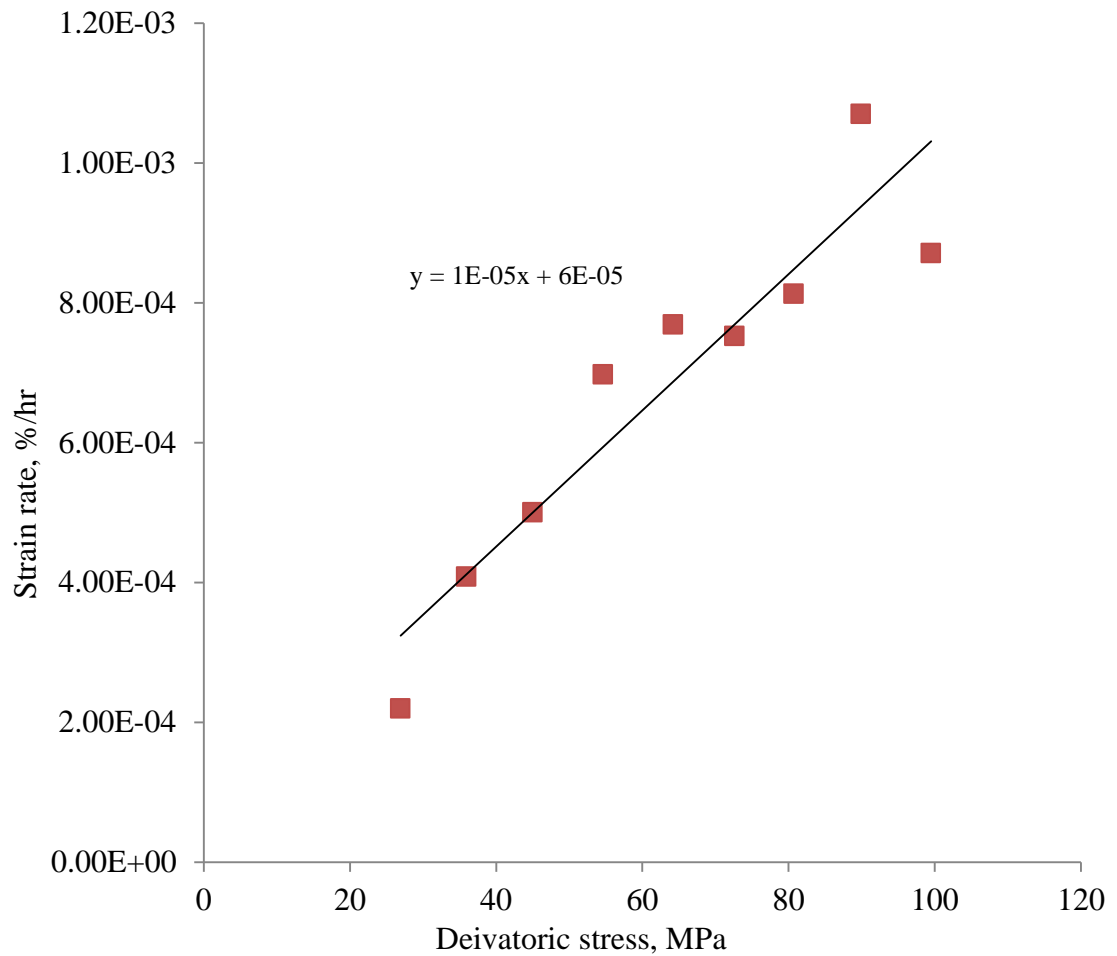
Figure 4.15 Strain rate-stress relations; confining pressure is 2755 psi, Marcellus-09-30

As shown in Fig. 4.15, the pseudo-steady strain rate increases roughly linearly with deviatoric stress, thus the creep can be modeled using linear viscoelastic models, such as Burgers and Maxwell, because Maxwell cannot model the transient creep portion of strain-time relation. Thus, Burgers model is used to model this multistage creep. Because the confining pressure of the first two stages jumps from 2320 psi (16 MPa) to 2755 psi (19MPa), thus the strain rates of the two stages are the rates under 2755 psi, but the elastic portions are under 2320 psi pressure. Thus the first two stages are neglected in fitting the Burgers model. A least-square fitting method was used to fit Burger model (Eq.1) to the strain-time curve obtained from 3rd to 7th stage creep:

$$\varepsilon = \frac{\sigma}{E_1} + \frac{\sigma}{\eta_1}t + \frac{\sigma}{E_2}\left(1 - e^{-\frac{E_2}{\eta_2}t}\right) \tag{1}$$

$$\dot{\varepsilon} = \frac{\sigma}{\eta_1} + \frac{\sigma}{\eta_2}e^{-\frac{E_2}{\eta_2}t} \tag{2}$$
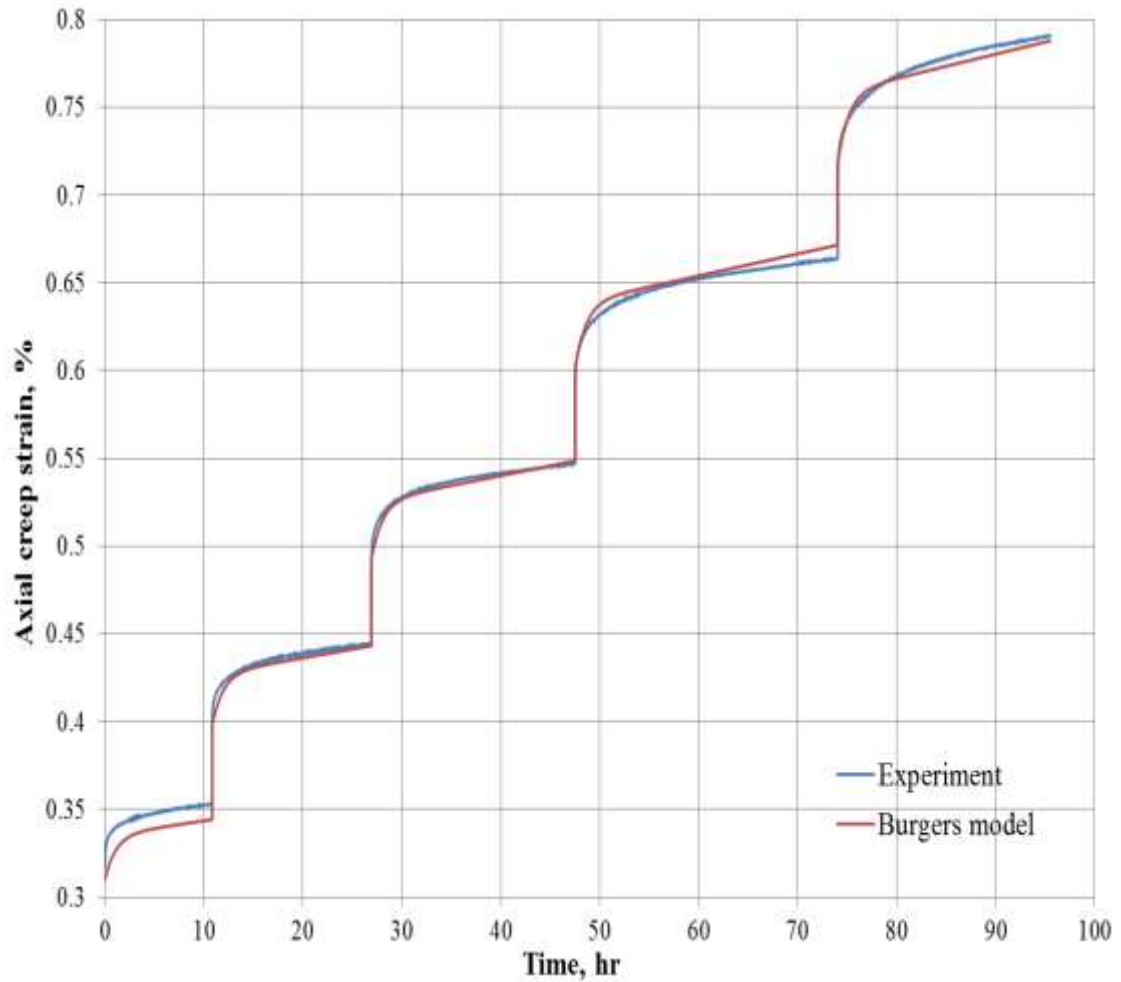
Figure 4.16 Comparisons between experimental creep strain and Burger creep reaction to five stresses, confining pressure 2755 psi. Marcellus-09-30

The two elastic and viscous parameters were obtained using the least-square fitting method. As one can see, the burgers model gives a relatively good fit to the creep data. The least-square error is 0.040238.

Table 4.3 Burger creep parameters

	E1 , psi	E2, psi	η_1, Pa/s	η_2, Pa/s
Marcellus 09-30 (2755 psi)	2556144	32059278	2.32E+10	8.87E+08
Barnett 03-20 (2320 psi)	4747809	354417895	9.46E+10	9.75E+09
Haynesville 5-22 (2320 psi)	2508572	46731509	1.36E+11	3.21E+09

The power law (power function of stress and time) has been widely used by various researchers to express strain-time relationships for nonlinear viscoelastic materials. It has the following form which is often called the nutting equation.

$$\varepsilon^c = k\sigma^p t^n \tag{3}$$

where ε^c is the creep strain without the instantaneous elastic strain, because the pseudo-steady strain rate increases almost linearly with deviatoric stress, thus p=1, the total strain of a constant stress creep test is

$$\varepsilon = \frac{\sigma}{E} + k\sigma t^n \tag{4}$$

Similarly, a least-square fitting method was used to fit power law model (Eq.4) to the strain-time curve obtained from 3rd to 7th stage creep. The least-square error of power law is 0.023684.

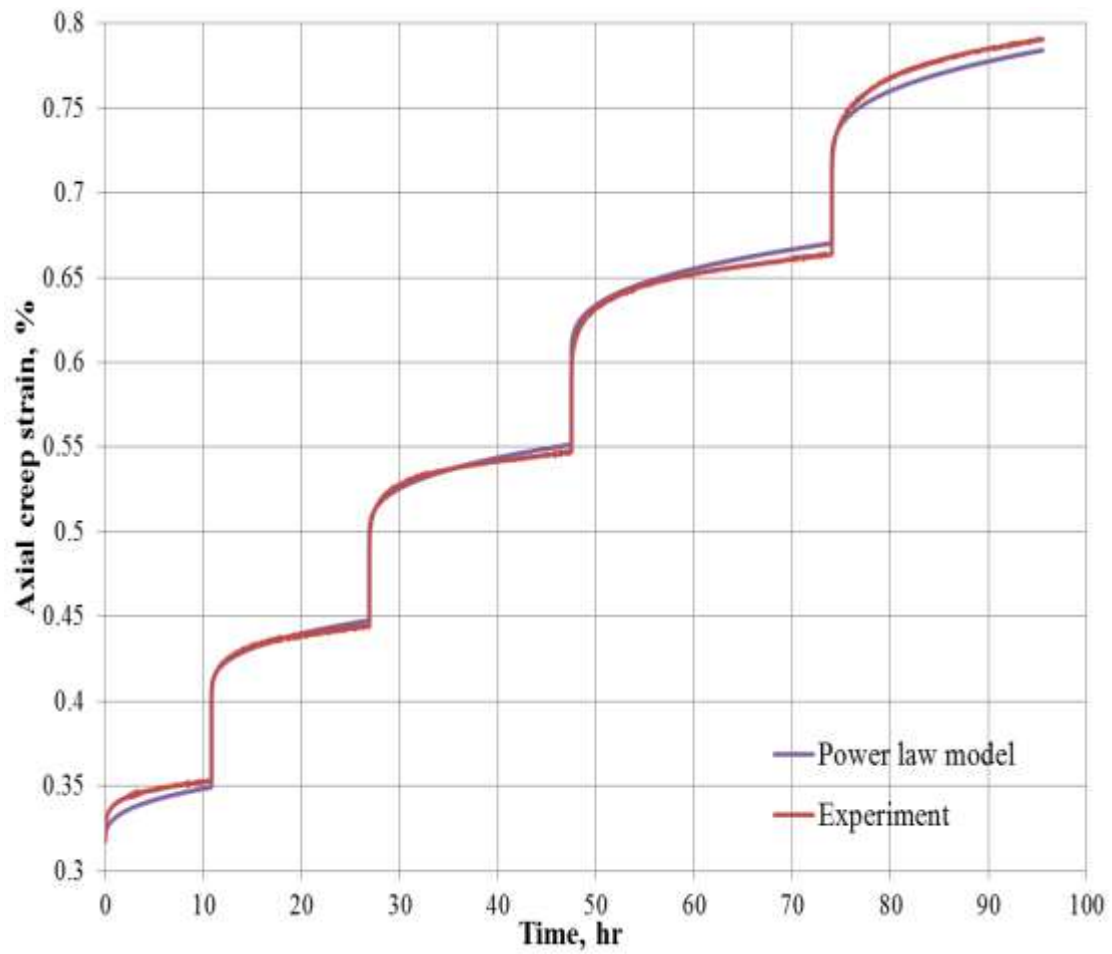**Figure 4.17 Comparisons between experimental creep strain and power law creep reaction to five stresses, Marcellus-09-30, confining pressure 2755 psi**

Table 4.4 Power-law creep parameters

	E, psi	k	n
Marcellus 09-30 (2755 psi)	2501320	1.46E-5	0.349379
Barnett 03-20 (2320 psi)	4821920	2.5898E-06	0.349378568
Haynesville 5-22 (2320 psi)	2521360	2.14E-06	0.473279

95
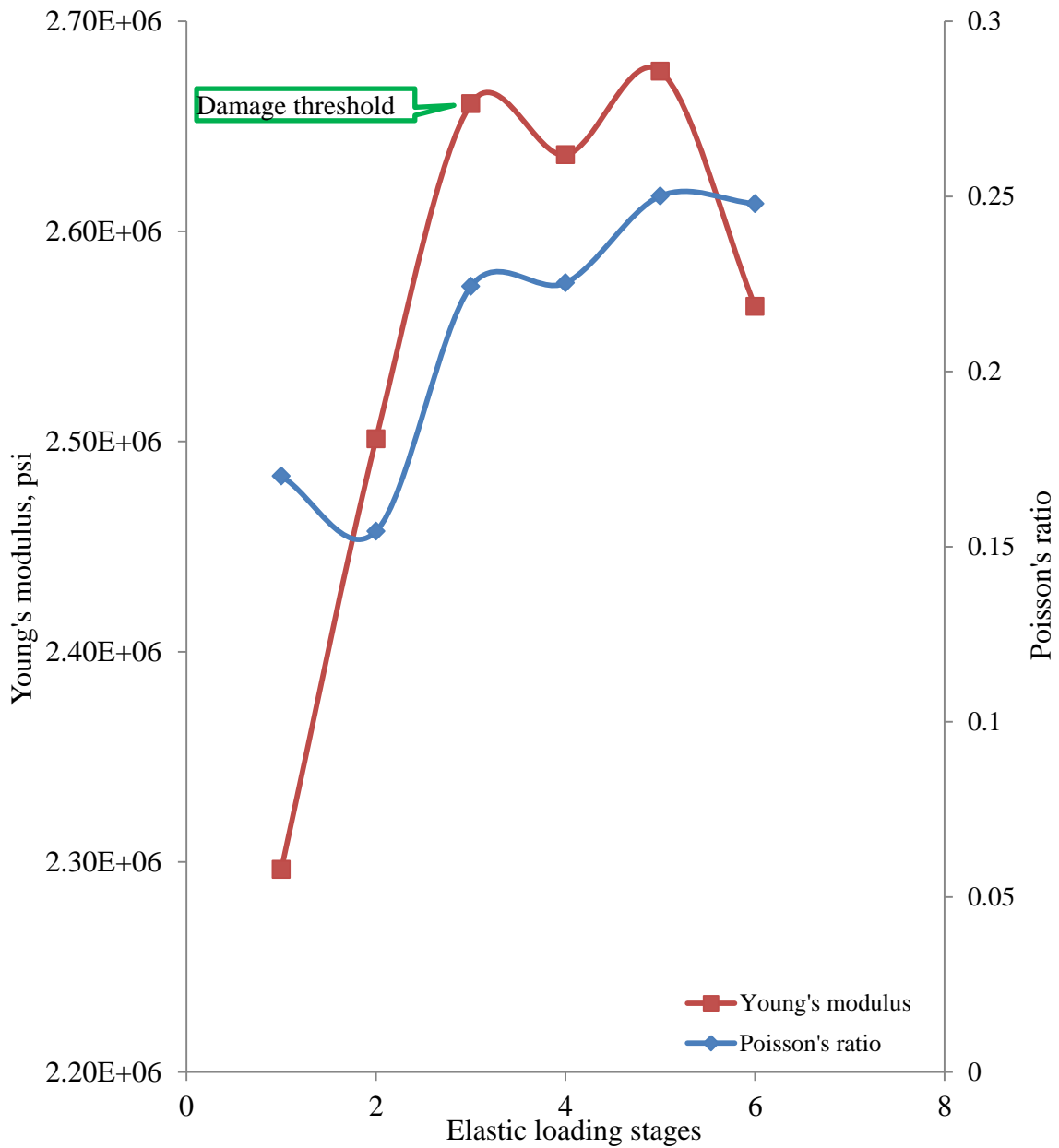
Figure 4.18 Young's modulus and Poisson's ratio change for every elastic loading stage, confining pressure is 2320 psi, Marcellus-09-30

As can be seen in Fig.4.18, the sample experienced initial hardening and then softening, we speculate that the hardening is caused by compaction as the stress increases, and the softening is caused by damage (microcracking).
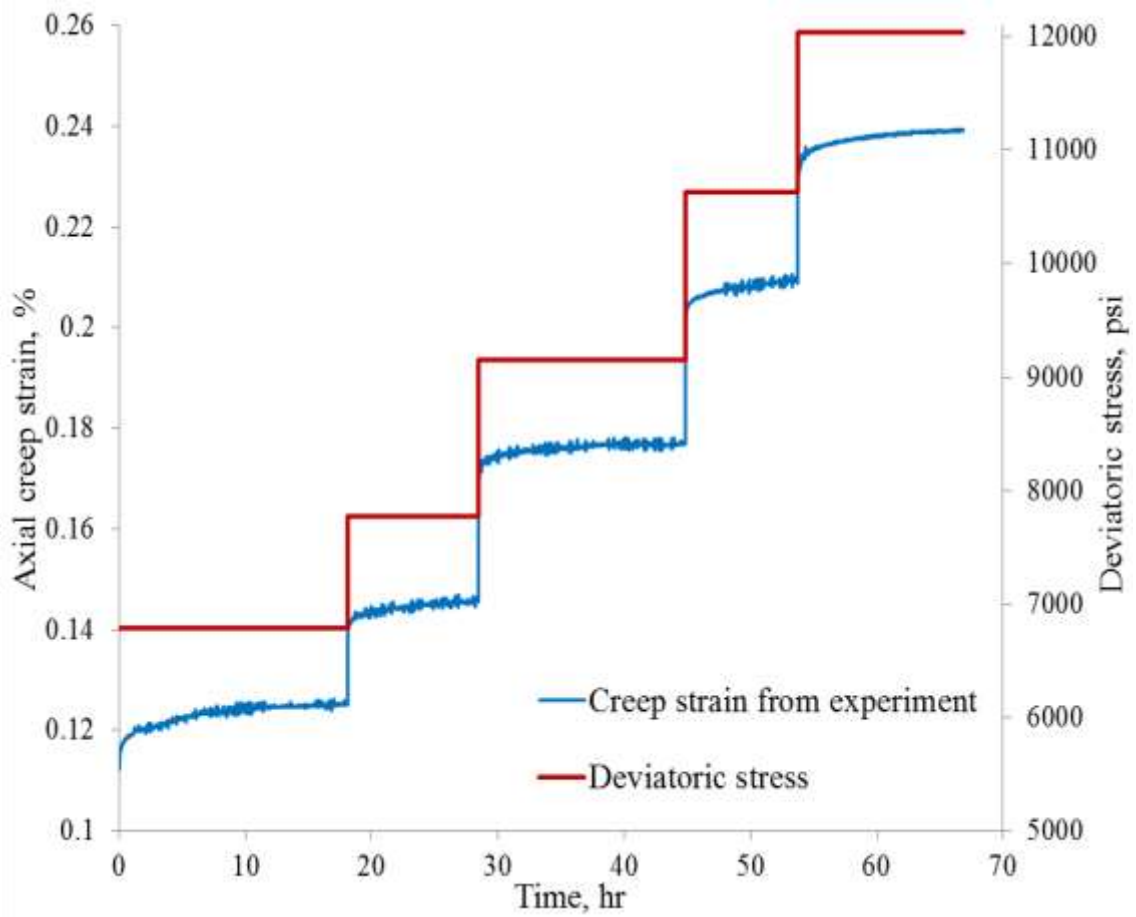
Figure 4.19 The multistage loading path and the axial strain response of Barnett 3-20, confining pressure is 2320 psi
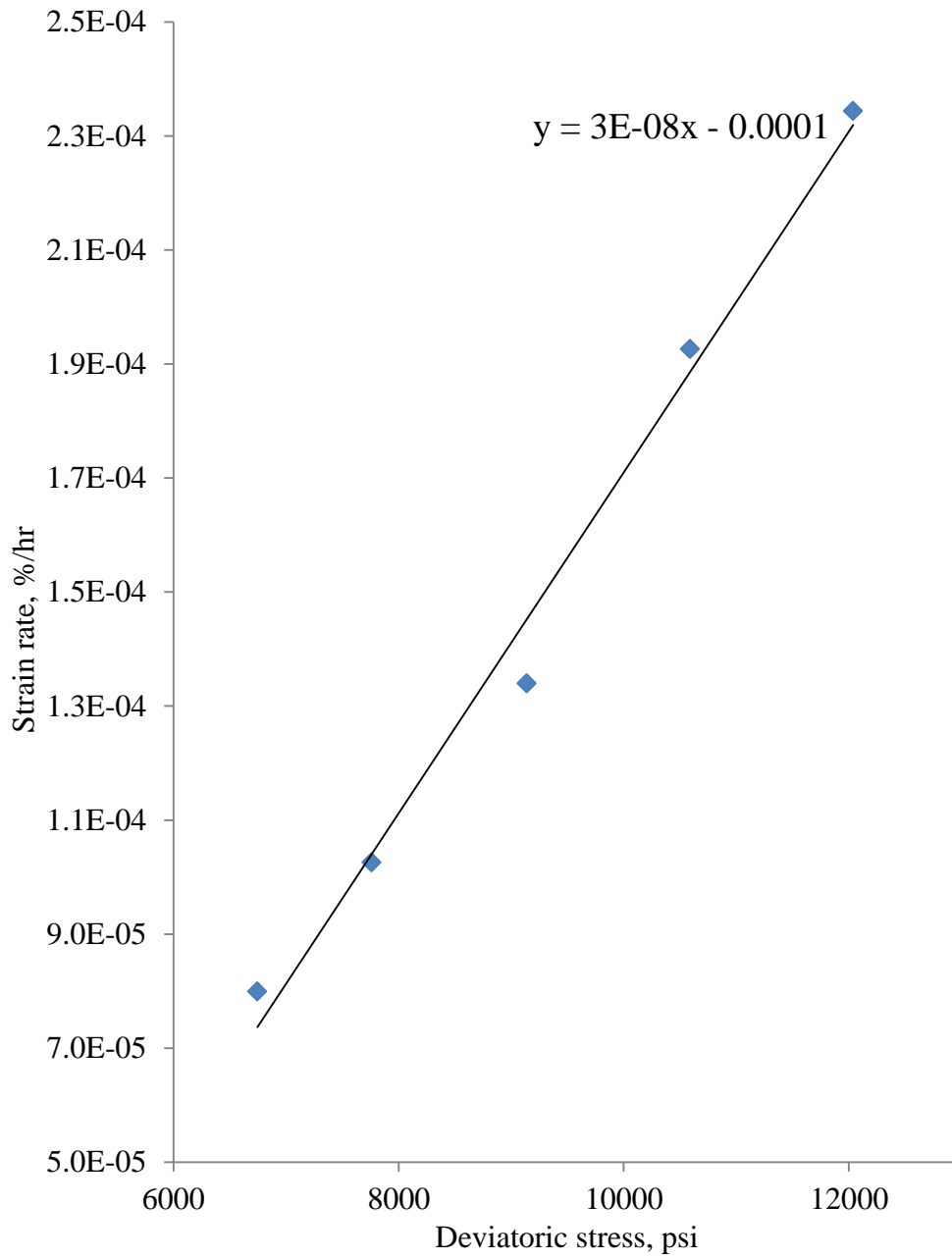
Figure 4.20 Strain rate-stress relation, confining pressure 2320 psi, Barnett 03-20

Figure 4.21 Comparison between creep strain and power law creep reaction to five stresses, confining pressure 2320 psi, Barnett 3-20
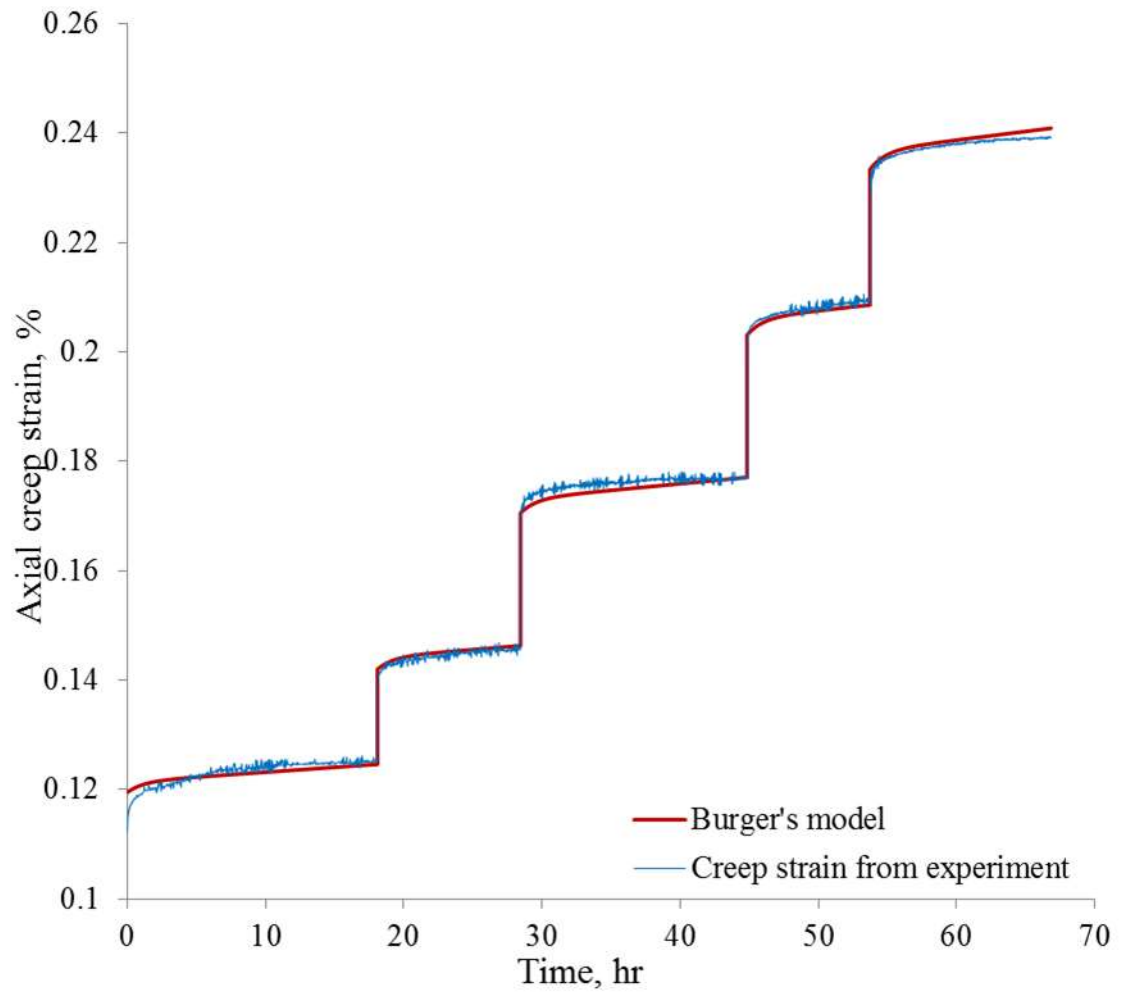
Figure 4.22 Comparisons between creep strain and Burger's creep reaction to five stresses, confining pressure 2320 psi, Barnett 3-20
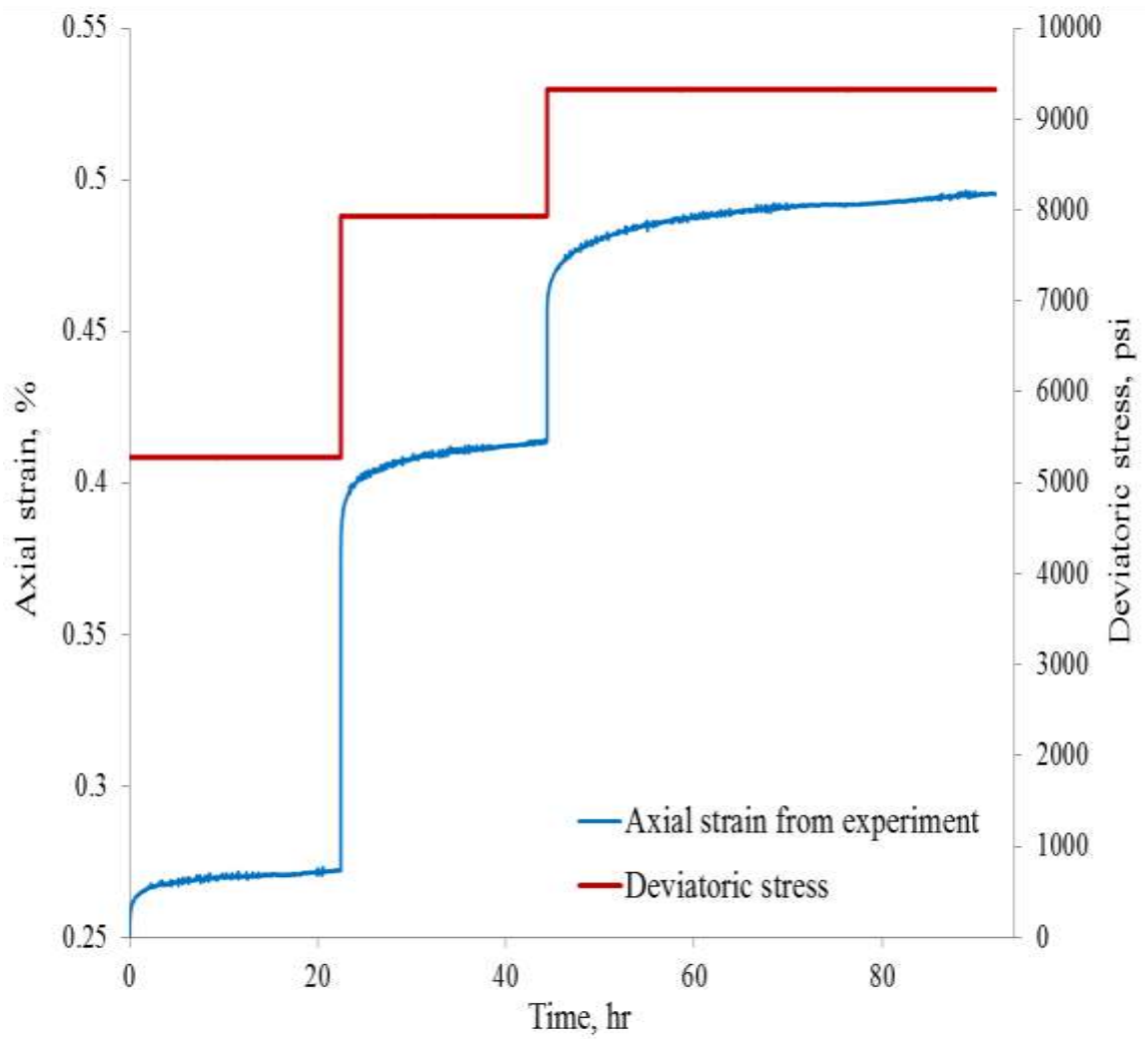
Figure 4.23 The multistage loading path and the axial strain response of Haynesville 5-22, confining pressure is 2320 psi
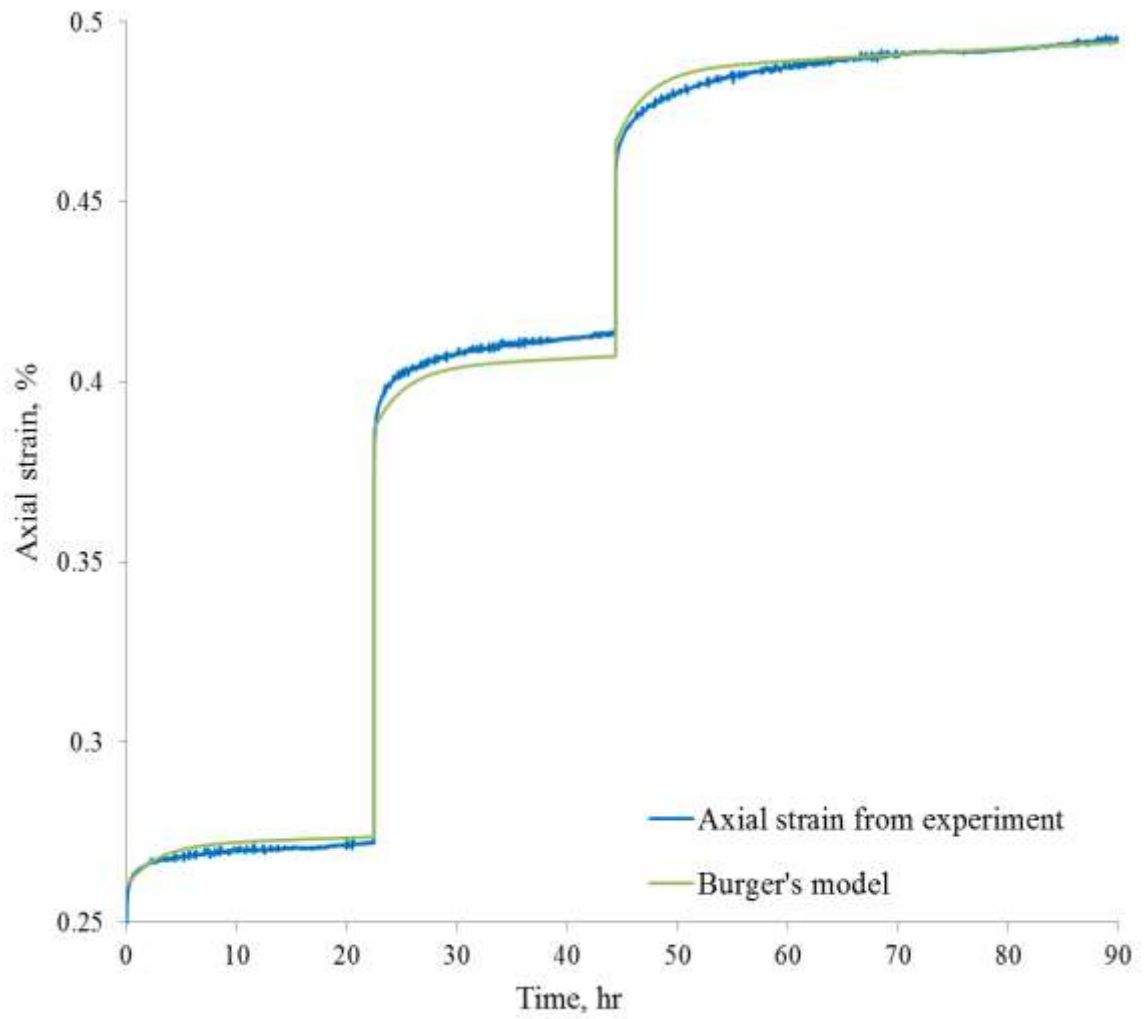
Figure 4.24 Comparisons between creep strain and Burger's creep reaction to three stresses, confining pressure 2320 psi, Haynesville 5-22
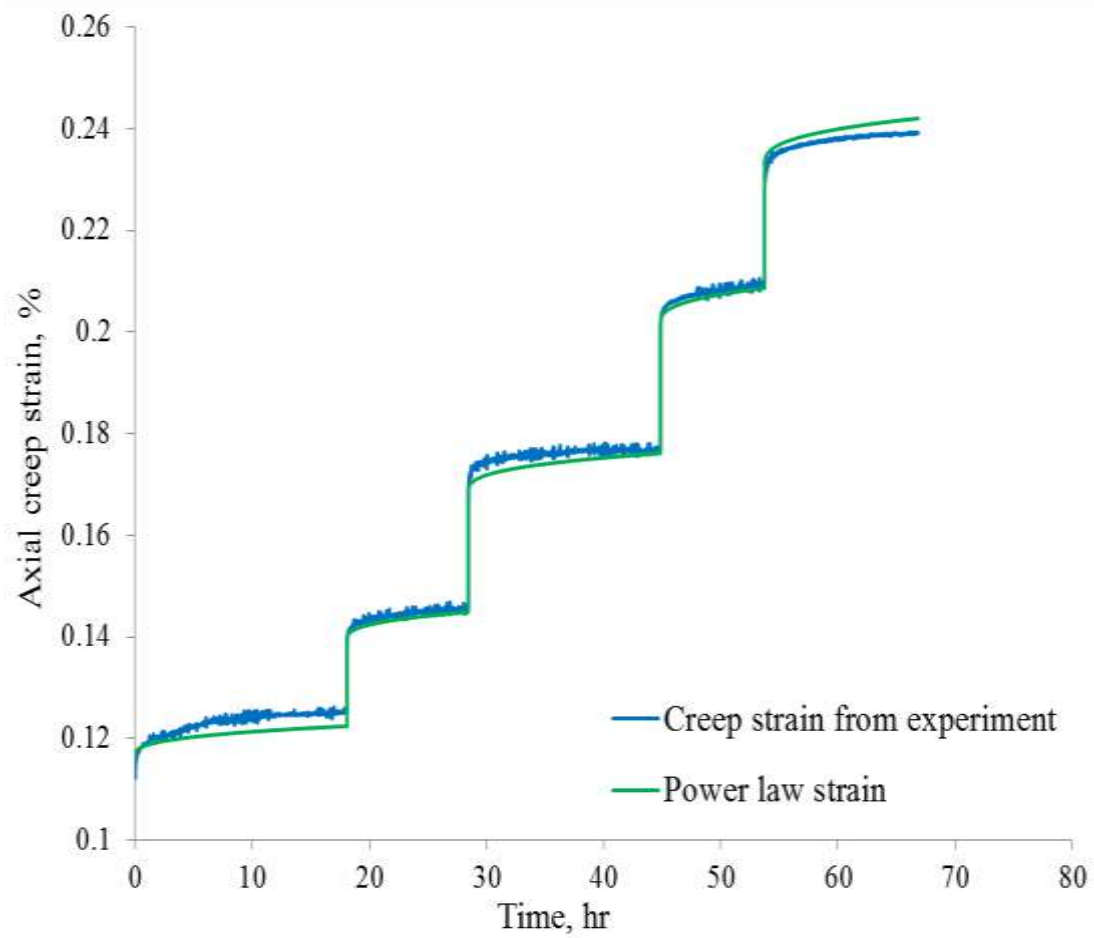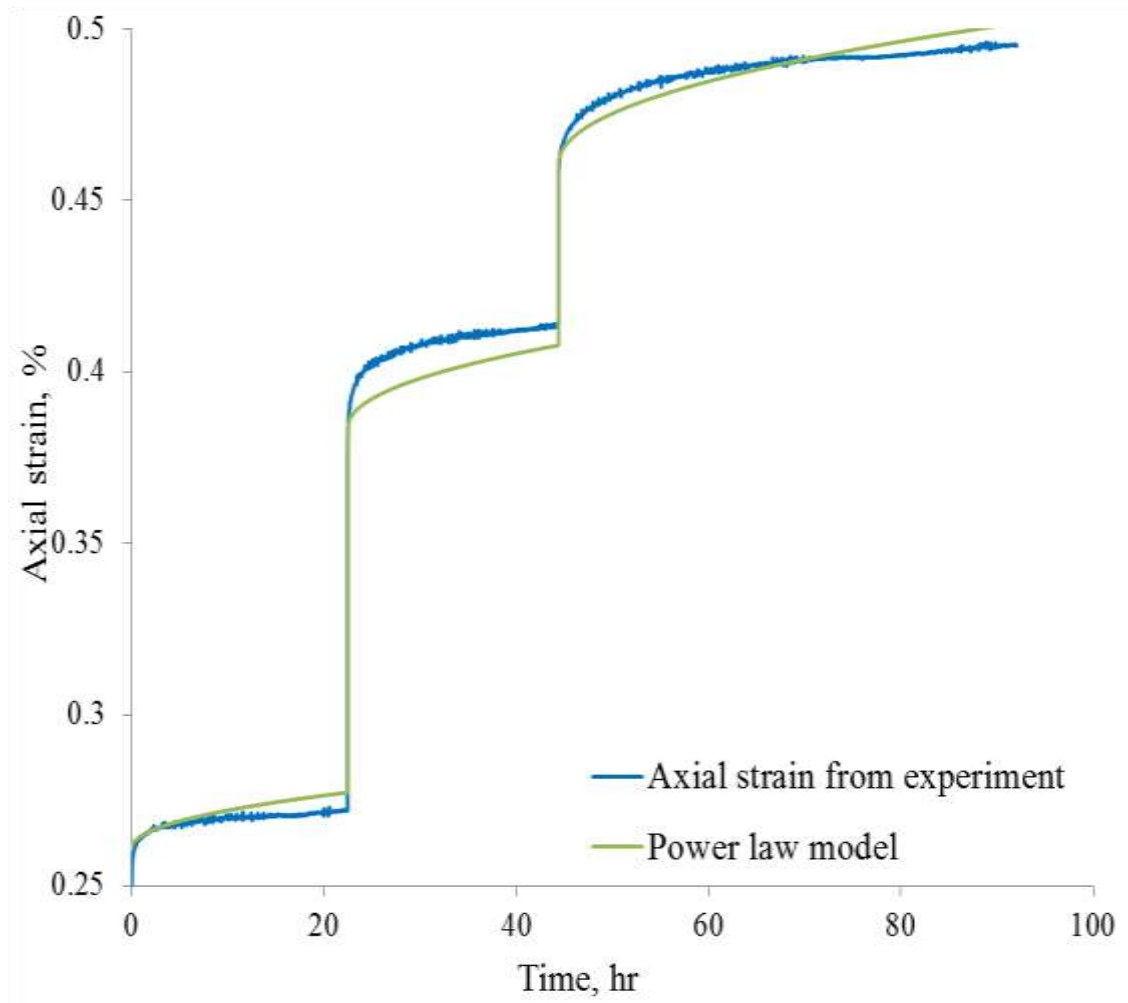
Figure 4.25 Comparisons between creep strain and power law creep reaction to three stresses, confining pressure 2320 psi, Haynesville 5-22

Figure 4.26 Young's modulus and Poisson's ratio change for every elastic loading stage, confining pressure 2320 psi, Haynesville 5-22
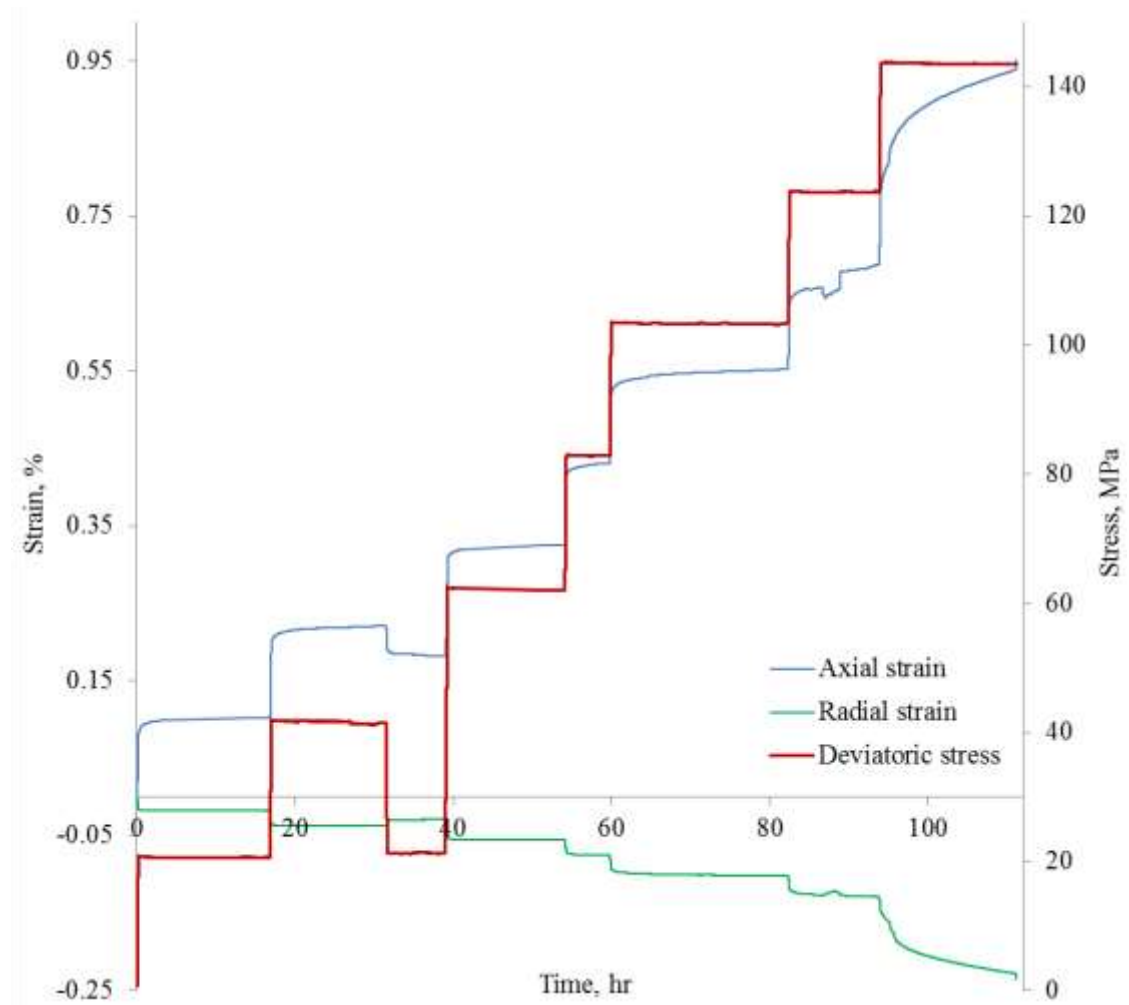
Figure 4.27 Strain responses and deviatoric stress path of Haynesville 07-11 (pc=4500 psi)

The sample Haynesville 07-11 was loading over 14500 psi (100 MPa), the sample failed at the last stress stage, the axial strain increased rapidly in a very short time, a macroscopic fracture was observed after sample disassembly.
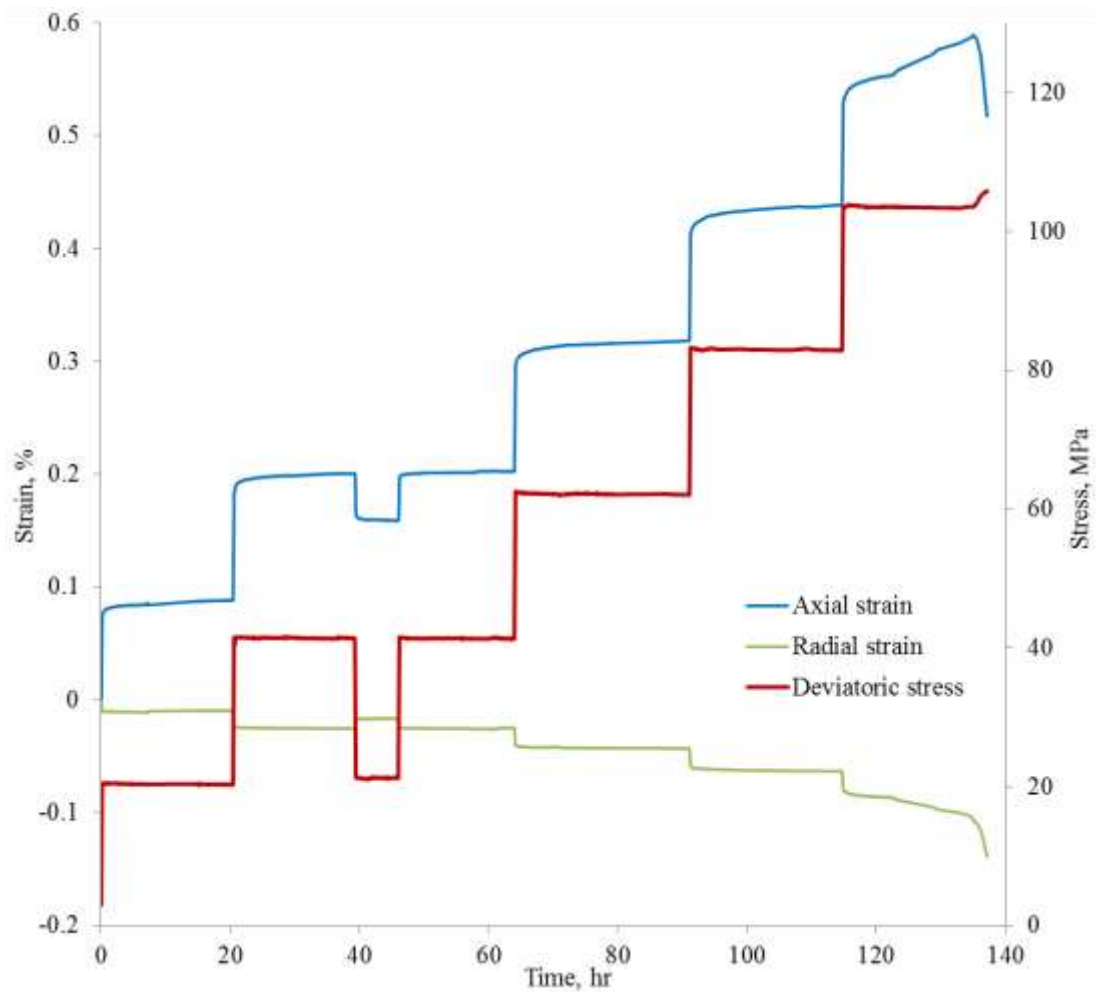
**Figure 4.28 Strain responses and deviatoric stress path of Haynesville 07-12
(pc=4500 psi)**

At last stress stage, confining pressure decreased gradually from 4500 psi to 100
psi due to the leakage of pressure vessel, the axial strain rate first increased then
decreased rapidly, this sudden change of strain is not explainable by the conclusion
drawn from previous tests.
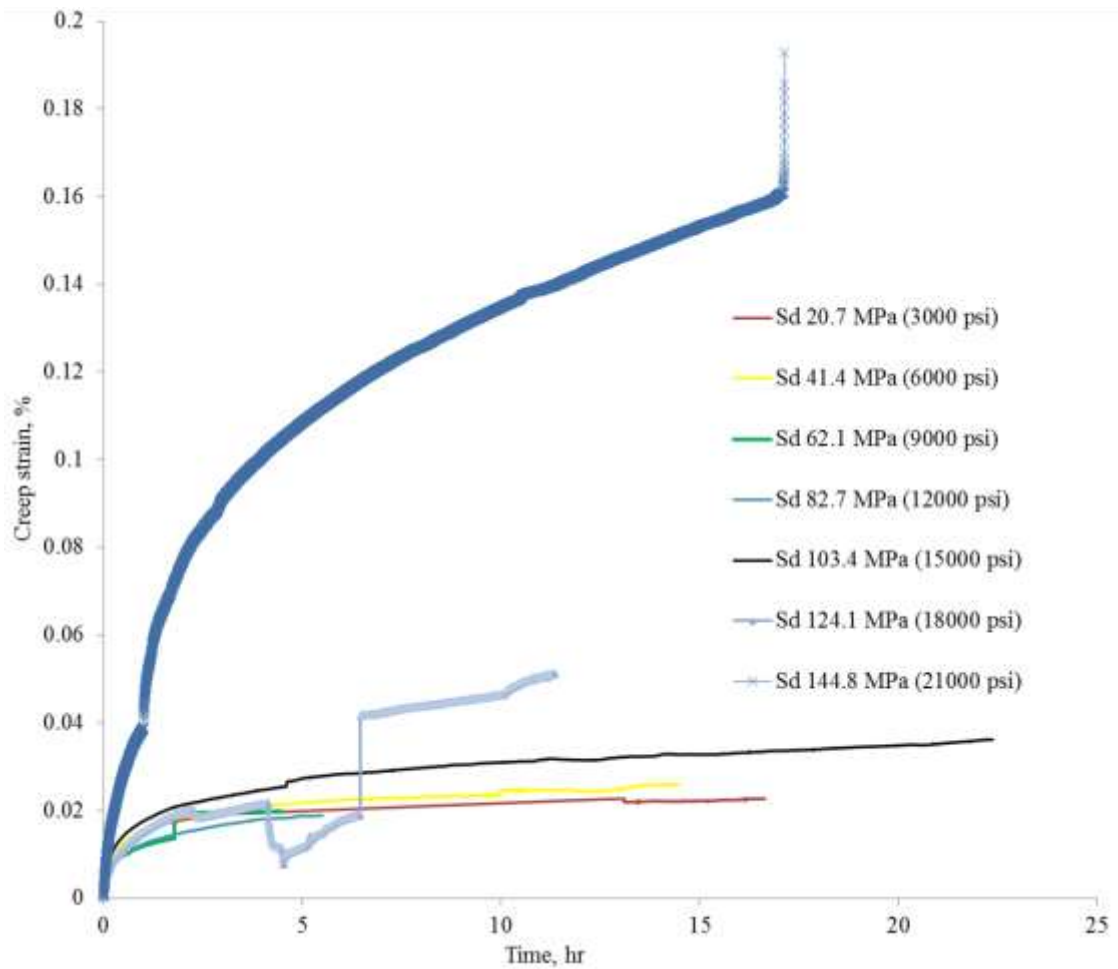
Figure 4.29 Creep strain at different deviatoric stress level, Haynesville 07-11

It is expected that higher deviatoric stress induces bigger creep strain, however at deviatoric stresses 9000 psi and 12000 psi, the trend is reversed and the creep strain of 12000 psi and 18000psi have sudden jumps, this might be caused by the external signal perturbation of the LVDT sensors.
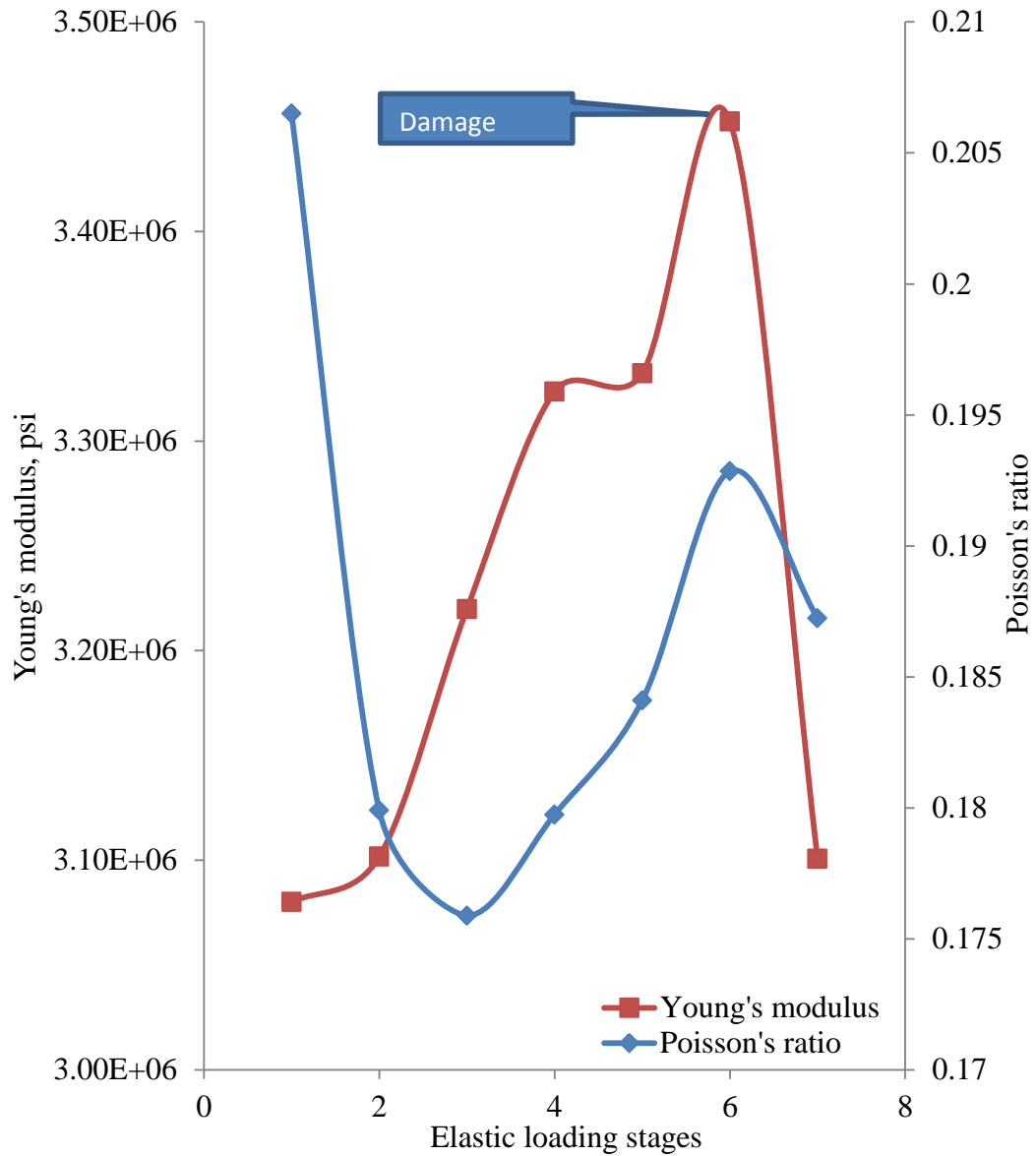
Figure 4.30 Young's modulus and Poisson's ratio change for every elastic loading stage, confining pressure 4500 psi, Haynesville 07-11

Similar to Fig.4.18, the sample experienced initial hardening and then softening, we speculate that the hardening is caused by compaction as the stress increases, and the softening is caused by damage (microcracking).
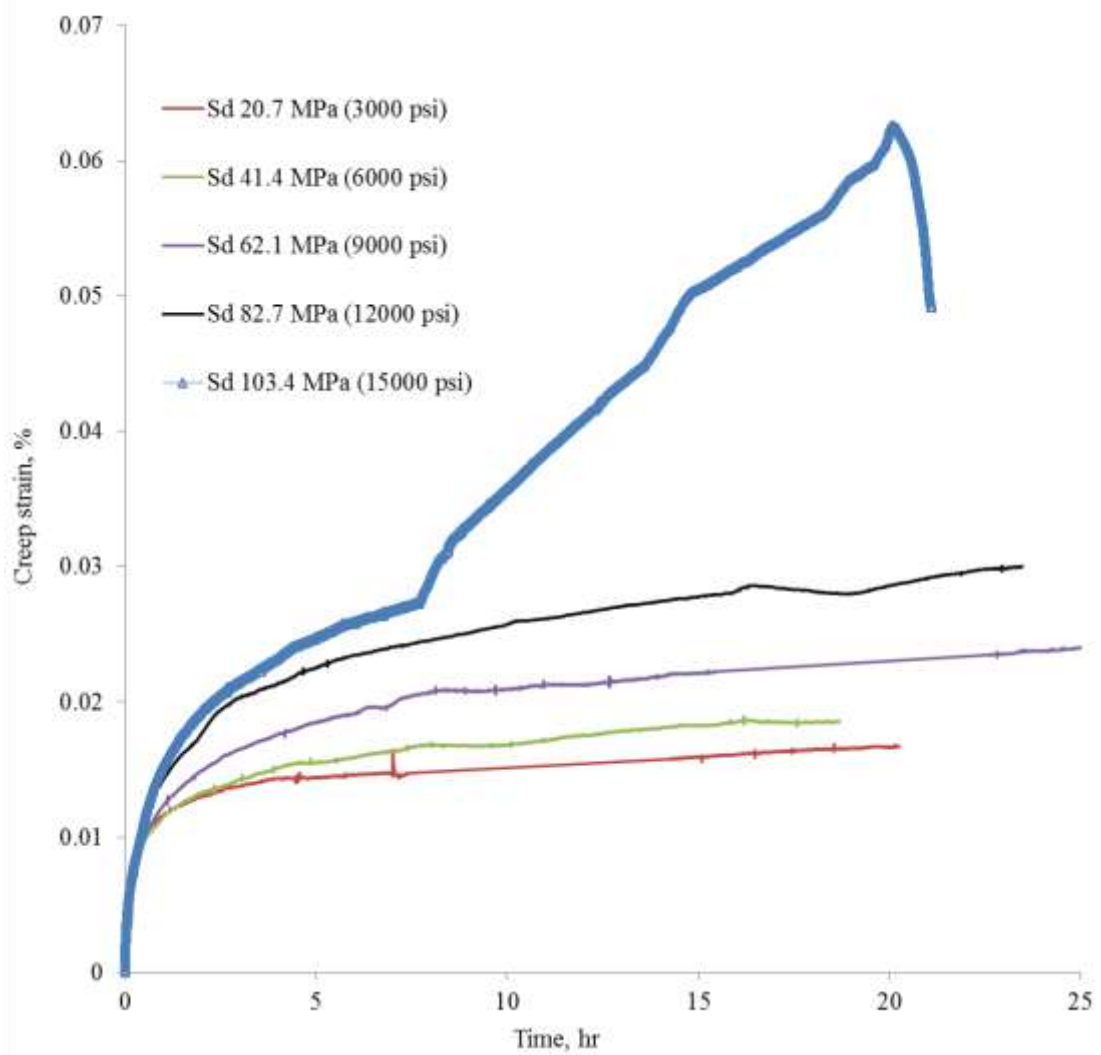
Figure 4.31 Creep strain comparison at different deviatoric stress level, Haynesville 07-12

The above figure demonstrates a trend of creep strain increasing with deviatoric stress, the amount of creep strain is plotted with the corresponding deviatoric stress in Fig. 4.34.
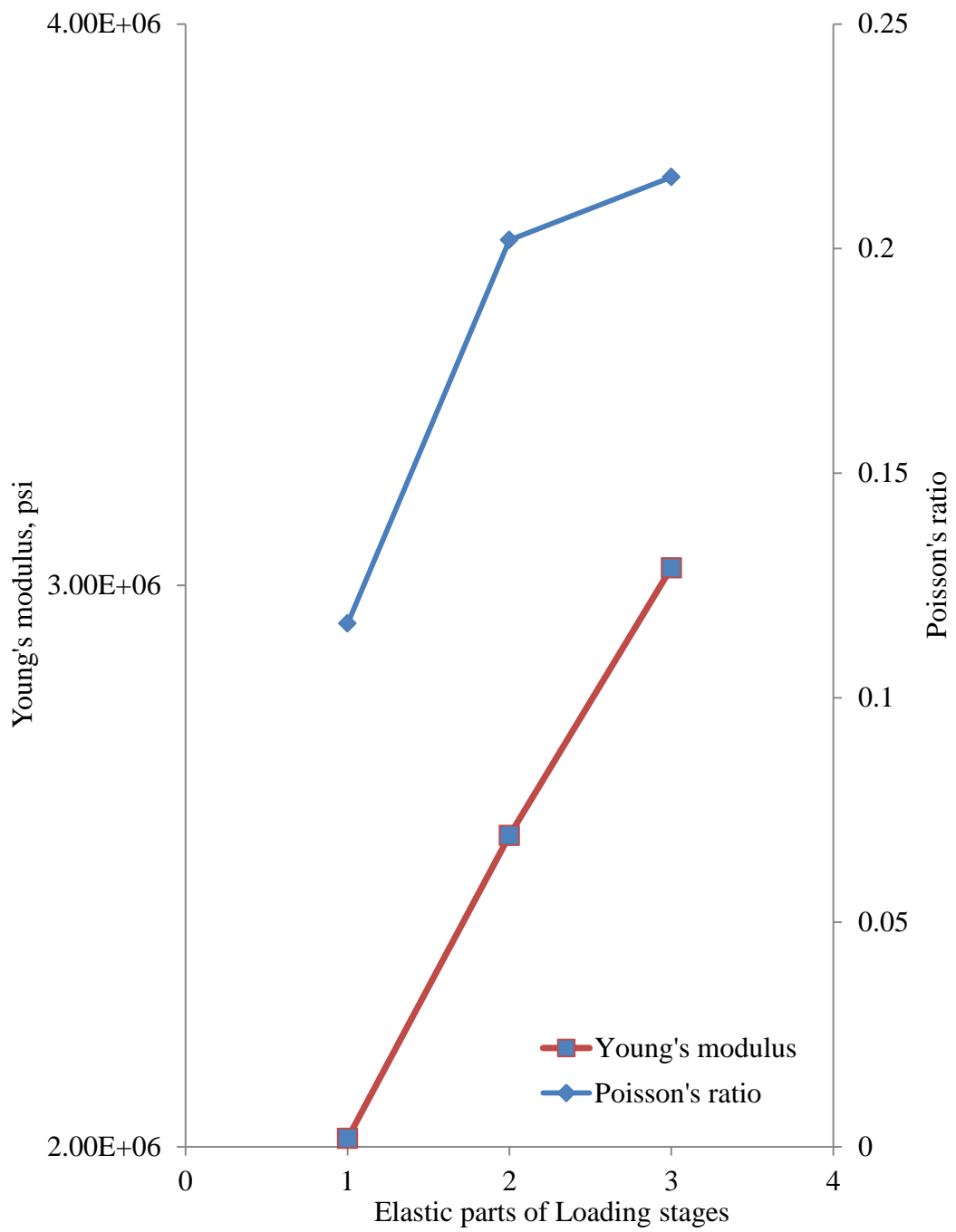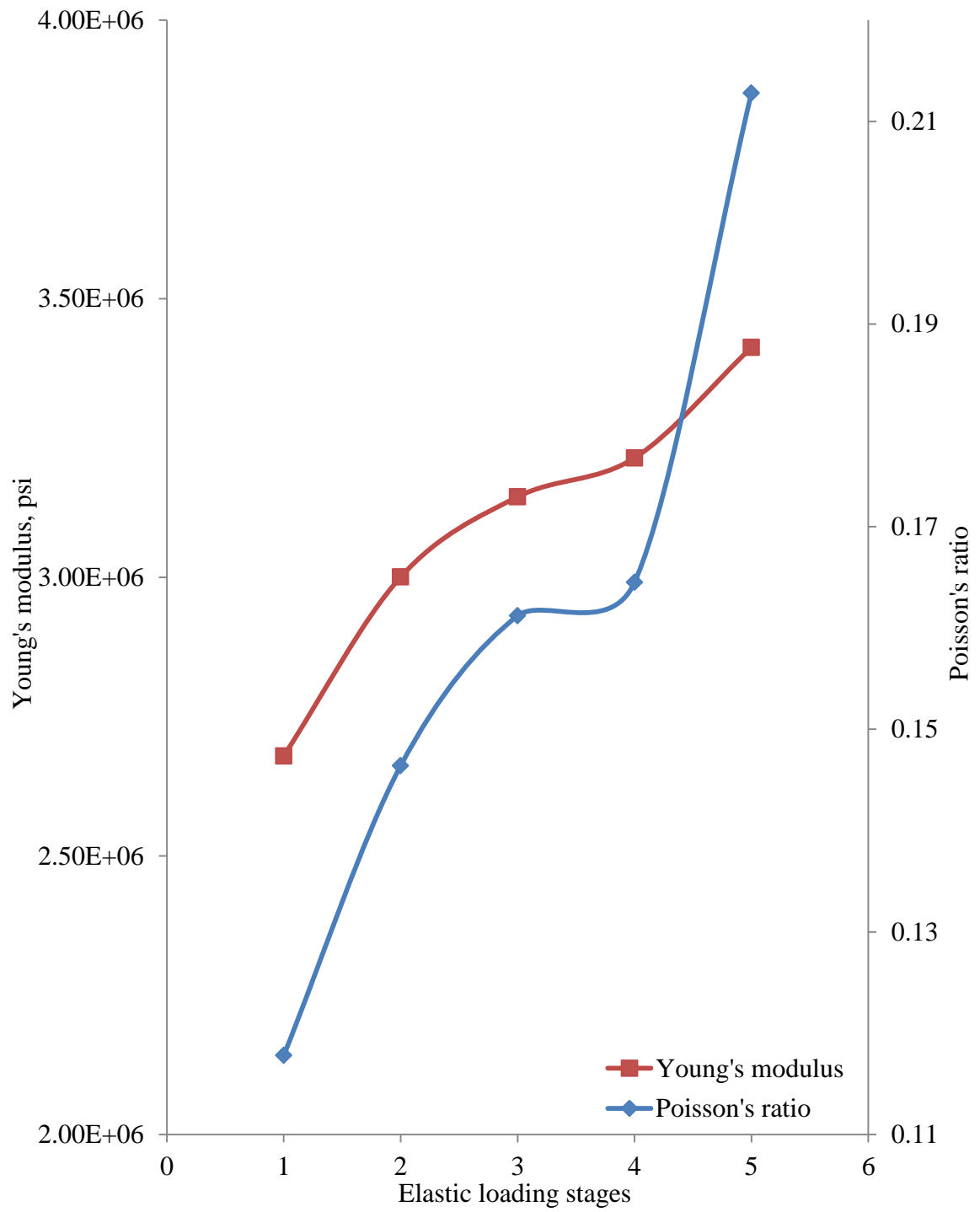
Figure 4.32 Young's modulus and Poisson's ratio change for every elastic loading stage, confining pressure 4500 psi, Haynesville 07-12
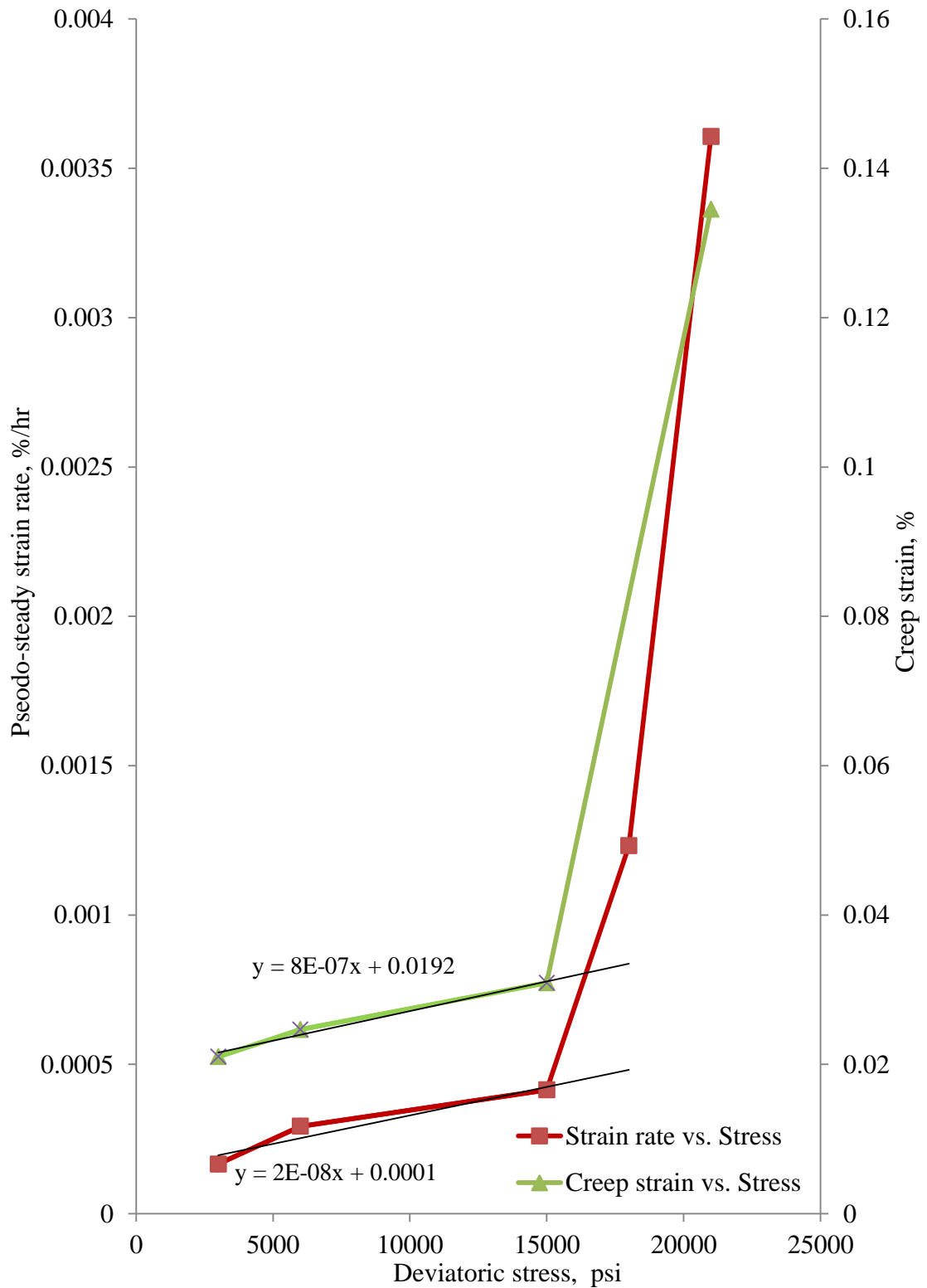
Figure 4.33 Creep strain and pseudo-steady strain rate variation with deviatoric stress, Haynesville 07-11
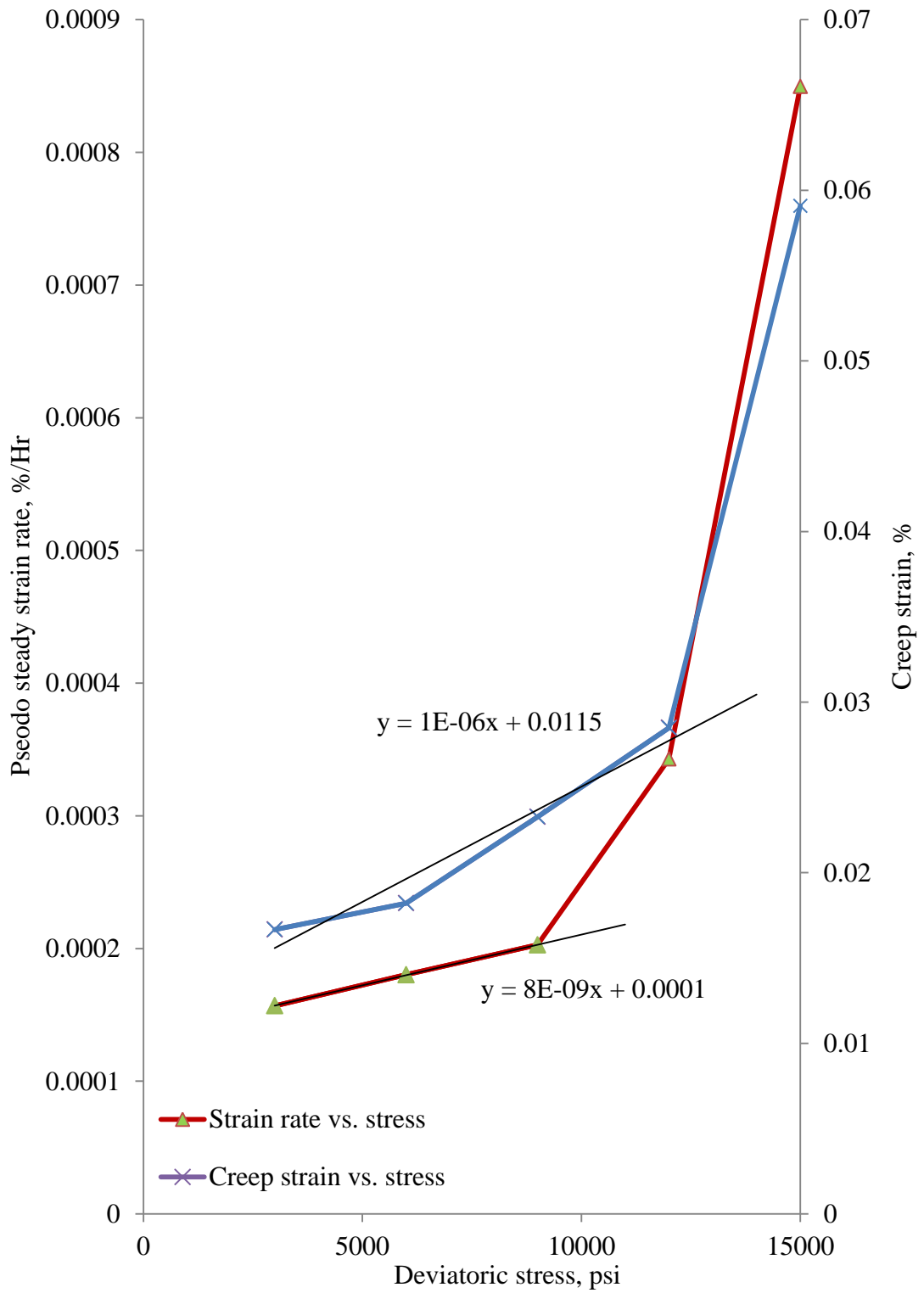
Figure 4.34 Creep strain and pseudo-steady strain rate variation with deviatoric stress, Haynesville 07-12

One can observe that both shale sample exhibit linear viscoelastic property at lower deviatoric stress level, however at high deviatoric stress level, creep strain rate and strain increase rapidly, deviating from the linear viscoelastic trend.

Figure 4.35 Macroscopic fractures induced by creep failure, Haynesville 07-11

As shown in Fig. 4.35, creep failure induced macroscopic fractures at high deviatoric stresses, one can postulate that microcracking contributes enormously to creep at high deviatoric stresses, however further verification is needed using acoustic emission system and microstructural observation. All samples were subject to multistage stress loading, which may have affected subsequent creep steps at higher loads due to the irreversible modifications of the microstructure in preceding steps at lower loads. For samples experiencing no damage, this approach may have resulted in lower strain rates than would be obtained in single runs at a constant stress.

Creep under Elevated Temperatures

After room temperature (25 ℃) creep test, Haynesville 07-12 sample was tested under a very small hydrostatic pressure and 3 temperatures; then the sample was subject to 3 hydrostatic pressures for hydrostatic creep under the designed temperature; lastly, deviatoric creep was conducted.
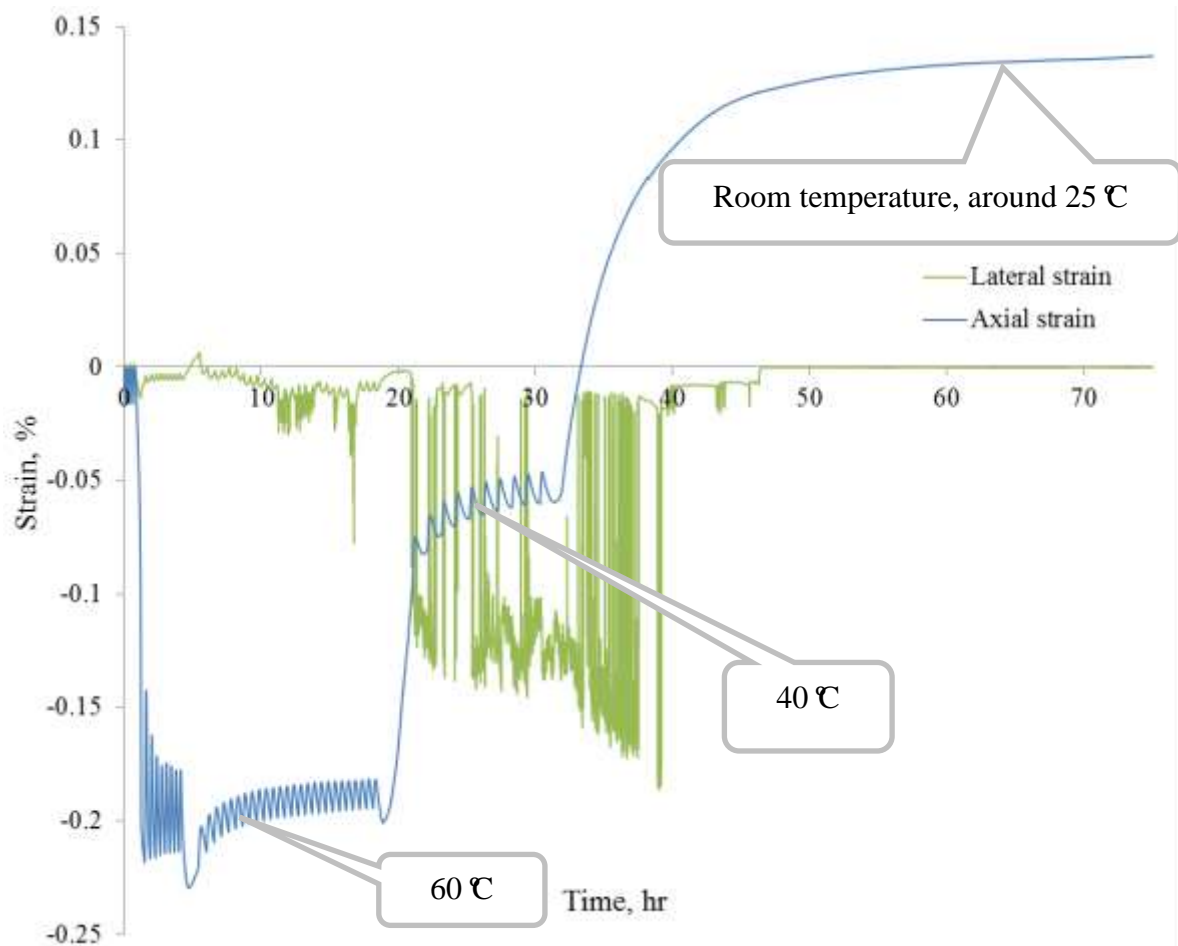
Figure 4.36 Hydrostatic creep strains under 60 psi hydrostatic pressure, 3 different temperatures, Haynesville 07-12

As shown in Fig. 4.36, there is a very obvious thermal expansion phenomenon in the axial direction, under very small hydrostatic pressure; the lateral thermal strain is very small compared to axial thermal strain. The temperature control system maintained

114

the cell within a 3 ℃ range about the target temperature, this thermal oscillation of the control system resulted in axial and later strain oscillation, which resembles a sine wave.
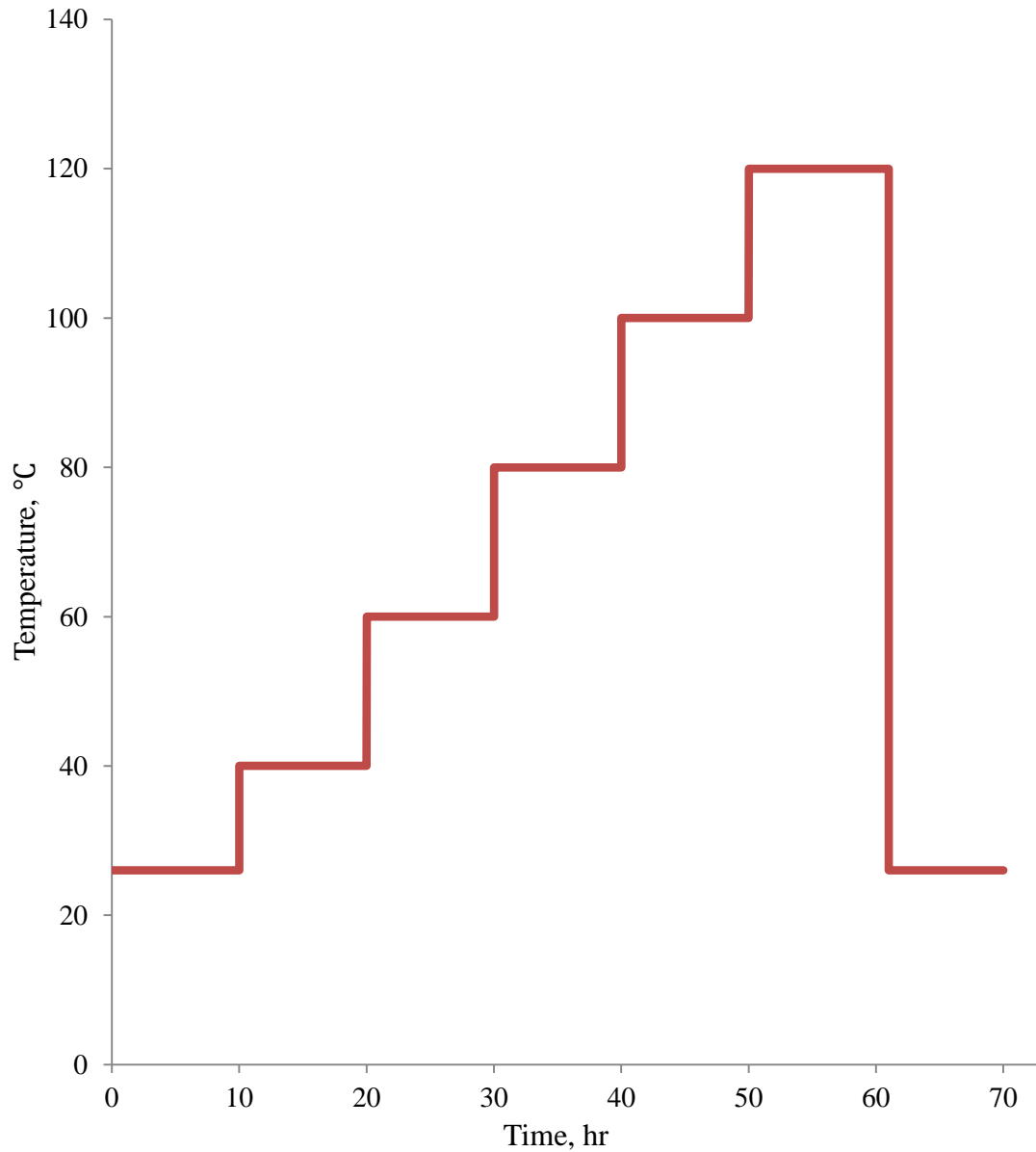
Figure 4.37 Multiple temperatures loading at each stress level

For the subsequent hydrostatic and deviatoric creep, the creep at ambient temperature is first performed for a desired length of time, after that, the temperature is increased to 40 ℃ and kept for the desired period of time, then the temperature is

increased to the next level, the temperature interval is 20 ℃, the highest temperature is 120 ℃.
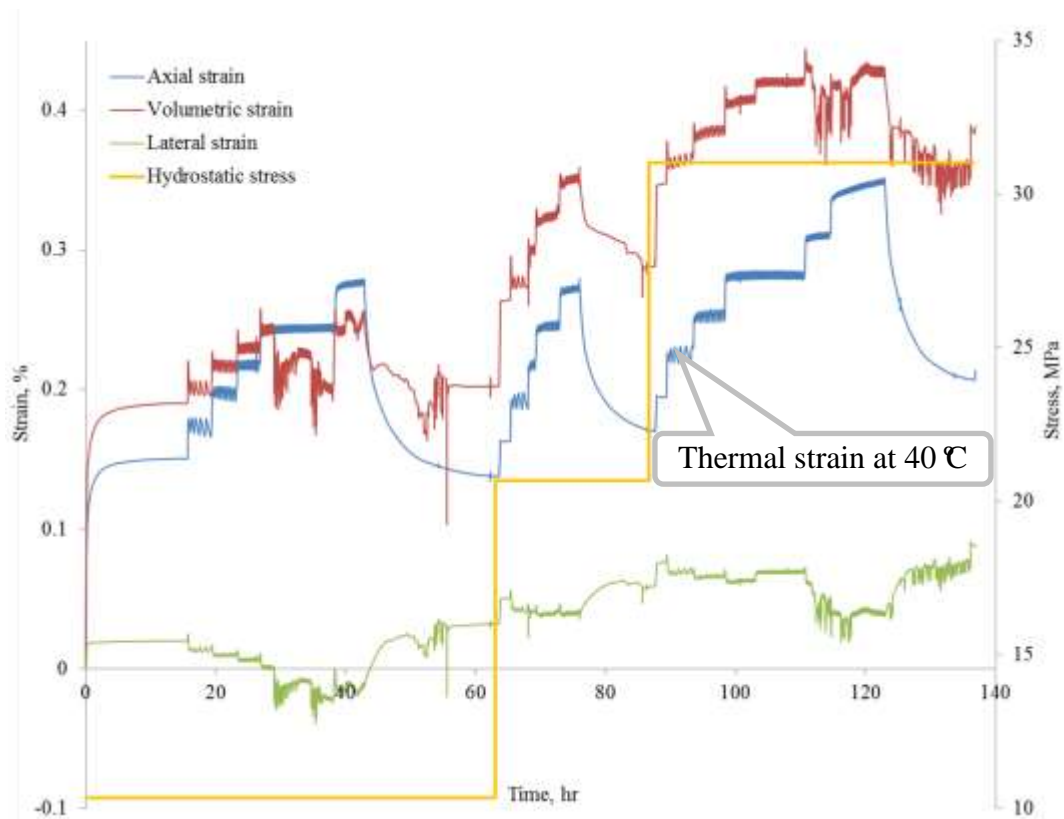
Figure 4.38 Hydrostatic creep strains under 3 hydrostatic pressures and 6 temperatures, Haynesville 07-12

From Fig.4.38, one can see that axial strain increases with temperature, the multiple step temperature loading is like multiple stress loading, and axial strain oscillates with oscillating temperature, however, the lateral strain decreases with temperature, which is unexpected, the sample is compressed by hydrostatic pressure and should be shrinking in all direction. This might be caused by the deformation (thermal expansion) of the Teflon heat-shrink tube wrapped on the sample, this speculation needs to be further investigated.
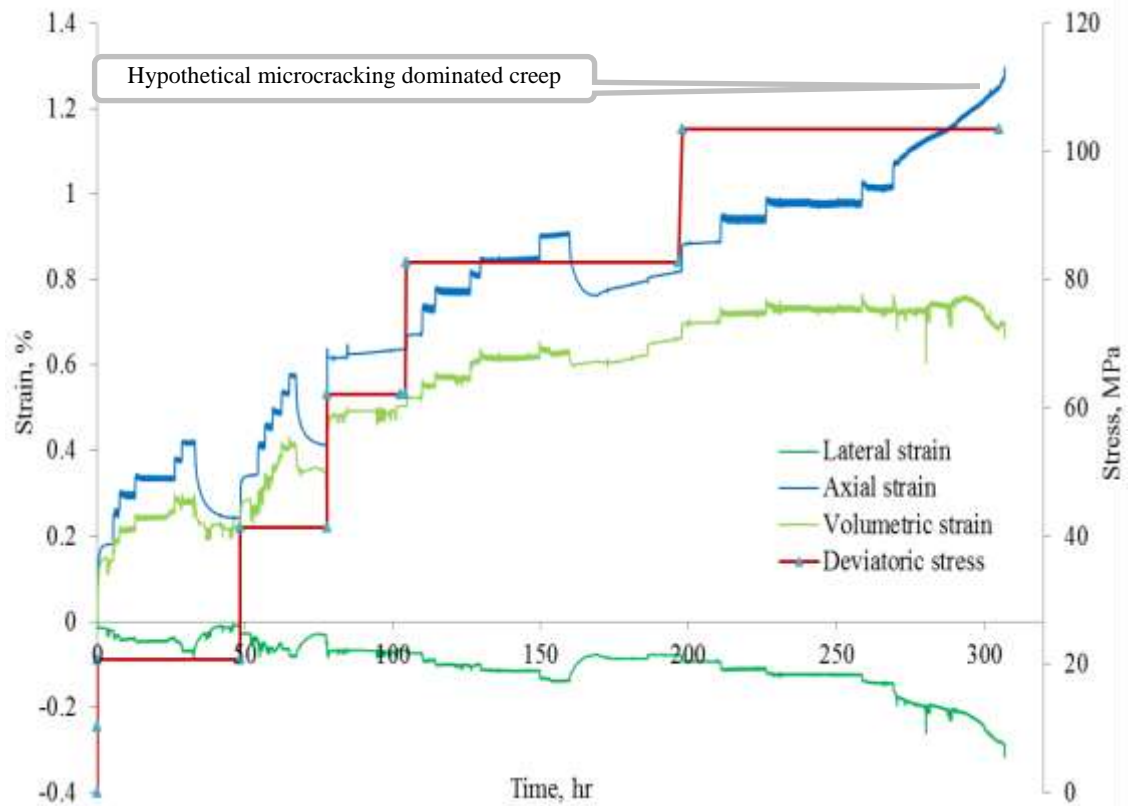
Figure 4.39 Deviatoric creep under 5 deviatoric stresses and 6 temperatures, Haynesville 07-12

The deviatoric creep of elevated temperature is conducted for around 300 hours. as one can see, the axial strain increases with temperature and oscillated with oscillating temperature. However, the general trend of oscillating axial strain is flat except that the last temperature stage shows a very fast creep strain rate followed by tertiary creep (sample failure), we speculate that this is dominated by microcracking, which needs to be confirmed by acoustic emission test. It is unclear why the oscillating axial strain shows a flat trend, it is possibly due to the LVDT drifting (inaccuracy) caused by higher temperature, and it is also possible that the creep strain is negated by the thermal expansion strain.
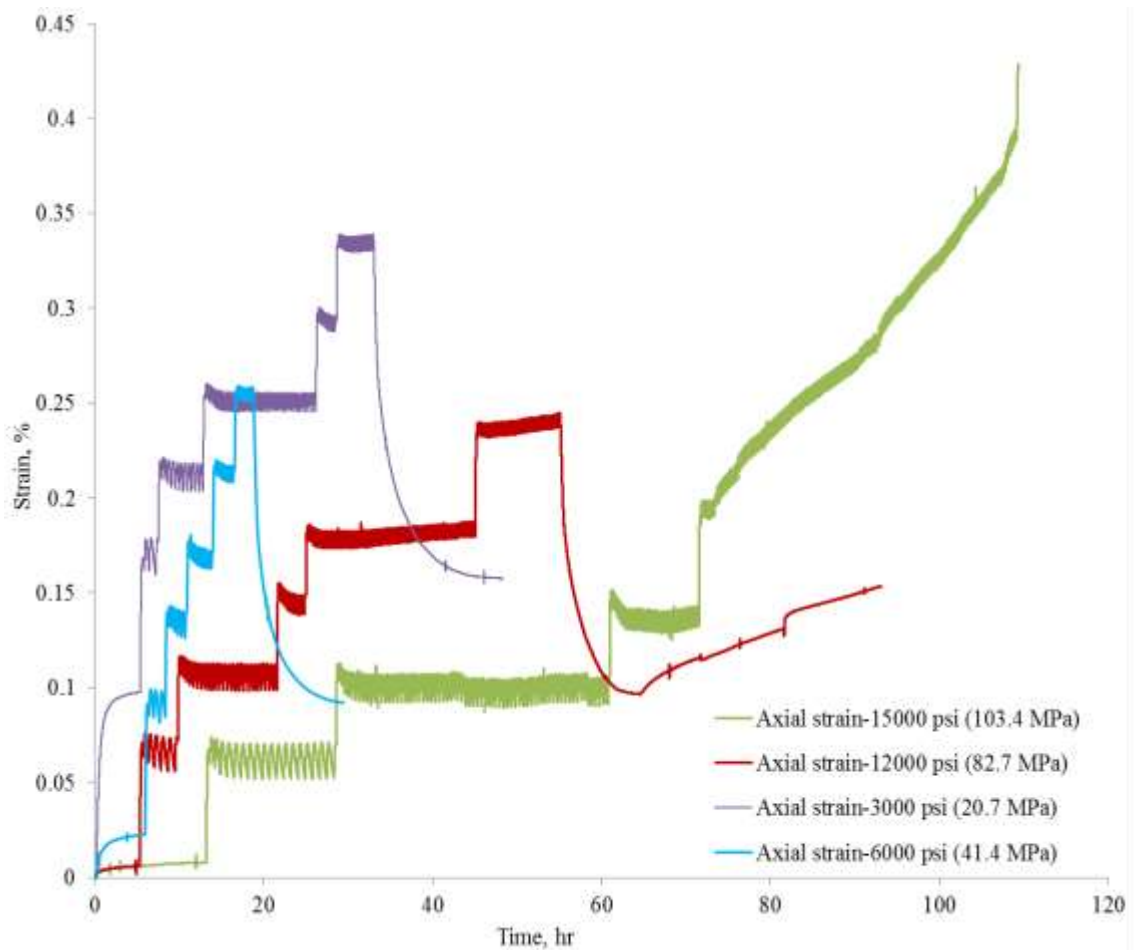
Figure 4.40 Creep strain comparison at different deviatoric stress and temperature, Haynesville 07-12

It is very clear that the creep strain of higher deviatoric stress is smaller than that of low deviatoric stress; this result is opposite to Fig.4.31. We speculate that higher temperature facilitates the compaction of clay and organic matters in the sample, which is the softer and more deformable content of the shale sample. At lower deviatoric stress, the creep strain is mainly the straining of the softer content in the sample; at high deviatoric stress, the creep strain is mainly the straining and microcracking of quartz, feldspar and carbonate content. More creep tests under elevated temperatures assisted by ultrasonic test and acoustic emission test need to be conducted to infer more information on this.
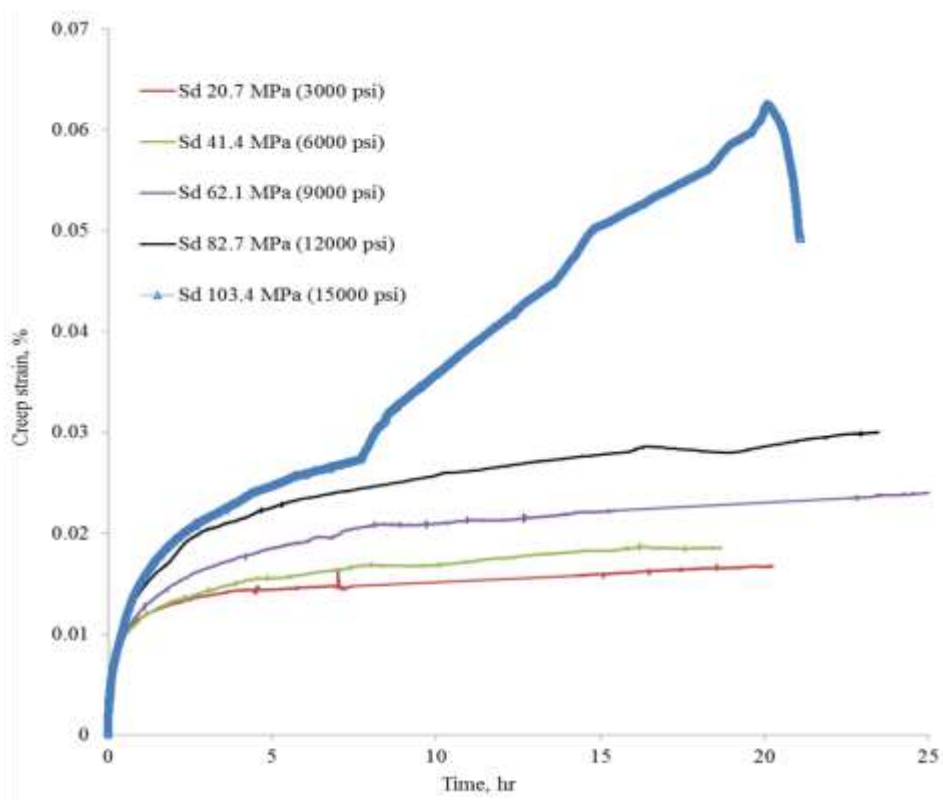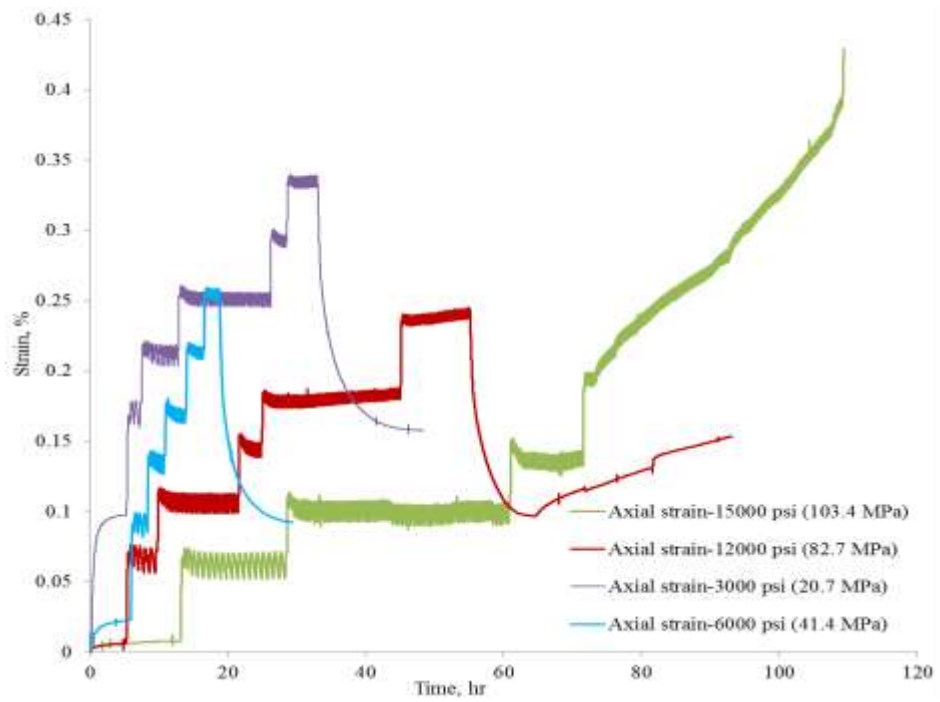
Figure 4.41 Deviatoric creep strain comparison between room temperature and elevated temperatures, Haynesville 07-12
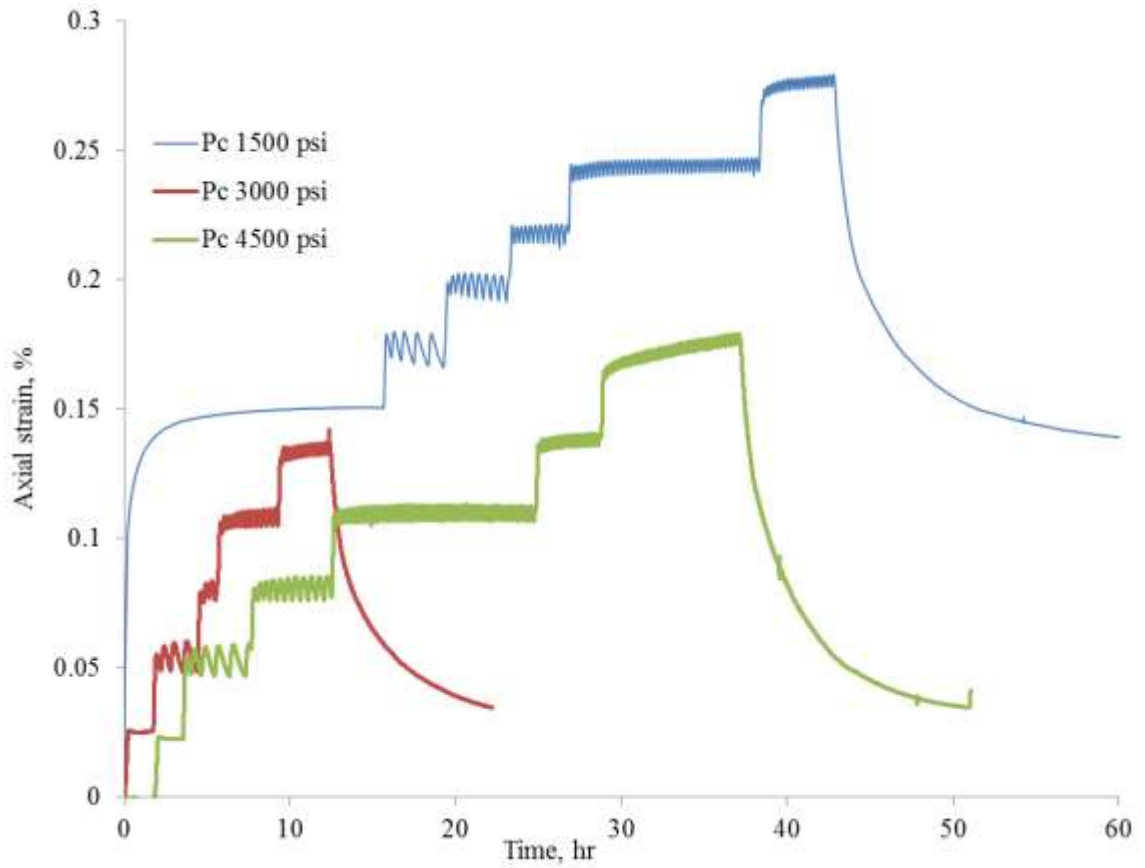
Figure 4.42 Hydrostatic axial creep strain comparison at different hydrostatic stress and temperature, Haynesville 07-12

The hydrostatic axial creep strain of higher hydrostatic stress is smaller than that of low hydrostatic stress.
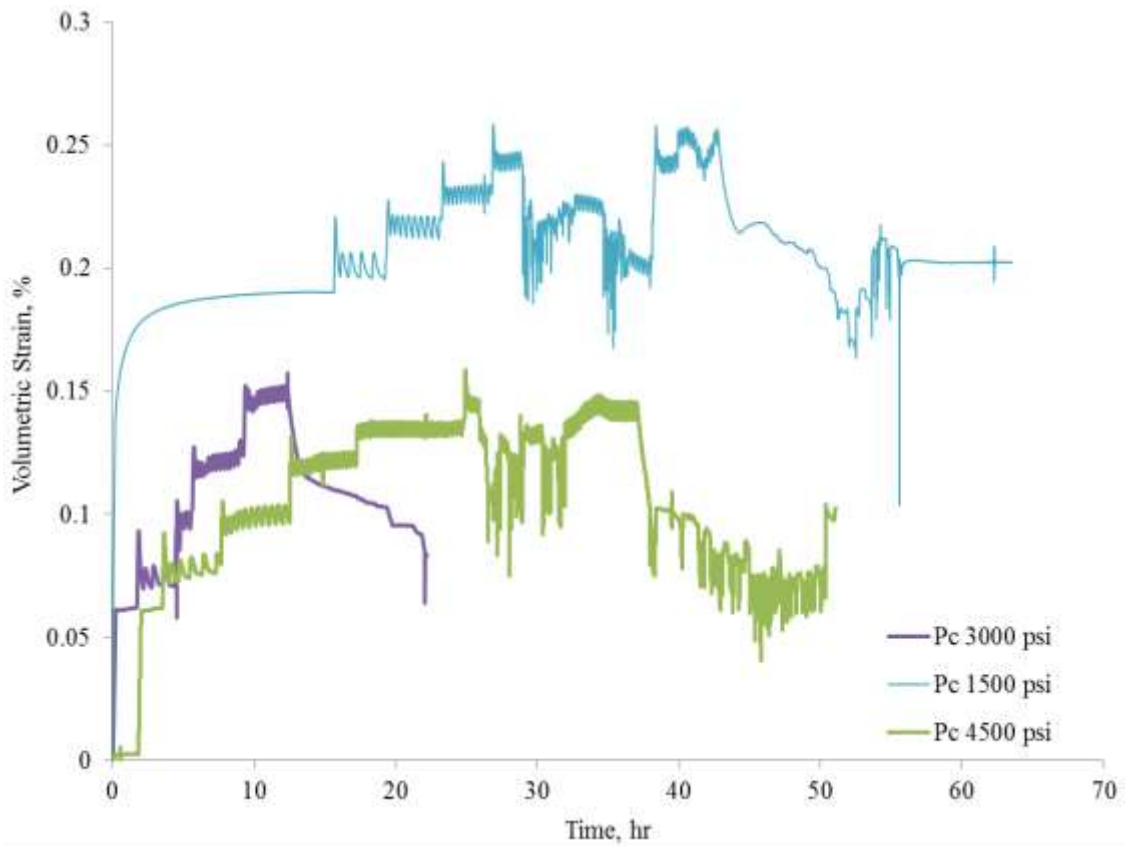
Figure 4.43 Hydrostatic volumetric creep strain comparison at different hydrostatic stress and temperature, Haynesville 07-12

It is interesting to see that after applying the first hydrostatic pressure and temperature on the sample, the sample shrinks much less under the second and third hydrostatic pressures as shown in Fig. 4.42 and 4.43, however, the trend is opposite in Fig. 4.11 without applying temperature.
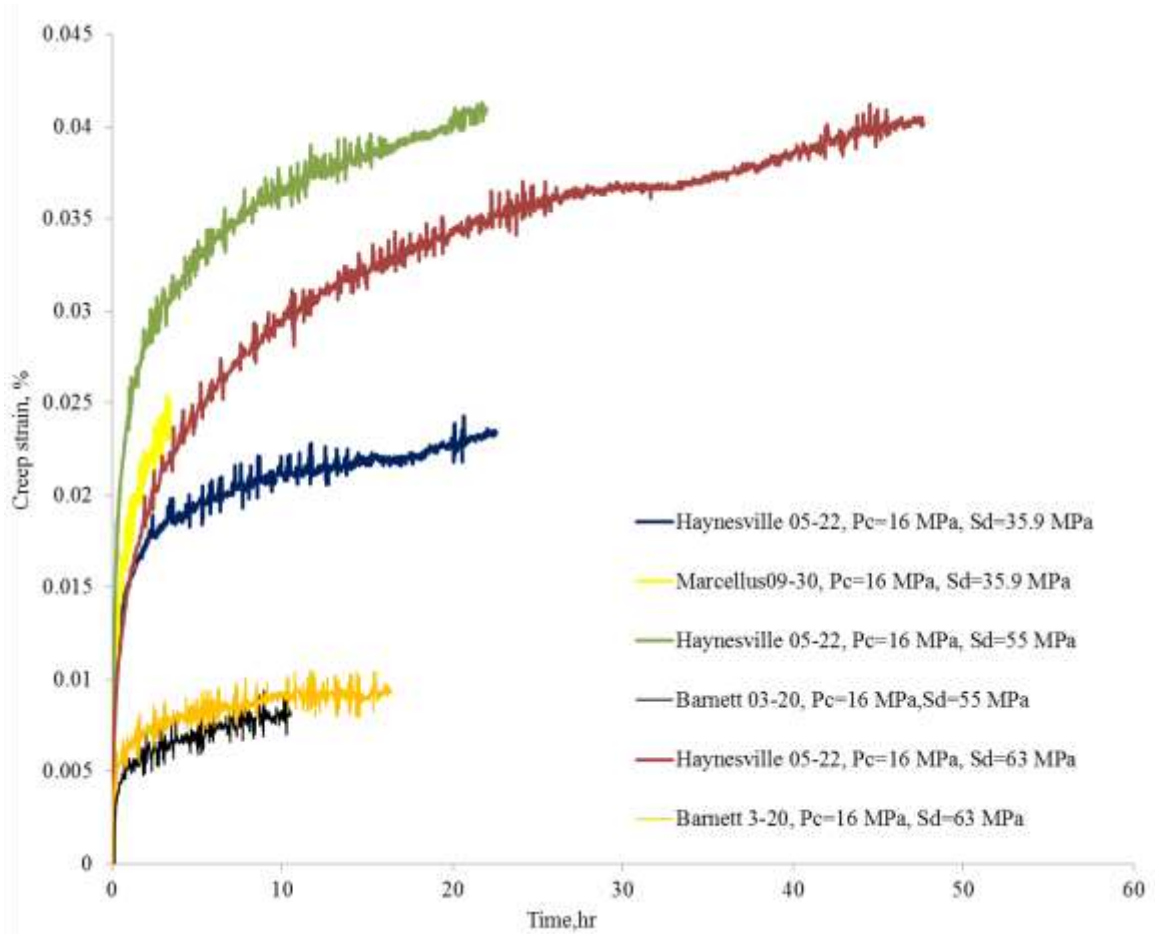
Figure 4.44 Comparisons between three pair of creep strains under the same confining pressure 2320 psi, and three deviatoric stresses

From Fig. 4.44, knowing their Young's modulus and clay content, one can tell that stiffer shale (less clay) creeps less under the same stress state and ambient conditions.
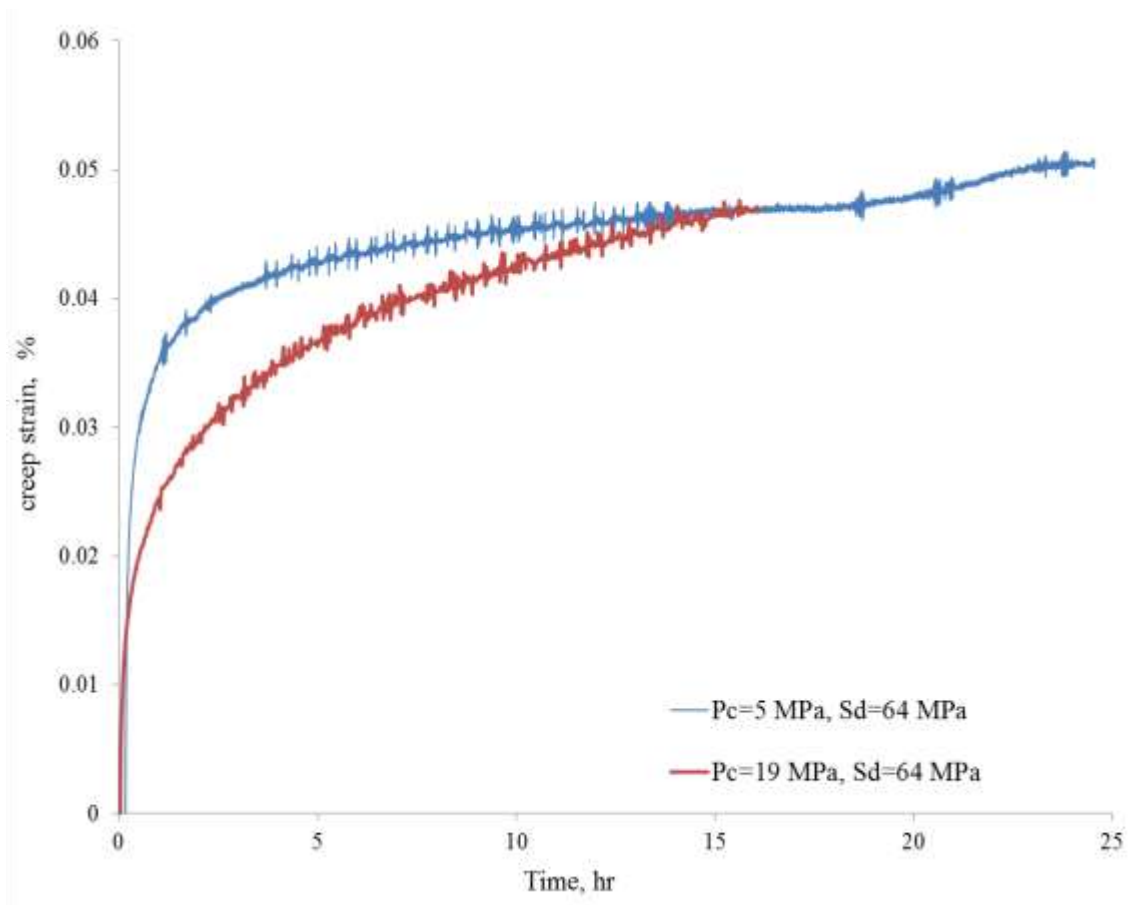
Figure 4.45 Comparisons of creep strain under the same deviatoric stress, two confining pressures. Marcelus09-30
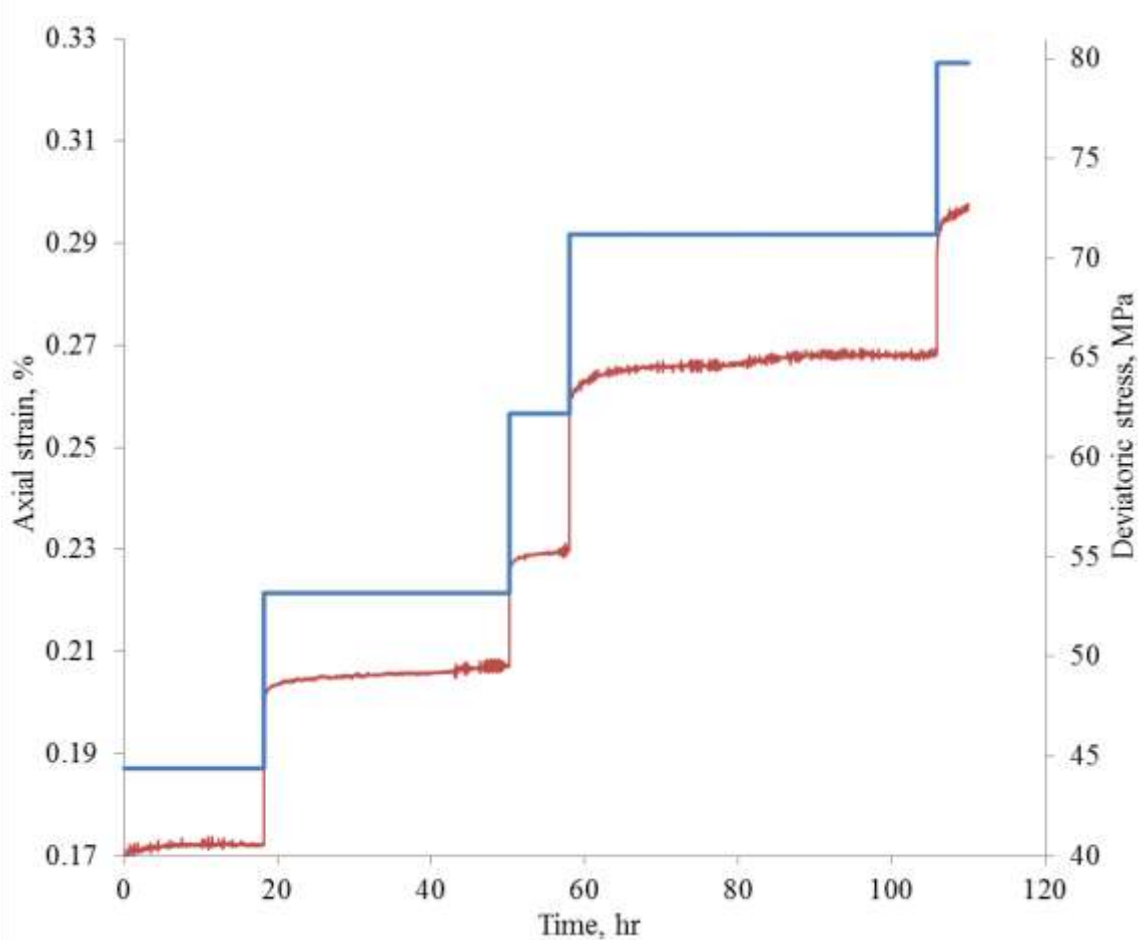
Figure 4.46 The multistage loading path and the axial strain of Barnett 3-20, confining pressure is 0 psi
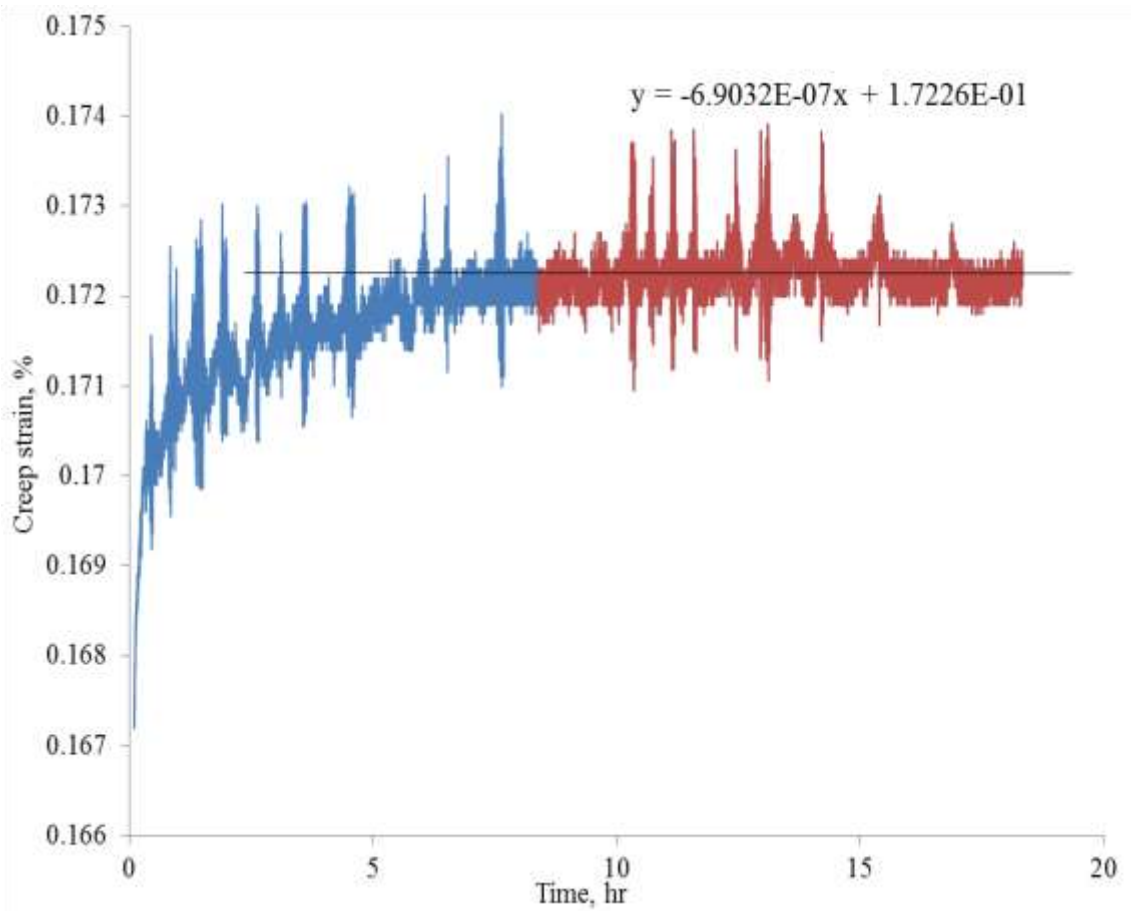
Figure 4.47 Creep strain and strain rate of Barnett 3-20 at Deviatoric stress 6744 psi
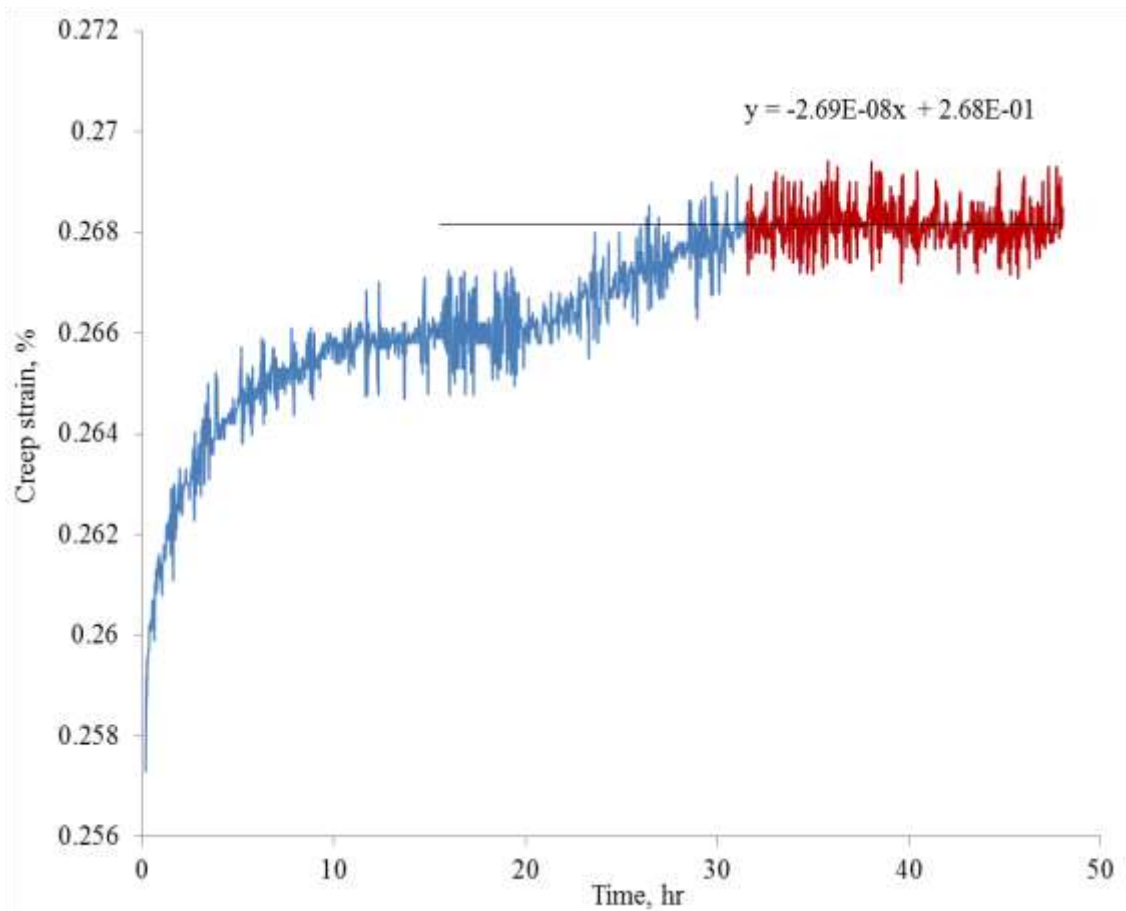
Figure 4.48 Creep strain and strain rate of Barnett 3-20 at Deviatoric stress 10587 psi

For uniaxial creep of Barnett 3-20, the strain rates of three creep stages show zero strain rates (it cannot be negative except at strain recovery). The last stage is not long enough to show the strain rate of steady-state creep.

Through the above observation, one can postulate that the uniaxial creep of Barnett 03-20 has a stress threshold for steady-state creep. Below this stress, there is no steady-state creep (strain-time curve is flat at the end); above this stress, one can observe the steady-state creep.

126
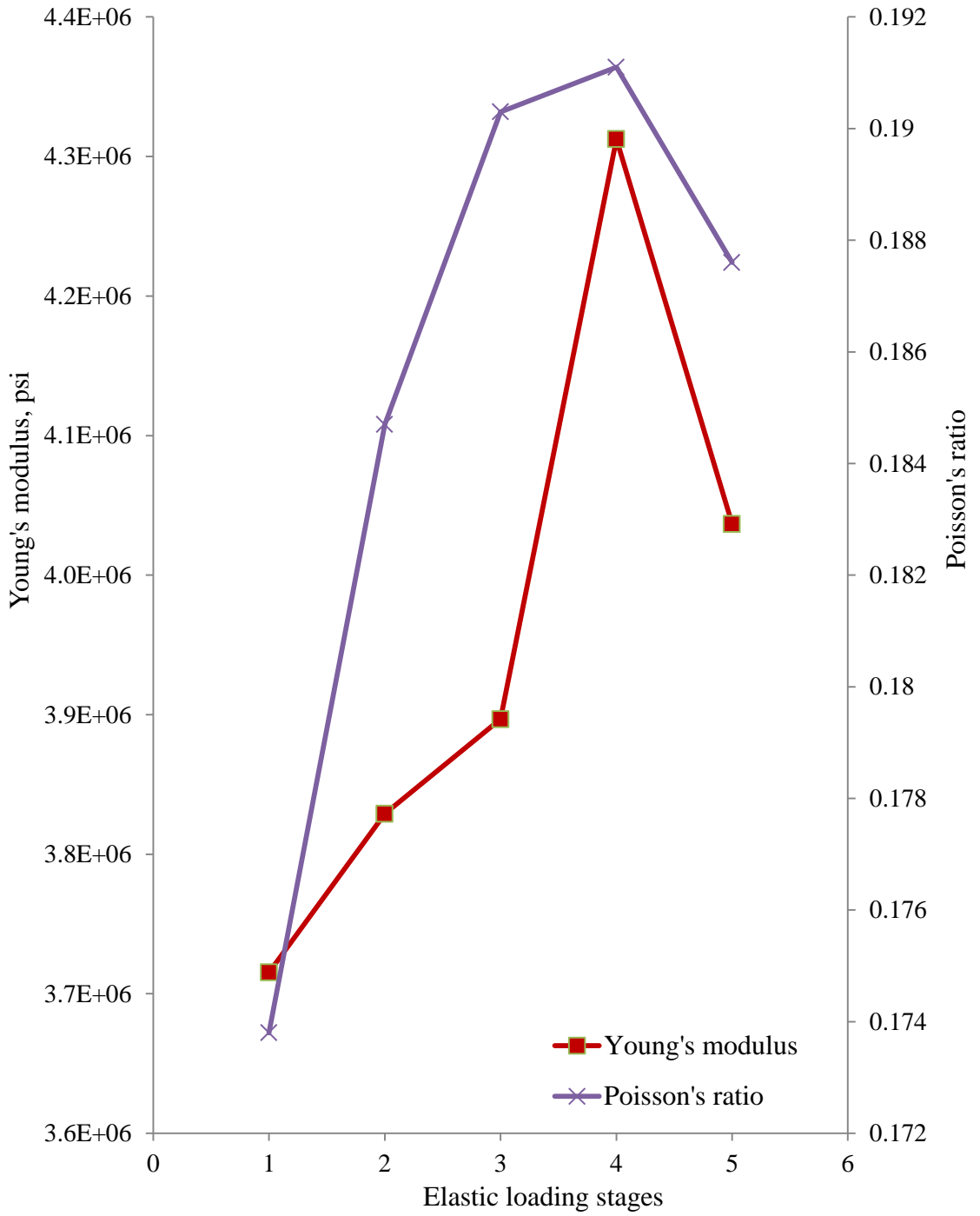
Figure 4.49 Young's modulus and Poisson's ratio change for every elastic loading stage, confining pressure 0 psi, Barnett 3-20
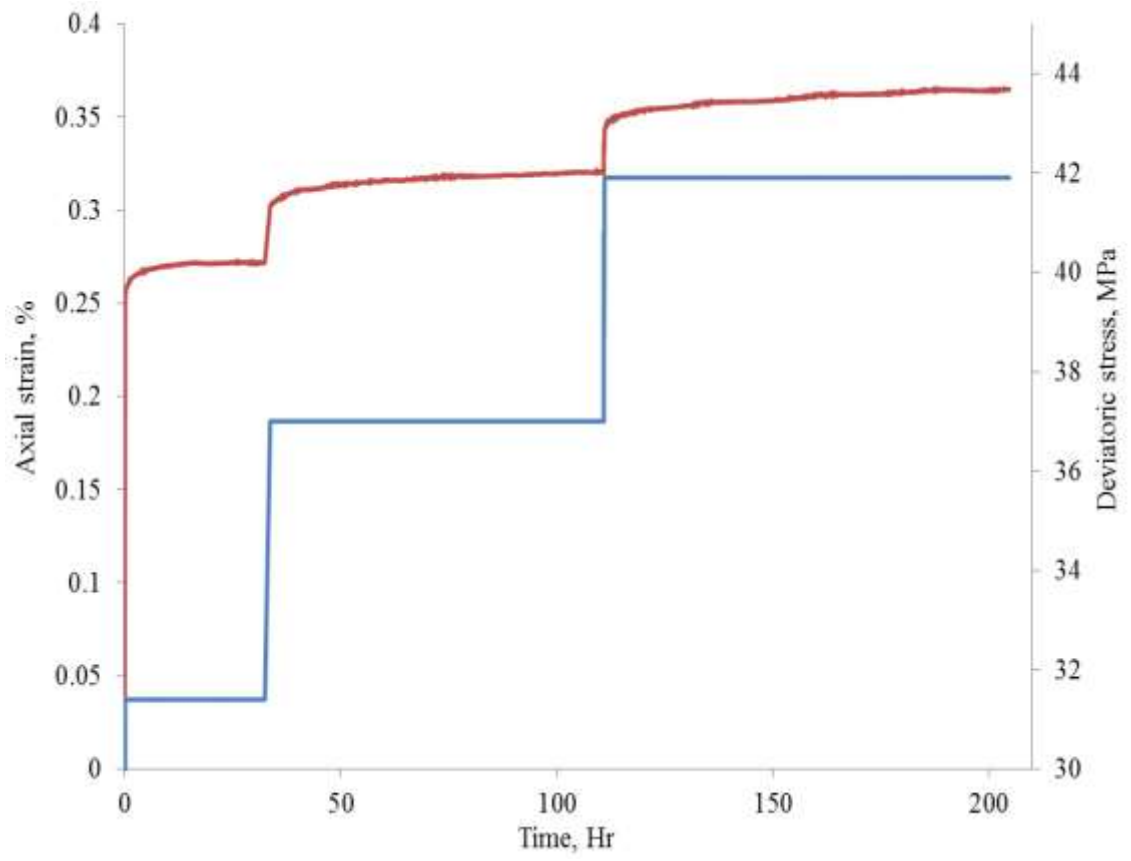
Figure 4.50 Multistage loading path and the axial strain of Mancos 7v, confining pressure is 0 psi
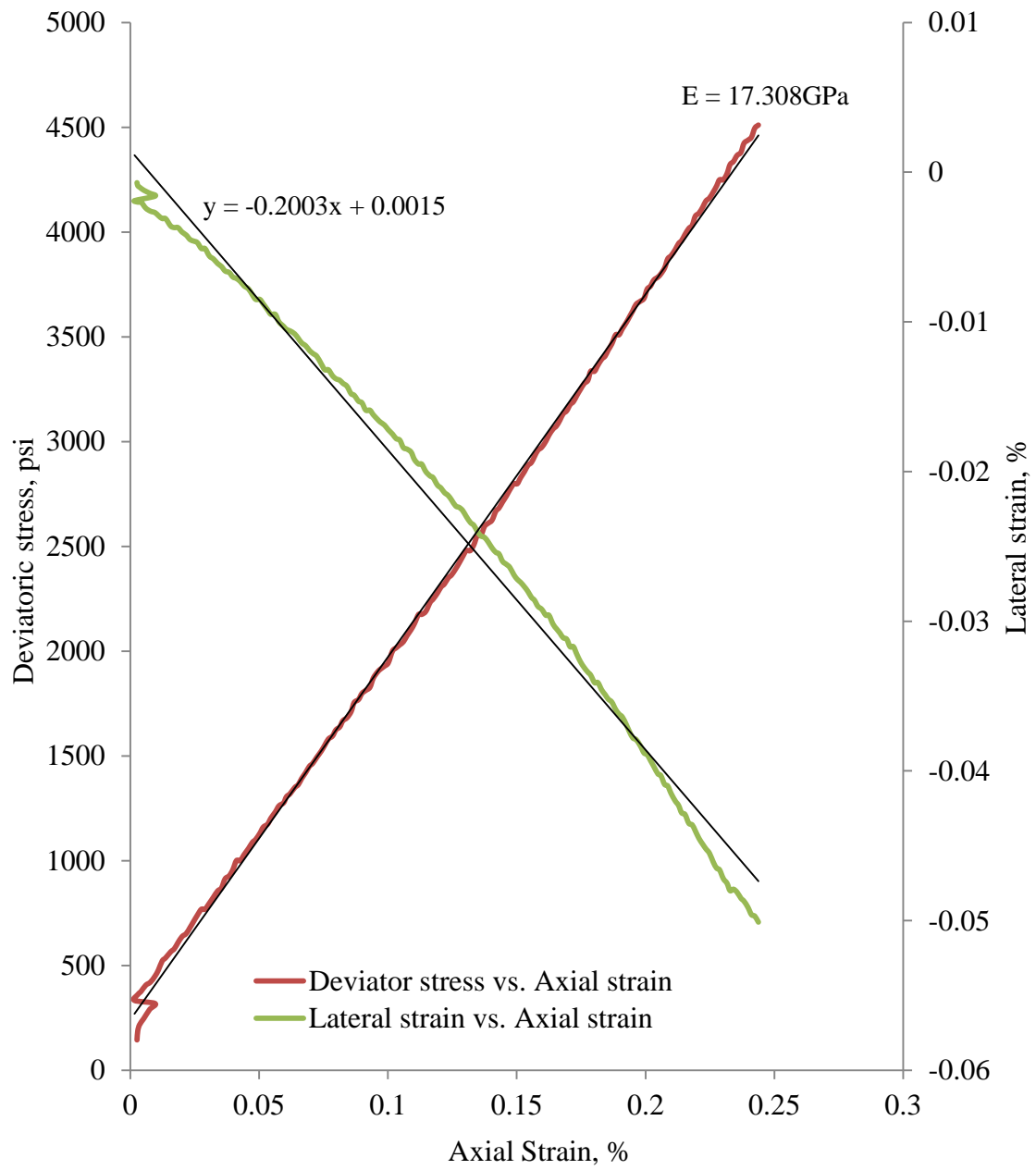
Figure 4.51 The stress-strain curve of the 1ˢᵗ stage (deviatoric stress 4496 psi) of Mancos 7v, the elastic part
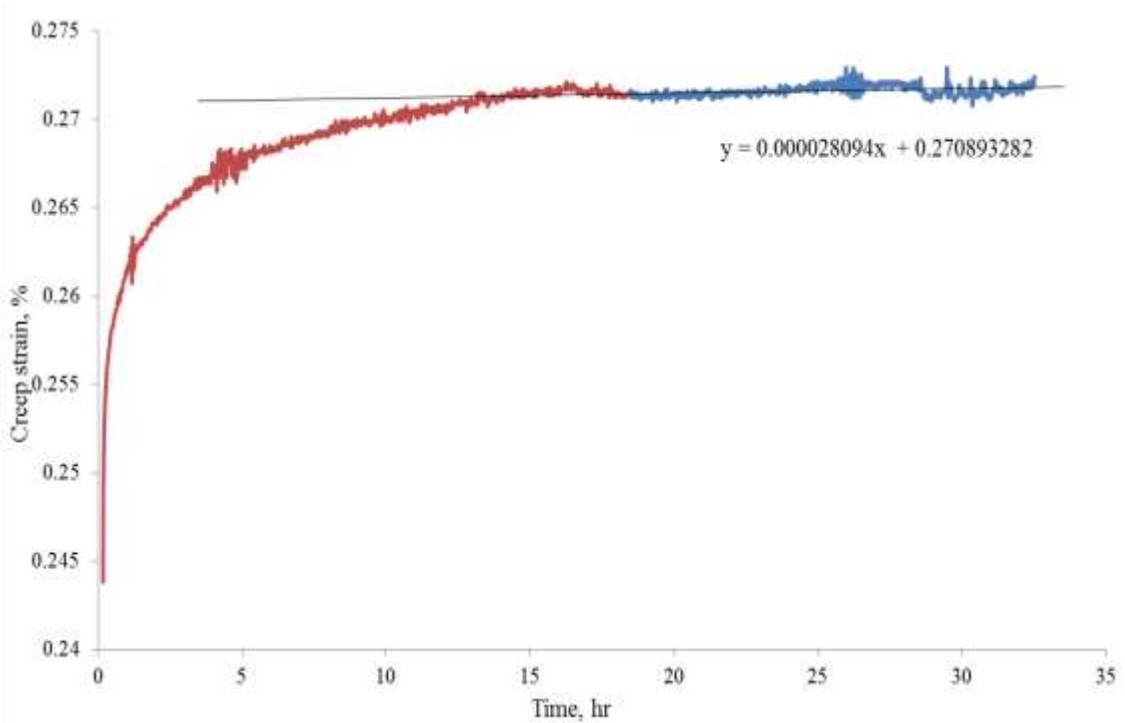
Figure 4.52 The axial creep strain and strain rate of Mancos 7v, the 1st stage (creep strain at 4496 psi)
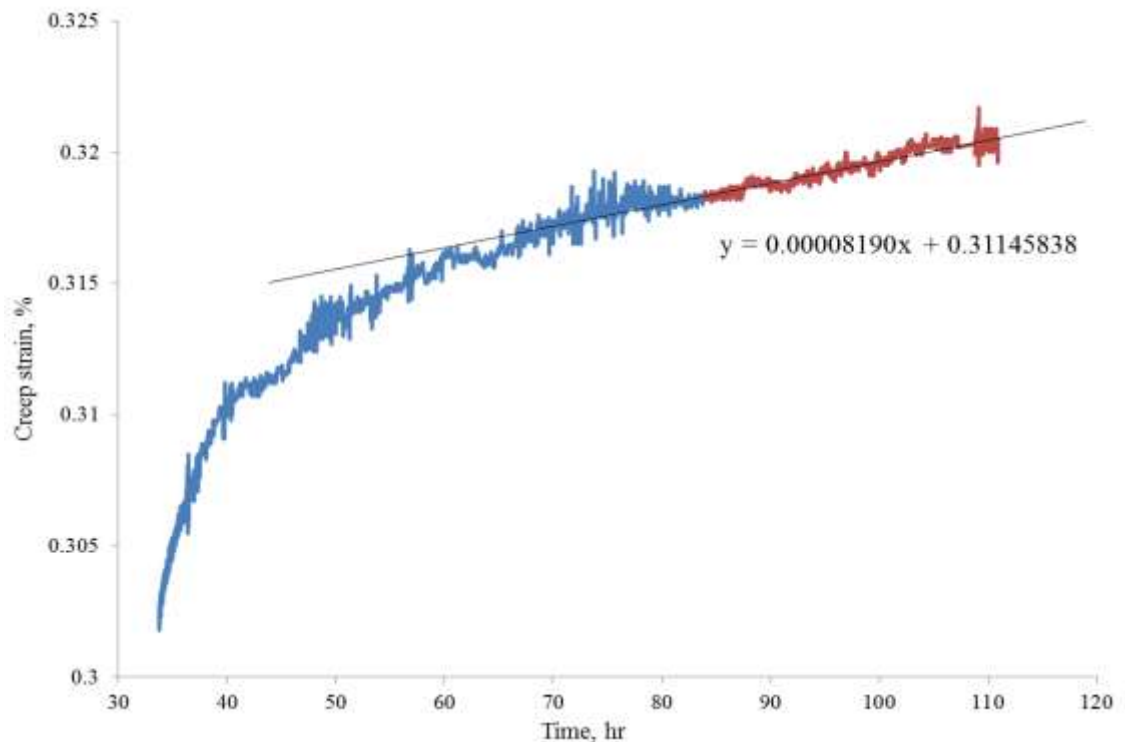
Figure 4.53 The axial creep strain and strain rate of Mancos 7v, the 2nd stage (creep strain at 5366 psi)
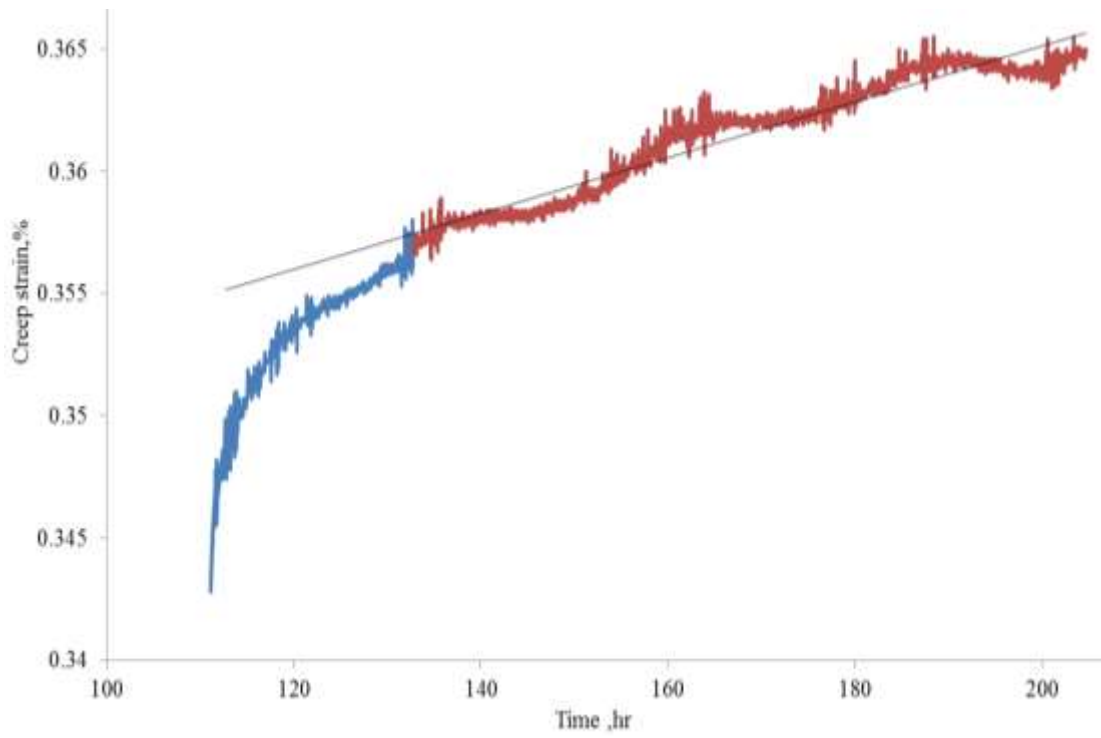
Figure 4.54 The axial creep strain and strain rate of Mancos 7v, the 3rd stage (creep strain at 6069 psi)
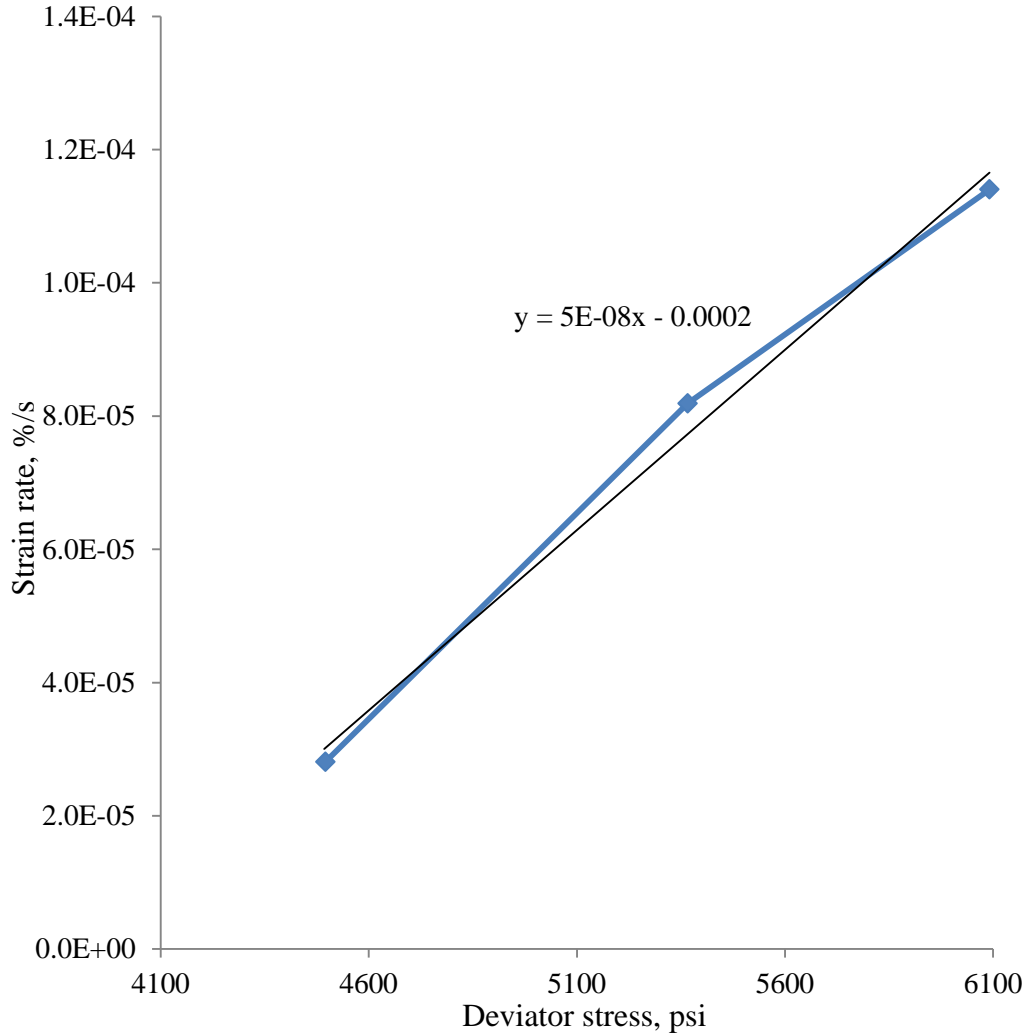
Figure 4.55 Strain rate-stress relation, Uniaxial, Mancos 7v

From Fig. 4.55, one can tell that there is a stress threshold for uniaxial creep of Mancos 7v, but a separate one stage creep test (deviatoric stress=3770 psi) contradicts the above, it gives a strain rate of 6.85E-8, even bigger than that at 6091 psi of the three stage test. Thus the result of Mancos 7v creep test was not compared to that of other samples because of the uncertainty and unreliability of strain rates.
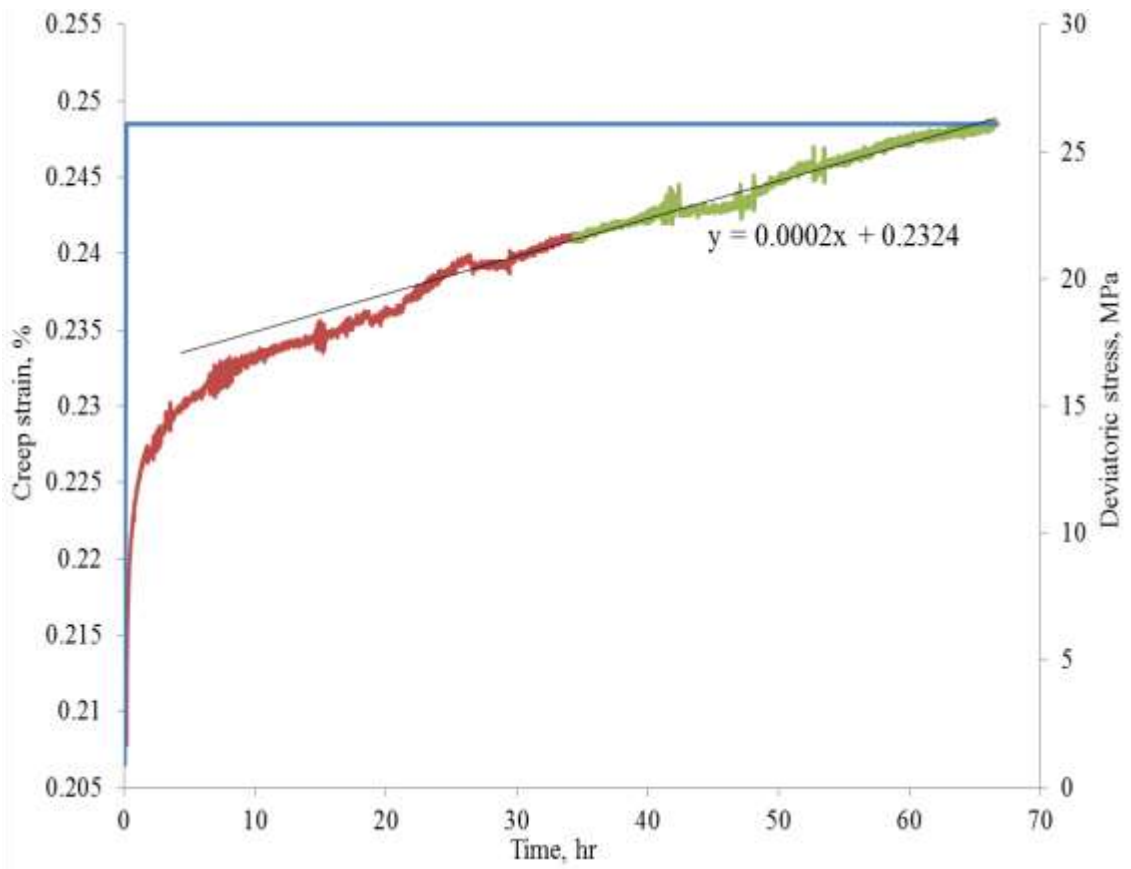
Figure 4.56 The axial creep strain and strain rate of Mancos 7v, a separate creep test
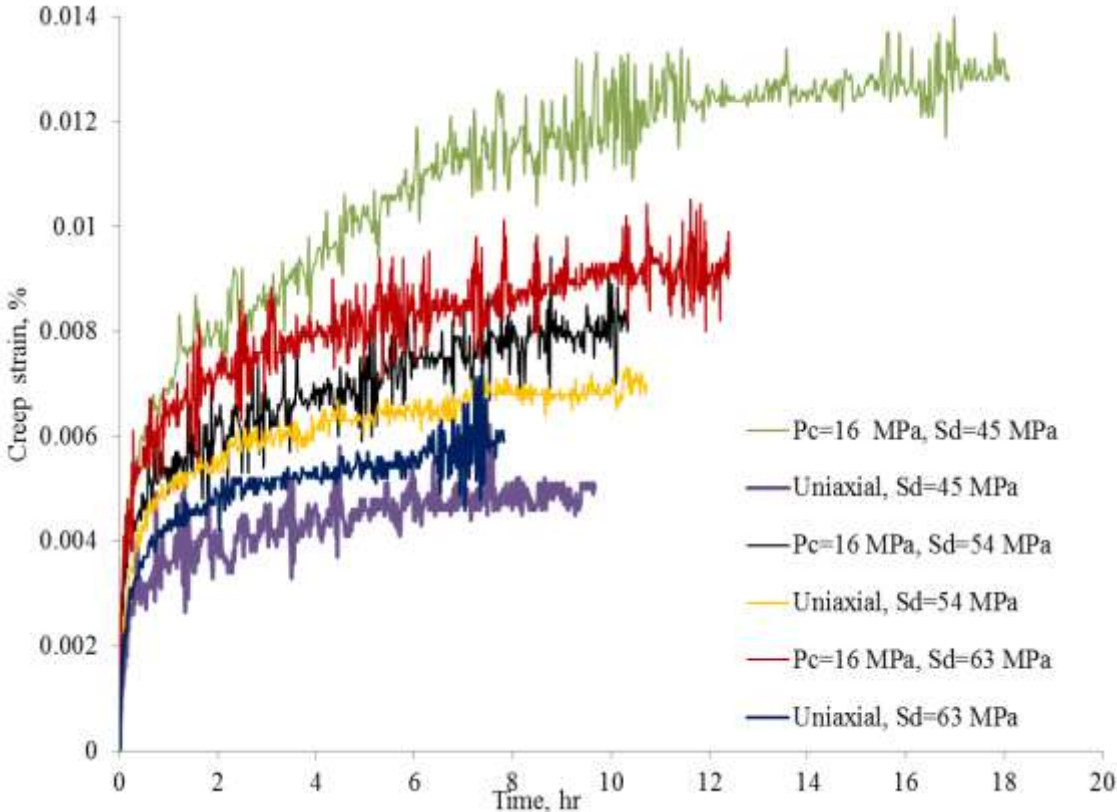
Figure 4.57 Comparisons of creep strain under two confining pressures. Barnet3-20
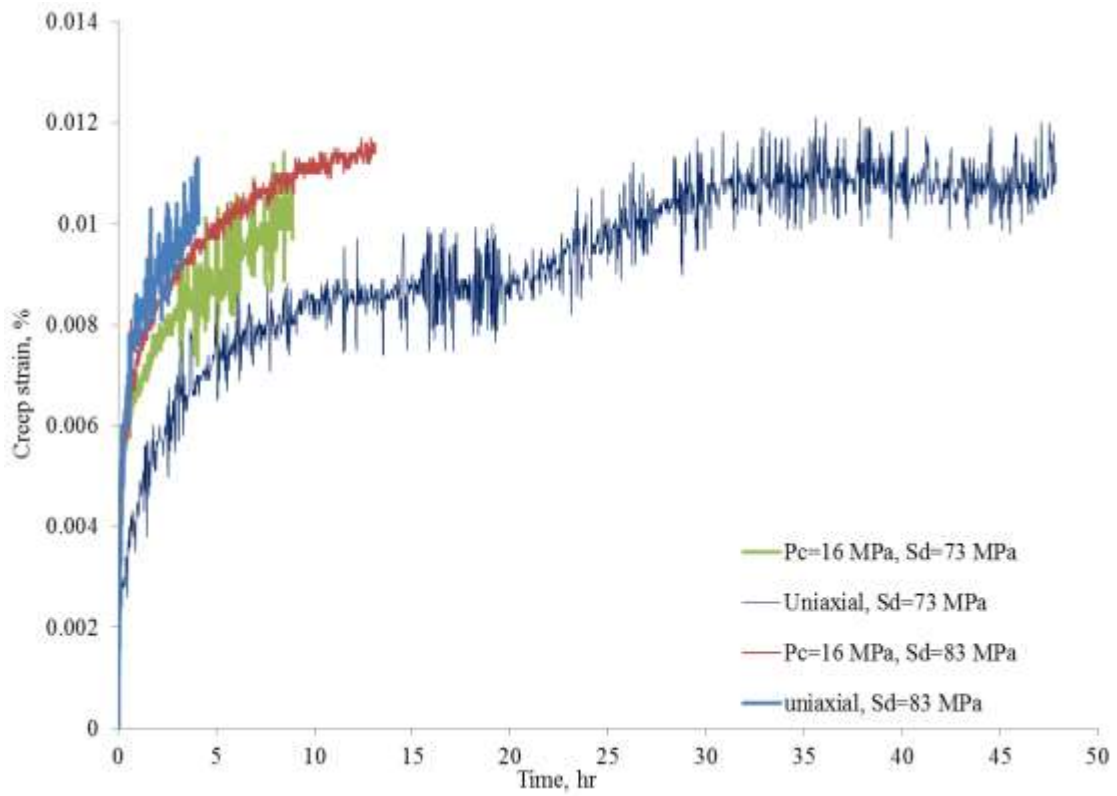
Figure 4.58 Comparisons of creep strain under two confining pressures. Barnet3-20
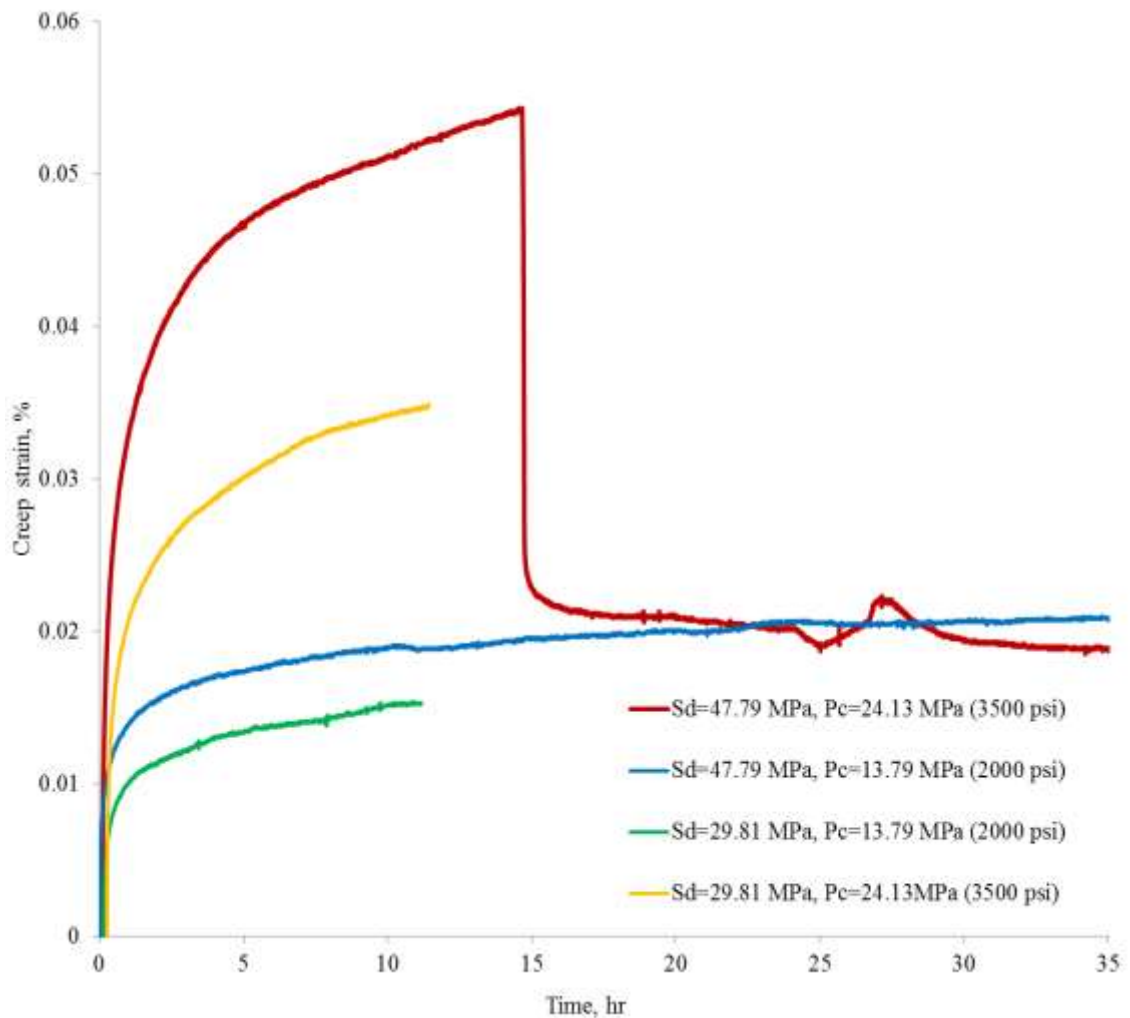
Figure 4.59 Confining pressure dependence of axial creep strain, Haynesville 5-22

It is noticeable that higher confining pressure increases the amount of creep strain under the same deviatoric stress when the deviatoric stress of uniaxial creep has not reached the creep stress threshold. However, when uniaxial deviatoric stress is greater than the stress threshold, the creep strain of uniaxial creep is bigger than that in triaxial condition.

CREEP MECHANISM

The creep strain in the radial direction is much smaller than the creep strain in the axial direction. Thus, it can be concluded that the sample is losing volume during

deviatoric creep stages. Since creep occurs under constant stress, the volume loss is most likely accommodated by pore volume loss or compaction of clays and organic matters. It is difficult to identify the creep mechanism by direct observation of the deformation structure in the samples we have tested. Studies of creep deformation in rocks (Lockner, 1993; Karner et al., 2003; Chester et al., 2005; Heap et al., 2009) usually identify the creep mechanism with direct observations of the deformation structure in the microscope. The extremely fine grain size of the shale makes it difficult to make clear observations on any individual structural features in the rock. A liquid/gas-shale rock system is also very heterogeneous, consisting of multiple minerals which make it impossible to single out one physical mechanism responsible for all of the observed creep strain. It is likely that multiple mechanisms are operating within different components of the rock. Measuring dynamic moduli (by ultrasonic velocities) and permeability measurement during creep could facilitate more definitive inferences. For a dry rock, the bulk modulus, K_{dry}, is a function of the average mineral modulus, K_m, pore stiffness, K_ϕ, and porosity, ϕ, given by the following equation (Mavko et al., 2009):

$$\frac{1}{K_{dry}} = \frac{1}{K_m} + \frac{\phi}{K_\phi}$$

(5)

Where the equation is shown for bulk modulus here, but the same applies to the p-wave and s-wave moduli. Thus, if the mineral properties are not changing during creep, the overall stiffening of the rock is caused by either porosity reduction or pore modulus stiffening, both related to compaction.

Microstructural (thin section and SEM) observations (Loucks et al., 2009; Sondergeld et al., 2010; Curtis et al., 2010) has revealed that most of the pore space in shale reservoir rocks resides in the clays and solid organics (Kerogen). Therefore,

137

compaction is likely responsible for the creep deformation occurring within the clays and organics in the rock. Compaction is evident from Young's modulus escalating with higher deviatoric stress (Fig 4.18, Fig 4.26, Fig 4.30, Fig 4.32 and Fig 4.49) This is conceivable as increase in clay content has been shown to enhance creep deformation in shale reservoir rocks (Sone et al., 2010, Li et al, 2012). Also, clay minerals are known to have anomalously low frictional coefficients (Moore and Lockner, 2004) which would help facilitate grain rearrangement. William D Ibanez et al reported for shale, the brittle and dilatant mechanism are also responsible for shale deformation at various strain rates; this is more pronounced at high deviatoric stress.
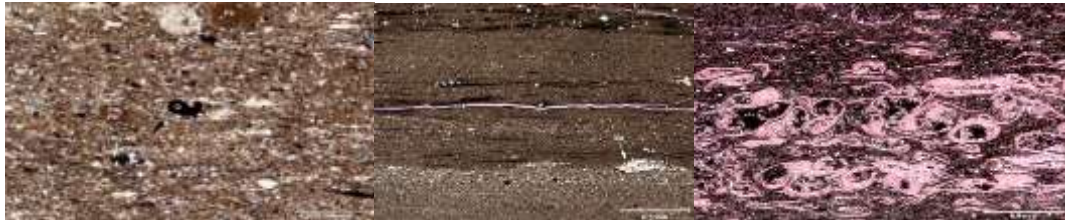
Figure 4.60 Thin sections of typical Barnett, Haynesville, and Marcellus shale

At high deviatoric stresses (over 2/3 of compressive strength), microcracking of the hard and less deformable content of shale such as quartz, feldspar, and carbonate, can contribute enormously to creep. Macroscopic fractures are induced by microcracking at high deviatoric stresses, acoustic emission system is needed to verify the contribution of microcracking.

DISCUSSION AND CONCLUSION

The above comparison and analysis suggest that Young's modulus and clay content are good indicators for evaluating viscoelastic properties of shales. Stiffer shale creeps less, shale with more clay content creeps more, Quantitative characterization of the viscoelastic properties of gas shale reservoir rocks is important for the successful exploitation of gas shale reservoir. Ductility not only affects the effectiveness of

138

hydraulic fracturing, but also influences the long-term reservoir response during depletion. Over geologic time scales, viscoelastic-plastic deformation can also change the stress state. Previous studies on creep behavior of reservoir rocks have suggested many formulations of constitutive law describing their time effect. Among these, the Burger's model and power law function of stress and time can describe creep deformation well. At high deviatoric stresses, microcracking begin to contribute to creep, the constitutive creep model will require damage mechanics parameters to fully describe creep deformation. Strain behavior caused by temperature loading is similar to that caused by stress loading, for the same elevated temperature; the creep strain of higher deviatoric stress is smaller than that of low deviatoric stress, which is opposite to the result of deviatoric creep under room temperature (Fig. 4.30). Further studies on the behavior of these rocks in in-situ conditions (temperature, humidity) assisted by ultrasonic test and acoustic emission test and more comparison with detailed mineralogy are needed for a thorough understanding.

REFERENCES

Chester, F. M., Chester, J. S., Kronenberg, A. K., and Hajash, A., 2007, Subcritical creep compaction of Quartz sand at diagenetic conditions: Effects of water and grain size, Journal of Geophysical Research, 112, B06203, doi:10.1029/2006JB004317.

Curtis, M. E., Ambrose, R. J., Sondergeld, C. H., and Rai, C. S., 2010, Structural characterization of gas shales on the micro- and nano-scales: CUSG/SPE Canadian Unconventional Resources & International Petroleum Conference, 137693.

Heap, M. J., Baud, P., Meredith, P. G., Bell, A. F., and Main, I. G., 2009, Time-dependent brittle creep in Darley Dale sandstone: Journal of Geophysical Research, **114**, B07203, doi:10.1029/2008JB006212.

Karner, S. L., Chester, F. M., Kronenberg, A. K., and Chester, J. S., 2003, Subcritical compaction and yielding of granular quartz sand: Tectonophysics, **377**, 357-381.

Li, Yawei., Ghassemi, Ahmad., 2012, Creep Behavior of Barnett, Haynesville, and Marcellus Shale, 46th US Rock Mechanics / Geomechanics Symposium, Chicago, IL, USA, 24-27 June 2012.

Lockner, D. A., 1993, Room temperature creep in saturated granite: Journal of

Geophysical Research, **98**, 475-487.

Loucks, R. G., Reed, R. M., Ruppel, S. C., and Jarvie, D. M., 2009, Morphology, Genesis, and Distribution of Nanometer-Scale Pores in Siliceous Mudstones of the Mississippian Barnett Shale: Journal of Sedimentary Research, **79**, 848-861.
Mavko, G., Mukerji, T., and Dvorkin, J., 2009, The Rock Physics Handbook Second Edition, Cambridge University Press.

Moore, D. E., and Lockner, D. A., 2004, Crystallographic controls on the frictional behavior of dry and water-saturated sheet structure minerals: Journal of Geophysical Research, **109**, B03401, doi:10.1029/2003JB002582.

Sondergeld, C. H., Ambrose, R. J., Rai, C. S., and Moncrieff, J., 2010, Micro-Structural Studies of Gas Shales: SPE Unconventional Gas Conference, 131771.

Sone, H., & Zoback, M. D. (2011, January). Visco-plastic properties of shale gas reservoir rocks. In 45th US Rock Mechanics/Geomechanics Symposium. American Rock Mechanics Association.

Chapter 5 Mechanical Properties of Intact and Jointed Welded Tuff from Newberry Volcano

ABSTRACT

In this paper we present the results of a testing program to characterize the rock mechanical properties of welded tuff from Newberry Volcano. The rock samples used in this work are four drill cores from the GEO-N2, GEO-N1, and Oxy-72 wells on the western flank of Newberry Volcano. Multistage triaxial compression tests were performed to determine Young's modulus, Poisson's ratio, and failure envelope. In addition, multistage triaxial shear tests were performed to determine the mechanical properties and shear strength of the fractures developed in triaxial compression tests. Joint roughness coefficient (JRC) and Joint Wall Compressive Strength (JCS) were obtained through back-analysis of the shear tests. It was found that the JCS of tested joints are larger than the intact rock Uniaxial Compressive Strength. The joint surfaces were characterized by a laser profilometer to correlate the surface roughness profile to the JRC from back-analysis of experimental data. Joint normal stiffness and shear stiffness were estimated and it was observed that a higher confining pressure results in higher joint shear stiffness. The stiffness is gradually reduced as the contact surfaces become smoother with additional shear displacement.

INTRODUCTION

In stimulation of an enhanced geothermal system (EGS), it is important to consider the fluid pathways between the injection and the production well(s), and the factors controlling them. The permeability of critically stressed fractures (CSFs) can be increased by reducing the effective stress through fluid injection. Critically stressed fractures are defined as pre-existing fractures that have slipped or are in the state of

incipient slip because of the in-situ stress conditions. For the Newberry geothermal field, the primary permeability is extremely low; therefore, the secondary permeability (fractures, joints, etc.) must be used for heat exchange surfaces. This is achieved by water injection to create slip on joints to enhance permeability through dilation. Numerical simulation of this process is very important for reservoir development and post-injection data analysis. Therefore, the mechanical and hydraulic properties of intact rock and jointed rock are needed.

To obtain the required mechanical properties of intact rock and rock joints, it is necessary to measure the properties in the field or laboratory tests. Triaxial compression and shear tests are commonly used for determining the failure properties of intact rock and the friction properties of a jointed rock specimen, respectively. Several triaxial compression and shear tests were performed and the results are presented in this paper. The rock samples described herein include core plugs from the GEO-N2, GEO-N1 and Oxy-72 wells on the western flank of Newberry Volcano. These cores were taken from depths more than 4000ft from the surface.

TRIAXIAL COMPRESSION AND SHEAR TESTS

Laboratory Compression Test

Rock mechanical properties and failure criterion are mainly obtained from laboratory triaxial testing. The most widely used failure criterion is the Mohr-Coulomb criterion. To obtain the Mohr-Coulomb failure envelope, conventional triaxial testing is used. Conventional triaxial testing is simple but requires multiple samples. Aside from limited availability, multiple samples also provide potential uncertainty in the resulting parameters due to sample heterogeneity, as different samples might have significant variations in strength. The multistage triaxial test (Kovari and Tisa, 1975) resolves the

uncertainty issue caused by heterogeneity. In this triaxial testing program, a single sample is compressed at different confining pressures and is subjected to deviatoric stress levels which do not cause irreversible or permanent damage. In each stage, a different confining pressure is used and the axial stress is increased via strain control until a predetermined stopping criterion is reached. The axial stress is decreased to the confining pressure and a new stage starts by applying a higher confining pressure. In the last stage, the sample is loaded until failure. The failure envelope can be estimated from the Mohr's circle resulting from the last loading stage and others obtained from the previous non-failure stages.

Different stopping criteria of the loading stage have been proposed by previous investigators, Kovari and Tisa (1975), Kovari et al. (1983), Kim and Ko (1979), Crawford and Wylie(1987). However, their stopping criteria have two drawbacks: the sample can deform irreversibly or even fail before the stopping point is reached; the construction of failure envelope from a failure Mohr circle and the previous non-failure ones is not well-established and can be subjective. Tran et al (2010) proposed the use of volumetric strain deflection point (maximum contraction point) as the stopping criterion of axial loading in multistage triaxial test. This new termination point resolves the drawbacks of existing methods and is easy to pick. They have reported that the best fit tangent line of non-failure Mohr circles has the same slope as the failure envelope, thus the failure envelope can be obtained by moving up the non-failure envelope.

Laboratory Shear Test

Triaxial shear and direct shear test are used to determine joint properties. Generally, these tests involve a constant normal stress and an increasing shear stress applied to the sample. Normal and shear stresses as well as normal and shear

143

displacement are recorded. Multistage testing refers to several tests undertaken at different normal stresses. The peak and residual shear strength can be estimated from the shear stress vs. shear displacement curve. A normal stress vs. shear stress curve can be drawn to demonstrate the shear strength characteristics of the discontinuity. Due to the difficulties in obtaining a sufficient number of identical samples, a single jointed sample is often used for multistage testing to extract the maximum information from a single sample. However, Barton (1973) reported that only low normal stress tests would provide reliable information on the peak strength characteristics of the discontinuity. Repeated shearing of the sample will crush the asperities and the rest of the test results fall somewhere between the peak and the residual values.

Joint Shear Criterion

The influence of joint roughness on its strength can be considered through the concepts of apparent friction angle and roughness coefficient (Patton, 1966):

$$\tau_p = \sigma \tan(\phi_\mu + i) \tag{1}$$

$$\tau_p = S_j + \sigma \tan(\phi_r) \tag{2}$$

Where Eqn. (1) is for small normal stress, Eqn. (2) for large normal stress, ϕ_μ is the friction angle of an ideally smooth joint surface, and i is the average asperities (teeth) inclination angle from the mean joint plane, ϕ_r is the residual friction angle when normal stress is larger than a critical normal stress. Actual data have shown a gradual transition from the initial slope at $\phi_\mu + i$ to the final slope at ϕ_r, because as the normal stress on the joint increases, it becomes easier to crush the asperity (teeth) rather than ride over them. Once the asperities are sheared, the joint friction angle is reduced to a new level namely, ϕ_μ (Fig. 5.1).

144
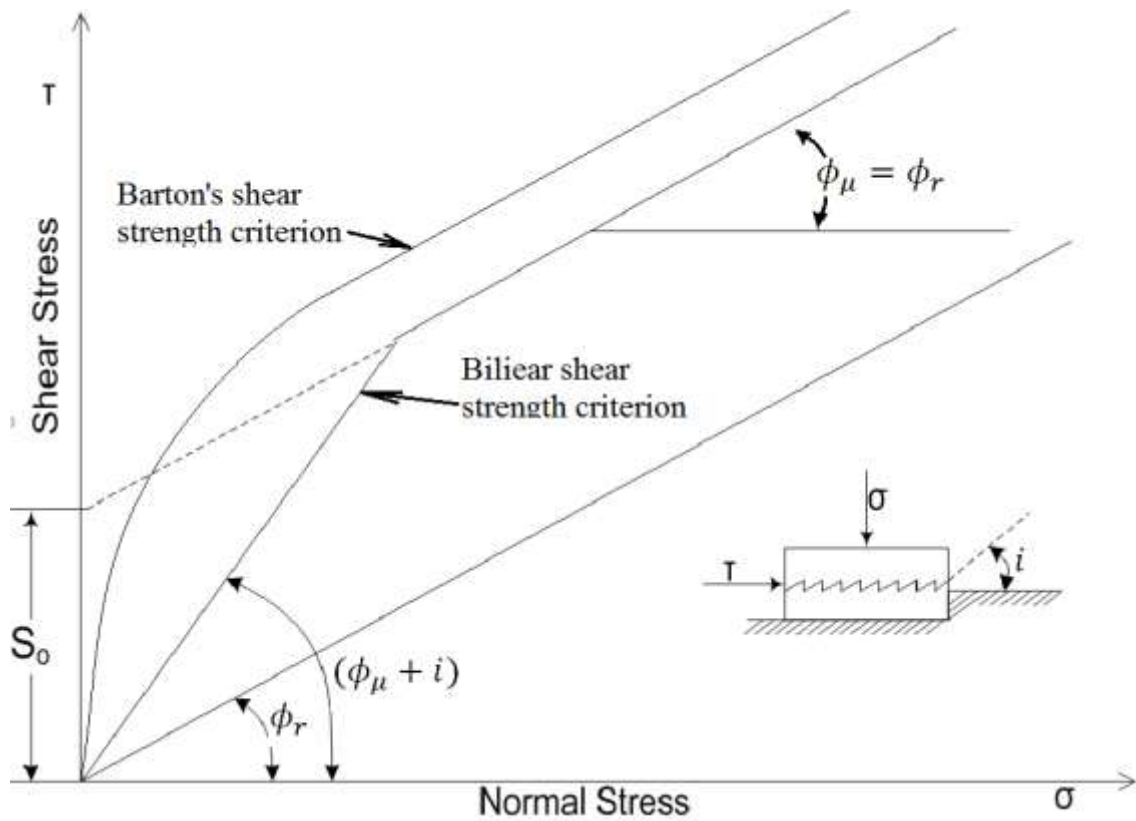
Figure 5.1 Barton's shear strength criterion and Patton's Bilinear shear strength criterion for an ideal asperity model of joint surface

In addition to Patton's bilinear model, a number of empirical models have been proposed, such as the parabolic models of Jaeger (1971). More elaborate models taking into account the surface roughness and dilation were proposed by Landanyi and Archambault (1970), Barton (1973) and Barton and Choubey (1977). Of these, Barton's model is widely used:

$$\tau = \sigma_n \tan[JRC \log_{10}(\frac{JCS}{\sigma_n}) + \phi_b]$$ (3)

Barton's model contains two empirical parameters namely, JRC (joint roughness coefficient), and JCS (joint wall compressive strength). The JRC (ranging from 0 to 20) is a dimensionless number that reflects the amount of surface undulations and asperities present in the discontinuity surface. The value of JCS is the normal stress at which the

dilatancy contribution is reduced to zero and is taken as equivalent to uniaxial compressive strength. ϕ_b is the angle of shearing resistance mobilized at high normal stress levels at which all dilatancy effects are suppressed, as all the asperities are sheared off forming a smooth shearing plane. It is characteristic of the rock mineralogy (Giani, 1992).

Estimation of JCS and JRC

JCS can be set equal to uniaxial compressive strength when the state of weathering of intact rock material and the joint walls is similar. Otherwise, the Schmidt hammer (Giani, 1992) technique is appropriate.

Barton and Choubey reported that JRC could be estimated through the back analysis of shear tests, where Eq. (3) is rearranged into the following form:

$$JRC = \frac{\arctan(\tau/\sigma_n) - \phi_b}{\log_{10}(JCS/\sigma_n)} \tag{4}$$

They also described a residual tilt test in which pairs of flat sawn surfaces are mated and the pairs of blocks are tilted until slip occurs. Maerz and Franklin (1990) proposed a roughness characterizing method using shadow profilometer.

Estimation of $\boldsymbol{\phi_b}$

The basic friction angle can be estimated from direct shear tests on smooth joint, clean surfaces that have been prepared by diamond saw cut as recommended by Hoek and Bray (1981). The friction angle for most smooth unweathered rock surfaces lies between 25° and 35° (Barton and Choubey, 1977). A tilt test may also be used (Stimpson, 1981) by utilizing following equation:

$$\phi_A = tan^{-1}(1.155 tan\, \alpha_s) \tag{5}$$

where ϕ_A is the basic friction angle for the upper piece of core and a_s is the angle at which sliding commences.

Scale Effects

There is significant scale effect in JRC and JCS (Barton and Choubey, 1977). As the joint length increases, joint wall contact is transferred to the larger and less steeply inclined asperities as the peak shear strength is approached, resulting in larger individual contact areas with correspondingly lower JCS and JRC values, causing a reduction in shear strength with size. Barton and Bandis (1982) proposed the following correction factors after undertaking extensive joint and joint replica testing and a literature review:

$$JRC_n \cong JRC_0 \left[\frac{L_n}{L_0}\right]^{-0.02JRC_0} \tag{6}$$

$$JCS_n \cong JCS_0 \left[\frac{L_n}{L_0}\right]^{-0.02JRC_0} \tag{7}$$

Where the subscripts "0" and "n" refer to laboratory scale (100 mm) and in situ block sizes, respectively. The JRC and JCS values used in Eqn. (3) refer to laboratory scale parameters (i.e., JRC_0 and JCS_0).

Joint Stiffness Characteristics

Joint stiffness parameters describe the stress-deformation characteristics of the joint and are fundamental properties in the numerical modeling of jointed rock. Usually they are measured in Direct Shear Test with joint displacement transducers. An indirect method using strain-gauge type extensometer in triaxial shear test can also be used (Rosso, 1976). Barton and Choubey (1977) suggested the following equation for the estimation of the peak shear stiffness (MPa/m):

$$K_s = \frac{100}{L_x} \sigma_n tan \left[JRC log_{10} \left(\frac{JCS}{\sigma_n}\right) + \phi r\right] \tag{8}$$

Where L_x is the joint length (m), the above equation assumes that the peak shear strength is reached after shearing approximately 1% of the joint length. The joint normal stiffness (K_n) is the normal stress per unit closure of the joint. It is influenced by the initial actual contact area, joint wall roughness, strength, deformability of the asperities, and properties of infill material (Bandis et al. 1983).

PETROLOGIC DESCRIPTION OF CORE SAMPLES

Petrographic thin section images were prepared for the description of N1-4013 samples (Fig. 5.2). As Fig. 5.3 shows, N1-4013 sample has a porphyritic to aphanitic texture and is intermediate in composition between porphyritic rhyolite and aphanitic andesite. The rock is a dacite or lithic tuff with predominantly andesitic composition with glassy light gray matrix. This tuff contains micro-porphyritic feldspar, quartz, and a small amount of amygdales, green smectite/clay and zeolite. A pre-existing vertical fracture (healed) is observed in N-4013-1H sample.

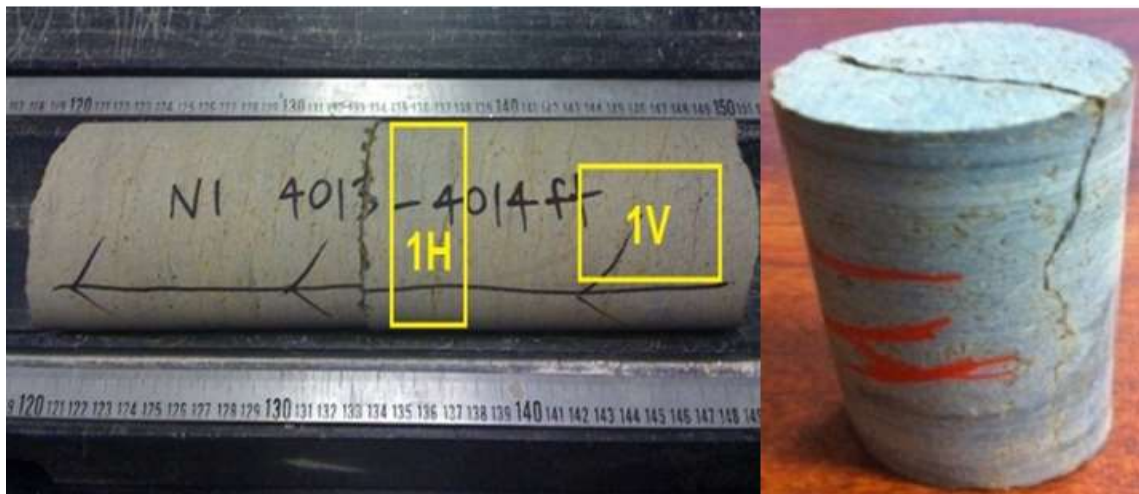**Figure 5.2 Drilled core N1 from 4013-4014 feet depth showing the location of the plugs; Core plugs of N1-4013-1H before triaxial tests**
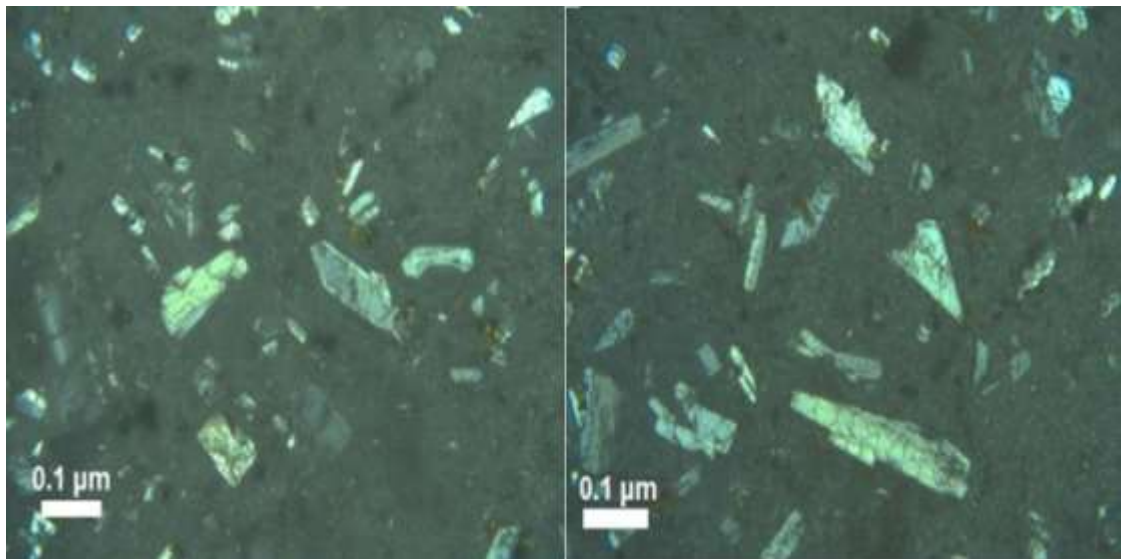
Figure 5.3 Petrographic images of core plugs N1-4013-1H and N1-4013-1V (right). Views are under crossed polarizers
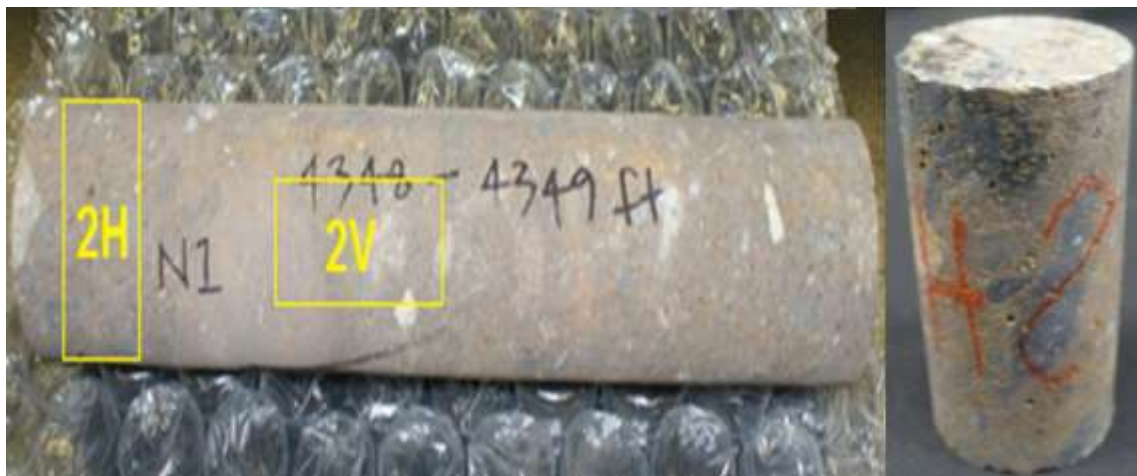

Figure 5.4 Drilled core N1 from 4348-4349 feet depth showing the location of the plugs; Core plug of N1-4348-2H before triaxial tests
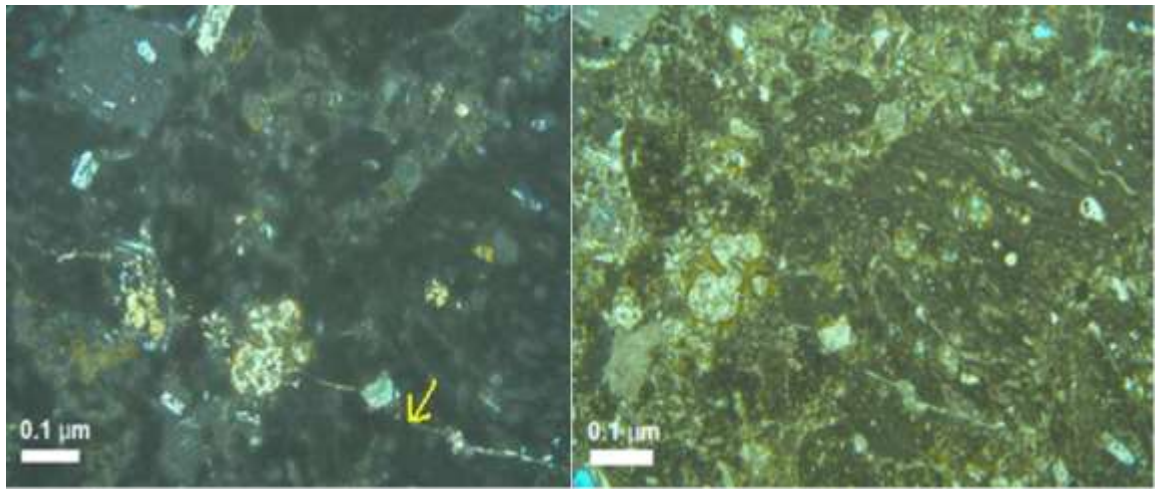
Figure 5.5 Petrographic images of core plug N1-4348-2H. Views are under crossed polarizers and plain light (right)

Core N1-4348-4349 (Fig. 5.5) has an aphanitic texture and is intermediate in composition between porphyritic rhyolite and aphanitic andesite. It is an intermediate tuff or rhyolite tuff, containing massive microcrystalline to cryptocrystalline minerals. The rock also contains bright colored fragments that are plagioclase minerals within a buff color clay matrix. The high clay content suggests ductile behavior; however, brittle behavior might also be present because of fine-grained and large crystals. In addition, small-sized vesicles are observed (blue color on the thin sections). A pre-existing fracture is shown in Fig. 5.5 (Yellow arrow) and is filled with calcite.
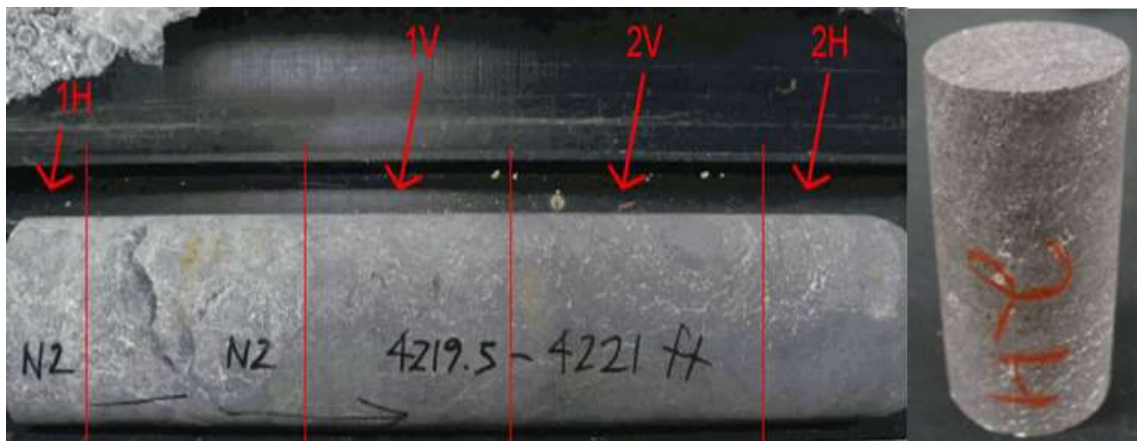
Figure 5.6 Drilled core N2 from 4219.5 feet depth showing the location of the plugs; Core plug of N2-4219.5-2H before triaxial tests
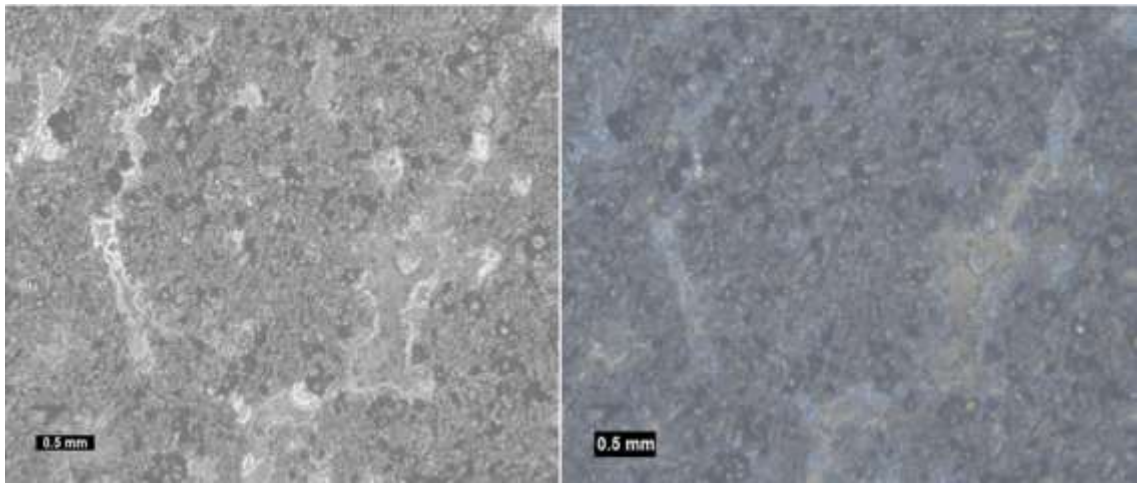
Figure 5.7 Thin section images of N2-4219.5. Views are under crossed polarizers
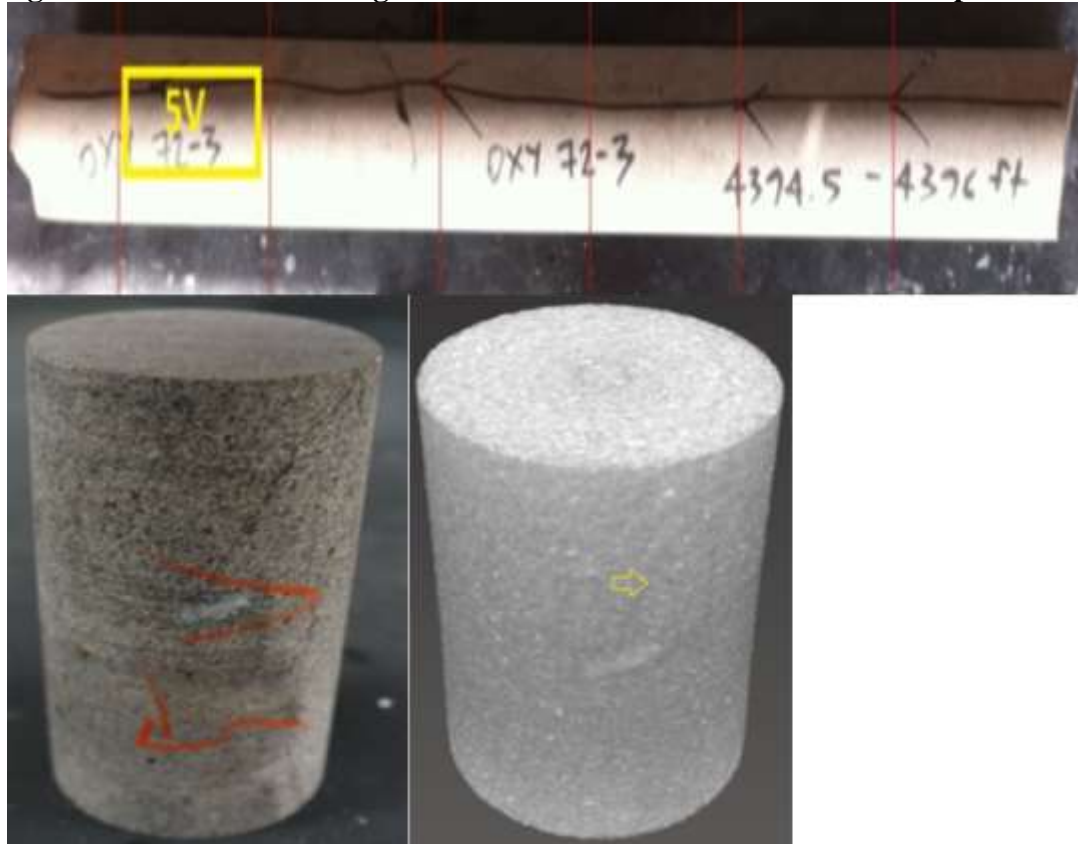
Figure 5.8 A drilled core OXY 72-3, from 4394.5-4396 feet depth; core plug OXY-5V and its 3D CT image prior to testing

The lithology of the core sample N2-4219.5 ranges from basaltic to andesitic in nature, consisting of plagioclase and quartz. The majority of the secondary minerals filling the non-clay fractures are silica and calcite.
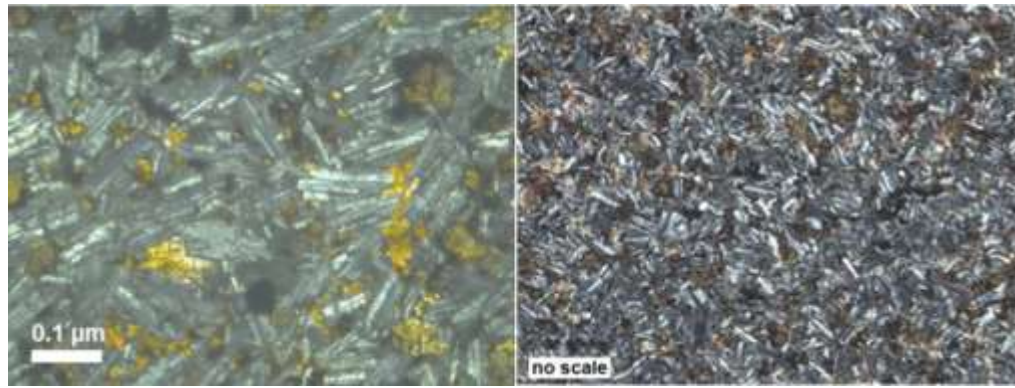
Figure 5.9 Petrographic images of the core plug OXY-5V. Views are under crossed polarizers

The plug OXY-5V has an aphanitic fine-grained texture (As Fig. 5.9). It is a mafic igneous basalt, with dominantly plagioclase (light-colored), and dark gray minerals (possibly iron-oxide minerals) with minor hematite. It is expected that the rock is rather brittle. A pre-existing healed fracture is observed in Oxy-5V sample.

EXPERIMENTAL PROCEDURES

The specimens were first fully saturated with water using a vacuum pump prior to being jacketed to isolate it from the confining oil. All the samples have standard 1"×2" cylindrical shape. Four multistage triaxial compression tests were carried out to determine the mechanical properties and obtain four Mohr-Coulomb failure envelopes; then four multistage triaxial shear tests were conducted to determine the frictional shear strength of the newly formed fractures/joints.

Multistage Triaxial Compression Tests

Each test has five different pressure stages; in the last stage, samples are compressed to failure to induce a macroscopic fracture. The axial stress was applied using axial strain control at a rate of 7E-6/s. Before the deviatoric loading was increased, the strain gauge readings were zeroed at 50 psi of deviatoric stress. The following procedure is followed:

1) The sample is subject to the first confining pressure (hydrostatical condition).

2) Axial load is increased via strain rate (7E-6/sec) control at constant confining pressure. Axial, lateral, and volumetric strains are recorded continuously.

3) The stage is over when the deflection point of the volumetric strain curve is reached ($d\varepsilon_v/ d\sigma=0$).

The axial load is slowly decreased to the confining pressure and the process is repeated for a new stage. Figs. 5.10-5.11 show the stress-strain curves for two of the samples. For non-dilatant specimen (N1-4348-2H), the stopping point was where the tangent modulus ($d\sigma/d\varepsilon_a$) decreases more than 2% from the linear portion of the curve. We assume that the ratio of ultimate strength to the stress at 2% tangent modulus deviation is constant for every pressure stage, the ratio can be determined in the last stage, thus the strengths of previous non-failure stages can be inferred with this ratio.

We determined the failure envelope for each sample by assuming that the best fit tangent line of non-failure Mohr circles has the same slope as the failure envelope.
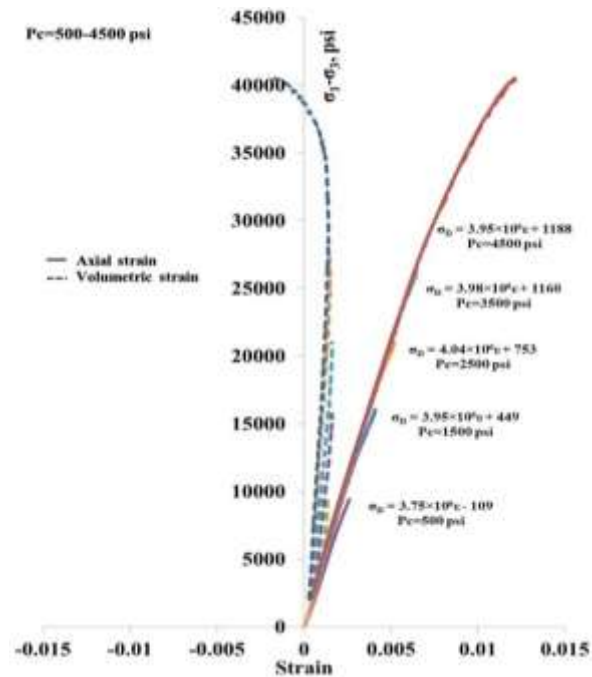
Figure 5.10 Stress-strain response at 5 stages of N1-4013-1H

153
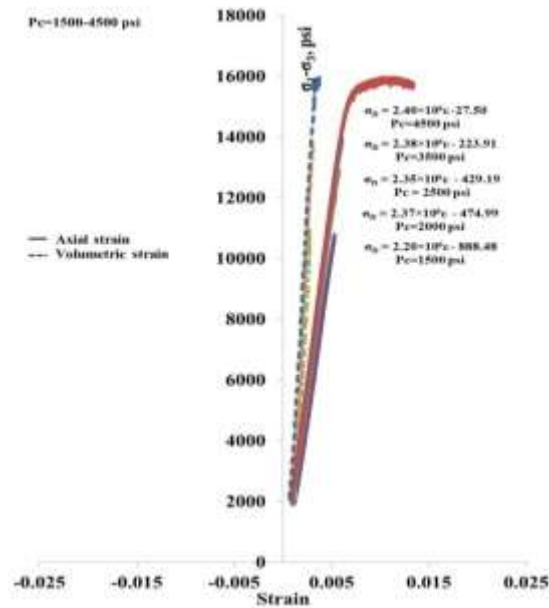
Figure 5.11 Stress-strain response at 5 stages of N1-4348-2H

Figure 5.12 The four samples after compression test, with compression-induced fractures, N1-4013-1H, N1-4348-2H, N2-4219.5-2H and Oxy-5V

Multistage Triaxial Shear Tests

Four multi-stage shear tests were performed on the four compression-induced jointed rock samples. One multi-stage triaxial shear test usually consists of 6-9 stages, one stage has one constant confining pressure. The following experimental procedure is followed:

1) The sample is pressurized (hydrostatically) to the first confining pressure.

2) Axial load is increased via strain control (7E-6/s) at constant confining pressure. Axial, lateral, and volumetric strains are recorded continuously.

154

3) The stage is over when the joint surfaces begin to slip, the deviatoric stress ceases to increase, and the stress-strain curve becomes flat.

4) The axial load is immediately decreased back to the confining pressure (hydrostatic stress state).

5) The confining pressure is increased to the next value.

6) Steps 2) to 5) are repeated for as many stages as required.

Figure 5.13 Sample (fractured tuff) assemble ready for multistage triaxial joint shear test

For the four tested samples, the used confining pressures of every stage are enumerated in Table 5.1.

Table 5.1 Confining pressures used during four multi-stage triaxial shear tests

Stage \ Sample	N1-4013 (1H)	N1-4348 (2H)	N2-4219.5 (2H)	Oxy-4395 (5V)
1	200	200	200	200
2	500	500	500	500
3	730	730	730	730
4	1020	1020	1020	1020
5	1450	1450	1450	1450
6	3200	3000	2176	4500
7	5500	4500	4500	6200
8			6100	

There are usually 3 confining pressures from 0 to 1000 psi, this is to better illustrate the gradual transition from the initial slope at $\phi_\mu + i$ to the final slope at ϕ_r of the shear strength envelope, the more stages one has from 0 to 1000Psi, the clearer the transition is. Test data is then used to develop shear strength envelope for the joint. The shear strength of the jointed specimen is determined by constructing Mohr circles for each stage of the test in the normal stress vs. shear stress domain. The failure inclination angle θ is pre-determined and is used to calculate the stresses on the failure plane for each stage (Goodman, 1989).

RESULTS AND INTERPRETATIONS

The results of the compression test are summarized in Table 5.2. It can be seen that the Oxy-4395-5V is much stronger than N1 and N2 samples, and has a larger elastic modulus; although there are pre-existing fractures in N1-4013-1H and Oxy samples, they still have higher strength and modulus than other two samples. The uniaxial compressive strengths, cohesions, internal friction angles obtained here are comparable to those published by Lutz et al. (2010). It was found that shear fractures induced in compression tests intersect the pre-existing fractures.

Table 5.2 Mechanical properties obtained from compression test

	N1-4013	N1-4348	N2-4219.5	Oxy-4395
Young's Modulus(psi)	3,945,273 (Pc=4500 psi)	2,402,227 (Pc=4500 psi)		6,822,836 (Pc=4500 psi)
Poisson Ratio	0.42	0.28		0.41
UCS, psi	20,314	8,743	8,352	17,719
Cohesion, psi	4,168	2,699	2,224	4,665
Friction angle	45.1º	26.3º	33.8º	39.1º

With the strength data of a multistage triaxial shear test, one can obtain the shear strength envelope of a jointed sample in normal-shear stress domain, together with the compressive (intact) strength envelope, as shown in Figs 5.14-5.17.
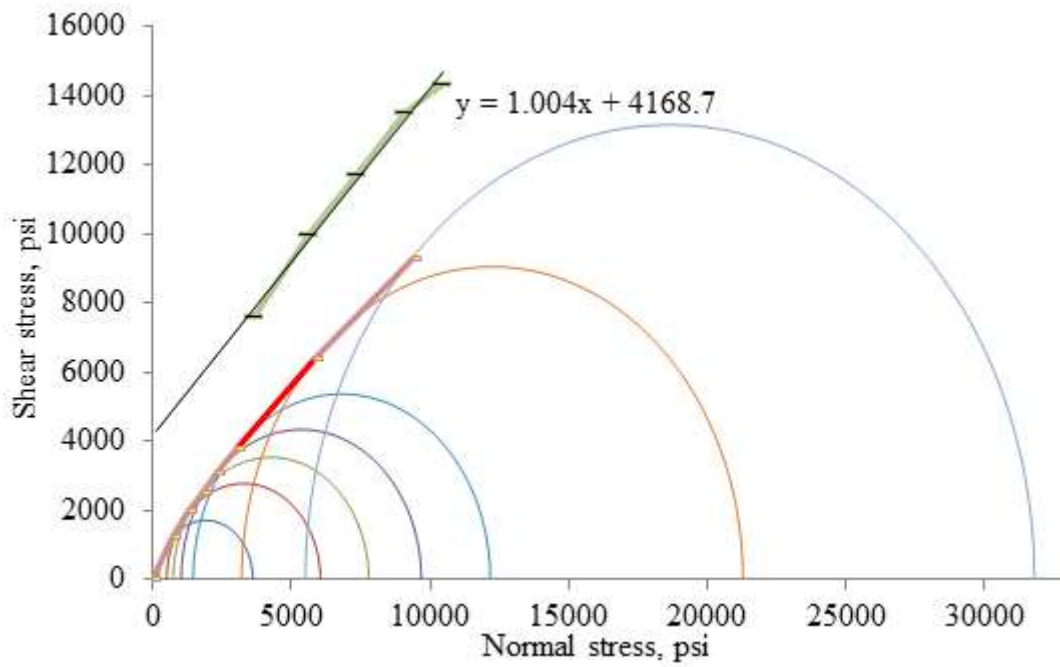
Figure 5.14 Intact rock compressive strength envelope, shear strength envelope and Mohr circles of N1-4013-1H sample
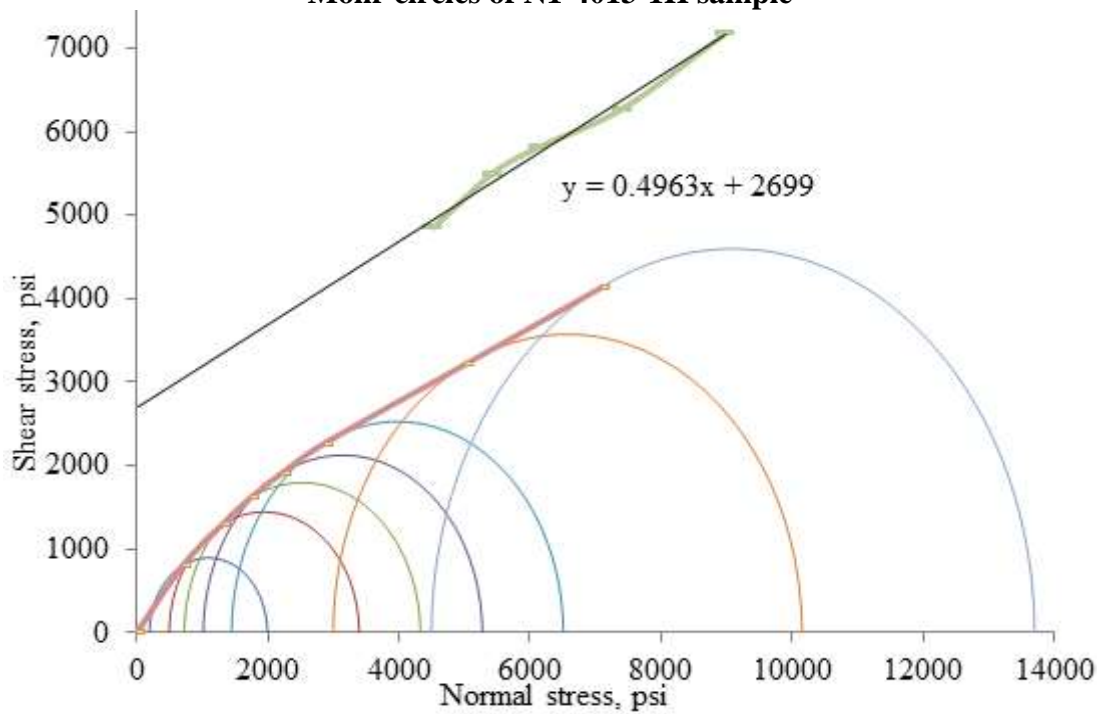

Figure 5.15 Intact rock compressive strength envelope, shear strength envelope and Mohr circles of N1-4348-2H sample

Figure 5.16 Intact rock compressive strength envelop, shear strength envelope and Mohr circles of N2-4219.5-2H sample

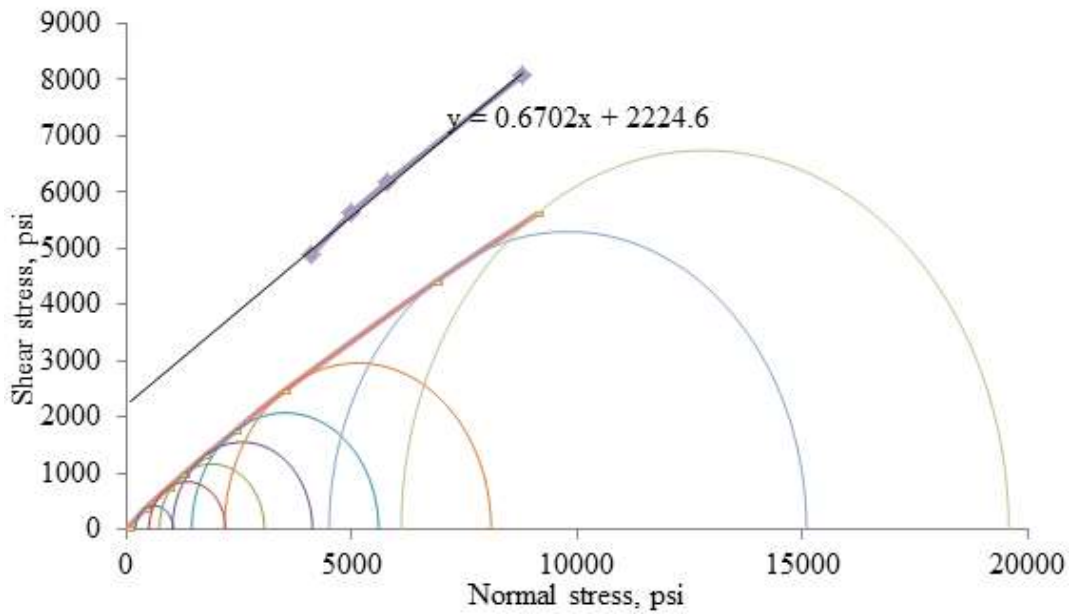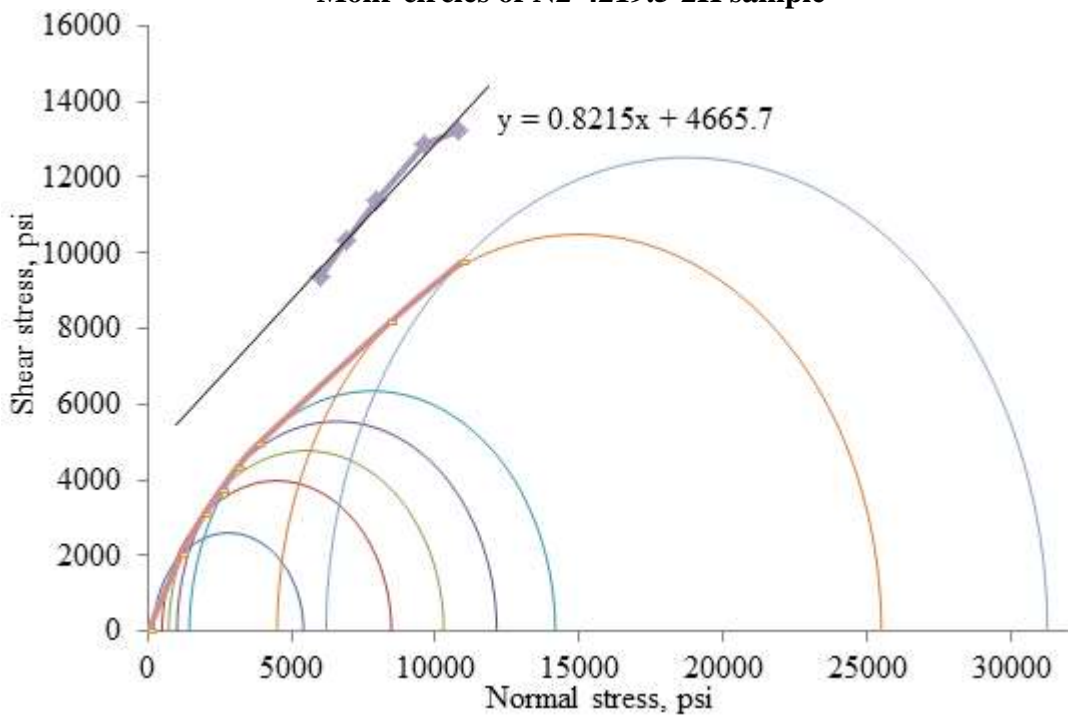**Figure 5.17 Intact rock compressive strength envelope, shear strength envelope and Mohr circles of Oxy-4395-5V sample**
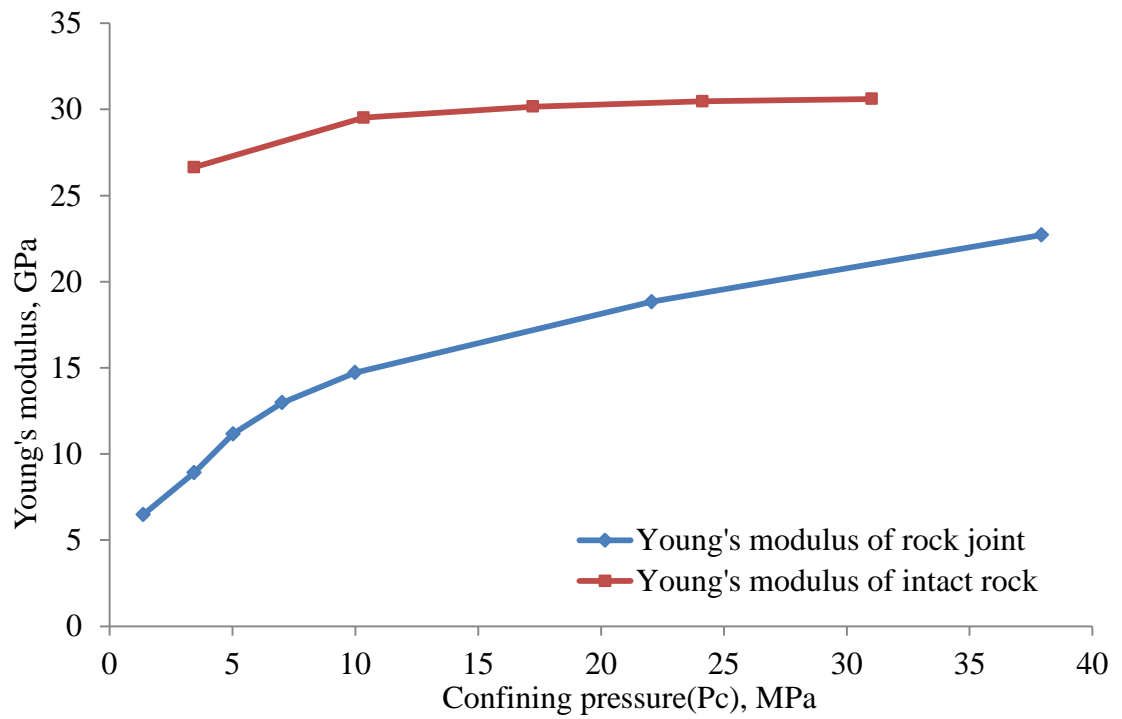
Figure 5.18 Young's modulus degradation from the intact rock to the jointed rock because of joint closure, N1-4013-1H
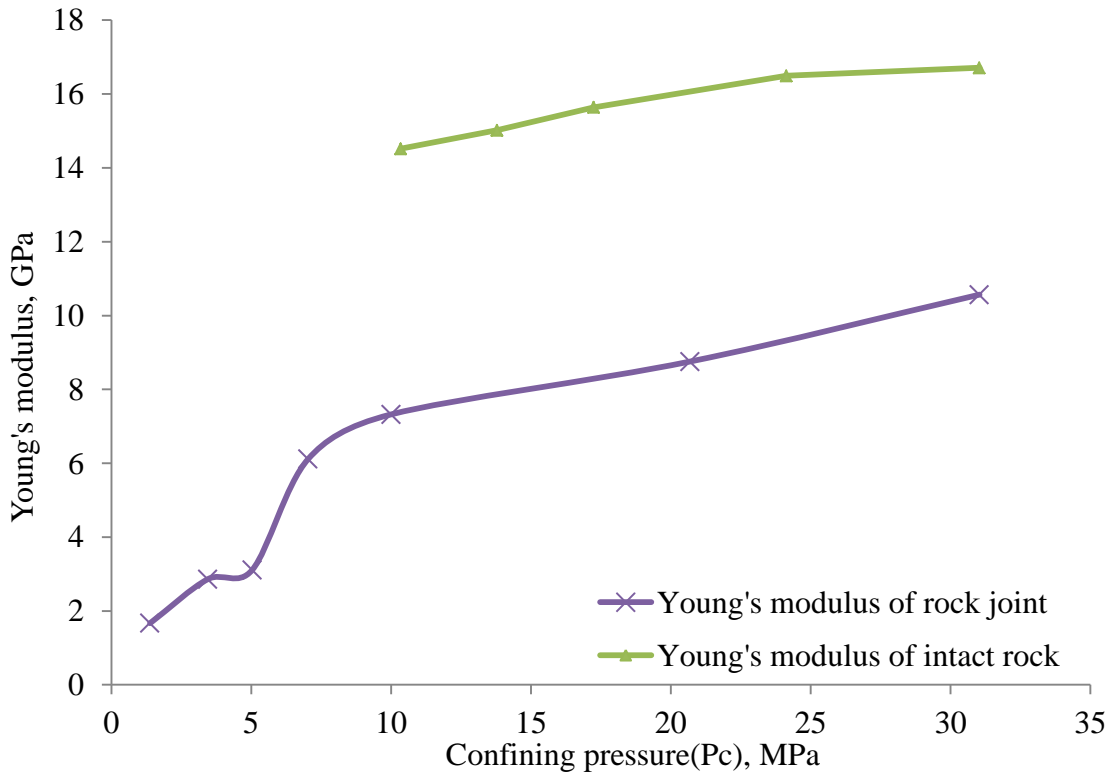
Figure 5.19 Young's modulus degradation from the intact rock to the jointed rock because of joint closure, N1-4348-2H

With a shear strength envelope, the JRC, JCS and ϕ_b in Barton's shear strength model can be determined through back-analysis. A least-square curve fitting method is used to determine the three parameters of a shear strength envelope, the equivalent friction angle of any point on Barton's JRC-JCS curve can be obtained by taking the inverse tangent of Barton's curve slope, as shown in Fig. 5.20. Similarly, the other shear strength envelopes are processed and the results are summarized in Table 5.3. As it can be seen in Table 5.3, the residual friction angles are smaller than the internal friction angles, because the asperities were sheared off after the repetitive shear tests; the fracture surfaces are smoother than the newly formed fracture surfaces.
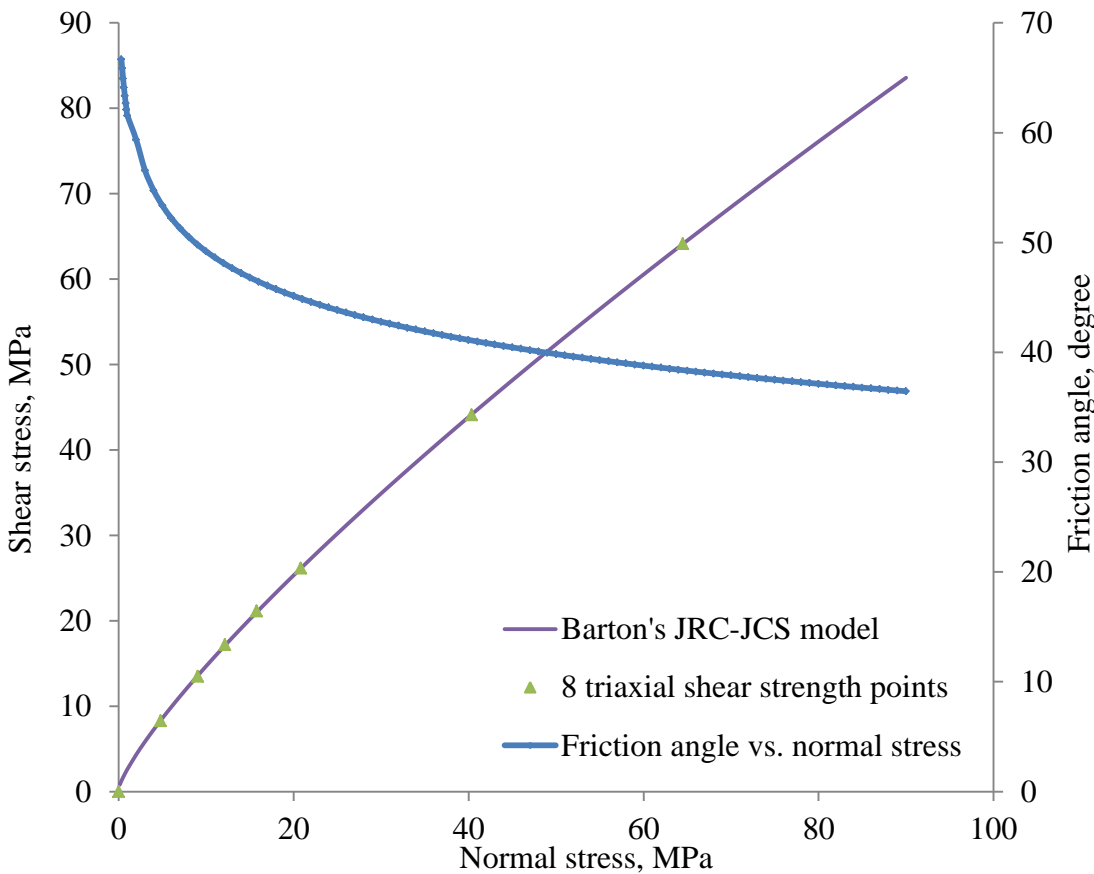
Figure 5.20 The 8 joint shear strength points, Barton's model curve, and friction angle trend, N1-4013-1H

Table 5.3 Summary of frictional angles and Barton's model parameters

Sample ID	Internal friction angle	$\phi_\mu + i$ (σ_n=0)	ϕ_b (ϕ_r)	i	JRC Gradient	JRC Degree	JCS MPa	UCS inferred MPa
N1-4013-1H	45.1°	66.7°	38.5°	28.3°	0.236	13.52	188.8	122.1
N1-4348-2H	21.3°	60.0°	19.2°	40.8°	0.353	20.00	170.2	74.6
N2-4219.5-2H	33.8°	47.6°	28.5°	19.1°	0.127	7.28	181.3	57.0
Oxy-4395- 5V	40.7°	53.7°	32.9°	20.8°	0.372	20.00	196.9	119.0

Joint Stiffness from Multistage Shear Test

The procedure proposed by Rosso (1976) is used for determining the joint stiffness using the test result of the multistage triaxial shear test and the results are shown in Figs 5.21-5.28 and Table 5.4.

Figure 5.21 Normal stiffness of N1-4013-1H

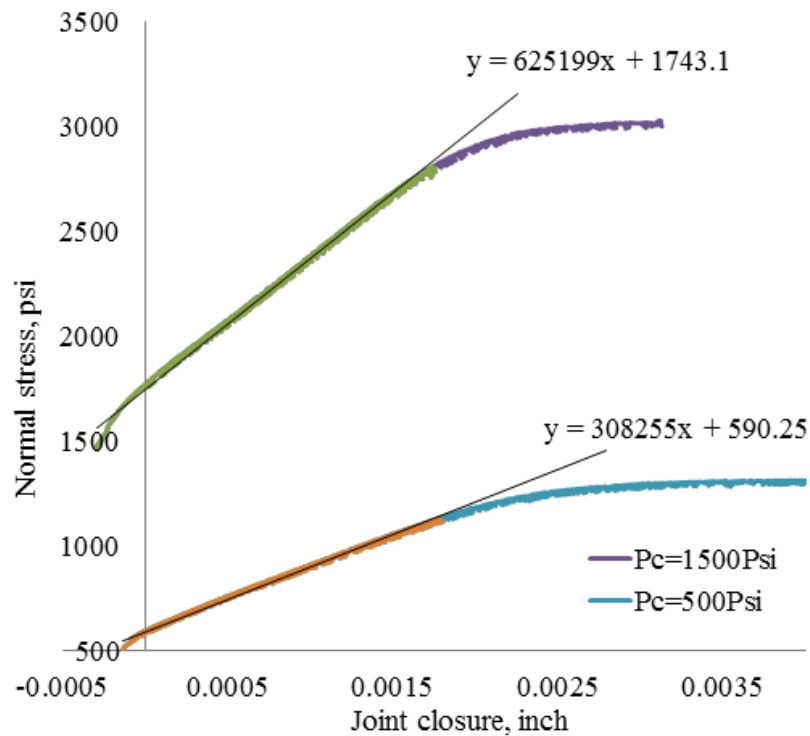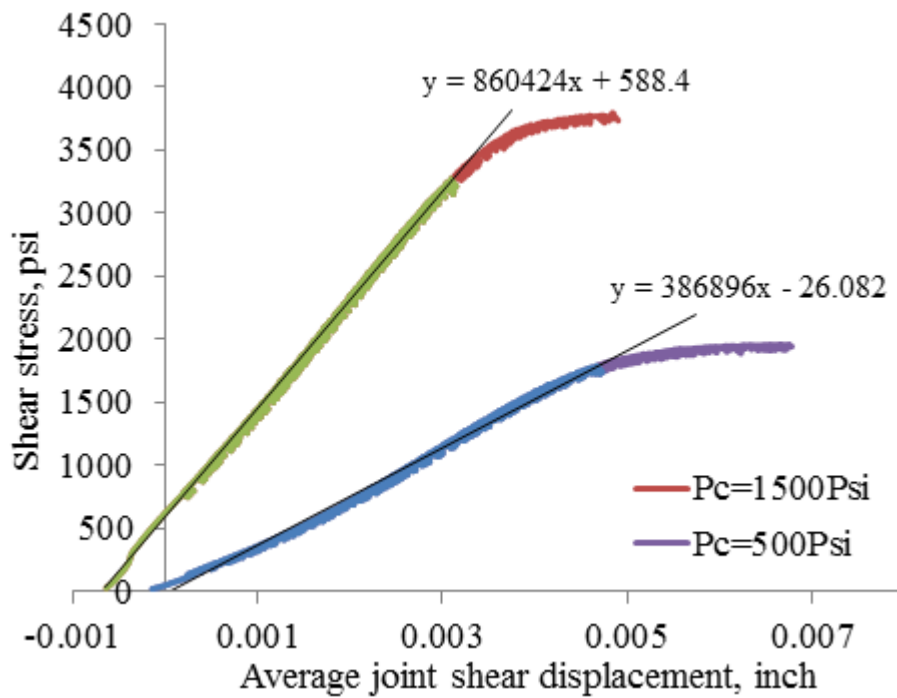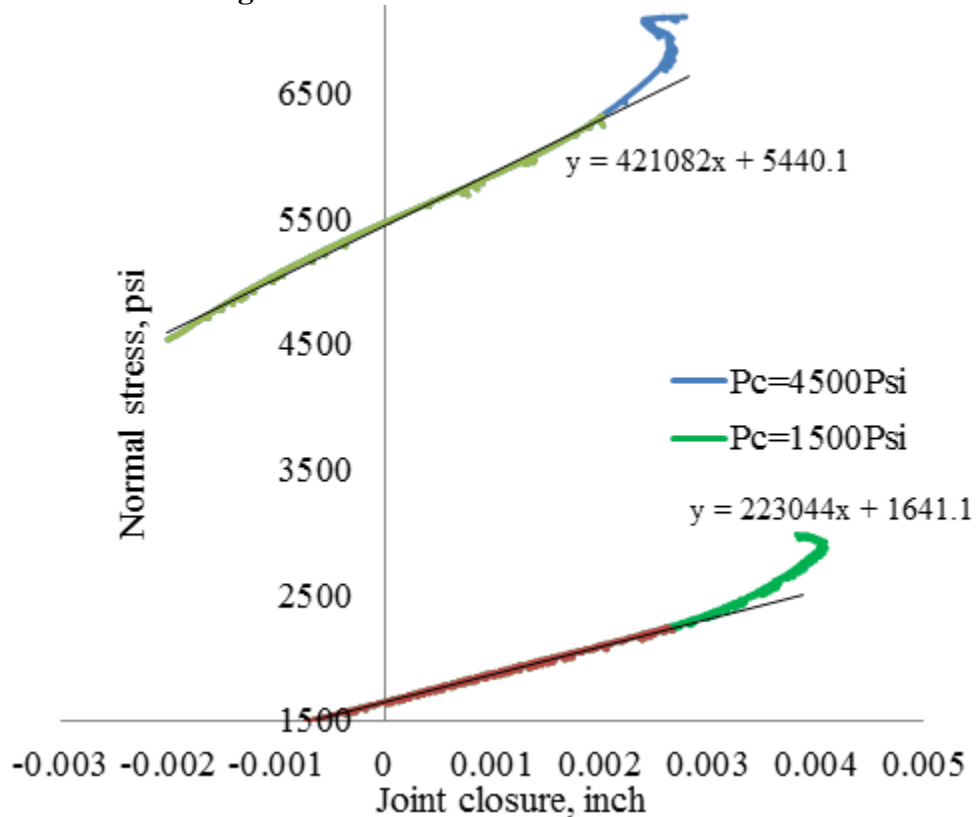**Figure 5.22 Shear stiffness of N1-4013-1H**

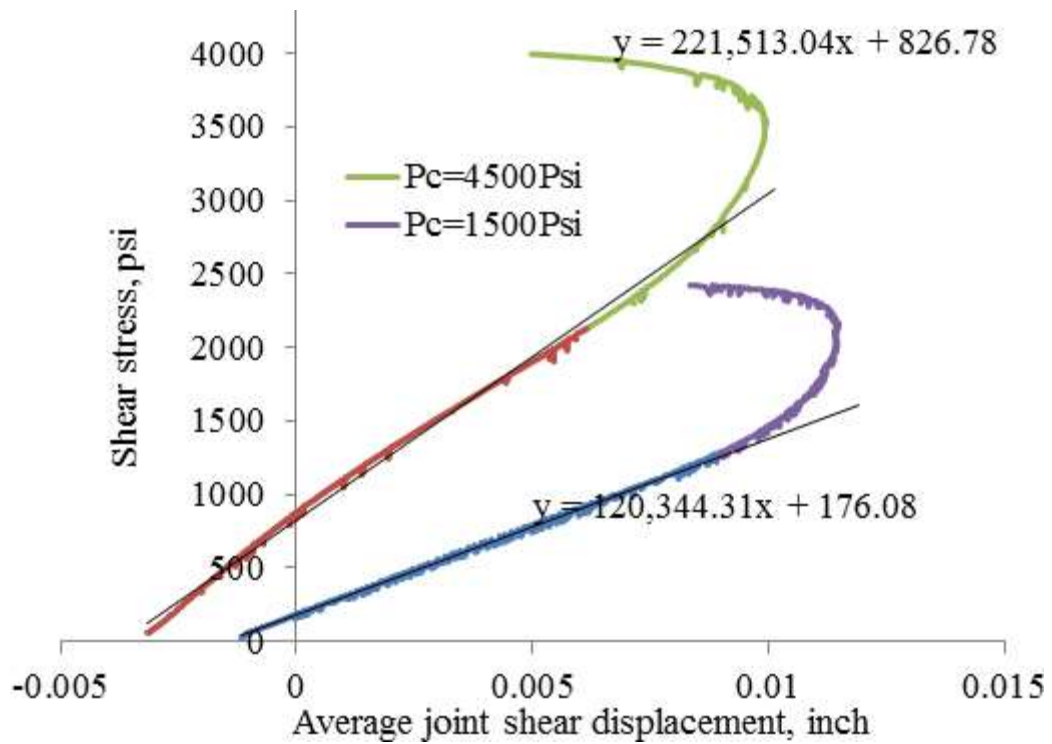**Figure 5.23 Normal stiffness of N1-4348-2H**

Figure 5.24 Shear stiffness of N1-4348-2H
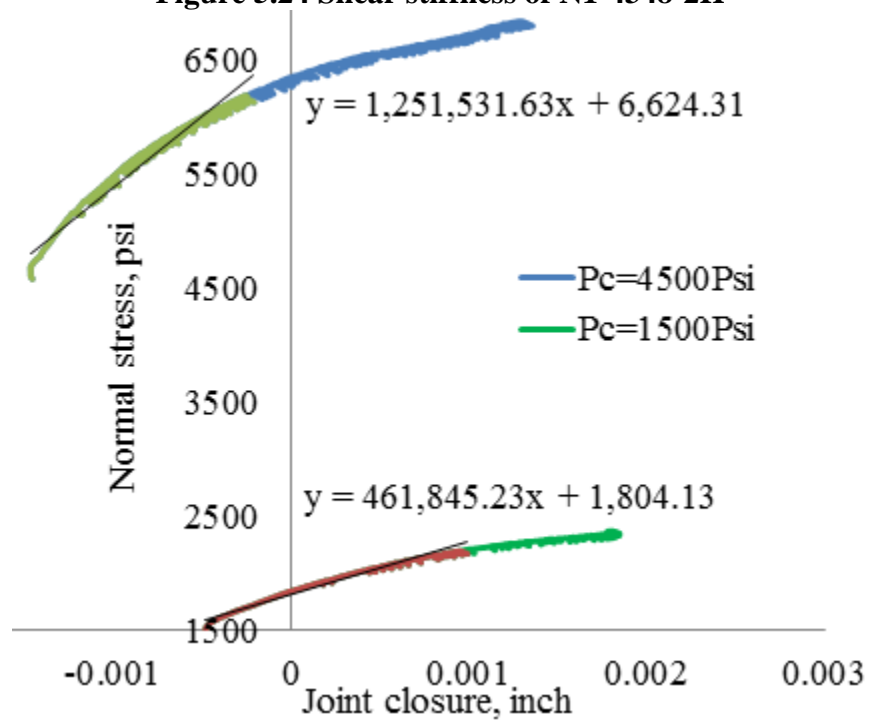
Figure 5.25 Normal stiffness of N2-4219.5-2H
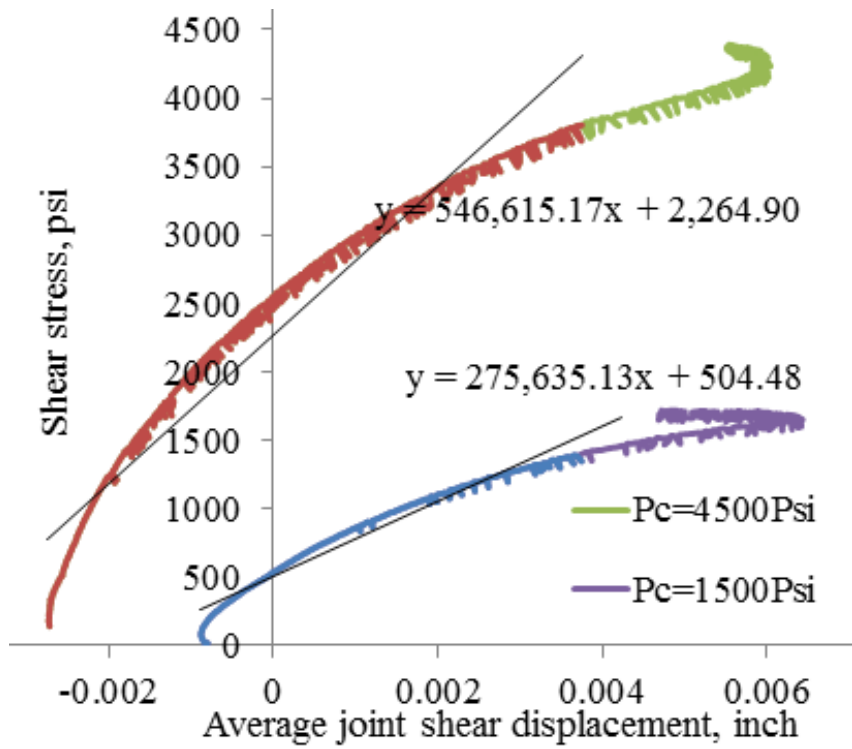
Figure 5.26 Shear stiffness of N2-4220-2H

$y = 546{,}615.17x + 2{,}264.90$

$y = 275{,}635.13x + 504.48$
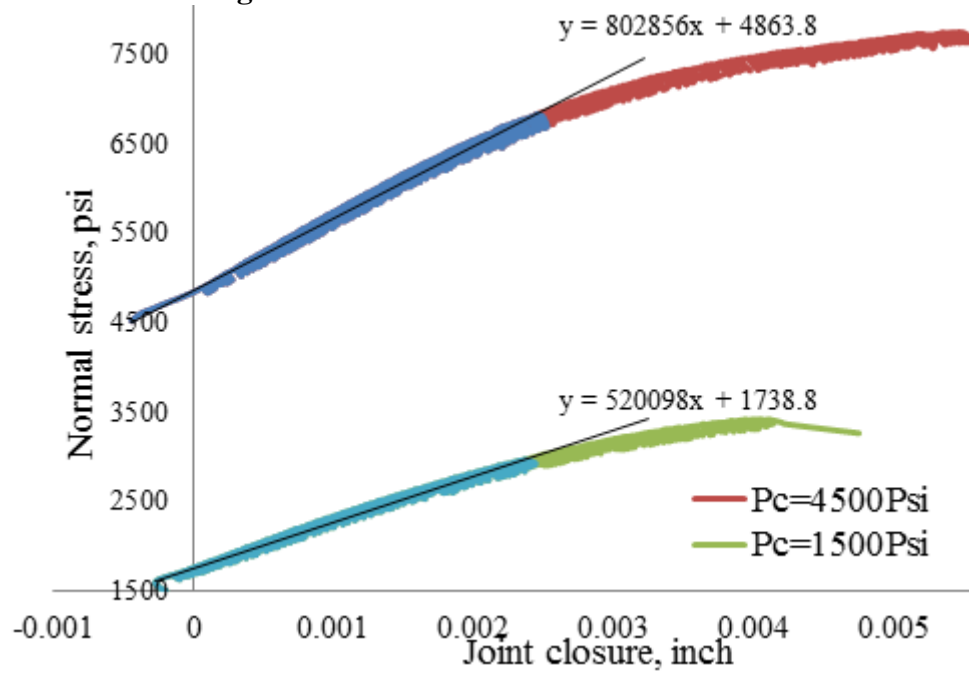
Figure 5.27 Normal stiffness of Oxy-4395-5V

$y = 802856x + 4863.8$

$y = 520098x + 1738.8$

164
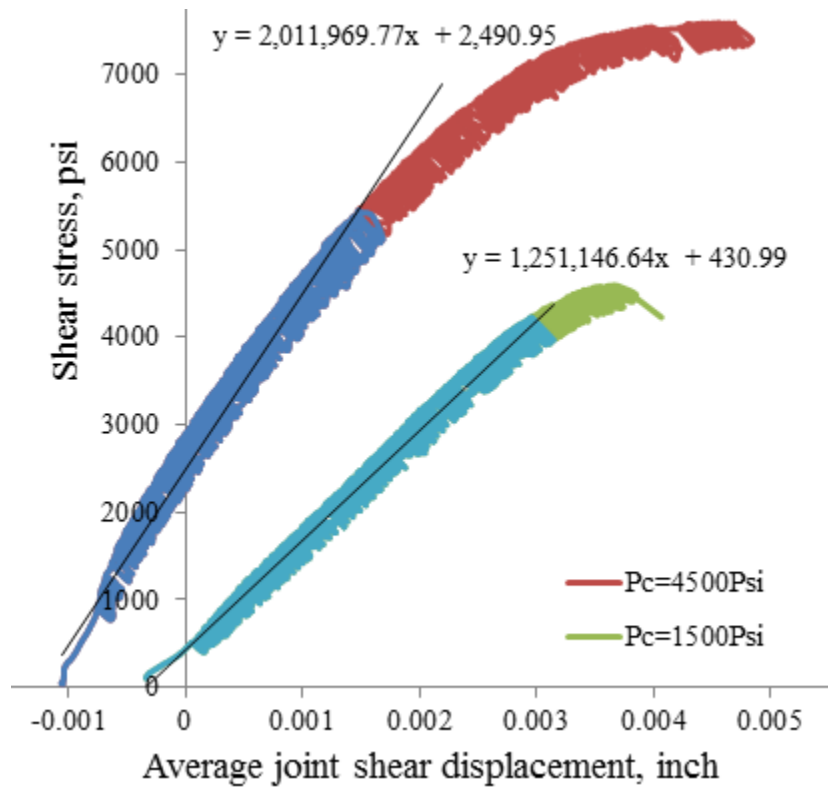
Figure 5.28 Shear stiffness of Oxy-4395-5V

Table 5.4 Summary of stiffness values

Pc, psi	Stiffness (psi/in)	N1-4013-1H	N1-4348-2H	N2-4220-2H	Oxy-4395- 5V
500	K_n	308255	×	×	×
	K_s	386896	×	×	×
1500	K_n	625199	223044	461845	520098
	K_s	860424	120344	275635	1251146
4500	K_n	×	421082	1251531	802856
	K_s	×	221513	546615	2011969

Joint Surfaces Characterization by Laser Profiler

The surface roughness of joints has a critical influence on the shear behavior. It is necessary to evaluate the surface roughness directly using surface profiling tools. In this work, the surface roughness is measured after shear tests using a non-contact type of joint roughness measurement system (laser displacement gauge) as shown in Fig. 5.29.

165

One pair of joint surfaces is scanned and the profiles are compared to a set of published standards of Barton (Fig. 5.30). It was found that for similar profiles, the JRC value obtained from back-analysis is smaller than that of Barton's standard profile.

Figure 5.29 Scanned surface roughness profiles of two fracture surfaces, N2-4219.5-2H

Figure 5.30 Barton's standard surface roughness profile

The surface roughness profile of N2-4220-2H is similar to 7th roughness profile of Barton's published standard, the JRC value is 12 to14, but back-analysis of 8 shear strength points gave a JRC value of 7.28 (Table 5.3). It should be noted that Barton's standard surf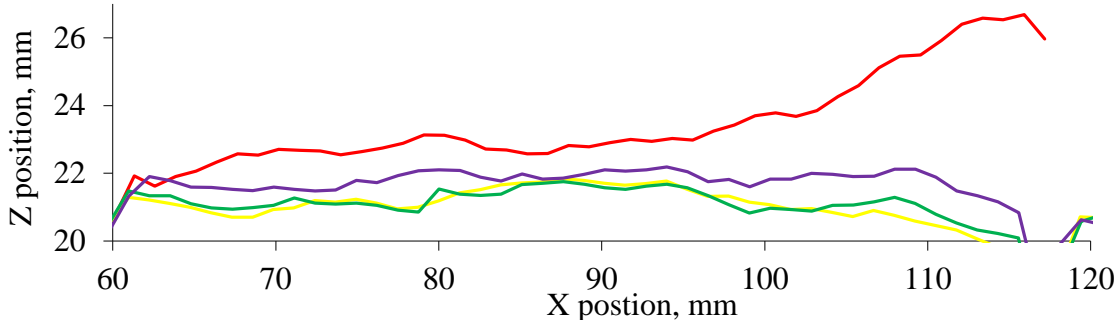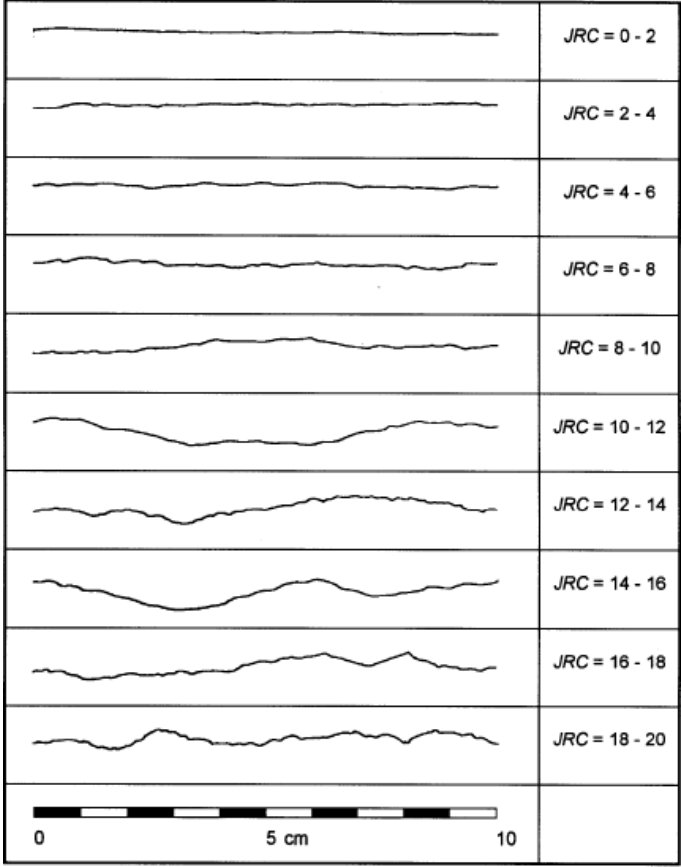ace roughness profile was obtained by shearing dry fractures, but in this study, the four fractured samples were still wet (saturation before testing) during shear tests. We speculate that water plays a large role in making the JRC from back-analysis smaller.

DISCUSSION AND CONCLUSION

Petrological analysis and mineralogical compositions of welded tuff correlate to their mechanical properties, sample with more clay content has low strength; fine-grained siliceous sample (Oxy-5v) is stronger than courser-grained samples; pre-existing closed fractures intersect with compression induced fractures, it indicates that the pre-existing fractures have very large shear strength and are not critically oriented in the specimen. Repetitive shearing of one fractured sample crush its asperities and make fracture surface smoother, thus the friction angle is reduced. The surface roughness of newly formed joint is not profiled in this study, a comparison between the roughness before and after shear test will give us more insight in asperity damage (shearing off). The JRC values from back-analysis are smaller than the value from visual comparison with Barton's standard JRC. We postulate that water might influence the shearing process, make the JRC values smaller, a shear test on a dry fracture might give higher JRC values; the JCS are bigger than the uniaxial compressive strength, this might be attributed to size effect. More detailed investigations are needed to resolve the above-mentioned uncertainties and questions.

REFERENCES

Barton N. (1972), "A model study of rock-joint deformation." *Int J Rock Mech Min Sci Geomech Abstr;* 9:579–602.

Barton N. (1973), "Review of a new shear strength criterion for rock joints," *Engineering Geology*, 7:287–332.

Barton N, Bandis S. (1982), "Effects of block size on the shear behavior of jointed rock," *23rd US Symposium on Rock Mechanics, Berkeley, CA,.* p. 739–60.

Barton N, Bandis S. (1990), "Review of predictive capabilities of JRC-JCS model in engineering practice," In: Barton N, Stephansson O, editors. *Proceedings of the International Symposium on Rock Joints*, Loen, Norway. Rotterdam: Balkema,. p. 603–10.

Barton, N. and Choubey,V. (1977), "The shear strength of joints in theory and in practice," *Rock Mech.*, vol. 10, pp. 1-65.

Brown W. S. & Swanson S. R. (1972), "Laboratory study of rock joint strength and stiffness under confining pressure," *Air Force Weapons Laboratory Final Report No, F29601-71-C-0050.*

Crawford, A. and D. Wylie. (1987), "A modified multiple failure state triaxial testing method," *28th US Rock Mechanics Symposium,* 133-140.

Dung T.Tran, Aristotelis Pagoulatos, Carl H. Sonderge, (2010), "Quantify Uncertainty of Rock Failure Parameters From Laboratory Triaxial Testings Using Conventional And Multistage Approaches," *44th U.S. Rock Mechanics Symp., June 27 - 30, 2010, Salt Lake City, Utah*

Giani GP.(1992), "Rock slope stability analysis," Rotterdam: A.A Balkema Publishers.

Goodman, R.E, (1989), "Introduction to Rock Mechanics, 2nd Edition"

Hoek E, Bray JW. (1981), Rock slope engineering, 3rd ed. London: Institute of Mining and Metallurgy.

Jaeger, J.C. (1971). "Friction of Rock and Stability of Rock Slopes," *Geotechnique,* 21 (2):97-134.

Kim, M. M., and H. Y. Ko.(1979), "Multistage triaxial testing of Rocks," *Geotechnical Testing* 2: 98-105.

Kovari, K., Tisa, A., Einstein, H., and J. A. Franklin, (1983), "Suggested methods for determining the strength materials in triaxial compression," *Int. J. of Rock Mech. & Min. Sci. & Geomechs Abs.* 20: 283-290.

Landanyi,B. & Archambault, G. (1970) "Simulation of the shear behavior of a jointed rock mass," *11th Symposium on Rock Mechanics, American Inst. Min. Met. Petr. Engineers*, New York, pp 105-125.

Maerz, N.H, Franklin, J.A., and Bennett, C. P,(1990), "Joint roughness measurement using shadow profilometry," *Int. J. Rock Mech. Min. Sci.,* 27(5), 329–343.

Patton, F. D. (1966), "Multiple modes of shear failure in rock," *Proc. 1st Int. Cong. Int. Soc. Rock Mech., Colouste Gulbenkian Foundation, Lisbon*, vol. 1, pp. 509-513.

Rosso, R.S. (1976), "A comparison of joint stiffness measurements in direct shear, triaxial compression and in situ." *Int. J. Rock Mech. Min. Sci. & Geomech. Abstr.*, 13:167-172

Stimpson, B. (1981), "A suggested technique for determining the basic friction angle of rock surfaces using core," *Int J Rock Mech Min Sci Geomech Abstr;*18:63–5.

Wawersik W. R. (1974), "Deformability and strength of singly and multiply jointed sandstone in quasi-static compression." *Defense NuclearAgency Contract No. DNA001-73-C-0034.*

Appendix A Procedure for Inelastic Strain (Damage) Controlled Compression Test (Chapter 2)

Procedure for creating new control variable Strain_inelastic in MTS software

1. Create a calculation parameter named unloading-moduli in calculation editor

2. Create a virtual channel named Strain_inelastic in station builder

3. Assign the equation $\varepsilon - \dfrac{\sigma}{E_u}$ to the Strain_inelastic in calculation editor

Procedure for damage controlled compression test

1. Drive specimen manually near to contact

2. Reset readings of axial and radial extensometers, actuator displacement, axial force

3. Drive specimen by moving actuator up until axial force is 0.5kN

4. Start programmed test control

5. Axial loading ramp to settle specimen

6. When axial stress exceeds crack damage stress (or volumetric strain reversal point), switch to inelastic strain control

Appendix B Procedure for Conventional and Damage Controlled

Brazilian Test (Chapter 3)

Procedure for the Load Controlled Brazilian Test in Confined Condition

1. Cut and prepare the specimens using appropriate means, end faces shall be flat within 0.25 mm, and square and parallel to within 0.25 °

2. Cut two circles of copper foil for the two end faces of a disc, and long strip copper foil for the periphery of the disc; wrap the disc with these three foils and solder the seams with soldering iron

3. The sealed specimen shall be wrapped around its periphery with one layer of the masking tape and mounted squarely in the loading jaw

4. Fill the GCTS triaxial cell with confining fluid

5. Lower the loading jaw with the specimen into the GCTS triaxial cell through the top hole of the cell, mound the loading jaw at the center of the S-shaped load cell, and put the loading plunger of the triaxial cell back into the top hole of the cell

6. Pressurize the triaxial cell to prescribed confining pressure

7. Drive the plunger manually using displacement control to just contact the specimen

8. Reset or zero readings of actuator displacement and forces

9. Start programmed test control at a rate 200 N/s

10. Stop the test when failure is observed

Procedure for the Damage Controlled Brazilian Test in Confined Condition

1. Cut and prepare the specimens using appropriate means, end faces shall be flat within 0.25 mm, and square and parallel to within 0.25 °

2. Cut two circles of copper foil for the two end faces of a disc, and long strip copper foil for the periphery of the disc; wrap the disc with these three foils and solder the seams with soldering iron

3. The sealed specimen shall be wrapped around its periphery with one layer of the masking tape

4. Glue two LVDT holder diametrically opposite on the periphery of the disc and mount two LVDT into the holders, as shown in Fig. 3.3

5. Mount the specimen assembly squarely in the loading jaw, put the loading jaw on top of the S-shaped load cell, as shown in Fig. 3.5

6. Close and refill the triaxial cell with confining fluid

7. Pressurize the triaxial cell to prescribed confining pressure

8. Drive the plunger manually using displacement control to just contact the specimen

9. Reset or zero readings of actuator displacement, forces, and LVDTs

10. Start programmed test control at a rate 0.00002 mm/s

11. Stop the test when post-peak plateau is observed